UC Berkeley

UC Berkeley Electronic Theses and Dissertations

Title

Tailoring spin and charge order of two-dimensional crystals through intercalation and heterostructure design

Permalink

https://escholarship.org/uc/item/5bx393x9

Author

Husremovic, Samra

Publication Date

2024

Peer reviewed|Thesis/dissertation

eScholarship.org Powered by the California Digital Library
University of California

Tailoring spin and charge order of two-dimensional crystals through intercalation and heterostructure design

by

Samra Husremović

A dissertation submitted in partial satisfaction of the

requirements for the degree of

Doctor of Philosophy

in

Chemistry

in the

Graduate Division

of the

University of California, Berkeley

Committee in charge:

Professor D. Kwabena Bediako, Chair
Professor Jeffrey R. Long
Professor Sayeef Salahuddin

Spring 2024

Tailoring spin and charge order of two-dimensional crystals through intercalation and heterostructure design

Copyright 2024
by
Samra Husremović

Abstract

Tailoring spin and charge order of two-dimensional crystals through intercalation and heterostructure design

by

Samra Husremović

Doctor of Philosophy in Chemistry

University of California, Berkeley

Professor D. Kwabena Bediako, Chair

This thesis describes the synthesis and fabrication of various two-dimensional (2D) crystals and heterostructures that exhibit long-range charge and spin ordering. By combining intercalation with the precise design of 2D interfaces, we tune and engender targeted magnetic and charge density wave (CDW) phases in 2D crystals. Furthermore, by marrying transmission electron microscopy (TEM) imaging, optical probes, and electron transport measurements, we establish robust structure-property relationships that may guide the development of 2D crystals for miniaturized electronic devices.

Chapter 1 presents a broad overview of the field of 2D magnets and CDWs. We discuss the fundamental hindrances in realizing magnetism in the atomically thin limit and build upon these insights to outline the design principles for 2D magnets. Further, intercalated transition metal dichalcogenides (TMDs) are introduced as promising material platforms for realizing 2D crystals with long-range spin order. This chapter also provides insights into the mechanisms underlying CDW formation through an orbital-based approach. Lastly, we give a brief introduction to the CDW properties of $1T-TaS_2$, a layered material that is extensively studied in this thesis.

Chapter 2 describes the first synthesis and magnetic characterization of iron-intercalated tantalum disulfide (Fe_xTaS_2) in the two-dimensional (2D) limit. The synthesized 2D Fe_xTaS_2 crystals exhibit hard ferromagnetic behavior down to the thinnest limit of this intercalation compound (Fe-intercalated bilayer TaS_2). Magnetic properties of this system are highly tunable and depend on the interplay between magnetocrystalline anisotropy, intercalation amount, homogeneity, and dimensionality.

Chapter 3 describes a synthetic framework for realizing heterostructures comprising intercalation compounds of TMDs through directed topotactic intercalation of van der Waals (vdW) assembled layers. The developed topochemistry method enables the creation of previously

inaccessible magnetic TMD heterostructures that demonstrate strong interfacial magnetic exchange effects only possible with atomically clean heterointerfaces.

Chapter 4 describes the topotactic transformation of nanothick $1T-TaS_2$ crystals into vertilateral heterostructures of $1T-TaS_2$ and H–TaS_2. These polytype heterostructures exhibit reliable multi-step resistance and chirality switching behavior encoded by the number of H–TaS_2 layers. The potential of strain engineering for realizing multifunctional phase change materials is also highlighted.

Chapter 5 describes the synthesis of Fe-intercalated polytype heterostructures comprising $1T-TaS_2$ and H–TaS_2. In these materials, modulating the intercalant amounts leads to simultaneous changes in long-range spin and charge ordering, which coexist in these materials. This chapter explores the competition and coexistence of structural and electronic phases, offering insights into designing multifunctional materials.

Chapter 6 describes the electronic and optical properties of moiré heterostructures comprising 2D $1T-TaS_2$ and monolayer $1H-WSe_2$. Interfacial charge transfer and moiré strain encode the global CDW ordering in $1T-TaS_2$ while simultaneously modulating the optoelectronic behavior of $1H-WSe_2$. This study outlines how local perturbations can be engineered to design ensemble electronic behavior.

Chapter 7 provides a brief summary of the tuning knobs used in this thesis and outlines possible avenues for future research.

Za moju porodicu.

Ku qoyskayga.

To my family.

Contents

Contents **ii**

List of Figures **iv**

List of Tables **vii**

1 Introduction **1**
1.1 Two-dimensional (2D) crystals 1
1.2 Two-dimensional magnetic crystals 3
1.3 Intercalated transition metal dichacogenides 7
1.4 Long-range charge order in 2D materials 10
1.5 Charge density waves in $1T-TaS_2$ 16
1.6 Similarities between long-range charge and spin order phases 18

2 Hard ferromagnetism down to the thinnest limit of iron-intercalated tantalum disulfide **19**
2.1 Abstract 19
2.2 Introduction 20
2.3 Results and discussion 21
2.4 Conclusions 36
2.5 Methods Chapter 2 37

3 Tailored topotactic chemistry unlocks heterostructures of magnetic intercalation compounds **43**
3.1 Abstract 43
3.2 Introduction 44
3.3 Results and discussion 45
3.4 Conclusion 67
3.5 Methods Chapter 3 67

4 Encoding multistate charge order and chirality in endotaxial heterostructures **73**
4.1 Abstract 73

4.2 Introduction 74
4.3 Results and Discussion 75
4.4 Conclusion 91
4.5 Methods Chapter 4 92

5 Intercalation simultaneously tunes spin and charge order in polytype heterostructures 96
5.1 Introduction 96
5.2 Results and Discussion 97
5.3 Conclusion 108
5.4 Methods Chapter 5 108

6 Local interface effects direct global charge ordering in a van der Waals heterostructure 110
6.1 Introduction 110
6.2 Results and Discussion 112
6.3 Conclusion 123
6.4 Methods Chapter 6 124

7 Conclusions and outlook 128

Bibliography 130

List of Figures

1.1 Mechanical exfoliation of graphite. 1
1.2 Tuning knobs for 2D materials. 2
1.3 Differences in magnetic ordering of 2D Ising and Heisenberg magnets. 4
1.4 Magnon density of states (DOS). 5
1.5 Boundary surfaces for d-orbitals and their complex linear combinations. 6
1.6 Interstitial sites in $2H$ TMDs. 8
1.7 Intercalation of $2H$ TMDs. 8
1.8 Qualitative d orbital splitting diagrams for Fe^{2+} centers in the octahedral (Oh) and trigonal antiprismatic (D_{3d}) ligand environments. 9
1.9 Superstructures of Fe intercalants in Fe_xTaS_2. 9
1.10 Dispersion relation for a 1D chain of hydrogen atoms. 11
1.11 Dispersion relation for a 1D chain of hydrogen atoms with a doubled unit cell. . 13
1.12 Energetic consequences of distorting a 1D chain of hydrogen atoms. 14
1.13 Lindhard response function for systems with different dimensionalities. 15
1.14 Nesting vectors for systems with different dimensionalities. 16
1.15 Charge density wave properties of $1T-TaS_2$. 17
1.16 Spin and charge order encode magnetoelectronic phases. 18

2.1 Synthesis and characterization of 2D Fe_xTaS_2. 22
2.2 Ordering of intercalants in annealed samples. 23
2.3 HRTEM along the c-axis of Fe_xTaS_2. 23
2.4 Raman of Fe_xTaS_2 samples imaged with DPC-STEM. 24
2.5 Magnetotransport of an 11-layer Fe_xTaS_2 crystal. 26
2.6 Magnetotransport of an 11-layer Fe_xTaS_2 crystal. 27
2.7 Uniaxial magnetocrystalline anisotropy in low-dimensional Fe_xTaS_2. 29
2.8 Preparation of heterostructures with ultrathin TaS_2. 30
2.9 Preparation of heterostructures with ultrathin TaS_2. 31
2.10 Uniaxial magnetocrystalline anisotropy in ultrathin Fe_xTaS_2. 32
2.11 Temperature-dependent hysteresis closure of the 5-layer device. 33
2.12 Temperature-dependent hysteresis closure of the 3-layer device. 34
2.13 Temperature-dependent hysteresis closure of the 2-layer device. 35
2.14 Temperature dependence of the remanent ρ_{AHE} for the 5-layer device. 36

3.1 Nanoscale solid-state intercalation of vdW crystals and pristine heterostructures. 46
3.2 Raman spectra of $2H-TaS_2$ upon annealing in contact with different Fe precursors. 47
3.3 Atomic-resolution imaging of sample S2. 47
3.4 Treatment of $2H-TaS_2$ flakes with different Fe precursors. 48
3.5 Compositional analysis of $Fe_xC_yO_z$ precursors. 48
3.6 EEL spectra of $Fe_xC_yO_z$ films formed on flakes S1–S3. 49
3.7 X-ray photoelectron spectroscopy (XPS) of Fe precursors. 50
3.8 Spatially resolved electron energy loss spectroscopy (EELS) of sample S3. 51
3.9 Solid-state reactions of polycrystalline TaS_2 and Fe_2O_3. 51
3.10 PXRD patterns after heating polycrystalline TaS_2 and Fe_2O_3 mixed in a 4:1 or 7:1 stoichiometric ratio for 7 days at 900 °C. 52
3.11 Precursor patterning process. 53
3.12 Probing uptake and diffusion of Fe in $2H-TaS_2$. 54
3.13 Analysis of temperature-dependent four-dimensional scanning transmission electron microscopy (4D-STEM) data. 55
3.14 Spatially mapping the band structure of ultra-clean intercalated heterostructures with nanoARPES. 56
3.15 Core-level spectra of the Fe_xTaS_2/hBN heterostructure. 57
3.16 Intensity distribution of Fermi surface cuts. 57
3.17 Quantitative analysis of nano angle-resolved photoemission spectroscopic (nanoARPES) data. 58
3.18 Raman spectra of the sample measured with nanoARPES. 59
3.19 Synthesis and characterization of Fe-intercalated $2H$–NbS_2/$2H-TaS_2$ heterostructures. 60
3.20 Synthesis and characterization of co-intercalated heterostructures. 61
3.21 Magnetotransport of iron-intercalated $2H$–NbS_2/$2H-TaS_2$ heterostructures. . . 63
3.22 Temperature-dependent resistance of device D1. 64
3.23 Temperature-dependent magnetotransport of device D1. 65
3.24 Angle-dependent MR of device D1. 66

4.1 Polytype and charge density wave (CDW) transformations in TaS_2 flakes. 76
4.2 Thermally induced polytype and CDW transformations of sample S2. 77
4.3 Selected area electron diffraction (SAED) of heterostructures with different polytype compositions. 78
4.4 Mapping heterochiral CDW domains with four-dimensional scanning transmission electron microscopy (4D-STEM). 79
4.5 Raman response of sample S3. 80
4.6 Modeling of the CDW order parameter in TaS_2 heterostructures. 81
4.7 High-resolution TEM of TaS_2 heterostructures. 82
4.8 Optical detection of chirality in TaS_2 heterostructures. 83
4.9 Polytype transformations of sample S4. 83
4.10 Multistate resistance switching in TaS_2 heterostructures. 85

4.11 Multistate chirality switching in TaS_2 heterostructures. 86
4.12 Reproducibility of resistance profiles for sample S1. 87
4.13 Transport measurements of sample S4. 87
4.14 Nucleation of endotaxial polytype transformation. 88
4.15 Nucleation of polytype transformations at macroscopic flake defects. 89
4.16 Polytype transformations with successive heating cycles. 90

5.1 Synthesis of Fe-intercalated polytype heterostructures. 98
5.2 Optical contrast changes of $1\,T-TaS_2$ resulting from annealing only versus thermally-driven intercalation. 99
5.3 Coexistence of intercalant and CDW superlattice ordering in TH-Fe_xTaS_2 heterostructures. 101
5.4 Electronic evidence of spin and charge ordering in TH-TaS_2 heterostructures. . . 103
5.5 Optical measurements of the interplay between intercalant and CDW ordering. . 104
5.6 Temperature-dependent Raman spectra of D3:R1, D3: R2 and a unintercalated TH-TaS_2 heterostructure. 105
5.7 Effects of intercalant ordering on the thermal hysteresis of the CDW phase. . . . 106
5.8 Switching of magnetic states in device D3 with 10 ms electrical pulses. 107

6.1 Electronic measurements of CDW phase transitions in $1H-WSe_2/1\,T-TaS_2$ heterostructures. 113
6.2 Electronic band structure of $1\,T-TaS_2$ and its heterinterface with $1H-WSe_2$. . . 115
6.3 Thickness and twist dependence of CDW ordering in $1\,T-TaS_2/1H-WSe_2$ heterostructures 116
6.4 Raman spectra of device D1. 117
6.5 CDW suppression in an nearly aligned heterostructure of 5-layer $1\,T-TaS_2$ interfaced with $1H-WSe_2$. 117
6.6 Local charge transfer characteristics across CDW phases and twist angles. . . . 118
6.7 Band structure calculations of the high-symmetry nearly aligned heterostructure and standalone $1\,T-TaS_2$ 119
6.8 Effects of heterostructuring on the optical properties of $1H-WSe_2$ 121
6.9 Raman spectra of $1H-WSe_2$ for the nearly aligned (S1) and misaligned (S3) heterostructures of 3-layer $1\,T-TaS_2$ and monolayer $1H-WSe_2$. 121
6.10 Temperature-dependence reflection contrast (RC) for samples S5 and S2. 122

7.1 Opportunities for tuning the properties of 2D crystals. 128

List of Tables

6.1 DFT parameters for $1T-TaS_2/1H-WSe_2$ heterostructures. 127

Acknowledgments

I would like to start this section by expressing my gratitude to my science mentors, beginning with Rachel Austin. Rachel profoundly influenced my life by instilling in me the belief that I could pursue a career in science. As my first college professor and an exceptional research mentor, she went above and beyond to support me academically and personally. Without Rachel, I would not be a chemist today.

I also want to thank Geneva Laurita, my mentor from Bates College, for providing invaluable support during my time at Bates and beyond. She has been an exceptional role model and has significantly contributed to my passion for materials chemistry.

I am sincerely grateful to my PhD advisor, Kwabena Bediako, for his unwavering support and guidance throughout my PhD journey. Being a part of his first cohort of students was both challenging and rewarding, and I experienced immense personal and professional growth while building the lab with Kwabena. He has always challenged me to think critically about my research, evaluate my findings, and plan the next steps. Despite being fans of rival football teams, Arsenal and Manchester United, I believe we have made an excellent team.

I would also like to express my sincere appreciation to the other mentors who have supported me throughout graduate school. Sinéad has been a great source of encouragement, which has been invaluable. Karen's patience in teaching me TEM techniques has also contributed significantly to my success. I would also like to thank other NCEM researchers, including Song, Rohan, Colin, Mary, John, and Jim, for their help and encouragement over the years. Additionally, I am grateful for the support of the Nanolab staff, especially Allison and Ryan, whose guidance and expertise in the clean room have boosted my confidence.

Moreover, I am incredibly thankful to all of my collaborators and coauthors who have engaged in scientific discussions with me and made this work possible. I want to extend a special appreciation to Medha and Katie for their valuable contributions in finalizing the last two chapters of my thesis.

Additionally, I am extremely grateful for my amazing labmates in the Bediako lab. Berit Goodge, Lilia Xie, Ellis Kennedy, Valerie McGraw, Jonathon Nessralla, Madeline Van Winkle, Matthew Erodici, Ted Zhang, Zhizhi Kong, Oscar Gonzalez, Isaac Craig, Sonal Maroo, Sanaya Fender, and Garrett Hegel, your support, friendship, and camaraderie have been vital to my success. I want to give a special thank you to Zhizhi for being a kind and patient friend and for always surprising me with candy. My undergrads, Linda and Alberto, have also made significant contributions to my PhD, and it has been an honor to be a part of their academic journey.

I also want to thank all my friends who have stood by me throughout these years. To my childhood friends Nidžara, Emina, and Lejna, thank you for your friendship from when we spent most of our time playing with Bratz dolls to now. It has been an honor sharing life milestones with you. To my college friends Shanina, Gideon, and Bantu, thank you for your encouragement along this journey. Lastly, I deeply appreciate the invaluable support from my friends at Berkeley: Priscilla, Mirza, Lydia, and Ziad.

I am also immensely thankful to my family for supporting me throughout my educational journey. My parents have always prioritized my well-being and encouraged my aspirations. A special thank you to my mom for inspiring me to pursue college in the US, which I would not have done otherwise. My brothers have been my biggest supporters, offering me endless love and motivation. My grandparents, Nadža, Emin, Sabina, and my late grandpa Šekib, have also been my greatest fans, even from afar. Although grandpa Šekib is no longer with us, I know he would have been immensely proud of me. My grandparents have played a pivotal role in my upbringing by taking care of me and providing me with the resources to succeed. I am deeply thankful for them. I would also like to extend my gratitude to my aunts Saka, Hajra, and Seka, as well as my uncle Muhamed and cousin Mia, for their support over the years.

A heartfelt thank you to my Aabo Ahmed and Hooyo Nassim for their love and support. Your encouragement has been pivotal in my success. I am also grateful for my Walaalos Samatar and Khayre, Walashay Asli, Habaryar Amina, Habaryar Suad, Habaryar Nafisa, Abti Ibrahim, and Shania Johnson. Being part of your family has provided me with a strong sense of belonging and has had an immensely positive impact on my PhD journey.

Lastly, I want to express my deepest gratitude to my husband, Guleed. His support, positivity, and kindness have made my PhD journey possible. Moreover, Guleed is also an amazing scientist whom I am constantly inspired by and learn so much from. Waan ku jeclahay.

Chapter 1

Introduction

1.1 Two-dimensional (2D) crystals

Two-dimensional crystals are materials that are one or a few atoms thick. One of the first studied 2D crystals was derived from graphite, a carbon-based mineral that comprises sheets of carbon atoms held together by weak van der Waals (vdW) forces (Figure 1.1). These weak interlayer interactions enabled Geim and Novoselov[1] to separate the atomic sheets of graphite with adhesive tape, yielding a single sheet of carbon atoms called graphene (Figure 1.1). In their groundbreaking research that earned them the Nobel Prize, they discovered that graphene, a semimetal, possesses exceptional electronic characteristics not observed in bulk

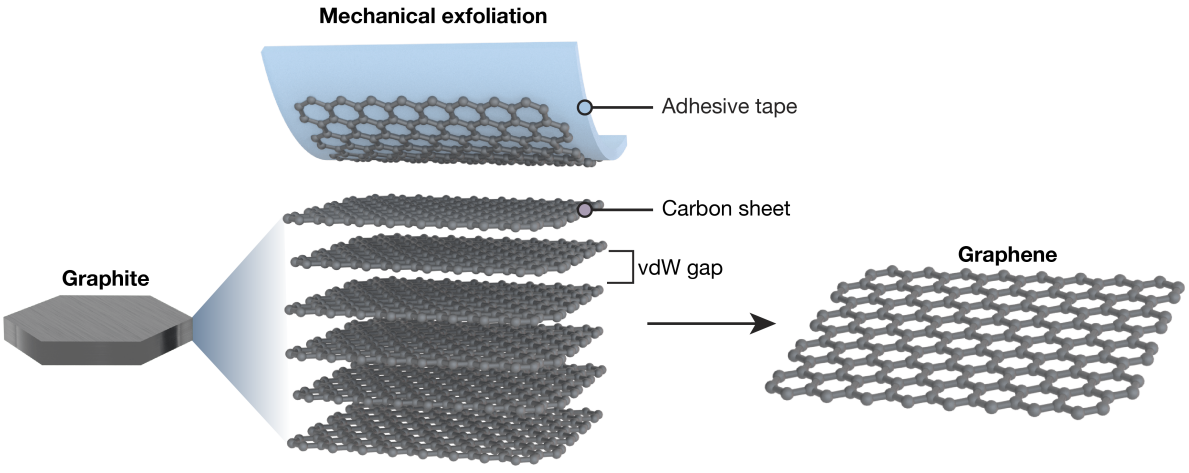


Figure 1.1: Mechanical exfoliation of graphite. Graphite consists of carbon sheets separated by van der Waals (vdW) gaps. These sheets can be isolated via mechanical exfoliation using adhesive tape, resulting in free-standing sheets of carbon known as graphene.

metallic graphite.[2] For instance, the charge carriers within graphene exhibit behaviors akin to massless particles moving at relativistic velocities. Subsequently, graphene and its analogs have been extensively studied, revealing a spectrum of exotic physical phases, encompassing superconductivity, ferromagnetism, and correlation-driven non-trivial topology.[3–7] These studies of graphene ignited the field of 2D materials, leading to extensive efforts to expand the library of 2D crystals, develop novel methods to tune and measure 2D systems and integrate them into technologically relevant device schemes.[8]

Two-dimensional (2D) materials offer a high degree of structural flexibility, providing a rich phase space for realizing targeted physical properties (Figure 1.2). These materials harbor surfaces that can be functionalized with a diverse range of organic and inorganic chemical species, which can also be intercalated between the van der Waals (vdW) layers.[9–12] Furthermore, additional variables uniquely addressable for 2D systems can be employed to transform the properties of these crystals. For instance, owing to the weak interlayer interactions in vdW materials, dissimilar layers can be assembled into heterostructures with complete structural freedom, and the layers can be stacked with arbitrary azimuthal orientations (twist angles). Through this approach, emergent physics that is not present in freestanding layers can be realized and deterministically altered.

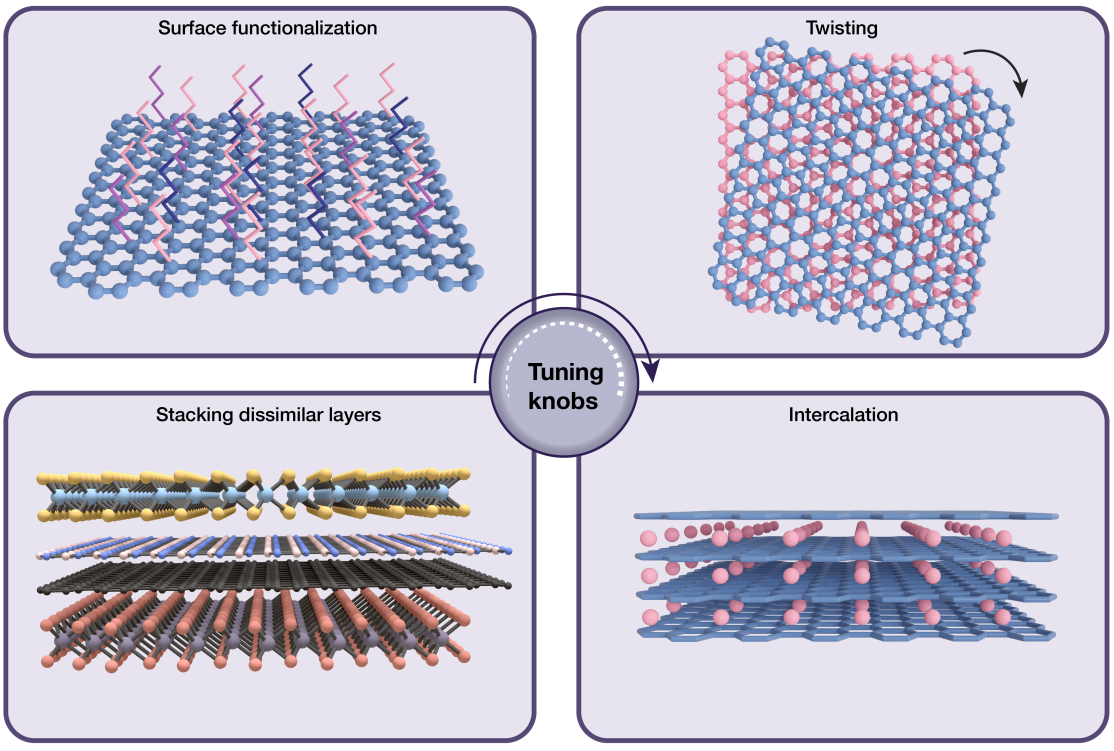


Figure 1.2: Tuning knobs for 2D materials.

The combination of solid-state synthesis, mechanical exfoliation, and post-synthetic tuning knobs have enabled researchers to realize 2D materials that exhibit a wide range of electronic properties.[8] These ultrathin materials offer a tantalizing opportunity as components of miniaturized next-generation electronic devices. However, until 2017, one technologically integral property was missing from the 2D materials library—magnetism. The long-awaited 2D magnetism was realized in $Cr_2Ge_2Te_6$[13] and Fe_3GeTe_2[14], opening doors to the fundamental understanding of long-range magnetic order in the 2D limit and the practical application of miniaturized magnetic devices.

1.2 Two-dimensional magnetic crystals

The relatively sluggish development of 2D magnets compared to other 2D materials may be attributed to the fundamental differences between 2D and 3D magnets. This is evidenced by the fact that when a bulk material is reduced to a two-dimensional form, its long-range magnetic order does not always persist. To understand this phenomenon, we will detail the fundamental differences between 2D and 3D magnets and outline how these translate into chemical design principles for novel 2D magnets.

For magnets with any dimensionality, we can write the energy associated with spins interacting with an external magnetic field (H) and other spins (S) by the spin Hamiltonian:[15, 16]

$$\mathcal{H} = -\sum_{i \neq j} J_{ij}(r)\hat{S}_i \cdot \hat{S}_j + \sum_i A(\hat{S}_i^z)^2 - \sum_{i \neq j} \vec{D}_{ij} \cdot (\hat{S}_i \times \hat{S}_j) - \sum_i \vec{\mu}_i \cdot \vec{H} \tag{1.1}$$

in which i and j are two lattice sites with a local magnetic moment and $\hat{S}_i$ and $\hat{S}_j$ are the spin operators. J_{ij} is an exchange constant that depends on the distance and dominant type of exchange interaction occurring between the magnetic moments, $\vec{D}_{ij}$ is a Dzyaloshinskii–Moriya vector, A is an easy axis anisotropy constant, $\vec{\mu}_i$ is the magnetic moment, and $\vec{H}$ is the magnetic field.

In equation 1.1, the first term, $-\sum_{i \neq j} J_{ij}(r)\hat{S}_i \cdot \hat{S}_j$, corresponds to spin-spin interactions including direct exchange, superexchange, and the Ruderman–Kittel–Kasuya–Yosida (RKKY) interaction[17, 18]. When the spin vector has no directional constraints, this interaction is termed the Heisenberg interaction, characterizing systems known as Heisenberg magnets (Figure 1.3a).[19, 20] Conversely, when spins are confined to a specific axis, their interaction is termed the Ising interaction (Figure 1.3b). The exchange interactions of Ising magnets can be represented as follows[19, 20]:

$$\mathcal{H}_{Ising} = -\sum_{i \neq j} J_{ij}(r)\hat{S}_i^z \cdot \hat{S}_j^z \tag{1.2}$$

The constraint of spins to an axis originates from the second term in equation 1.1. This term ($\sum_i A(\hat{S}_i^z)^2$) characterizes magnetic anisotropy (MA), a property of spins to exhibit a preferred orientation within the material due to their crystallographic environment

(magnetocrystalline anisotropy), shape, or stress.[21] We note that the first two terms of equation 1.1 are the most pertinent for the discussion herein.

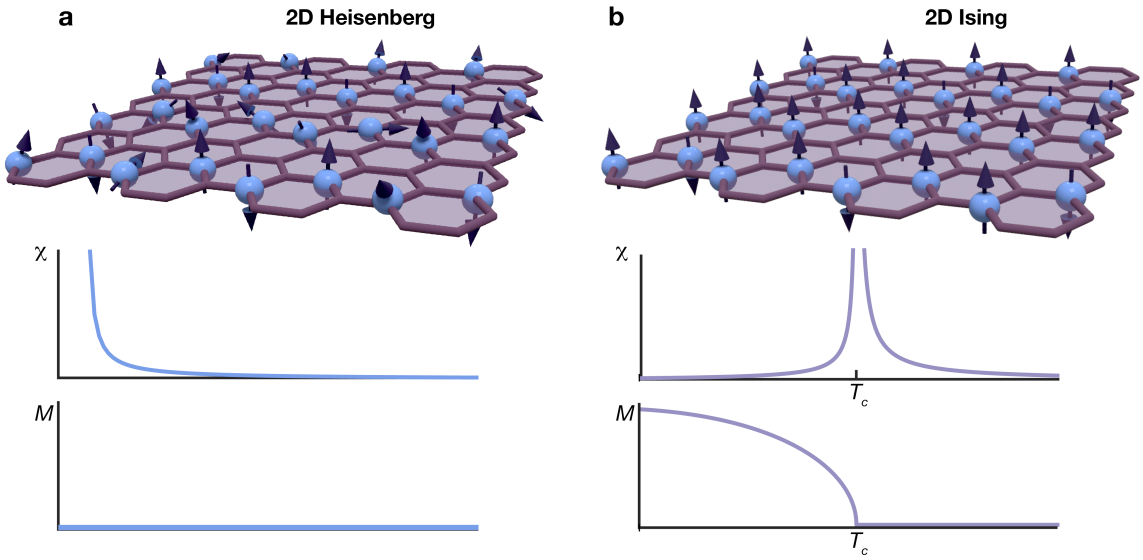


Figure 1.3: Differences in the magnetic ordering of 2D Ising and Heisenberg magnets. **(a, b)** Spin orientations and temperature-dependent magnetic susceptibility (χ) and magnetization (M) for systems described by the 2D Heisenberg **(a)** and 2D Ising **(b)** spin Hamiltonians. $T = T_c$ marks the magnetic ordering temperature. 2D Heisenberg magnets do not evince long-range magnetic order above zero temperature, while 2D Ising magnets display an onset of magnetism below $T = T_c$, where $T_c > 0$.

In 3D systems, long-range magnetic order can be stabilized with exchange interactions alone, and MA is not a prerequisite.[22, 23] However, for 2D magnets, MA is necessary for stabilizing long-range order.[13, 22, 23] Specifically, 2D Heisenberg systems lack magnetic anisotropy, and as per the Mermin–Wagner–Hohenberg theorem,[24, 25] they cannot display long-range magnetic order above zero temperature (Figure 1.3a). On the other hand, 2D Ising magnets possess uniaxial magnetic anisotropy and they can exhibit long-range magnetic order at nonzero temperatures (Figure 1.3b), as demonstrated by the exact solution of the 2D Ising(-Lenz) model[26, 27] by Onsager[28].

To understand the distinctions in magnetic behavior across different dimensions and spin orientations, we examine the prevalence of low-energy spin-wave excitations in these systems.[13, 22, 23] These excitations, called magnons, agitate spins and disrupt their long-range ordering (Figure 1.4a). Consequently, the presence of a non-negligible magnon density of states (DOS) at low energies can prevent the onset of magnetism at nonzero temperatures. As seen in Figure 1.4b, 2D and quasi-2D (multilayer) materials exhibit a large DOS of low-energy magnons compared to their 3D analogs.[13, 18, 22, 23] However, in the presence

of magnetic anisotropy, a gap appears in the magnon DOS at low energies, hence precluding the existence of low-energy magnons and enabling long-range magnetic order even in 2D systems (Figure 1.4c).

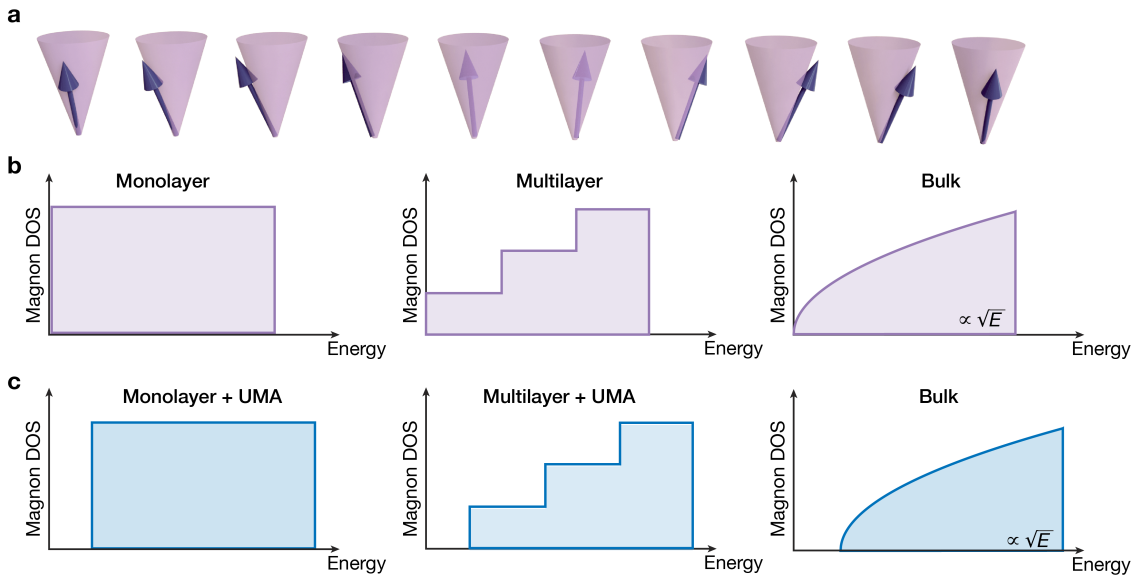


Figure 1.4: Magnon density of states (DOS). **(a)** Schematic illustration of a magnon. **(b, c)** Magnon DOS for systems of varying dimensionalities, shown without **(b)** and with **(c)** uniaxial magnetic anisotropy (UMA). The introduction of UMA results in the emergence of a gap in the magnon DOS.

When developing new 2D magnets, it is paramount to incorporate magnetic anisotropy. The most effective approach for achieving this is by designing magnetocrystalline anisotropy (MCA), a property of materials where crystal structure locks spins into a particular orientation.[15] To achieve large MCA, two key ingredients are necessary: spin-orbital coupling and unquenched orbital angular momentum (UOAM). While increasing spin-orbital coupling can be straightforward by incorporating heavy elements into the structure, designing for UOAM is more complex. A simplified, orbit-oriented approach for designing significant UOAM will be discussed below.

Design of unquenched orbital angular momentum (UOAM)

To design systems with large UOAM, we will first start by broadly defining this property of materials, as adapted from reference [29].

In this thesis, we will focus on transition metal spin-bearing ions whose frontier orbitals are d orbitals. Notably, d orbitals (Figure 1.5, top) do not individually exhibit angular momentum. Instead, their electron distributions remain stationary, resembling standing

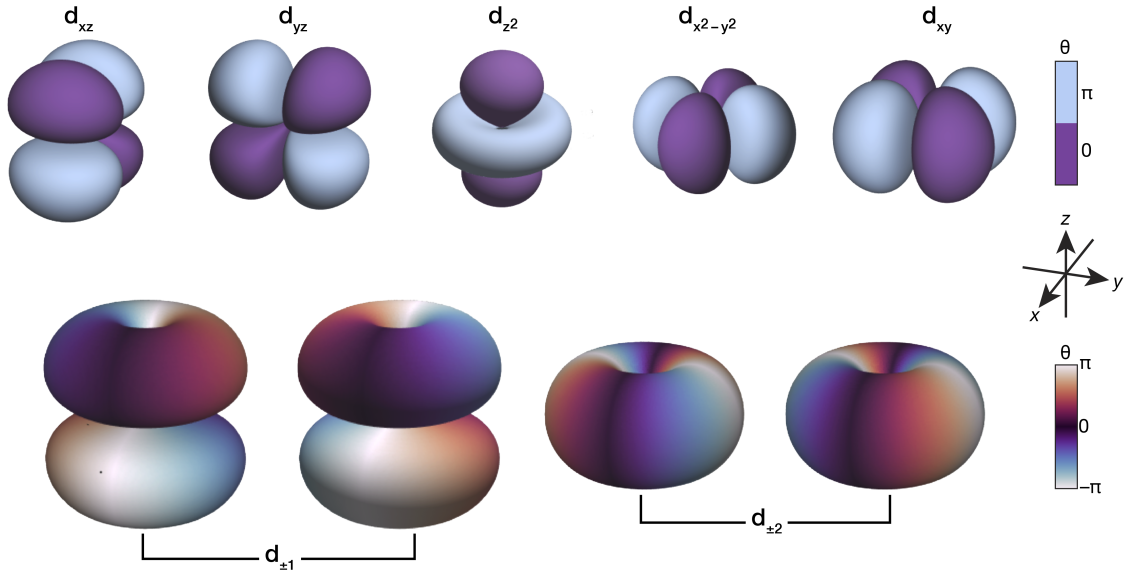


Figure 1.5: Boundary surfaces for d-orbitals and their complex linear combinations. Here, $d_{\pm1} = d_{xz} \pm id_{yz})/\sqrt{2}$ and $d_{\pm2} = d_{x^2-y^2} \pm id_{xy})/\sqrt{2}$. The orbital phase is denoted by θ. Consequently, the sign for the real-space orbitals is determined by $\cos\theta$.

waves in classical mechanics. However, their complex linear combinations possess well-defined angular momentum, analogous to traveling waves in classical mechanics. These linear combinations for d ($l = 2$) orbitals are:

$$d_{\pm1} = (d_{xz} \pm id_{yz})/\sqrt{2} \tag{1.3}$$

$$d_{\pm2} = (d_{x^2-y^2} \pm id_{xy})/\sqrt{2} \tag{1.4}$$

Note, we will refer to $d_{x^2-y^2}$ and d_{xy} as one rotation pair, and d_{xz} and d_{yz} as the second rotation pair since orbitals within each pair are related by a rotation around the z axis. The complex linear combinations of the rotation pairs are illustrated in Figure 1.5. Here, $d_{\pm2}$ orbitals carry $\pm2\hbar$ angular momenta about the z-axis, while $d_{\pm1}$ orbitals carry $\pm\hbar$ angular momenta about the z-axis. It is important to note that complex linear combinations of rotation pairs form if their component orbitals are degenerate (in other words, rotation pairs can hybridize/mix if they are degenerate). Moreover, for CLCs to carry unquenched orbital angular momentum, the two conjugate pairs must be unequally populated with electrons (this ensures $L \neq 0$).

In summary, to ensure significant UOAM, the focus should be on creating materials where the ligand environment of the spin-bearing centers results in (1) the degeneracy of orbitals within the rotation pairs and (2) an unequal population of orbitals within the rotation pairs. However, it is important to acknowledge that this design principle serves

as a guideline and does not comprehensively describe extended solids due to factors such as band formation, band hybridizations, and second-order perturbations from spin-orbit coupling (SOC), which may restore some UOAM.[29] Nevertheless, the rational design of spin-bearing centers with a large UOAM can serve as a valuable and intuitive blueprint for novel 2D magnets. Accordingly, materials that enable precise control over the placement of spin-bearing ions and their oxidation states offer a promising platform for realizing atomically thin crystals hosting long-range spin coherence.

1.3 Intercalated transition metal dichacogenides

Parts of this section were adapted or reproduced from: Xie, L. S.; Husremovic, S.; Gonzalez, O.; Craig, I. M.; Bediako, D. K. *Journal of the American Chemical Society* **2022**, *144*, 9525–9542.[30]

Author contributions: S.H., O.G., and I.M.C. contributed equally to this work.

Transition metal dichalcogenides (TMDs) are a class of materials in which transition metals coordinated by bridging chalcogenides form two-dimensional layers that stack via van der Waals (vdW) interactions along the crystallographic c axis. These materials crystallize in different polytypes where transition metals occupy trigonal prismatic (D_{3h}) or octahedral (O_h) crystallographic environments.[31] Regardless of the polytype, these layered crystals contain unoccupied octahedral and tetrahedral interstitial sites in the vdW interface, which are amenable to intercalation (Figure 1.6). As follows, this structure permits a myriad of species to be intercalated into these vdW interfaces, including spin-bearing transition metals (Figure 1.7).[32–35] The oxidation state and crystallographic preferences of spin-bearing intercalants determine the UOAM of the material. Therefore, the facile selection of intercalant species positions intercalated TMDs as promising platforms for designing systems with high MCA.

Iron-intercalated tantalum disulfide (Fe_xTaS_2) exhibits strong MCA attributed to the trigonally distorted octahedral ligand field surrounding Fe^{2+} centers (Figure 1.8).[36] The trigonal elongation renders the $d_{x^2-y^2}$ and d_{xy} orbitals degenerate and unequally filled, engendering significant UOAM ($L = 2$) and thus substantial MCA (Figure 1.8). Consequently, strong out-of-plane spin anisotropy and hard ferromagnetism are observed in this system.[37, 38]

In addition to MCA, another crucial factor in modulating the magnetic behavior of $Fe_{1/4}TaS_2$ is the ordering of Fe ions in the ab plane. In Fe_xTaS_2, perfect Fe superlattices from with $x = 1/4$ and $x = 1/3$. For instance, considering $2H$-MS_2 with a lattice constant a_0, a supercell with $a' = 2a_0$ arises at $x = 1/4$, while $a' = \sqrt{3}a_0$ is observed at $x = 1/3$. Deviating from these ordered supercells introduces inhomogeneous iron ordering and exchange interactions, often leading to competing magnetic interactions and more complex ground states.[39] Nevertheless, this disorder also gives rise to intriguing phenomena, such as very large magnetoresistance.[40] Thus, Fe_xTaS_2 serves as a rich magnetic platform for investigating how

modulating dimensionality, intercalant ordering, and interface effects modulate the long-range order in systems with large MCA.

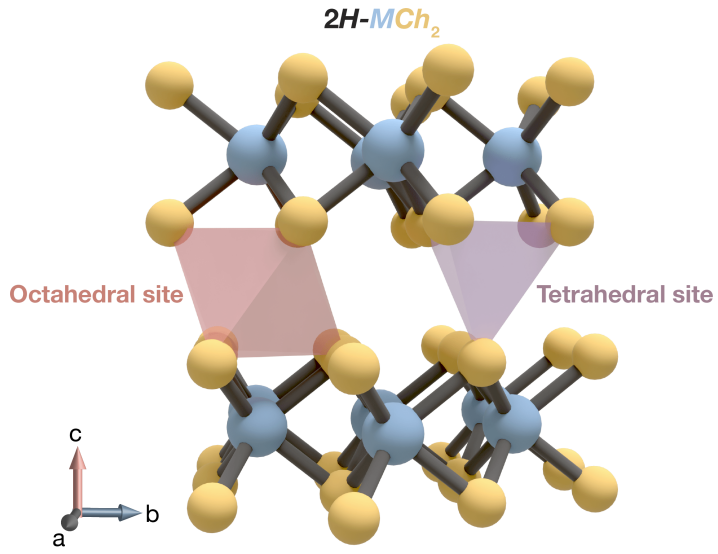


Figure 1.6: Interstitial sites in $2H$ TMDs. Native $2H$ TMDs contain empty octahedral and tetrahedral interstitial sites that are amenable to intercalation.

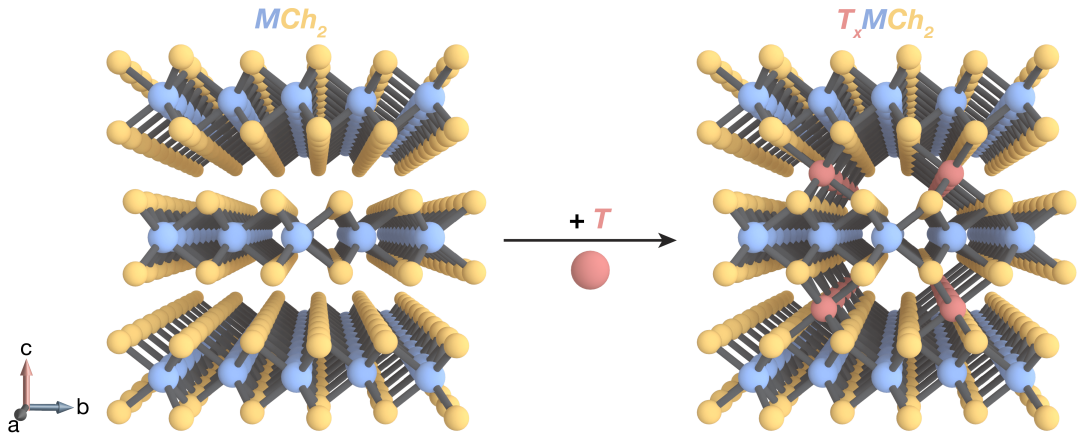


Figure 1.7: Intercalation of $2H$ TMDs. $2H$ TMDs with the formula MCh_2 can be intercalated with transition metals (T) to yield T_xMCh_2.

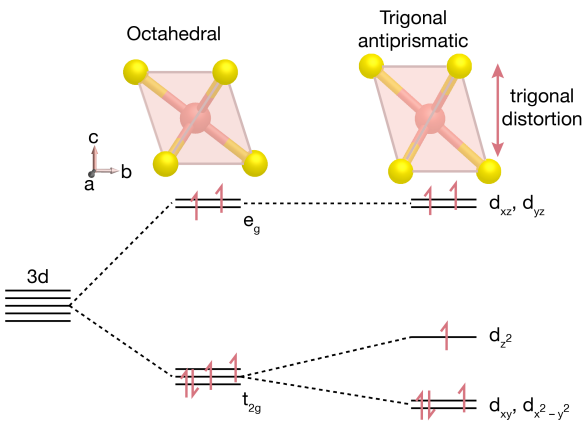


Figure 1.8: Qualitative d orbital splitting diagrams for Fe^{2+} centers in the octahedral (Oh) and trigonal antiprismatic (D_{3d}) ligand environments. The D_{3d} point group is representative of Fe in Fe_xTaS_2.

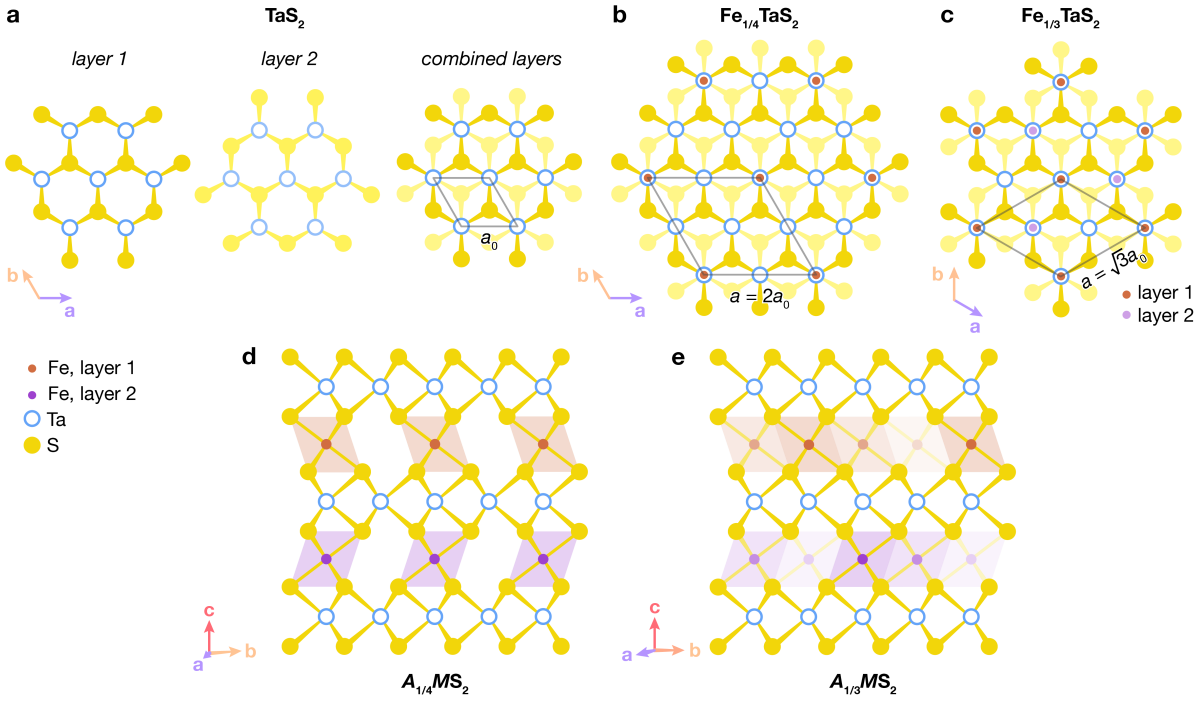


Figure 1.9: Superstructures of Fe intercalants in Fe_xTaS_2. **(a)** Structures of two unintercalated $2H-TaS_2$ layers with a lattice constant a_0. **(b)** $Fe_{1/4}TaS_2$ with a supercell lattice constant of $a' = 2a_0$. **(c)** $Fe_{1/3}TaS_2$ whose lattice constant is $a' = \sqrt{3}a_0$. **(d,e)** Structures of $Fe_{1/4}TaS_2$ and $Fe_{1/3}TaS_2$ viewed perpendicular to the c crystallographic axis.

1.4 Long-range charge order in 2D materials

Charge density waves (CDWs) are electronic phases characterized by static changes in the distribution of electronic charge coupled with lattice distortions. These phases are often accompanied by significant and reversible shifts in electrical resistance, which can be used for information processing and storage in phase-change memory.[41] Additionally, since both CDWs and unconventional superconductivity result from strong electronic correlations, they are often competing quantum phases.[42–44] Therefore, understanding how CDWs originate and identifying the variables we can adjust to control them is essential for developing novel electronic materials and high-temperature superconductors. However, despite extensive research, the origin of CDWs is still a topic of debate. This chapter aims to describe the proposed mechanisms of CDW formation, focusing on the orbital approach for deriving the electronic structure of extended solids. Moreover, we will examine outstanding questions in this research area and explore opportunities for tailoring CDW behavior using the unique tuning knobs available for 2D materials.

Electronic instability in 1D systems

To understand CDW formation in 2D crystals, we will first describe CDW formation in simpler, 1D systems. The formation of CDWs in 1D systems was first described by Peierls, who predicted a fundamental electronic instability in 1D chains of atoms, driving a periodic lattice distortion.[45, 46] Here, we will explain the origin of this instability using the tight-binding approach adapted from references [45, 47–50].

First, consider a 1D chain of hydrogen atoms, spaced apart by distance a and each labeled by an index n (Figure 1.10a). On each atomic site, there is a half-filled H 1s atomic orbital, ϕ_n. Using ϕ_n as the basis function, we can write out the following symmetry-adapted linear combinations (SALCs), also known as Bloch functions:

$$\Psi_k = \sum_n e^{ikna}\phi_n \tag{1.5}$$

Here, k is an index describing which irreducible representation Ψ transforms as. This index also has a physical meaning; each k is a wave vector and a measure of momentum ($p = \hbar k$, where p is the crystal momentum). Now, we will evaluate the Bloch functions at $k = 0$ and $k = \pi/a$.

$$\Psi_0 = \sum_n e^0\phi_n = \sum_n \phi_n = \phi_1 + \phi_2 + \phi_3 + \phi_4 + ... \tag{1.6}$$

$$\Psi_{\frac{\pi}{a}} = \sum_n e^{\pi in}\phi_n = \sum_n (-1)^n\phi_n = \phi_1 - \phi_2 + \phi_3 - \phi_4 + ... \tag{1.7}$$

The wave function is most bonding and has the lowest energy at $k = 0$ (Figure 1.10b). Conversely, the wave function at $k = \pi/a$ represents the most antibonding state, thus having the highest energy (1.10b). The wave functions display different numbers of nodes between

these extremes. Note that the range of distinct k values extends from $-\pi/a$ to π/a, defining the first Brillouin zone. Wave vectors at the Brillouin zone boundary are termed Fermi wave vectors (k_F), and assessing only unique k values within the range of $-k_F$ to $+k_F$ fully characterizes a crystalline system that follows periodic boundary conditions.

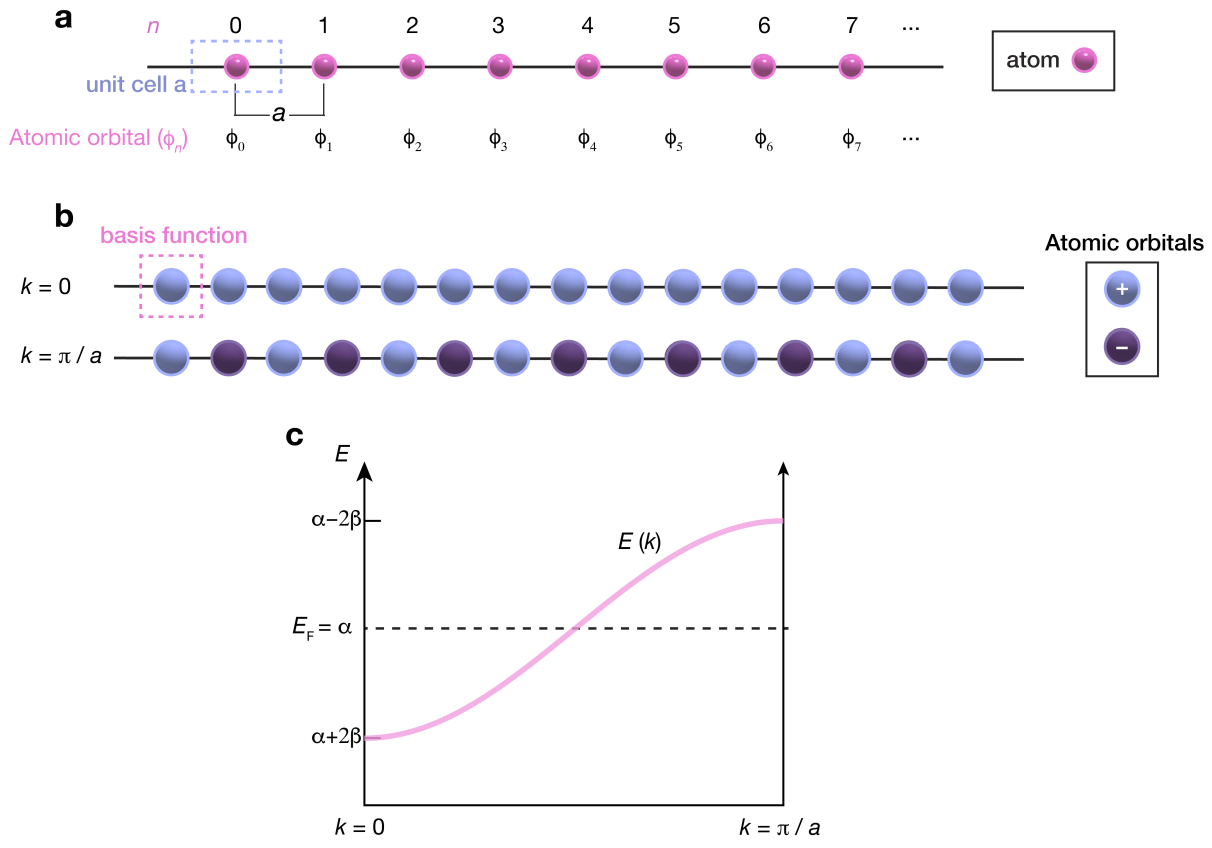


Figure 1.10: Dispersion relation for a 1D chain of hydrogen atoms. Constructing the dispersion relation (E vs k) for a 1D chain of hydrogen atoms using the tight-binding approach. **(a)** Illustration of the 1D chain of hydrogen atoms with a unit cell a. Each atom is labeled by an index n. The basis wavefunction for each atom (a H 1s orbital) is labeled with ϕ_n. **(b)** Linear combinations of atomic orbitals (LCAO), also known as Bloch functions, at $k = 0$ and $k = \pi/a$ points in reciprocal space. **(c)** Dispersion relation, $E(k)$, for the 1D chain of H atoms. Here, α is on-site energy, and β is the interaction energy between neighboring orbitals.

Considering only nearest-neighbor interactions, an analytical expression for the energy of Bloch functions can be written as:[50]

$$E(k) = \alpha + 2\beta cos(ka) \tag{1.8}$$

in which α is the on-site energy of the H 1s orbital and β is the interaction energy between two orbitals. The derived dispersion relation, describing the relationship between energy and momentum, is shown in Figure 1.10c. It is important to note that plots of $E(k)$ are commonly referred to as band structures, and this terminology will be used throughout the remainder of this thesis. Each band has a capacity for two electrons, yet given our basis function contains only one electron, the Fermi level (E_{F}) resides precisely at the midpoint of the band (refer to Figure 1.10c).

Next, we will expand the unit cell size from a to $2a$ while maintaining the structure of the 1D chain (see Figure 1.11a). Unit cell doubling necessitates the creation of new basis functions. These comprise the bonding and antibonding molecular orbitals constructed from two H 1s atomic orbitals (Figure 1.11b). As follows, the number of bands at each unique k point, now ranging from $-\pi/2a$ to $\pi/2a$, doubles (Figure 1.11c), and the dispersion relation folds on itself along $k = \pi/2a$ (Figure 1.11d).

Following band folding, there are two degenerate states at $k = \pi/2a$—one occupied by electrons and the other empty (Figure 1.11c–d). Removing the degeneracy of these bands would lower the energy of the occupied electronic states, indicating an electronic instability within the system. To remove this instability, 1D chains undergo distortion, resulting in the formation of an alternating pattern of long and short bonds (Figure 1.12a). This structural symmetry breaking lifts the degeneracy of bands at $k = \pi/2a$ (Figure 1.12b–d), leading to the emergence of a band gap that reduces the energy of the filled bands.

Notably, while the propensity for distortion is the strongest for systems with half-filled bands, any 1D system with partially filled bands is susceptible to Peierls' distortion.[47] To expand on this, we define the band filling factor (f) as 1 if all bands are fully occupied and 0 if all bands are unoccupied. If $f = 1/m$, then $k_F = \pi/ma$, where a is the unit cell of the undistorted lattice. Thus, according to our treatment of the 1D chain of H atoms with $f = 1/2$ and $m = 2$, distortions that increase unit cell size by a factor of m will introduce a band gap at the Fermi level, lowering the energy of the system.[47] As follows, electron filling determines the energetically favorable distortions and is a crucial factor in fine-tuning and modifying CDW systems.

To gain a deeper understanding of the Peierls' distortion mechanism, we examine the free electron gas model. In this model, electrons follow the Lindhard function in response to an external perturbation (Figure 1.13).[45] For a 1D electron gas, the real part of the Lindhard response function diverges at $k = k_{\mathrm{F}}$, indicating an electronic instability and the presence of zero-energy electronic excitations at this wavevector.[44] These electronic excitations screen lattice vibrations (phonons) at $2k_{\mathrm{F}}$, consequently lowering their energy. This strong modification of phonon modes due to their interaction with electrons is called the Kohn anomaly.[45] The Kohn anomaly displays a strong temperature dependence; at the CDW transition temperature, phonon energy decreases to zero at $2k_{\mathrm{F}}$, and this "frozen" phonon leads to a lattice distortion.[44, 45] The Kohn anomaly underscores the importance of electron–phonon interactions in realizing CDWs. In the next section, we will discuss how the strength of this coupling becomes critical for stabilizing CDWs in 2D and 3D systems.

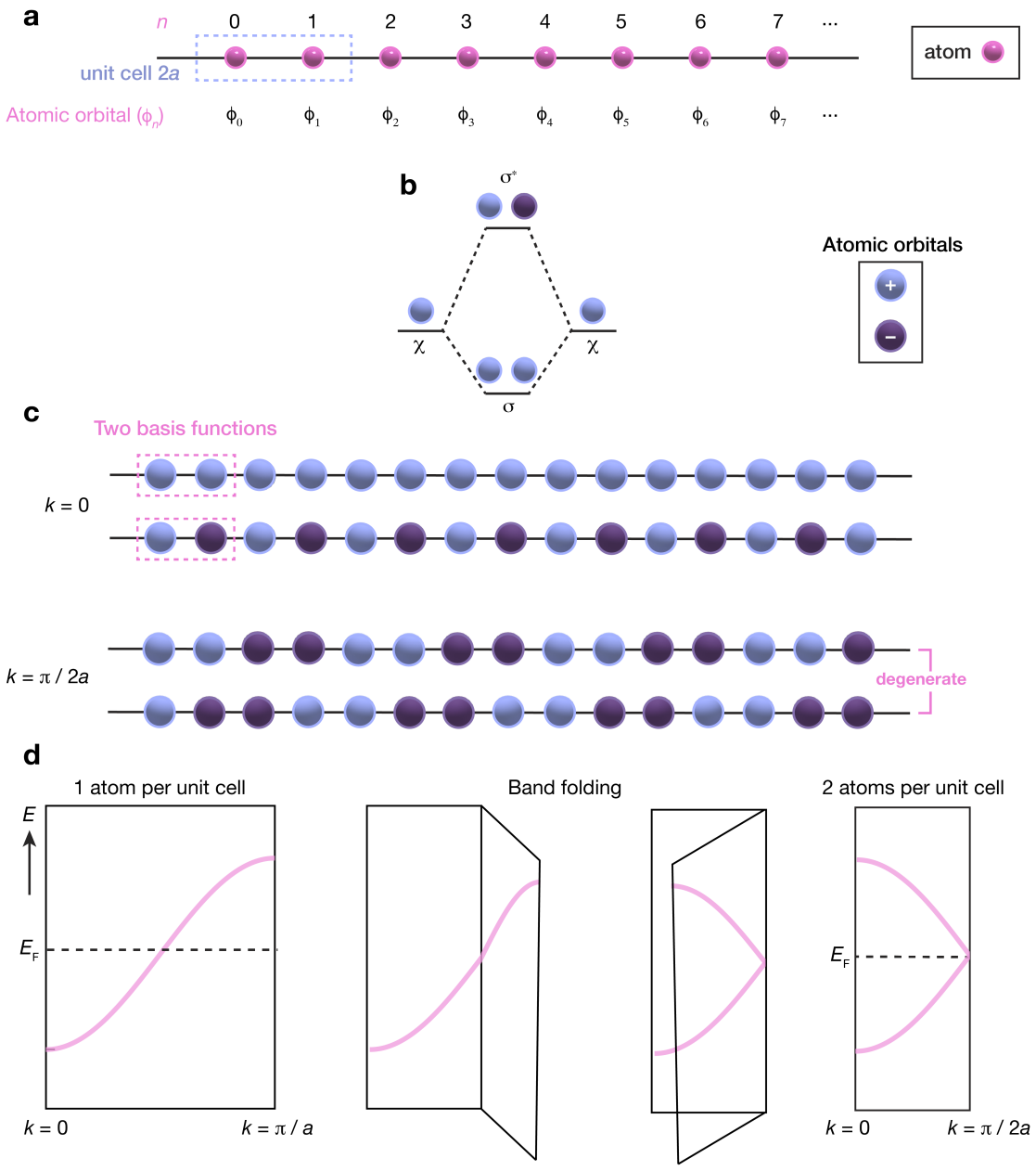


Figure 1.11: Dispersion relation for a 1D chain of hydrogen atoms with a doubled unit cell. **(a)** Linear chain H atoms whose unit cell was increased from a to $2a$. **(b)** Basis functions are constructed by forming bonding (σ) and antibonding (σ^*) molecular orbitals (MOs) from H 1s atomic orbitals (ϕ). **(c)** Bloch functions constructed with σ and σ^* basis functions at $k = 0$ and $k = \pi/a$. The number of bands at each k point doubles. **(d)** Band folding resulting from doubling of the unit cell.

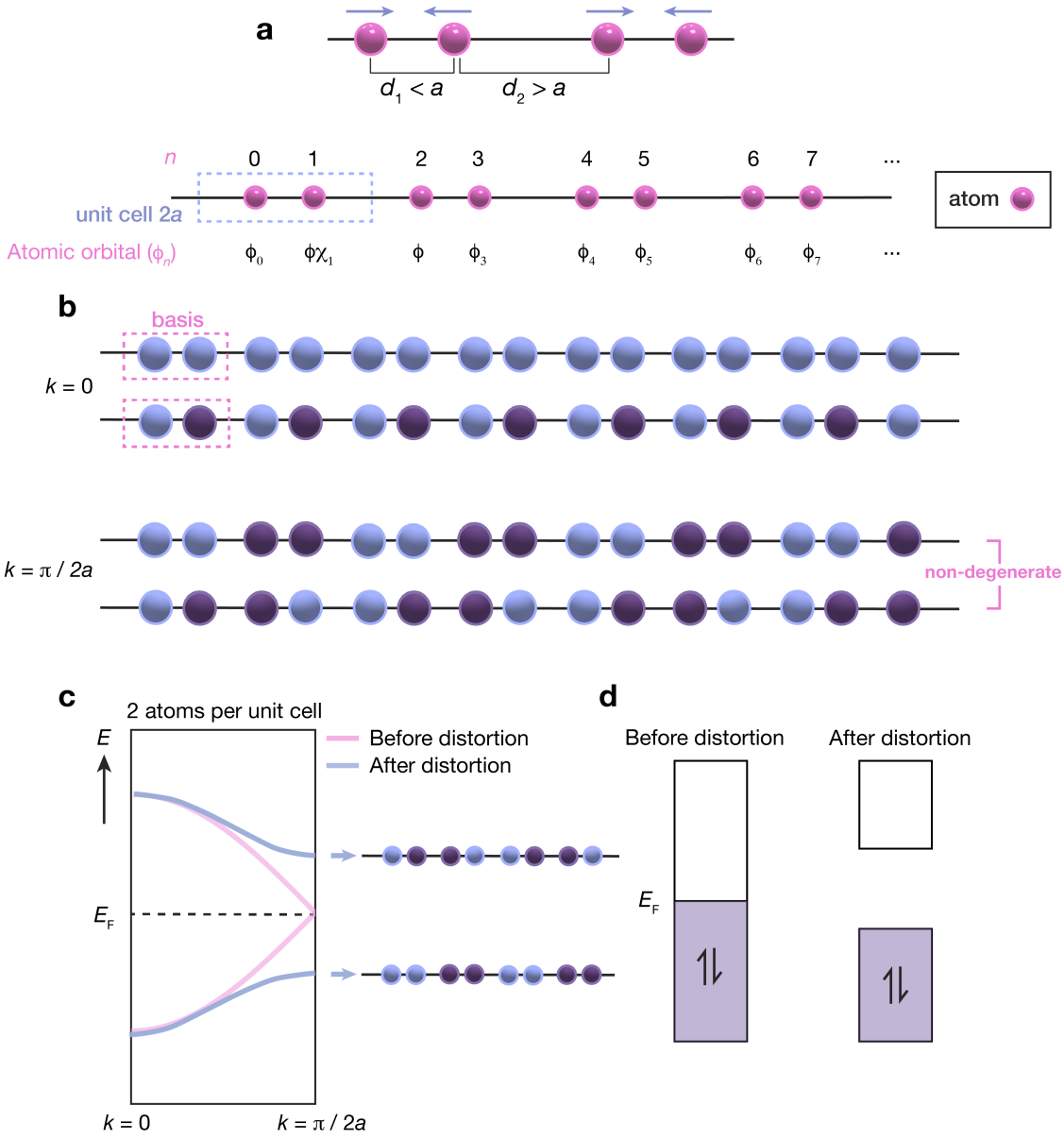


Figure 1.12: Energetic consequences of distorting a 1D chain of hydrogen atoms. **(a)** A 1D chain of hydrogen atoms exhibiting a periodic distortion, with neighboring distances alternating between short ($d_1 < a$) and long ($d_1 > a$), where a represents the interatomic spacing in an undistorted chain. **(b)** Bloch functions constructed of the distorted chain at $k = 0$ and $k = \pi/a$. **(c, d)** Change in the dispersion $E(k)$ **(c)** and band diagram **(d)** upon the onset of distortion.

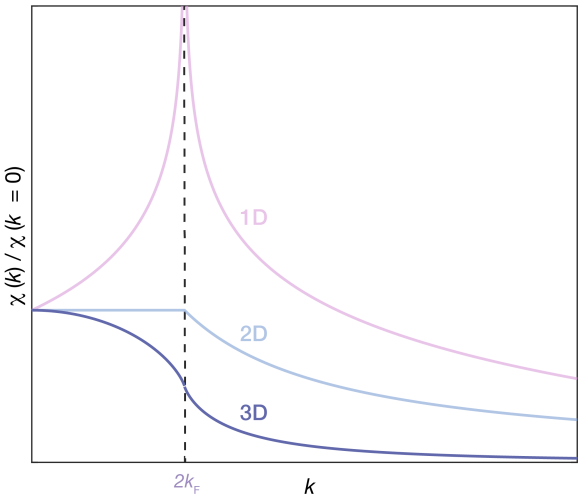


Figure 1.13: Lindhard response function for systems with different dimensionalities. Lindhard response function ($\chi(k)$ for 1D, 2D and 3D systems. For 1D, the function diverges at $k = 2k_{\mathrm{F}}$, while for 2D and 3D the function has a singularity at $k = 2k_{\mathrm{F}}$.

CDWs in 2D systems

The electronic instability inherent in 1D systems diminishes for 2D and 3D materials. This is evident in their Lindhard response function, which evinces a singularity at $k = 2k_F$ but does not diverge like the 1D response function (Figure 1.13).[45] To intuitively understand the differences in electronic instability between 1D and 2D systems, we will examine the differences in their Fermi surfaces, which are isoenergy cuts of $E(k)$ at $E = E_{\mathrm{F}}$.

In 1D systems, the Fermi surface is characterized by two points, namely $k_x = -k_F$ and $k_x = +k_F$, which are connected by a nesting vector, $\mathbf{q}_{nesting} = 2k_{\mathrm{F}}$ (Figure 1.14a). When the system is expanded into two dimensions, disregarding inter-chain coupling, the Fermi surface consists of two parallel lines separated by the vector $q = 2k_{\mathrm{F}}$, which are perfectly aligned when one segment is displaced by q (Figure 1.14c). This nesting of the Fermi surface by q indicates the presence of an electronic instability in the system, as distortions can create a gap at the nesting vector q, thereby stabilizing filled states. The extent of this instability is determined by the number of states connected by q on the Fermi surface, with a larger number resulting in a more pronounced instability. Since 2D systems have a circular Fermi surface and a smaller number of states nested by q, their electronic instability is diminished (Figure 1.14c). It is important to note that even in 2D and 3D systems, quasi-1D band pockets at the Fermi level can form (Figure 1.14d), resulting in Fermi nesting and electronic instability. However, this nesting is often imperfect, and the onset of CDWs may only open band gaps in parts of the Fermi surface, leaving metallic states behind that can lead to superconductivity.[51]

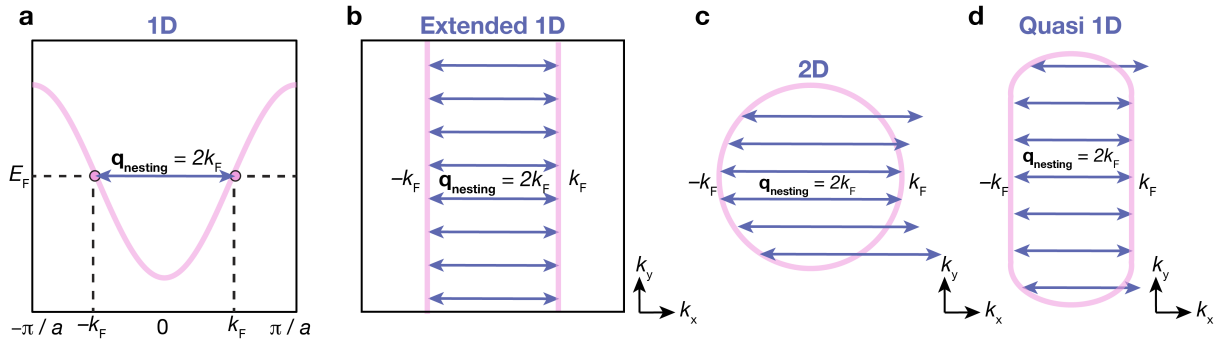


Figure 1.14: Nesting vectors for systems with different dimensionalities. Nesting vector for a 1D **(a)**, extended 1D **(b)**, 2D **(c)** and quasi 1D **(d)** systems.

Theoretical and experimental evidence supports that the importance of Fermi surface nesting diminishes in the regime of strong electron–phonon coupling.[52] This may seem surprising, given that electron–lattice interactions are central to the Peierls' mechanism (Fermi surface nesting mechanism). However, in the Peierls' picture, the coupling between electrons and phonons is, in fact, weak.[52] Consequently, the hallmarks of this distortion are: (1) band gap opening only for states nested by q, (2) a sharp peak in the Lindhard function, and (3) a Kohn anomaly at q. However, real materials rarely display these characteristics.[44, 53–55] Therefore, alternative explanations of CDW formation have been proposed, such as k-dependent electron–phonon coupling.[44, 53, 56–59]. Nevertheless, a unified mechanism for the formation of CDWs has remained elusive, thus necessitating an individual evaluation of the underlying mechanism for each material.

1.5 Charge density waves in $1T$–TaS_2

$1T-TaS_2$ is a van der Waals (vdW) crystal (Figure 1.15a) with a diverse charge density wave (CDW) phase diagram.[52] Below $\sim$ 500 K,[61–63] intralayer star of David (SOD) lattice distortion clusters form (Figure 1.15b), with twelve Ta ions contracting towards a central Ta ion. The tiling of these SOD units across the ab plane defines the CDW phase of $1T-TaS_2$. The incommensurate phase (IC-CDW), typically observed between 500 K and 350 K, shows sporadic nucleation of SOD units across the material, often attributed to Fermi nesting instability (Figure 1.15c,d).[64] Transitioning into the nearly-commensurate phase (NC-CDW), often observed between 350 K and 180 K, is marked by the formation of SOD domains separated by discommensuration networks. Subsequently, below $\sim$ 180 K, these networks vanish, leading to the formation of the commensurate phase (C-CDW), where the CDW supercell is commensurate with the underlying lattice and displays a $\sqrt{13} \times \sqrt{13}a$ periodicity, where a is the in-plane lattice constant of $1T-TaS_2$. In $1T-TaS_2$, changes in the CDW

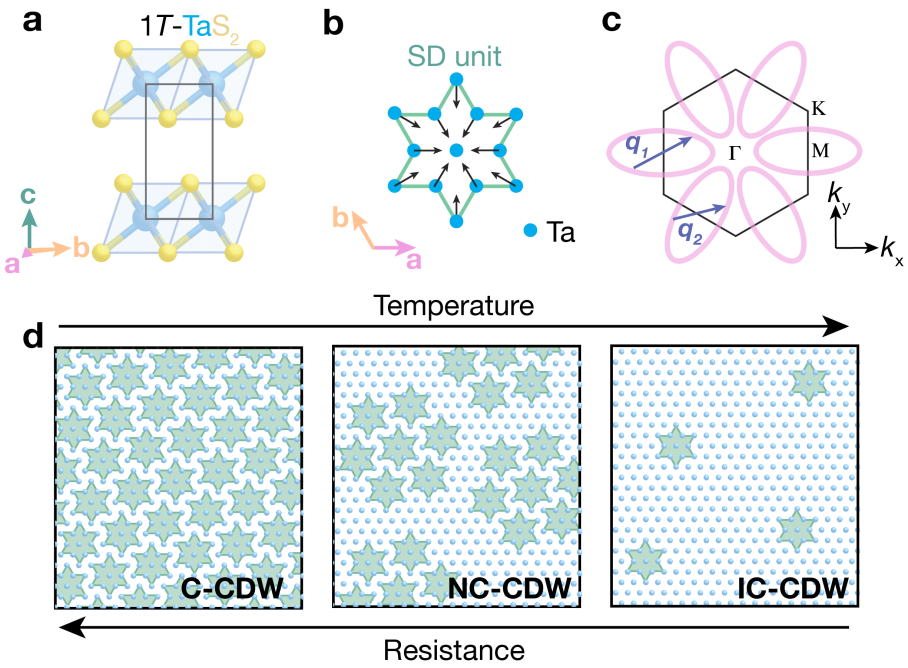


Figure 1.15: Charge density wave properties of $1T-TaS_2$. **(a)** Unit cell of $1T-TaS_2$ in the undistorted phase (Spacegroup: $P\bar{3}m1$). Data from reference [60]. **(b)** The star of David (SOD) distortion unit of $1T-TaS_2$. **(c)** Diagram illustrating the Fermi surface of $1T-TaS_2$ at 370 K, with nesting vectors q_1 and q_2 indicated. **(d)** Tiling of SOD clusters in the commensurate (C-CDW), nearly-commensurate (NC-CDW) and incommensurate (IC-CDW) phase. The tiling of clusters increases with decreasing temperature and is concurrent with increasing electrical resistance.

phase are accompanied by large changes in resistance, with the C-CDW exhibiting insulating behavior. This result was initially surprising, as the simple band model would predict metallic behavior for the C-CDW state. Specifically, in each SOD cluster, the central Ta ion hosts unpaired electrons and forms a half-filled band, which should be metallic.[64] However, due to strong electron–electron correlations, the system undergoes a Mott–Hubbard-type transition, resulting in a pseudogap formation at $E = E_F$.[64–67]

In addition to the in-plane ordering of SOD clusters, these distortion units also exhibit out-of-plane periodicity that evolves across the CDW phases. In the IC-CDW and NC-CDW phases, stacking along c is well-ordered, with 3 layers contributing to the CDW unit cell.[68–72] Conversely, in the C-CDW phase, SOD units dimerize along the c-axis but lack long-range coherence.[64, 70, 72] Nevertheless, it was found that different stacking periodicities of SOD dimers engender distinct electronic signatures.[64, 70] As follows, modulating interlayer interactions is a promising avenue for modifying CDW phases of $1T-TaS_2$ and unlocking complex correlated electronic phenomena.

1.6 Similarities between long-range charge and spin order phases

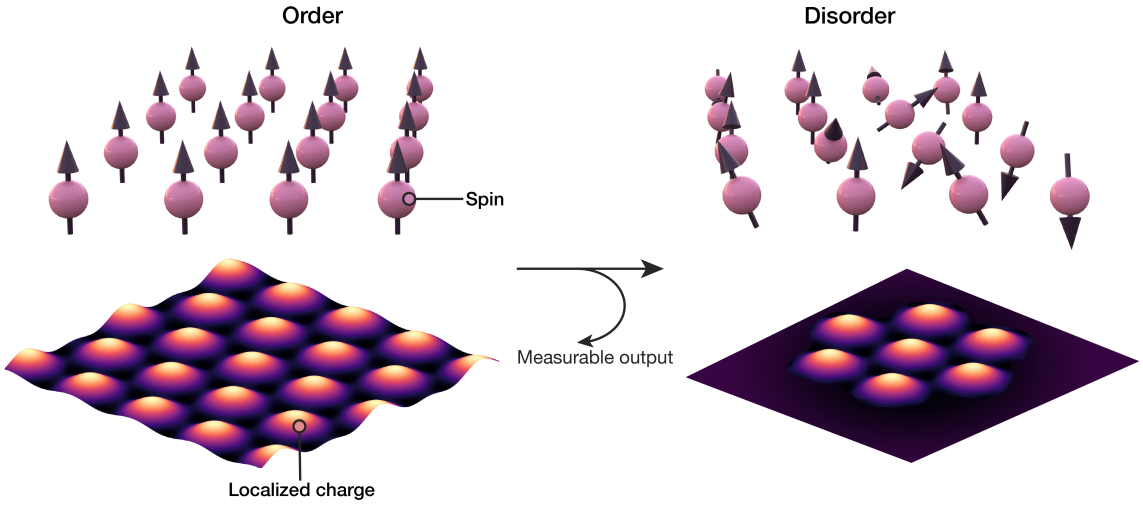


Figure 1.16: Spin and charge order encode magnetoelectronic phases. Changes in the ordering of spin or charge typically lead to a measurable output that can be harvested to encode, read out, and store information.

At first glance, magnetism (spin ordering) and charge density waves (charge ordering) may appear as quantum phases with few if any similarities since spins respond to magnetic fields, while CDWs are typically inert to them. However, these quantum phases share significant similarities that allow us to apply knowledge from one phase to another. Firstly, the crystallographic structure plays a pivotal role in defining both magnetic and CDW phases. Secondly, both phases form domains whose evolution and inter–domain interactions are crucial for explaining the observed physical properties. Thirdly, for both magnets and CDW materials, structural defects significantly affect the domain morphology and evolution when externally perturbed. Lastly, changes in magnetism (spin order) and charge density wave phases (charge order) often yield measurable outputs that can be harnessed for encoding, storing and reading out information (Figure 1.16). Consequently, enhancing the understanding of systems exhibiting charge ordering, spin ordering, or the coexistence of both phenomena, is essential for developing next-generation computing technologies.

Chapter 2

Hard ferromagnetism down to the thinnest limit of iron-intercalated tantalum disulfide

Parts of this section were adapted or reproduced from: Husremović, S.; Groschner, C. K.; Inzani, K.; Craig, I. M.; Bustillo, K. C.; Ercius, P.; Kazmierczak, N. P.; Syndikus, J.; Van Winkle, M.; Aloni, S.; Taniguchi, T.; Watanabe, K.; Griffin, S. M.; Bediako, D. K. *Journal of the American Chemical Society* **2022**, *144*, 12167–12176.[73]

Author contributions: S.H. and D.K.B conceived the study. S.H. made the samples and carried out magnetotransport measurements with assistance from J.S and N.P.K.. S.H conducted TEM studies with assistance from K.C.B., S.A. and M.V.W. C.K.G. carried out studies on the TEAM 0.5 microscope. K.I., I.M.C. and S.M.G. carried out the DFT calculations. T.T. and K.W. provided the bulk hBN crystals. S.H. analyzed the experimental data. S.H. and D.K.B. wrote the manuscript. All the authors contributed to the overall scientific interpretation and edited the manuscript.

2.1 Abstract

Two-dimensional (2D) magnetic crystals hold promise for miniaturized and ultralow power electronic devices that exploit spin manipulation. In these materials, large, controllable magnetocrystalline anisotropy is a prerequisite for the stabilization and manipulation of long-range magnetic order. In known 2D magnetic crystals, relatively weak magnetocrystalline anisotropy results in typically soft ferromagnetism. Here, we demonstrate that ferromagnetic order persists down to the thinnest limit of Fe_xTaS_2 (Fe-intercalated bilayer $2H-TaS_2$) with giant coercivities up to 3 T. We prepare Fe-intercalated TaS_2 by chemical intercalation of van der Waals layered $2H-TaS_2$ crystals and perform variable-temperature quantum transport,

transmission electron microscopy, and confocal Raman spectroscopy measurements to shed new light on the coupled effects of dimensionality, degree of intercalation, and intercalant order/disorder on the hard ferromagnetic behavior of Fe_xTaS_2. More generally, we show that chemical intercalation gives access to a rich synthetic parameter space for low-dimensional magnets, in which magnetic properties can be tailored by the choice of the host material and intercalant identity/amount, in addition to the manifold distinctive degrees of freedom available in atomically thin, van der Waals crystals.

2.2 Introduction

The recent discovery of long-range magnetic ordering in the atomically thin layers of $Cr_2Ge_2Te_6$,[13] CrI_3,[74] and Fe_3GeTe_2[14, 75] has spurred intense interest into the development of "two-dimensional" (2D) magnetic crystals. The experimental paradigm that has generated the most consistent success in this area has generally been to exfoliate layered van der Waals (vdW) crystals that are known to exhibit magnetic ordering in the bulk. In addition to serving as promising candidates for a new generation of compact, energy-efficient spin-based electronics,[76–79] these 2D magnets are exceptional platforms for exploring fundamental principles pertaining to the stabilization of long-range magnetic order at low dimensions. According to the Mermin–Wagner–Hohenberg theorem, long-range magnetic order in 2D systems should not be stable in an isotropic model.[24, 80] However, intrinsic magnetocrystalline anisotropy (MCA)—which imparts a preferential spin orientation—plays an integral role in stabilizing the long-range magnetic order in 2D vdW magnets.[22, 23] Still, the overwhelming majority of ferromagnetic 2D crystals are soft, possessing weak coercive fields, which arise from relatively weak MCA.[81] The development of new atomically thin materials with strong and predictable control over MCA is imperative for tailoring magnetism in 2D materials that may serve as testbeds for fundamental theory and pave the way towards ultralow power spintronic technologies.

Transition metal dichalcogenides (TMDs) intercalated with open-shell transition metals comprise a family of materials with inherently tunable MCA, which makes them appealing targets for realizing 2D magnets with deterministic properties. The strength of MCA in intercalated TMDs is determined by the respective magnitudes of spin-orbit coupling (SOC) and unquenched orbital angular momentum (OAM) of the spin-bearing ions.[30, 36, 82, 83] While the SOC is increased when the host lattice or the intercalants comprise heavy elements, the OAM of spin-bearing ions is shaped by their oxidation states and coordination environments imposed by the interlayer galleries.[30, 36, 82–85] However, low-dimensional analogs of these systems have not been magnetically characterized; strong interlayer interactions in the effectively ionic, bulk crystals of these intercalation compounds have, so far, precluded exfoliation of pristine, large 2D flakes suited for magnetic studies.[40, 86–88] Consequently, the manifold possibilities for designing a new class of 2D magnets with controllable MCA by exploiting the tunable vdW interface, host lattice, and intercalant identity/stoichiometry remain untapped.

In this work, we discover the persistence of long-range ferromagnetism in a transition metal-intercalated TMD, Fe_xTaS_2, down to the 2D limit. We show that chemical intercalation of iron between layers of the exfoliated, pristine host lattice $2H-TaS_2$ gives access to this intercalation compound with controlled dimensionality from a few layers down to the thinnest limit, Fe-intercalated bilayer $2H-TaS_2$. We find very strong MCA in these 2D materials, associated with the high unquenched OAM of the trigonal antiprismatic (i.e. trigonally elongated pseudo-octahedral) Fe centers and SOC from the Ta-based host. This large MCA is reflected in magnetotransport measurements, which reveal that anisotropy-stabilized hard ferromagnetic behavior is retained in the 2D limit, producing giant coercive fields up to 3 T. Furthermore, we find that the degree of intercalation and order/disorder in intercalated species heavily influences the magnetoelectronic behavior, establishing this family of intercalation compounds as versatile platforms for designing 2D magnets.

2.3 Results and discussion

Fabrication of vdW heterostructures, chemical intercalation, and structural characterization

Few-layer Fe_xTaS_2 was synthesized by intercalating iron into mechanically exfoliated $2H-TaS_2$ flakes using a procedure adapted from established methods for soft chemical intercalation of metals using molecular precursors containing zerovalent metal centers.[89–93] In a typical procedure, $2H-TaS_2$ flakes were mechanically exfoliated onto SiO_2/Si substrates and capped with electrically insulating hexagonal boron nitride (hBN) to prevent degradation of the TaS_2 basal plane, while exposing one or more edges of the TMD flake.[94] Under an inert atmosphere, the SiO_2/Si substrates bearing these vdW heterostructures are immersed in a 10 mM solution of $Fe(CO)_5$ in toluene, acetone, or acetonitrile at 50–55 °C for about 24 hours as depicted in Figure 2.1a. After washing with fresh solvent, samples were annealed under high vacuum (10^{-7} Torr) at 350 °C for 30 minutes. The annealing step was added to the synthetic procedure because Raman modes and superlattice diffraction spots associated with Fe ordering emerge only after intercalated samples have been vacuum annealed (Figure 2.2).

To examine the composition and structure of our Fe_xTaS_2 thin crystals, we obtained and high-resolution TEM (Figure 2.3), scanning TEM (STEM) combined with energy-dispersive X-ray spectroscopy (EDS) and differential phase contrast (DPC)-STEM with atomic resolution (Figure 2.1b–c). The *c*-axis HRTEM (Figure 2.3) data verify that the *ab* atomic periodicities match the expected values for bulk Fe_xTaS_2, and EDS measurements of cross-sectioned thin crystals confirm the incorporation of Fe into TaS_2 after chemical intercalation (Figure 2.3b). The Fe intercalants occupy 6-coordinate interstitial sites between the layers of $2H-TaS_2$, as revealed by DPC-STEM of cross-sectioned Fe_xTaS_2 samples (Figure 2.1c) displaying a prominent $\sqrt{3}a \times \sqrt{3}a$ superstructure in their Raman spectra (Figure 2.4). Computational image analysis of our STEM-DPC micrographs shows that the pseudo-octahedral Fe coordination environments are trigonally elongated by 8.0(6) %. The

magnitude of this experimentally determined distortion is congruous with the ~ 8 % trigonal distortion predicted by our DFT calculations. The trigonally elongated pseudo-octahedral Fe coordination has also been reported for bulk Fe_xTaS_2 prepared via high-temperature chemical vapor transport crystal growth (Figure 2.1d).[37, 95]

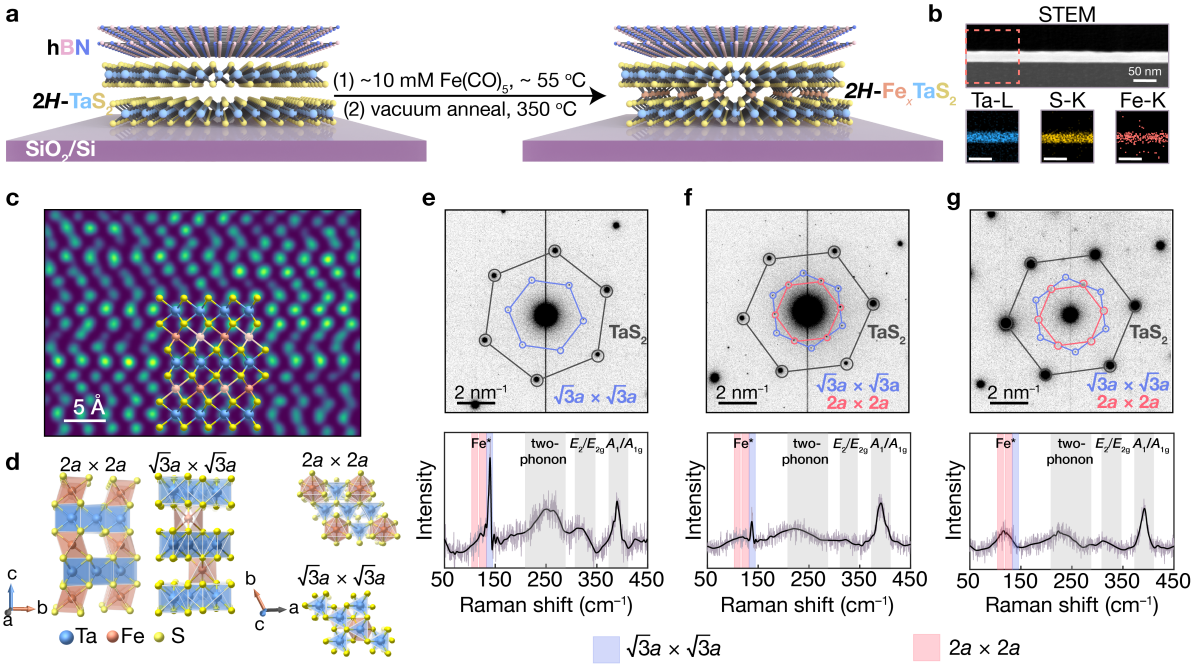


Figure 2.1: Synthesis and characterization of 2D Fe_xTaS_2. **(a)** Schematic illustration of iron intercalation into the hBN/$2H-TaS_2$ heterostructure and formation of Fe_xTaS_2. **(b)** STEM-EDS scans perpendicular to the c-axis of a cross-sectional Fe_xTaS_2 sample (white region in STEM image). The dashed red box in the STEM image marks the area where EDS data was collected. **(c)** DPC-STEM micrograph of a cross-sectioned Fe_xTaS_2 sample along the $[10\bar{1}0]$ zone axis of the $2H-TaS_2$ lattice. The structure of $Fe_{1/3}TaS_2$ (ref 30) is overlaid with the micrograph. (d) Published crystal structures for bulk $Fe_{1/4}TaS_2$ (ref [37]) and $Fe_{1/3}TaS_2$ (ref [95]). **(e)–(g)** Pairs of Raman spectra and NBED patterns of three chemically intercalated Fe_xTaS_2 flakes on electron-transparent Si_3N_4 grids. In each case, Raman spectra and NBED data were measured in identical regions of the flake. The first-order Bragg spots of the $2H-TaS_2$ host lattice and the Fe superlattices are marked in the NBED patterns. Raman spectra are normalized to the A_1/A_{1g} peak, and the spectral regions where phonon modes for different superlattices are expected[96] are highlighted. The raw data are represented in light gray, while dark gray lines represent denoised traces.

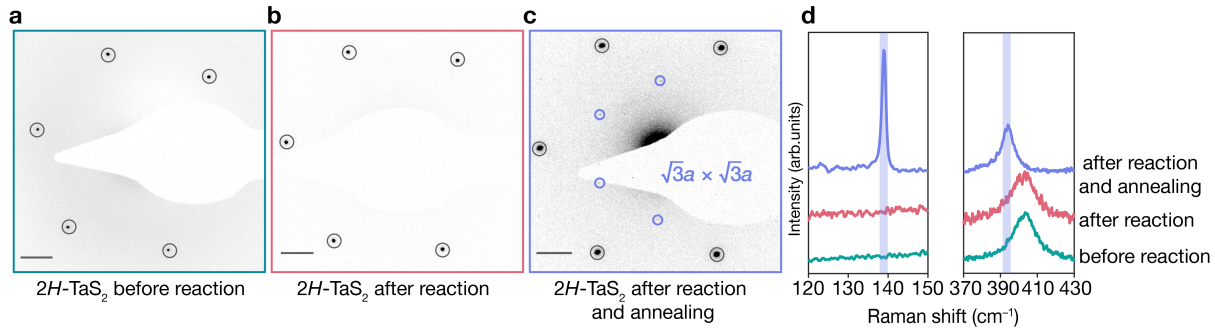


Figure 2.2: Ordering of intercalants in annealed samples. Selected area electron diffraction (SAED) pattern of a $2H-TaS_2$ flake suspended on a TEM grid **(a)** before the intercalation, **(b)** after intercalation and **(c)** after intercalation and annealing. The first-order Bragg spots of the $2H-TaS_2$ host lattice and the Fe superlattices are marked in the NBED patterns. **(d)** Raman spectra of a $2H-TaS_2$ flake on SiO_2/Si: (a) before intercalation, (2) after intercalation, and (3) after intercalation and annealing. The Raman spectra are normalized to the A_1/A_{1g}. The Raman data was smoothed with the Savitzky–Golay filter.

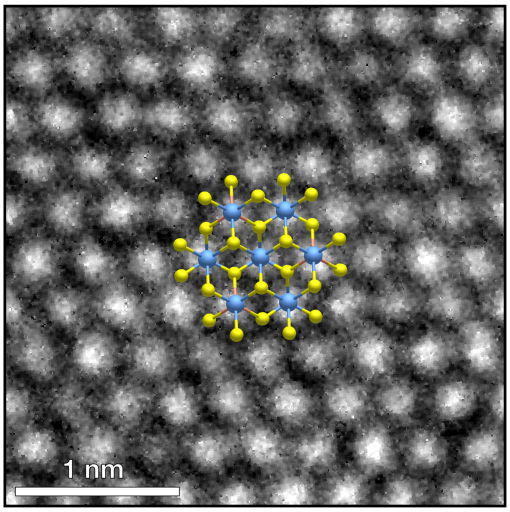


Figure 2.3: HRTEM along the c-axis of Fe_xTaS_2. HRTEM of a Fe_xTaS_2 crystal imaged along the c-axis of the flake. A CIF file of $Fe_{1/3}TaS_2$ (ref [95]) along the [0001] axis is overlaid with the micrograph.

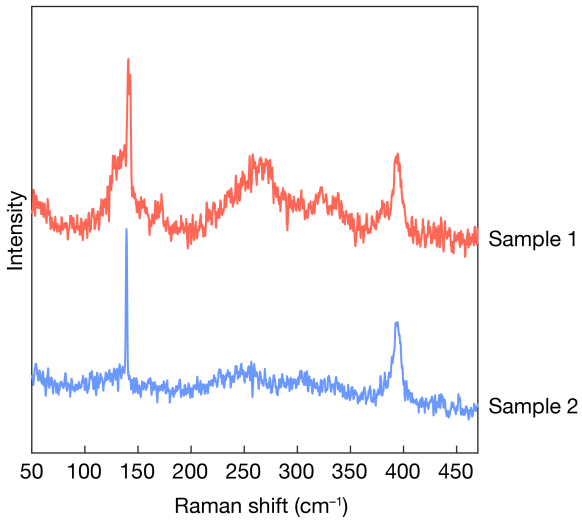


Figure 2.4: The Raman spectra of Fe_xTaS_2 that were cross-sectioned and measured with DPC-STEM. The Raman spectra are normalized to the A_1/A_{1g}. The data was smoothed with the Savitzky–Golay filter.

In bulk Fe_xTaS_2 analogs, depending on the stoichiometry, superlattices with $2a \times 2a$ or $\sqrt{3}a \times \sqrt{3}a$ periodicity are observed (where a = the lattice constant of $2H-TaS_2$), with perfect superlattices at $x = 0.25$ and 0.33, respectively (Figure 2.1d).[37, 39, 95] To examine if analogous intercalant ordering is present in our chemically treated few-layer materials, we measured both nanobeam electron diffraction (NBED) patterns and Raman spectra within 500 nm of each other on samples mounted on silicon nitride transmission electron microscopy (TEM) grids. As shown in Figures 2.1e–g, NBED patterns of Fe_xTaS_2 samples prepared by chemical intercalation and annealing exhibit superlattice spots that are not present in $2H-TaS_2$, and the accompanying Raman spectra display a new set of peaks in the low-frequency region (100–150 cm^{-1}). These fingerprints of Fe ordering are consistent with previous literature on bulk Fe_xTaS_2.[96, 97] For example, the sample that displays sharp $\sqrt{3}a \times \sqrt{3}a$ superlattice spots in NBED data also exhibits an intense Fe in-plane (Fe*) mode at 140 cm^{-1}, which is characteristic of the $\sqrt{3}a \times \sqrt{3}a$ superstructure (Figure 2.1e).[96] In contrast, as shown in Figures 2.1f–g, samples that evince two clear superstructures (both $\sqrt{3}a \times \sqrt{3}a$ and $2a$ *times*$2a$) in NBED data are characterized by generally broader and less intense Raman features that span the energy ranges expected for each type of Fe superlattice ordering. For these dual-superlattice samples, sharp Fe-related Raman features may be absent (Figure 2.1g) or show a red-shift (Figure 2.1f) compared to the crystals that host a single, dominant Fe superstructure (Figure 2.1e). Further, a comparison of these data reveals that the sharpness of Fe-related NBED spots and Raman-active Fe* phonon modes appear to be correlated; samples with diffuse superlattice spots in NBED show broad Fe*

features in Raman spectra (Figure 2.1g), while samples with sharp superstructure spots in NBED present more well defined Fe* peaks in Raman spectra (Figure 2.1e,f). These data demonstrate that chemical intercalation is a viable method for accessing Fe_xTaS_2 in the few-layer limit with the potential to vary stoichiometry and homogeneity. We find that all Raman spectra in Figure 2.1e–g display a red shift of the A_{1g} mode by 8–10 cm^{-1} from the expected value for $2H-TaS_2$. This shift is consistent with electron transfer from Fe to the host lattice, in agreement with our DFT calculations.[98, 99] For all calculated structures and magnetic configurations, we found that Fe converges to a +2 oxidation state, matching published experimental data on bulk Fe_xTaS_2.[100–102] We note that without annealing these chemically intercalated materials, we neither observe superlattice spots in NBED data nor significant changes to the Raman spectra (Figure 2.2). These observations suggest that a modest thermal treatment is required both for ordering of Fe in the vdW interface between TaS_2 layers as well as charge transfer from the intercalants to the host lattice.

Variable temperature transport measurements

We interrogated the magnetoelectronic behavior of chemically intercalated Fe_xTaS_2 flakes by fabricating mesoscopic Hall bar devices for variable temperature magnetotransport measurements (Figure 2.5a). In these experiments, we simultaneously monitored the longitudinal (ρ_{xx}) and transverse Hall resistivity (ρ_{xy}) as a function of temperature (T) and external magnetic field (H) to evaluate magnetic order in our materials via its effect on electronic transport. Figure 2.5 presents a representative set of results for a hBN/11-layer Fe_xTaS_2 heterostructure on a supporting SiO_2/Si substrate. Confocal Raman spectroscopy data (Figure 2.5b) acquired along the measurement channel of the Hall bar are consistent with a dominant $\sqrt{3}a \times \sqrt{3}a$ superstructure that gives rise to a strong peak at 139 cm^{-1}, albeit showing evidence for the coexistence of a much less dominant $2a \times 2a$ superlattice in a weaker broad feature spanning 100–135 cm^{-1}. The coexistence of two superlattices can be a result of either stoichiometric inhomogeneities within the spot size (ca. 500 nm) of the Raman laser and/or deviations of x from the commensurate amounts of 1/4 and 1/3.[40, 103] These possibilities were evaluated by cross-sectioning devices with focused ion beam and using STEM-EDS to map the Fe–Ta ratio. These measurements reveal an effectively consistent Fe:Ta value of 0.26 ± 0.02 along the Hall bar channel (Figure 2.5c).

To compare the Fe:Ta stoichiometry measured in thin flakes with the values determined for bulk (3D) crystals, we must consider that terminating Ta ions from the top and bottom TaS_2 layers contribute substantially to the measured elemental composition of thin crystals. Consequently, the ratio of Fe to Ta should be lower in thin samples compared to their structurally equivalent 3D analogs. We can convert between the Fe:Ta values measured in thin samples (x_t) possessing L number of layers and the stoichiometry of their compositionally equivalent bulk analogs (x_b) using the following expression:

$$x_b = x_t/(1 - \frac{1}{L}) \tag{2.1}$$

With this expression, we find that the equivalent bulk stoichiometry, $x_b = 0.29 \pm 0.02$ for our sample shown in Figure 2.5, confirming that the degree of intercalation represents a slight deviation from the commensurate value of $x = 1/3$. To facilitate comparison with the magnetotransport behavior of bulk crystals, all stoichiometries given for thin samples in this paper are converted to x_b.

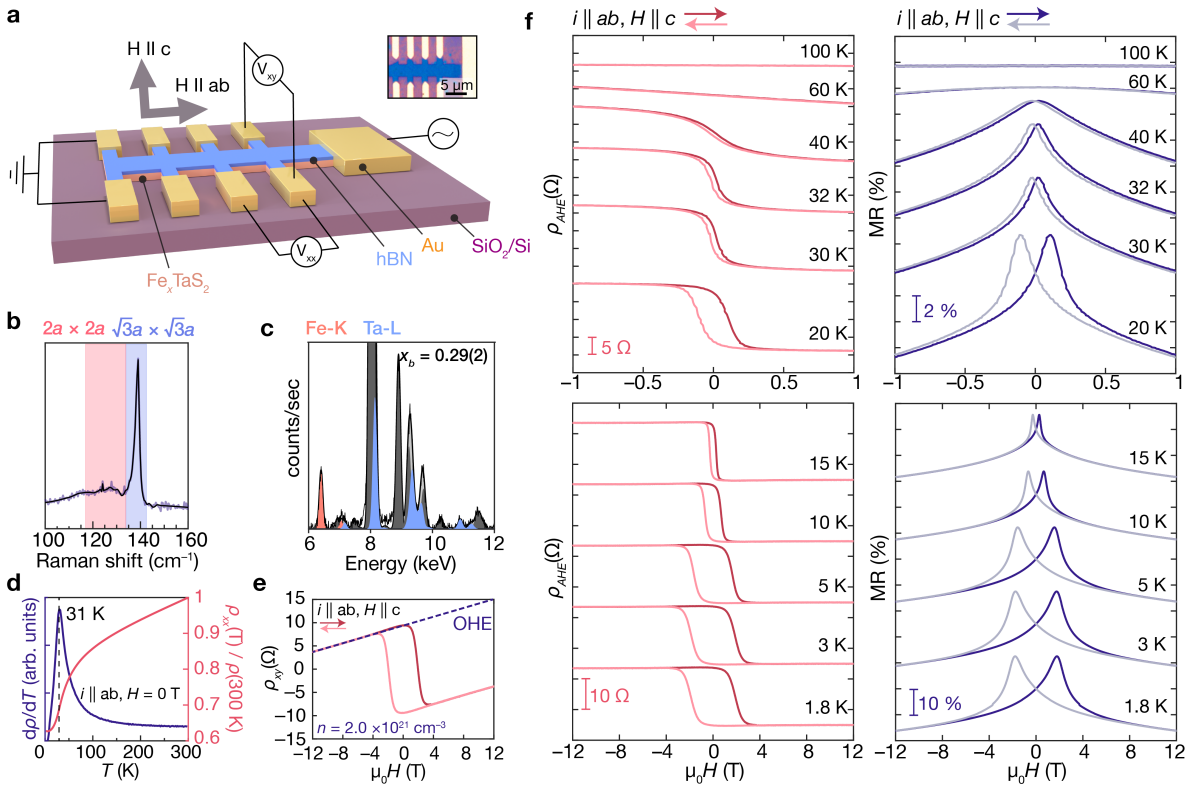


Figure 2.5: Magnetotransport of an 11-layer Fe_xTaS_2 crystal. **(a)** Schematic of the hBN/11-layer Fe_xTaS_2 device on SiO_2/Si. (b) Cumulative low-frequency Raman spectrum across the Hall bar channel of the device. **(c)** Representative cross-sectional STEM-EDS of the device. **(d)** Temperature-dependent longitudinal resistivity and its first derivative with respect to temperature of the hBN/11-layer Fe_xTaS_2 heterostructure. **(e)** Hall resistivity at 1.8 K with the ordinary Hall effect (OHE) highlighted. **(f)** Temperature dependence of anomalous Hall resistivity ρ_{AHE} (left), and magnetoresistance, MR (right), as a function of H.

Temperature-dependent longitudinal resistance measurements revealed a phase transition upon cooling. An inflection in ρ_{xx} and corresponding peak in $\mathrm{d}\rho_{xx}/\mathrm{d}\rho_{xx}$ at 31 K indicate that the sample underwent a phase transition at this temperature (Figure 2.5d).[14] To probe the nature of this low-temperature phase, we measured the field-dependent Hall resistivity, ρ_{xy}, at 1.8 K as shown in Figure 2.5e. This Hall resistivity signal can be related to the magnetization

(M) of the sample through the following expression:[38, 104, 105]

$$\rho_{xy} = \frac{1}{ne}\mu_0 H + \mu_0 R_s M \tag{2.2}$$

where n is the carrier density, e is the elementary charge, μ_0 is the vacuum permeability, H is the applied field, and R_s is the anomalous Hall coefficient. The first term of Equation 2.2, $\mu_0 H/ne$, is referred to as the ordinary Hall effect (OHE), while the second term, $\mu_0 R_s M$, is the anomalous Hall resistivity, ρ_{AHE}. Analysis of the former uncovers that the major charge carriers in this 2D crystal are holes, with a carrier density of $2 \times 10^{21}\mathrm{cm}^{-3}(2 \times 10^{27}\mathrm{m}^{-3})$ at 1.8 K. These results, which are in agreement with measurements of bulk crystals (2.6), reveal the presence of hole pockets at the Fermi level after intercalation.[36, 103, 105] Although the OHE reveals valuable information about the basic electronic structure of our materials, it does not convey any information on magnetism. Insight into the long-range magnetic ordering of few-layer Fe_xTaS_2 was obtained by extracting the magnetization-dependent ρ_{AHE} as well as measuring the magnetoresistance (MR), which reflects the evolution of scattering interactions between charge carriers and magnetic moments. The hysteretic behavior of ρ_{AHE} and MR displayed in Figure 2.5f reveal that the material is a hard ferromagnet with a very large coercive field (H_c) that reaches 2 ± 0.1T at 1.8 K. To the best of our knowledge, this is the largest H_c value recorded among 2D ferromagnetic crystals to-date.[14, 106–110]

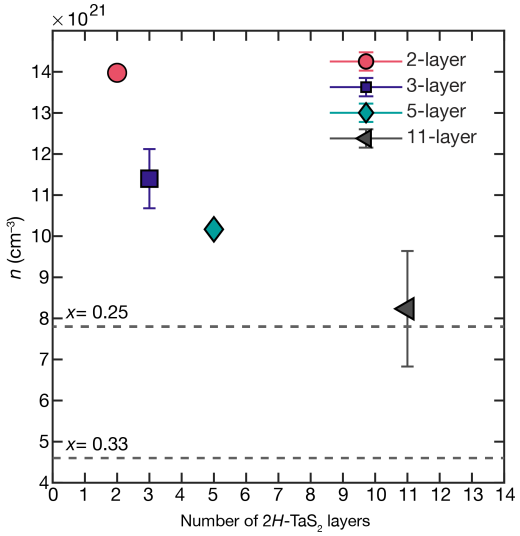


Figure 2.6: Carrier density of measured Fe_xTaS_2 devices obtained from fitting the ordinary Hall effect term (ρ_{OHE}) at 200 K. Carrier density values for bulk $x = 0.25$[38] and $x = 0.33$[103] crystals, which were extracted from the literature, are indicated in dashed lines.

The broadness of ρ_{AHE} and MR switching profiles is consistent with the presence of inhomogeneous MEIs arising from some magneto-structural disorder. This behavior is

reminiscent of off-stoichiometric bulk Fe_xTaS_2, in which crystallographic defects (Fe vacancies or interstitials) weaken the coupling between neighboring Fe centers.[39, 40] The resulting inhomogeneous coupling of magnetic moments across the crystal broadens the hysteresis curves and may engender MR through spin-disorder scattering.[39] Indeed, we find that the maximum value of MR decreases as the temperature approaches the Curie temperature (T_C), which is estimated to be about 31 K from the inflection in ρ_{xx}(T) shown in Figure 2.5d. This observed change in MR with temperature is consistent with a spin-disorder scattering mechanism.[40] Interestingly, while we might expect fully closed hysteresis loops above this ordering temperature, Figure 2.5f instead shows that both MR and ρ_{AHE} traces retain their hysteretic behavior up to 40 K, consistent with the persistence of some long-range magnetic order above 31 K. This discrepancy in the apparent TC prompted us to further examine the magnetic ordering temperature.

Magnetic phase transitions and magnetocrystalline anisotropy (MCA) in thin Fe_xTaS_2

By fitting the temperature dependence of the remanent ρ_{AHE} signal to the power-law form $\alpha(1 - T/T_C)^\beta$, it is possible to extract both the T_C and the critical exponent (β) for the magnetic material.[14] β provides insight into the nature of the magnetic phase transition in the crystal and enables us to identify its universality class, which characterizes the dimensionality of our system, the symmetry of its magnetization, and the range of spin–spin interactions.[111, 112] This analysis and the discontinuity in $\rho_{AHE}(T)$ around 31 K before full hysteresis closure (Figure 2.7a) suggest the presence of two magnetic phase transitions at about 31 K and 41 K, which we discuss in detail later. The critical exponent of the low-temperature magnetic phase, $\beta = 0.31 \pm 0.04$, closely matches the theoretical value for the 3D Ising model $\beta = 0.325$,[113] which describes systems with uniaxial MCA. To experimentally examine the MCA, we compare the MR curves with the external field applied parallel to the c-axis (H $\parallel$ c) with those in which the external field is applied along the ab-plane (H $\parallel$ ab) in Figure 2.7b. The MR profile is hysteretic only for H $\parallel$ c, consistent with an easy-axis along c, and a strong out-of-plane MCA in few-layer Fe_xTaS_2.

Magnetic behavior, transport, and Fe disorder in the ultrathin limit of Fe_xTaS_2.

The large MCA in Fe_xTaS_2 prepared by chemical intercalation raised the possibility of anisotropy-stabilized long-range ferromagnetism in ultrathin Fe_xTaS_2 with even fewer layers. Hysteretic magnetotransport features of intercalated 2-, 3-, and 5-layer TaS_2 flakes (Figure 2.8) confirm that hard ferromagnetism is retained down to the thinnest limit of Fe_xTaS_2 (Figure 2.9a). All measured devices (Figure 2.9b) exhibit hysteretic MR profiles only for $H \parallel c$, confirming their large out-of-plane MCA (Figure 2.10). This observation of ferromagnetism and large MCA in few-layer Fe intercalated TaS_2 is supported by Density Functional Theory

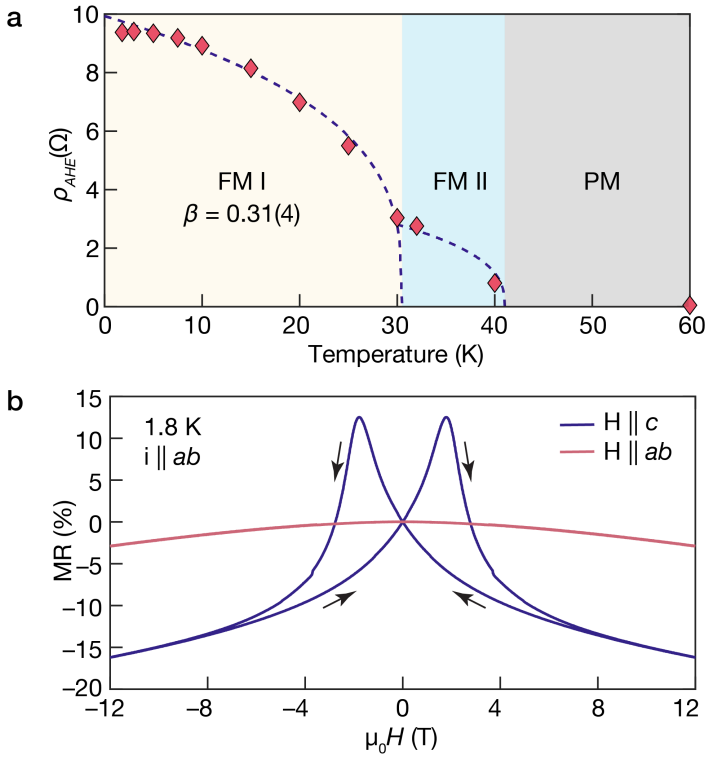


Figure 2.7: Uniaxial magnetocrystalline anisotropy in low-dimensional Fe_xTaS_2. **(a)** Temperature dependence of the remanent ρ_{AHE} for the 11-layer device of Fe_xTaS_2. Ferromagnetic (FM) and paramagnetic (PM) phases are highlighted. Dashed lines represent the least squares fit to the formula $\alpha(1 - T/T_{\mathrm{C}})^{\beta}$. (b) MR of the device with the external field parallel and perpendicular to the c-axis.

(DFT) calculations. In these computations, we considered four $\sqrt{(3)}a \times \sqrt{(3)}a$ superlattices of Fe_xTaS_2 with L = 2, 3, 4, 5 TaS_2 layers. For all L-layer systems, we find a high-spin ferromagnetic order with calculated Fe magnetic moments of 3.3–3.5 μ_{B} per site. For all calculated heterostructures and magnetic configurations, we find that Fe converges to a d^6 manifold (i.e. an Fe^{2+} oxidation state), which aligns with literature on bulk Fe_xTaS_2.[36] Consistent with our experiments, we find the easy-axis to be out-of-plane with a calculated MCA in the 5-layer case of 6 meV per formula unit (1.5 meV/Fe). The origin of this anisotropy is the large out-of-plane orbital moment, which was previously calculated to be of 1.0 μ_{B}/Fe in the bulk case. Notably, the large MCA in our crystals is expected to dominate over shape anisotropy, which is an important factor for thin films with smaller MCA.

Additional magnetotransport measurements also reveal that these thin crystals have high carrier densities and hole carriers (Figure 2.9). However, despite these similarities, their magnetic behaviors are substantially different. The 5-layer $Fe_{0.38(2)}TaS_2$ crystal displays only slightly broadened ρ_{xy} and MR hysteresis curves, suggesting a small degree of inhomogeneous

MEIs in this material. In contrast, the 3-layer sample, $Fe_{0.37(2)}TaS_2$, which possesses a comparable stoichiometry to the 5L crystal, exhibits substantially broader magnetization switching. These data indicate that stoichiometry may not be the primary determinant of magnetic order in 2D Fe_xTaS_2. Instead, dimensionality may play the dominant role in shaping magnetic properties. Indeed, the ρ_{xy} and MR features found in measurements of the 2-layer crystal, $Fe_{0.58(14)}TaS_2$ are comparable to those of the 3-layer crystal, despite a significant difference in stoichiometry. This strong influence of dimensionality on magnetic order may stem from its impact on intercalant ordering via electronic and/or structural effects. For example, measurements of bulk crystals of a related system, Fe_xTiS_2, reveal that the ordering of intercalants in the plane is sensitive to the structure of Fe intercalants along the *c*-axis.[114–116] By extension, we suggest that decreasing numbers of layers could result in a reduced tendency for ordering Fe centers in-plane. Moreover, in the low-dimensional limit, intercalation may produce distinct Fe intercalant structural phases that may not be present in bulk crystals, a behavior that can also be theoretically understood from the Mermin–Wagner framework as applied to 2D crystallization processes.[117]

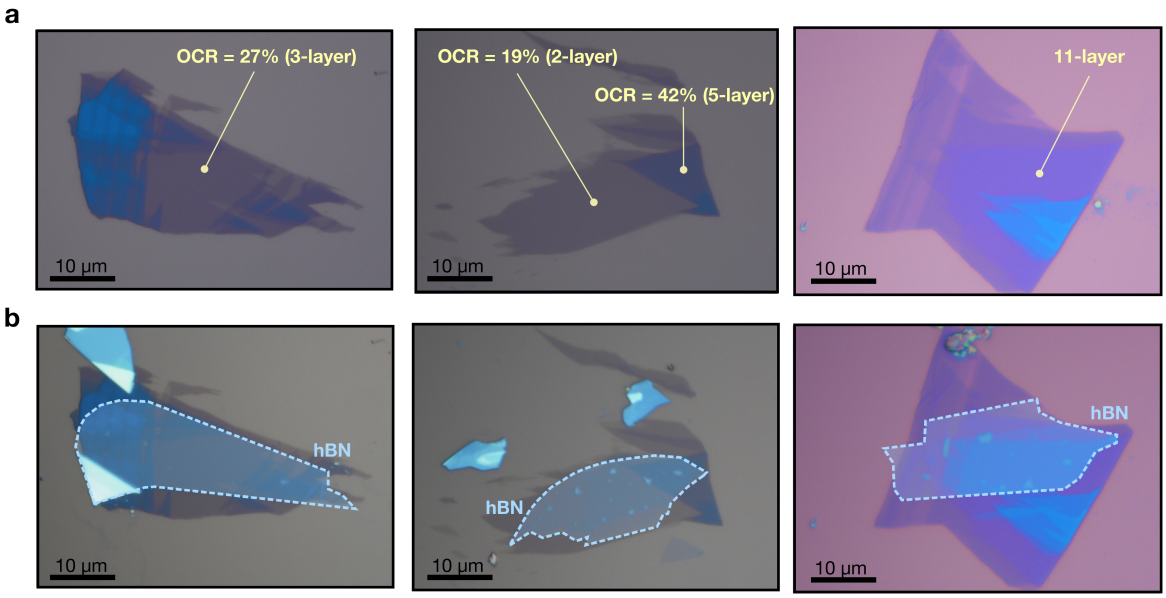


Figure 2.8: **(a)** Optical micrographs of $2H-TaS_2$ flakes after mechanical exfoliation. Uniform flake areas, whose layer count is marked in yellow, were nanofabricated into devices. The red channel optical contrast (OCR) is indicated for flakes whose layer count was obtained with optical contrast measurements. **(b)** Flakes after encapsulation with hexagonal boron nitride (hBN). The hBN-covered flake areas are false-colored in light blue.

To evaluate the extent of this intercalant ordering in these ultrathin intercalation compounds, we used confocal Raman spectroscopy to probe the Fe superlattice modes in the

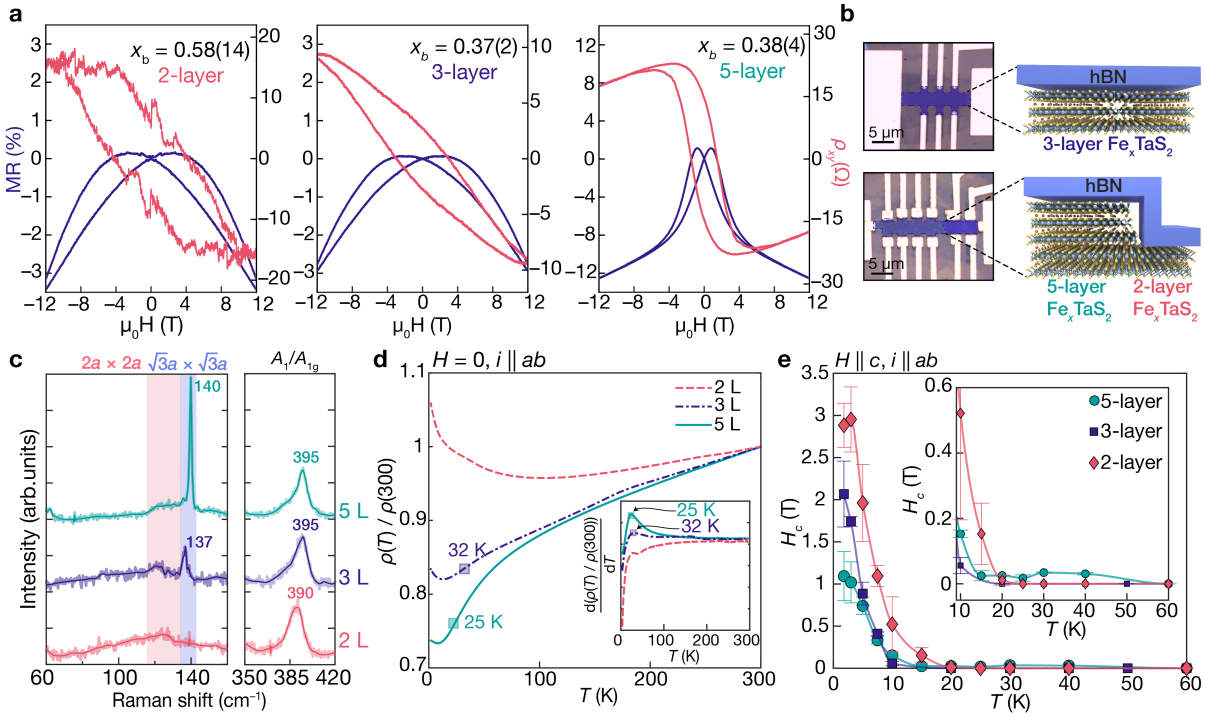


Figure 2.9: **(a)** Magnetotransport measurements, **(b)** optical micrographs with heterostructure schematics, **(c)** cumulative Raman spectra, **(d)** temperature-dependent longitudinal resistivities and their first derivatives with respect to temperature and **(e)** temperature-dependent coercivities for the 5-, 3- and 2-layer devices. In **(c)**, the Raman data is normalized to the A_1/A_{1g} peak. In **(d)**, (ρ (T)/ ρ(300 K))/dT maxima are marked on the ρ $(T)/\rho$(300 K) curves for the 3-layer and 5-layer devices.

intercalated 5-, 3- and 2-layer crystals. Figure 2.9c shows that the superlattice structures and order in these few-layer devices indeed differ appreciably. We find that the 5-layer sample is mostly ordered in the $\sqrt{3}a \times \sqrt{3}a$ superstructure, with a hallmark sharp and intense Fe* feature close to 140 cm^{-1}.[96] In the 3-layer device, the characteristic $\sqrt{3}a \times \sqrt{3}a$ and $2a \times 2a$ superstructure modes are broader and closer in intensity, consistent with increased disorder and the presence of both superlattices, notwithstanding an effectively identical composition to the 5-layer crystal. Finally, the bilayer sample exhibits a substantially broad feature in the low-frequency region, pointing to a high level of intercalant disorder. Although sharp Fe-related modes are absent in this sample, the red-shifted A_1 mode reveals that the TaS_2 lattice has been electron-doped[98, 99] and STEM-EDS confirms the substantial intercalation of Fe. Taken together, we suggest that structural disorder, which is encouraged by reduced dimensionality, likely promotes the observed broadened magnetic responses in ultrathin Fe_xTaS_2.

Traditionally considered an undesirable property of crystals, intercalant disorder plays a

key, useful role in defining and manipulating the magnetic properties of magnetic intercalation compounds. In Fe_xNbS_2 crystals with x near 1/3, disorder results in a spin-glass phase that coexists with the antiferromagnetic state, and this disorder-induced spin glass enables the switching of antiferromagnetic domain orientations and electronic conductivity with small electrical pulses.[118–122] In bulk Fe_xTaS_2 crystals, disorder has been demonstrated to increase ferromagnetic hardness, as defects can pin magnetic domains and increase the coercivity. Congruently, apparent intercalant disorder in our bilayer and 3-layer Fe_xTaS_2 crystals may, together with intrinsically large MCA, be one origin for the observed giant coercivities reaching 2.9 ± 0.3 T and 2.1 ± 0.4 T, respectively (Figure 2.9a). In contrast, the coercivity of the more ordered 5-layer Fe_xTaS_2 is lower, amounting to 1.1 ± 0.3 T at 1.8 K.

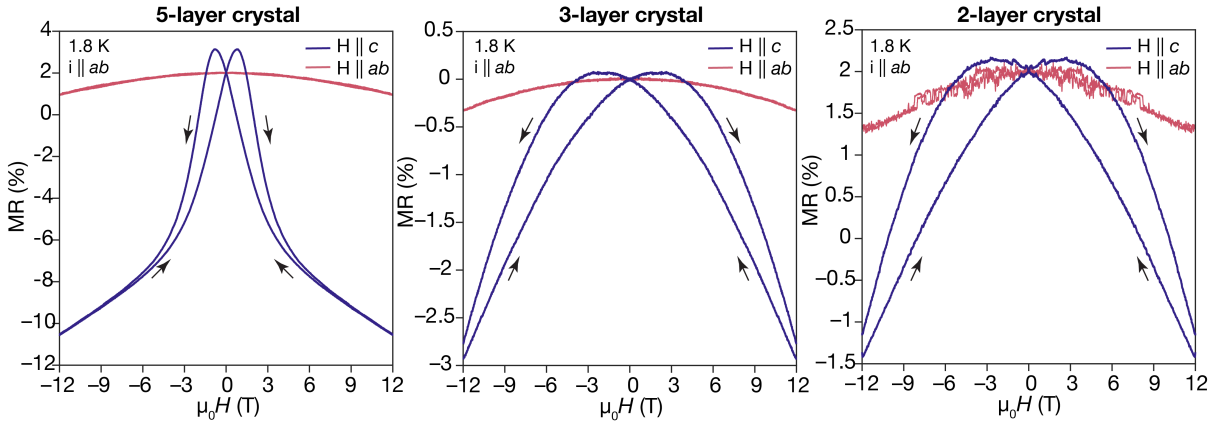


Figure 2.10: Uniaxial magnetocrystalline anisotropy in ultrathin Fe_xTaS_2. MR of the 5-layer $Fe_{0.38(4)}TaS_2$, 3-layer $Fe_{0.37(2)}TaS_2$ and 2-layer $Fe_{0.58(14)}TaS_2$ crystals with the external magnetic field parallel and perpendicular to the crystallographic c-axis.

Notwithstanding the very large coercivities measured for these few-layer magnetic crystals, it is noteworthy that these coercive fields are slightly lower than those measured for analogous bulk Fe_xTaS_2.[39] These discrepancies in H_c could suggest that the overall strength of MEIs may decrease in the few-layer limit. However, our analysis of ordering temperatures in these few-layer crystals reveals that the overall MEIs, while perhaps slightly weaker, may be quite comparable to those found in bulk crystals of similar composition. This insight was gleaned from a consideration of their Curie temperatures, determined from the temperature dependence of their longitudinal resistivities (Figure 2.9d) and coercivities (Figure 2.9e). Based on the inflections in ρ_{xx} and $\mathrm{d}\rho_{xx}/\mathrm{d}T$ shown in Figure 2.9d, the 5- and 3- layer crystals magnetically order below 25 K and 32 K, respectively. However, as we discuss in more detail below, the closure of their hysteresis, i.e., onset of $H_c = 0$, does not coincide with the inflections in ρ_{xx} (Figure 2.9e, Figure 2.11, Figure 2.12). For the 5-layer crystal, the magnetic hysteresis instead closes between 40 K and 60 K, about 20 K higher than the temperature of

inflection in ρ_{xx}. The hysteresis observed in the 3-layer crystal instead closes below the ρ_{xx} inflection temperature (between 10 and 20 K), as observed in bulk $Fe_{1/3}TaS_2$.[103]

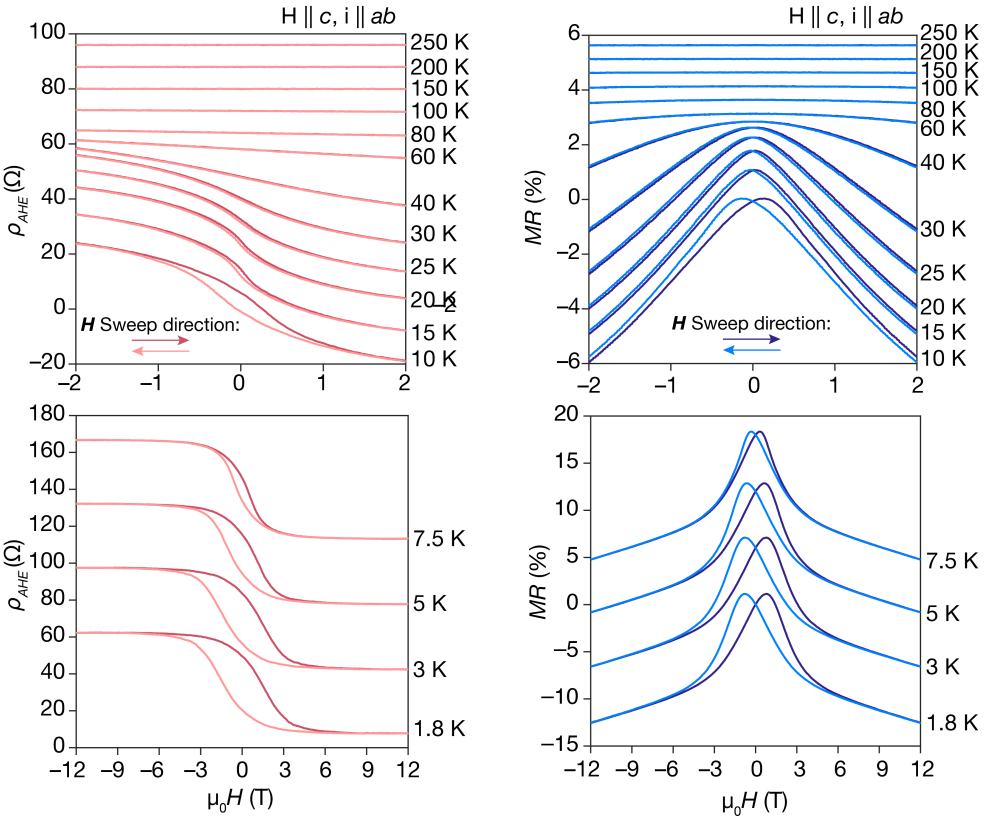


Figure 2.11: Temperature dependence of the symmetrized anomalous Hall resistivity (ρ_{AHE}) and magnetoresistance (MR) for the 5-layer $Fe_{0.38(4)}TaS_2$ device.

For the bilayer crystal, Figure 2.9d also shows that decreasing temperatures do not produce the characteristic sharp drop in ρ_{xx} below a magnetic ordering temperature, as observed in crystals with $L \geq 3$ layers. Instead, ρ_{xx} exhibits an upturn in resistivity for T < 100 K to reach a low-temperature resistivity greater than the ρ_{xx} value measured at room temperature. This upturn in ρ_{xx} has not been observed in bulk crystals of Fe_xTaS_2 and may be a result of Kondo-like scattering or weak localization,[111, 123–126] both of which can result in an increase in resistivity with decreasing temperature in metals. Because ρ_{xx} for the bilayer sample does not exhibit any features typically attributed to a magnetic phase transition, we estimate T_{C} as between 20 and 25 K based on the disappearance of hysteresis in ρ_{xx} over this temperature range (Figure 2.13). In summary, these measured ordering temperatures for few-layer Fe_xTaS_2 are comparable to the T_{C} for $x = 0.33$ bulk crystals (around 38 K),[14, 39] signifying that it is likely the intraplanar MEIs, which are retained in the 2D limit, that are the dominant coupling interactions in Fe_xTaS_2 flakes.

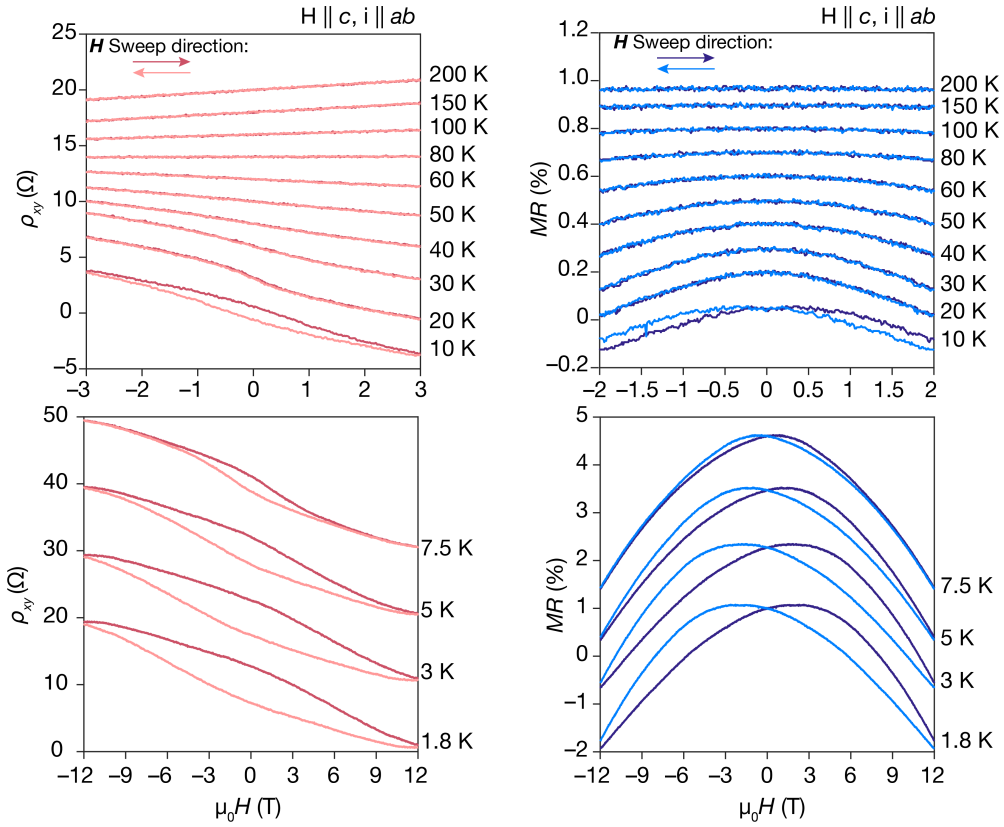


Figure 2.12: Temperature dependence of the symmetrized ρ_{xy} and magnetoresistance (MR) for the 3-layer $Fe_{0.37(2)}TaS_2$ device.

Co-existing magnetic phases in few-layer Fe_xTaS_2.

As described above, in all measured few-layer samples, there exist discrepancies between ordering temperatures determined from inflections in ρ_{xx}(T) and those measured from the closure of magnetic hysteresis. Moreover, the temperature dependence of remanent ρ_{AHE} for the 5-layer Fe_xTaS_2 (Figure 2.14) appears to display more than one magnetic transition. This behavior, which was also observed for the 11-layer crystal (Figure 2.7a), again points to the presence of multiple co-existing ferromagnetic phases. Although one possible origin is superlattice inhomogeneity/disorder, these crystals display Raman spectra (Figures 2.5b, 2.9c) that are consistent with an overwhelmingly dominant $\sqrt{3}a \times \sqrt{3}a$ Fe superlattice. We therefore interrogated other possible origins of these magnetic transitions using DFT computations. Interestingly, in addition to the high-spin ground state, we also find metastable zero-spin and intermediate-spin solutions in our DFT calculations. For the 2-layer case, we find the zero-spin state is 461 meV per formula higher in energy than the high-spin (3.5 μ_{B}/Fe) case. We also find an intermediate spin state with 2.1 μ_{B}/Fe that is 273 meV per

formula unit higher in energy than the high-spin case. In both cases, the magnetic moment reduction occurs with a decrease in the van-der-Waals gap—the interplanar S–S distance changes from 2.89 Å (high spin) to 2.83 Å (intermediate spin) to 2.56 Å (zero spin), with a corresponding reduction in Fe–S bond lengths. Along with this reduction in Fe moment and interlayer separation in going from the high- to intermediate-spin cases, we find that the Ta projected moment significantly increases from 0.03 μ_B per Ta in the high-spin case to 0.15 μ_B per Ta in the intermediate-spin case for those two Ta closest to the Fe. These Ta moments are antiferromagnetically coupled to the Fe moments. Our calculations suggest that the Ta acquires this net moment because of charge redistribution to the neighboring Ta sites with the reduction of the interlayer distance. We observe similar trends for the full L-layer series studied with changes in Fe magnetic moments resulting in modification of the interlayer separation and charge transfer to the neighboring Ta sites. We note, however, that in all cases we find a high-spin ground state.

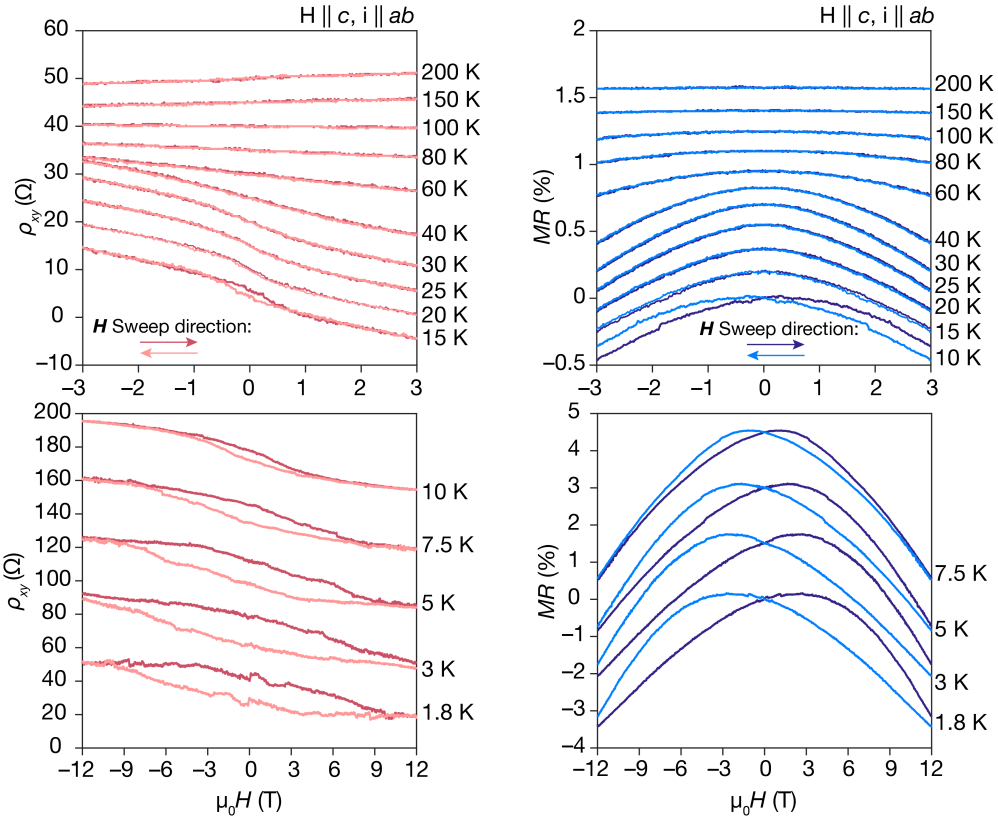


Figure 2.13: Temperature dependence of the symmetrized ρ_{xy} and magnetoresistance (MR) for the 2-layer $Fe_{0.58(14)}TaS_2$ device.

These theoretical results point to other possible origins of the multiple magnetic phases observed in experiments, independent of intercalant/superlattice disorder. Firstly, we identify

metastable spin states in our DFT calculations that are strongly dependent on the interlayer separation and the resulting Fe local environment. This strong structural dependence on the total magnetization could give rise to spin state transitions upon thermal lattice contraction. Secondly, we find that the Ta atoms adjacent to our Fe intercalants acquire a non-negligible moment (0.15 μ_B/Ta in the 2-layer case) depending on the interlayer separation. This moment on Ta could also result in a separate magnetic ordering temperature. Future experimental and theoretical studies on 2D Fe_xTaS_2 spanning a greater range of stoichiometries, and degrees of intercalant ordering may reveal additional details on how magneto-structural disorder and lowered dimensionality affect the value of T_C and competing long-range magnetic orders.

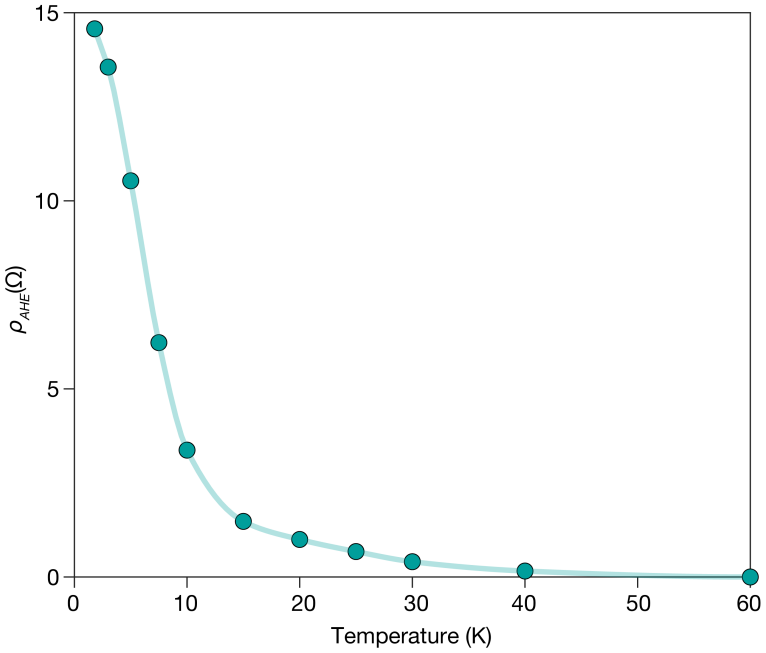


Figure 2.14: Temperature dependence of the remanent ρ_{AHE} for the 5-layer $Fe_{0.38(4)}TaS_2$ device.

2.4 Conclusions

We have demonstrated that long-range ferromagnetic order persists down to the thinnest limit of the magnetic intercalation compound Fe_xTaS_2. Combined structural, spectroscopic, and magnetoelectronic characterization indicates that both intercalant order/disorder and stoichiometry influence the magnetic properties of these low-dimensional materials. Nevertheless, overall, the high MCA expected from the coordination environment imposed by the vdW interface between TaS_2 sheets appears to stabilize long-range, hard ferromagnetic ordering in

samples of all thicknesses. More broadly, our results demonstrate a versatile platform for developing 2D magnets with magnetic properties that can be manipulated by modulating their intercalation amount, dimensionality, and structural homogeneity. This work opens the door to modulating the MCA and MEIs of intercalated TMDs by marrying the synthetic versatility of soft chemical intercalation[39, 90–93] with distinctive techniques developed for fabricating vdW architectures and controlling the emergent physics in atomically layered materials, such as layer count,[74, 127] deterministic assembly of vdW heterostructures,[128, 129] electrostatic gating,[76, 77] strain,[130, 131] and the introduction of an interlayer twist.[132, 133] Exploring this constellation of tuning knobs is poised to produce novel 2D intercalation compounds that enable the exploration of exotic emergent magnetic phases as well as materials for low energy switching of magnetism.

2.5 Methods Chapter 2

Mechanical exfoliation of hexagonal boron nitride (hBN)

The mechanical exfoliation of hBN (used as received from T. Taniguchi and K. Watanabe) is performed outside the glovebox. First, 90 nm SiO_2/Si chips are cut into $\sim 1 \times 1$ cm pieces and cleaned for 60 minutes in an ozone cleaner. Immediately before the chip cleaning is complete, 4 hBN crystals ($\sim$1.5 mm $\times$ 1.5 mm) are tessellated with adhesive tape (Magic Scotch). Then, the chips are removed from the ozone cleaner, placed shiny-side-up onto the tape, and pressed for 10 minutes with finger pressure. After this, the tape is swiftly taken off the chips.

Mechanical exfoliation of $2H^{-}TaS_2$.

The mechanical exfoliation of $2H-TaS_2$ (HQ Graphene) is done in an Ar glovebox using an adhesive tape (Magic Scotch). First, 90 nm SiO_2/Si chips are cut into $\sim$1 $\times$ 1 cm pieces and cleaned for 2 minutes in an oxygen plasma cleaner. The chips are left on the glovebox hotplate at 200 °C while tessellating a large $2H-TaS_2$ crystal ($\sim 3 \times 3$ mm) with the adhesive tape. Then, the chips are taken off the hotplate, placed shiny-side-up onto the tape and pressed for 10 minutes with finger pressure. After this, the tape is swiftly taken off the chips.

Encapsulation of $2H^{-}TaS_2$ with hBN

Our samples were prepared with the dry transfer method using a home-built micro-manipulation stage in an Ar glovebox. In a typical procedure, we prepared a polymeric stamp consisting of a poly(bisphenol A carbonate), PC, film covering a polydimethylsiloxane (PDMS) stamp on a glass slide. To assemble the polymer stamp, we first prepared a solution of PC by making a 5% w/w solution of PC (Sigma Aldrich) in chloroform (Lab Chem). The PC solution was placed onto a glass slide using a glass pipette and spread by sandwiching the PC-covered slide

with a clean glass slide. The two slides were quickly separated and placed PC-side-up onto a hotplate at 120 °C. After 5 minutes of baking, a relatively uniform PC film was formed. This film was cut into small squares (2 mm × 2 mm) using a razor blade. The squares were placed onto a 4 mm × 4 mm PDMS square that has been attached to a glass slide. When this PC/PDMS stack was completed, it was placed on a hotplate at 120 °C for 2 minutes. Next, the PC/PDMS polymer stamp was used to pick up hBN, which was subsequently placed onto a $2H-TaS_2$ flake. The edges of the $2H-TaS_2$ flake were left uncapped to enable subsequent intercalation. Next, the hBN was released on the $2H-TaS_2$ flake by melting the PC stamp at 160 °C. For thicker $2H-TaS_2$ flakes (> 6 layers), the PC film was dissolved in chloroform for 20 minutes under an ambient atmosphere. The chip containing the sample was then subsequently washed with isopropanol (Sigma Aldrich) and dried with flowing N2. For thinner samples (< 6 layers), the PC film was dissolved in dichloromethane (Fisher Scientific) for 20 minutes in an Ar-filled glovebox. The sample was then rinsed in toluene and dried with flowing Ar.

Sample preparation for transmission electron microscopy (TEM)

Samples for imaging along the crystallographic *c*-axis

TEM samples for imaging along the c-axis were prepared on silicon nitride holey TEM grids with a 200 nm membrane thickness (Norcada). The previously described dry transfer method was used to transfer $2H-TaS_2$ flakes from the SiO_2/Si support onto the silicon nitride membrane. Immediately before stacking, the TEM grid was cleaned for 5 minutes in an oxygen plasma cleaner.

Cross-sectional samples for imaging along the *ab*-plane

Cross-sectional TEM samples were prepared with FEI Helios 660 and Thermo Scientific Scios 2 focused ion beam scanning electron microscopy (FIB-SEM) systems. A 200 nm coating of Pt or C was deposited over the device's Hall bar channel using an electron beam at 5 kV and 1.6 nA. This was followed by a deposition of 2.5 μm Pt or C layer using a gallium-ion beam at 30 kV and 0.1 nA. The initial bulk-out was performed with a 30 kV Ga beam and 3 nA current, while the bulk-out cleaning was done with a 1 nA current. For the initial thinning, a 30 kV Ga beam was used, while the current was increasingly lowered as the sample became thinner. Initial thinning was started with a 1 nA current, while the final current for the rough thinning was typically 0.3 nA. After the sample was approximately 150 nm thick, we switched to the 5 kV and 40 pA settings. The final polishing was done at 2 kV and 40 pA to reduce the ion beam damage. Note that sample damage occurs at the interfaces of Fe_xTaS_2 with other layers, including SiO_2 and hBN. This was evident from HRSTEM, where Fe_xTaS_2 layers at interfaces look deformed and blurred. Typically, the first 1–3 layers of Fe_xTaS_2 that interface SiO_2 are deformed and blurred, while up to one layer is blurred at the hBN/TaS_2 interface. This deformation and apparent amorphization of layers stems from the FIB preparation. We

conclude this based on the Raman spectra of atomically thin devices before the FIB process. These Raman spectra retain vibrational modes associated with layer vibrations, which would be absent for amorphous or completely deformed samples.

Chemical treatment of $2H-TaS_2$ flakes

Acetone (Sigma-Aldrich) was freeze-pump-thawed and then dried over CaCl2 (Acros Organics) for more than 12 hours before the reaction. Acetonitrile (Fisher Scientific) and toluene (Fisher Scientific) were obtained from a solvent purification system and dried over 3 Å molecular sieves for at least 12 hours before the reaction. All solvents were handled under an inert atmosphere and passed through a 0.2 μm PTFE syringe membrane filter (VWR) before use to prevent the introduction of particulate matter into the reaction flask.

Method 1: Treatment with $Fe(CO)_5$ in toluene

10 mL of toluene, a Teflon boat, and a Teflon-coated stir bar were added to a glass scintillation vial and heated to 55 °C in a hotplate heating block. Then, mechanically exfoliated $2H-TaS_2$ (HQ Graphene) on a supporting substrate was placed into the Teflon boat and 14 µL of $Fe(CO)_5$ (Sigma Aldrich) was dispensed into the reaction vial. The vial was closed with a Teflon cap and the solution was left to stir for ∼24 hours at 55 °C with a dim white light placed next to the vial to promote slow $Fe(CO)_5$ photodecomposition. After the reaction, the chip was washed three times in warm toluene and then dried in Ar. The sample was then annealed in high-vacuum (approximately 10^{-1} Torr) by rapidly warming to 120 °C at 60 °C/min with a 5 minute hold, followed by heating at 11.5 °C/min to 350 °C and a 30 minute hold at 350 °C, before cooling to room temperature at 13.5 °C/min.

Treatment with $Fe(CO)_5$ in acetonitrile or acetone

In an Ar-filled glovebox, mechanically exfoliated $2H-TaS_2$ (HQ Graphene) flakes on a supporting substrate were placed into a round-bottom flask and sealed. The flask was evacuated and flushed with N_2 gas on a Schlenk line. Dry, degassed solvent (10 mL) was added to the flask and heated to 50 °C. 14 μL (0.02 g) of $Fe(CO)_5$ was then injected into the reaction flask which was maintained at 50 °C for 24 hours under flowing N_2. During the reaction, a dim white light was placed next to the flaks to promote slow Fe(CO)5 decomposition. After 24 h, the chip was rinsed three times in dry solvent, followed by another rinse in degassed acetone and ethanol. The sample was then annealed in high-vacuum conditions using the same procedure described in Method 1.

Nanofabrication

All nanofabrication steps were performed in the Marvell Nanofabrication Laboratory after the chemical intercalation and annealing of samples. In a typical fabrication procedure, we used

electron beam lithography (Crestec CABL-UH Series Electron Beam Lithography System) to define electrical contacts. Reactive ion etching (RIE) with a mixture of 35 sccm CHF3 and 5 sccm O_2 (Plasma-Therm PK-12 RIE) for 30 seconds was used to remove hBN and expose fresh Fe_xTaS_2. Immediately afterwards, Cr/Pt (2 nm/100 nm) was evaporated onto Fe_xTaS_2 (NRC thermal evaporator). After lift-off, electron-beam lithography was used to define a Hall bar-shaped etch mask. The subsequent etching of the Hall bar shape for thin samples (¡ 6 layers) was performed by reactive ion etching with 35 sccm CHF_3 and 5 sccm O_2. On the other hand, thicker samples were etched with ∼25 etch cycles of XeF_2 (Xetch instrument) for 20 seconds at 3.2 Torr. After the hBN/Fe_xTaS_2 etching, the samples were cleaned for 20 seconds in a 40 sccm O2 plasma and subsequently the residual PMMA resist was dissolved in acetone.

Transmission electron microscopy (TEM)

High-resolution TEM and nanobeam electron diffraction (NBED) measurements were performed on a JEOL 2100-F TEM operated at 200 kV at the Molecular Foundry. For NBED, the nanobeam spot radius was set to 90 nm. Selected area electron diffraction (SAED) patterns were obtained with a 40 μm diameter aperture using an FEI Tecnai T20 S-TWIN TEM operated at 200 kV.

STEM-EDS of cross-sectional TEM samples was performed on the FEI TitanX microscope at the National Center for Electron Microscopy (NCEM). The microscope was operated at 60 kV with a probe convergence angle of 10 mrad and a beam current of $\sim$ 150 pA. The total acquisition time varied from 3 to 20 minutes, depending on the signal-to-noise ratio. STEM-EDS maps were collected in multiple regions of the cross-sectional samples, and the averages and standard deviations of these data sets were reported in the main paper.

HRSTEM imaging of layers was conducted on an FEI TitanX microscope operated at 200 kV with a convergence angle of 10 mrad and a half collection angle of 52 mrad. Differential phase contrast (DPC) STEM measurements were acquired on the TEAM 0.5, which is a Titan 80-300 with a probe corrector, at NCEM. The microscope's accelerating voltage was 300 kV, the convergence angle was 30 mrad, and the beam current was 70 pA. The 4D-STEM scans were acquired using the 4D Camera with a frame time of 11 μsec per probe position, 576 $\times$ 576 pixels, and 1024 $\times$ 1024 probe positions. The DPC-STEM data was acquired simultaneously with HAADF-STEM images.

Electron energy loss spectroscopy measurements were acquired on the TEAM 1 which is a Titan 80-300 with a probe corrector. The microscope's accelerating voltage was 300 kV, the convergence angle was 17.1 mrad, and the beam current was 87 pA. The collection semi-angle was 41.9 mrad. The dispersion on the spectrometer was 90 meV/channel. Spectra was summed over three passes across the samples, with an exposure of 0.01 seconds/pixel.

STEM-EDS analysis

Analysis of the STEM-EDS data was carried out in the Bruker Esprit 1.9 software. Series Fit deconvolution was employed to deconvolute overlapping peaks. Next, to estimate the atomic percentage (at. %) of the amount of Fe coming from the TEM column, we analyzed a $2H-TaS_2$ sample that was not intercalated. We determined that the at. % ratio of Fe to Co coming from the column is approximately 1:1. Thus, by identifying the at. % of Co in the EDS signal of our intercalated samples, it was possible to determine the amount of signal coming from the stainless-steel column. This "column iron" background contribution was subtracted from the total Fe at. % to determine the final iron intercalation amount.

Raman spectroscopy

Ultra-low frequency (ULF) Raman spectroscopy (Horiba Multiline LabRam Evolution) was conducted using a 633 nm laser excitation at a power of 50–80 μW with 10-second acquisition times and five accumulations. Baseline correction was performed by fitting a polynomial curve to the background. Raman maps of the Hall bar channel were obtained after magnetotransport measurements, with typical step sizes of 1 μm. These spectra were summed to obtain cumulative Raman spectra displayed in the main paper.

Transport measurements

Transport measurements were performed using standard lock-in techniques. In brief, a small 0.5–1 μA alternating current (17.777 Hz) was applied between the source and drain contacts. Concurrently, the four-probe longitudinal (V_{xx}) and transverse (V_{xy}) voltage drops were measured with a lock-in amplifier (Stanford Research SR830). All phases were $\leq$ 3nd so from the measured values, resistances could be determined with Ohm's law. Measurements were obtained across the Hall bar channel, and values extracted from these measurements (e.g. coercive fields) were averaged from all measured values. The standard deviation (1 σ) obtained from these measurements is reported as the error in the main paper.

Unless otherwise indicated, the field-dependent R_{xx} and R_{xy} data were symmetrized (anti-symmetrized) in accordance with established methods:[134]

$$\begin{aligned}
R^{Forward}_{xx,symm}(\mu_0 H) &= \frac{1}{2}[R^{Forward}_{xx,raw}(\mu_0 H) + R^{Reverse}_{xx,raw}(-\mu_0 H)] \\
R^{Reverse}_{xx,symm}(\mu_0 H) &= \frac{1}{2}[R^{Reverse}_{xx,raw}(\mu_0 H) + R^{Forward}_{xx,raw}(-\mu_0 H)] \\
R^{Forward}_{xy,symm}(\mu_0 H) &= \frac{1}{2}[R^{Forward}_{xy,raw}(\mu_0 H) - R^{Reverse}_{xy,raw}(-\mu_0 H)] \\
R^{Reverse}_{xy,symm}(\mu_0 H) &= \frac{1}{2}[R^{Reverse}_{xy,raw}(\mu_0 H) - R^{Forward}_{xy,raw}(-\mu_0 H)]
\end{aligned} \tag{2.3}$$

The field-dependent R_{xx} signal was converted to magnetoresistance using Equation 2.4.

$$MR(\%) = \frac{R_{xx}(H) - R_{xx}(H=0)}{R_{xx}(H=0)} \times 100\% \tag{2.4}$$

The measured transverse resistance (R_{xy}) was separated into the ordinary Hall effect term (R_{OHE}) and the anomalous Hall effect term (R_{OHE}) according to the following equation:

$$R_{xy} = R_{\mathrm{OHE}} + R\mathrm{AHE} = \frac{1}{ne}\mu_0 H + R_{\mathrm{AHE}} \tag{2.5}$$

where n is the 2D carrier density, μ_0 is the vacuum vacuum permeability, and H is the applied magnetic field ($H \parallel c$). The R_{OHE} term is linearly proportional to the applied magnetic field and was used to calculate the carrier density of the device. The R_{AHE} term reported herein is directly proportional to the magnetization of the sample[38] and was obtained by subtracting the R_{OHE} term from the measured R_{xy} signal.

Electronic band structures and density of states were calculated in the density functional theory framework using the Vienna Ab-initio Simulation Package (VASP).[135–139] Projector augmented wave pseudopotentials[139, 140] included Fe $3d^6 4s^2$, Ta $5p^6 5d^3 6s^2$, S $3s^2 3p^4$ electrons as valence. The structures were constructed in a $\sqrt{3} \times \sqrt{3}$ supercell of $2H-TaS_2$ and a 15 Å vacuum gap was included out-of-plane. The PBEsol exchange-correlation functional[141] was used with 800 eV plane wave energy cut-off and a 10×10×1 Gamma-centered k-point grid, which converged the total energy within 1 meV per formula unit. Hubbard U corrections were applied to the Fe d-orbitals by the Liechtenstein method[142] with U = 4.0 eV and J = 0.7 eV. This is consistent with previous studies that used similar values of U and J to account for the Fe-d localization.[36] We further validated this choice of U by comparing our calculated lattice parameters of bulk $Fe_{1/4}TaS_2$ with experiments, finding that a U of 4.0 eV gave in-plane and out-of-plane lattice parameters within 1% of those measured. Structure optimizations to a force tolerance of 2 meVÅ^{-1} gave the following in-plane lattice parameters: 2-layers: 5.723 Å, 3-layers: 5.729 Å, 4-layers: 5.718 Å, and 5-layers: 5.710 Å. Spin-orbit coupling was included for the magnetocrystalline anisotropy calculations only.

Chapter 3

Tailored topotactic chemistry unlocks heterostructures of magnetic intercalation compounds

Parts of this section were adapted or reproduced from: Husremović, S.; Gonzalez, O.; Goodge, B.; Xie, L.; Kong, Z.; Zhang, W.; Ryu, S. H.; Ribet, S.; Bustillo, K.C.; Song, C.; Ciston, J.; Taniguchi, T.; Watanabe, K.; Ophus, C. M.; Jozwiak, C.; Bostwick, A.; Rotenberg, E.; Bediako, D. K. *Submitted* **2024**.

Author contributions: S.H. and D.K.B. conceived the study. S.H., O.G., and W.Z. fabricated the samples. S.H., B.H.G., K.C.B, and C.S. imaged samples using TEM. S.H., L.X., O.G., S.H.R., C.J., A.B., E.R. performed nanoARPES experiments. Z.K. performed the XPS study. S.H., S.M.R., and C.O. developed the code for the virtual apertures. T.T. and K.W. provided the hBN crystals. S.H. and D.K.B. wrote the manuscript with input from all co-authors.

3.1 Abstract

The construction of thin film heterostructures has been a widely successful archetype for fabricating materials with emergent physical properties. This strategy is of particular importance for the design of multilayer magnetic architectures in which direct interfacial spin–spin interactions between magnetic phases in dissimilar layers lead to emergent and controllable magnetic behavior. However, crystallographic incommensurability and atomic-scale interfacial disorder can severely limit the types of materials amenable to this strategy, as well as the performance of these systems. Here, we demonstrate a method for synthesizing heterostructures comprising magnetic intercalation compounds of transition metal dichalcogenides (TMDs), through directed topotactic reaction of the TMD with a metal oxide. The mechanism of

the intercalation reaction enables thermally initiated intercalation of the TMD from lithographically patterned oxide films, giving access to a new family of multi-component magnetic architectures through the combination of deterministic van der Waals assembly and directed intercalation chemistry.

3.2 Introduction

Solid heterostructures make it possible to leverage the proximity of disparate electronic phases to engineer exotic physical phenomena[143–145]. Magnetic multilayers are among the most technologically relevant of these systems, with the pioneering discovery of giant magnetoresistance serving as a major milestone in the development of magnetic memory, sensors, and spintronic devices more broadly[146, 147]. Beyond elemental multilayers, the assembly of binary or ternary metal compounds into heterostructures vastly expands the range of possible functionality in such systems, as the ground state magnetic/electronic behavior of the constituent layers can be considerably more diverse[148, 149]. Equally important is the control over the integrity of interfaces between dissimilar materials. Interfacial atomic disorder–such as that endemic to heterostructures of some oxides and heterojunctions of polar compound semiconductors–can play a defining role in the properties of the architecture[150, 151].

Transition metal dichalcogenides (TMDs) intercalated with spin-bearing transition metals are appealing targets for bespoke magnetic heterostructures because they exhibit a wide range of properties that would be attractive in the design and study of magnetic multilayers: hard ferromagnetism in $Fe_{0.25}TaS_2$[37–39, 73], chiral magnetic textures in $Cr_{0.33}TaS_2$ and $Cr_{0.33}NbS_2$[152–155], electrically driven collinear antiferromagnetic switching in $Fe_{0.33}NbS_2$[120, 156], triple-Q antiferromagnetic ordering and topological Hall effect in $Co_{0.33}TaS_2$ and $Co_{0.33}NbS_2$[157, 158], and recently proposed so-called altermagnetic order in $V_{0.33}NbS_2$[159]. Their diverse properties emerge from the interplay between the host lattice structure, intercalant identity and superlattice symmetry, stoichiometry, and disorder/homogeneity[30, 155]. Integrating these versatile crystals into van der Waals (vdW) heterostructures with customizable interfaces may unlock a new frontier of magnetic architectures with designed interfacial interactions and magnetoelectronic properties. However, the absence of effective synthesis methods has impeded the development of 2D heterostructures comprising magnetic intercalated TMDs. Even established techniques for fabricating heterostructures of layered crystals, such as mechanical exfoliation followed by vdW assembly, are not viable for intercalated crystals: the strong interlayer interactions imparted by the intercalants pose significant challenges in isolating thin crystals,[160] which are integral components of heterostructures. Prior work on vdW assembly of intercalated TMDs has been limited to preparing magnetic tunnel junctions with incidental oxide formation at ill-defined and poorly controlled interfaces[160, 161].

Here, we demonstrate a synthetic framework to create pristine heterostructures comprising magnetic TMD intercalation compounds of $2H-TaS_2$ and $2H$–NbS_2 containing Fe and Co.

Previous work has shown that treatment of TMDs with solutions of zerovalent transition metals can lead to TMD intercalation compounds, with the reaction mechanism remaining elusive. We show that this topochemical reaction involves the formation of a metal oxide film derived from the zero-valent metal carbonyl precursor. We then establish that this metal oxide film releases divalent metal ions into the TMD upon annealing. Concomitantly, the oxide-exposed TMD surfaces sacrificially oxidize, thereby supplying the necessary charges to electron-dope the remaining pristine TMD layers for charge balance. Leveraging these new mechanistic insights, we develop an approach for patterning metal oxide precursor films onto TMDs that (1) facilitates studies of intercalant diffusion/ordering; (2) produces ultraclean surfaces to allow electronic structure measurements by nano-angle-resolved photoemission spectroscopy (nanoARPES); and (3) enables distinctive magnetic heterostructures of TMD intercalation compounds with atomically clean heterointerfaces. These insights and methodology establish a versatile route to new families of multi-component spintronic architectures through the combination of directed nanoscale solid-state intercalation chemistry with the myriad structural tuning knobs available for vdW heterostructures.

3.3 Results and discussion

Synthesis of few-layer intercalation compounds with solid-state topochemistry

We first illustrate the basic synthetic approach by focusing on a single intercalant species (Fe) and host lattice ($2H-TaS_2$), demonstrating how nanoscale solid-state reactions offer a versatile method for synthesizing low-dimensional TMDs intercalated with transition metals. In previous work[73, 93] it has been shown that 2D flakes treated with zero-valent metal carbonyls in organic solvents (like $Fe(CO)_5$ in acetone) (Figure 3.1a, left) often necessitate vacuum annealing to evince clear signs of intercalation in their Raman spectra, such as the appearance of new phonon modes associated with the intercalant superlattice and Raman peak shifts indicative of charge transfer to the layered host lattice. Indeed, we find this thermal treatment to be consistently required in the case of $2H-TaS_2$ (Figure 3.2)[73]. Here, to first understand the effect of this thermal treatment at an atomic level, we use atomic-resolution high-angle annular dark-field scanning transmission electron microscopy (HAADF-STEM) to examine samples heated to different temperatures. HAADF-STEM imaging was performed on cross-sectional samples made from $2H-TaS_2$ flakes on SiO_2/Si treated with 10 mM $Fe(CO)_5$/acetone and subjected to thermal annealing at 100 °C (Figure 3.1b), 200 °C (Figure 3.3) or 350 °C (Figure 3.1c). These samples, labeled S1–S3, display substantial structural differences: whereas interstitial sites in the vdW interface of S1 and S2 appear largely vacant, S3 displays a high occupancy of intercalants in the pseudo-octahedral sites. To identify these intercalants and compositionally characterize S1–S3, we complement this atomic-resolution imaging with spatially resolved electron energy loss spectroscopy (EELS). EEL spectra of S1–S3 reveal the spectroscopic fingerprint of Fe only for the sample annealed at 350 °C (S3)

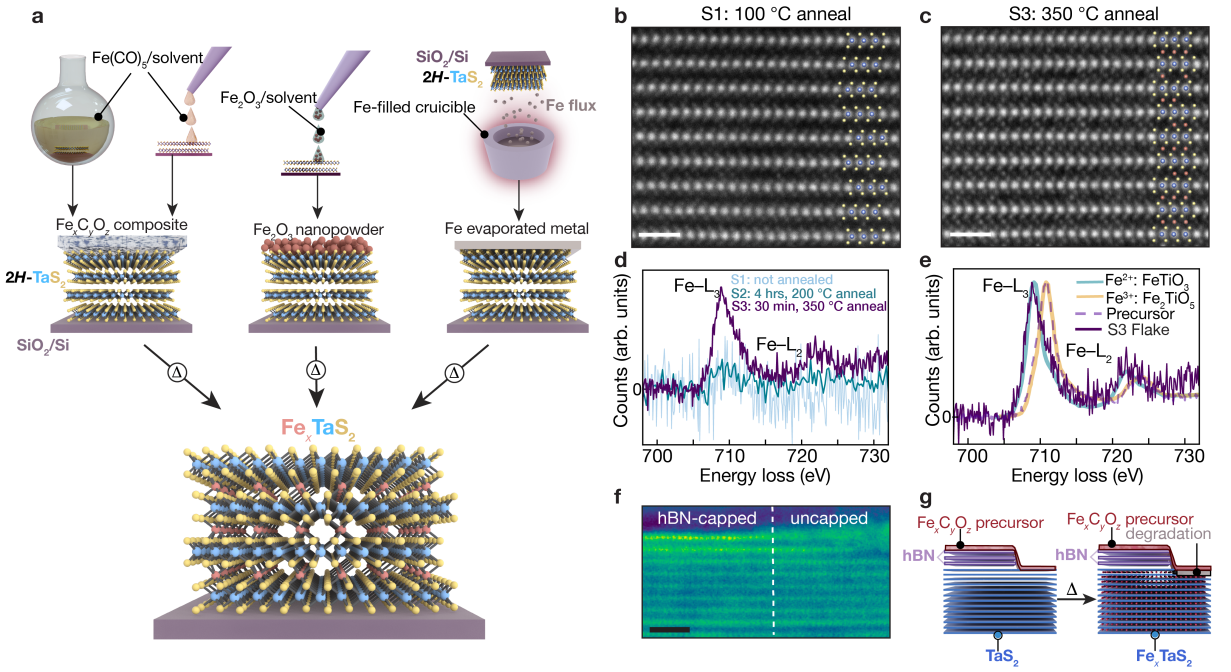


Figure 3.1: Nanoscale solid-state intercalation of vdW crystals and pristine heterostructures. **(a)** Schematic of depositing Fe precursors onto $2H-TaS_2$ crystals on SiO_2/Si support followed by vacuum annealing to yield Fe-intercalated $2H-TaS_2$ (Fe_xTaS_2). **(b,c)** High-angle annular dark-field scanning transmission electron microscopy (HAADF-STEM) atomic-resolution images along the $[10\bar{1}0]$ zone axis of $2H-TaS_2$ flakes labeled S1 and S3 immersed in $Fe(CO)_5$/acetone for 24 hours at 48 °C and subsequently vacuum annealed at 100 °C for 12 hours (S1) **(b)** and 350 °C for 30 minutes (S3) **(c)**. Micrographs are overlaid with the structure of $2H-TaS_2$ (ref [162]). Intercalants are marked in (c). Scale bars in (b,c): 1 nm. **(d)** Cumulative electron energy loss (EEL) spectra of $2H-TaS_2$ flakes labeled S1–S3 treated in $Fe(CO)_5$/acetone and vacuum annealed with distinct thermal conditions. Spectra are normalized by total acquisition time. **(e)** Cumulative EEL spectra of flake S3 and the composite $Fe_xC_yO_z$ that formed during the $Fe(CO)_5$/acetone treatment. Experimental spectra, normalized by the L_3 peak maxima, are overlaid with literature spectra for $(Fe^{2+})TiO_3$[163] and $(Fe^{3+})_2TiO_5$[163]. Data in (d) and (e) was obtained at ∼100 K. **(f)** High-resolution STEM micrograph of a $2H-TaS_2$ flake that was partially capped with hexagonal boron nitride (hBN), treated with $Fe(CO)_5$/isopropanol, and vacuum annealed at 350 °C for 1.5 hours. Scale bar: 2 nm. **(g)** Schematic of the thermally activated reaction between hBN/$2H-TaS_2$ and $Fe_xC_yO_z$.

(Figure 3.1d). Taken together, HAADF-STEM, EELS, and Raman data show that substantial intercalation does not occur during treatment in $Fe(CO)_5$ solution alone, even with prolonged (24.5 h) soaking in a 10 mM solution of the zerovalent metal carbonyl. Instead, we observe the formation of a thin film on the surface of the chip (Figure 3.4) containing Fe, C, and O in a molar ratio of approximately 1:3.5:3 and 1:1:2 before and after annealing, respectively (Figure 3.5). Upon annealing at 350 °C (in a process that necessitates exposing the film for a few minutes to ambient conditions) under high vacuum, $2H-TaS_2$ flakes in contact with this film are topochemically converted to Fe_xTaS_2 in a solid-state reaction. The chemical details of this topochemical reaction are now discussed.

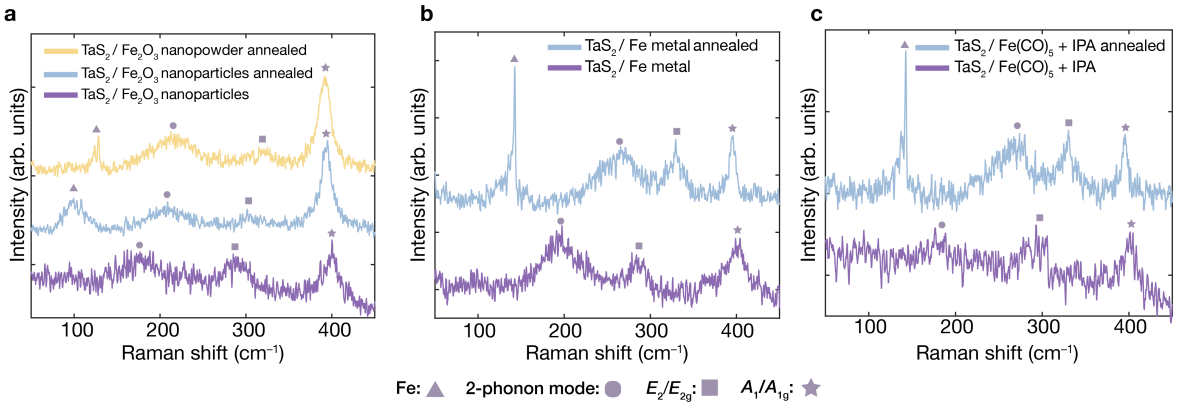


Figure 3.2: Raman spectra of $2H-TaS_2$ upon annealing in contact with different Fe precursors. **(a–c)** Change in the Raman spectra of $2H-TaS_2$ upon annealing to 350 °C in contact with Fe_2O_3 nanoparticles/nanopowder **(a)**, evaporated Fe **(b)**, $Fe_xC_yO_z$ precursor deposited from $Fe(CO)_5$/isopropanol. Raman symmetry labels are added in (a–c) according to the legend outlined below the spectra.

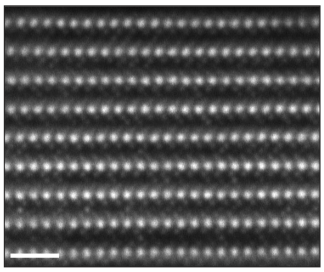


Figure 3.3: Atomic-resolution imaging of sample S2. HAADF-STEM of sample S2, a $2H-TaS_2$ flake immersed in $Fe(CO)_5$/acetone for 24 hours at 48 °C and subsequently annealed to 200 °C for 4 hours. Scale bar: 1 nm.

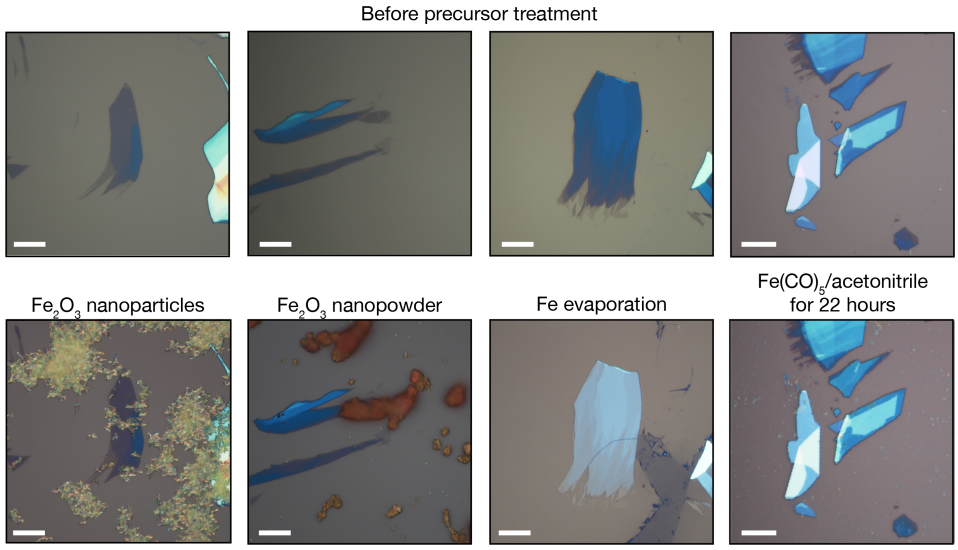


Figure 3.4: Treatment of $2H-TaS_2$ flakes with different Fe precursors. Optical micrographs of $2H-TaS_2$ flakes before and after treatment with various Fe precursors. Scale bars: 10 μm.

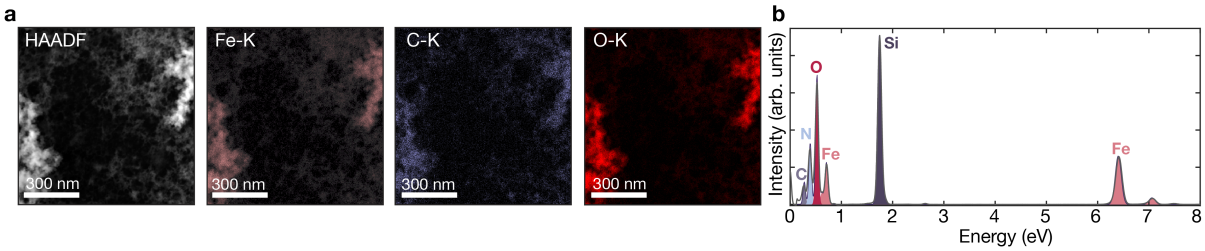


Figure 3.5: Compositional analysis of $Fe_xC_yO_z$ precursors. (a) Scanning transmission electron microscopy coupled with energy-dispersive X-ray spectroscopy (STEM-EDS) of $Fe_xC_yO_z$ made by drop casting a 370 mM solution of $Fe(CO)_5$/toluene onto a 30 nm silicon nitride TEM membrane. **(b)** Cumulative STEM-EDS spectrum of the sample from (a). **(c–f)** high-angle annular dark-field STEM (HAADF-STEM) images with marked composition of the indicated regions for $Fe_xC_yO_z$ prepared by drop-casting $Fe(CO)_5$/toluene

Nature of the intercalation reaction with carbonyl-derived films

To probe the redox process accompanying intercalation, we examine the Fe species in the carbonyl-derived films and $2H-TaS_2$ using a combination of EELS and X-ray photoelectron spectroscopy (XPS) (Figures 3.6–3.8). While Fe^{3+} is the majority species in the films (Figure 3.1e, Figure 3.6, Figure 3.7a–d, Figure 3.8), Fe centers intercalated between $2H-TaS_2$ layers exist exclusively as Fe^{2+} (Figure 3.1e)[163, 164], in agreement with prior work[73, 102]. We gained additional insight into the intercalation redox chemistry through solid-state reactions between TaS_2 and Fe_2O_3 powders. These reactions form products with three distinct crystallite colors/shapes and a yellow powder (Figure 3.9a–d). Raman spectra of these products are consistent with the phonon modes of Fe_xTaS_2, Ta_2O_5, $1T-TaS_2$, and sulfur, respectively (Figure 3.9e). The formation of products possessing compositions consistent with Ta_2O_5 and Fe_xTaS_2 from the reaction of TaS_2 with Fe_2O_3 is validated by SEM-EDS analysis (Figure 3.9f,g). Moreover, powder X-ray diffraction analysis (Figure 3.10) supports a product mixture of Fe_xTaS_2, Ta_2O_5, $1T-TaS_2$, and $2H-TaS_2$ from these solid-state reactions. From these data, we surmise that reaction of TaS_2 and Fe_2O_3 leads to a disproportionation of Ta^{4+} in TaS_2 to Ta_2O_5 and reduced (electron-doped) TaS_2 intercalated with Fe^{2+}, (*i.e.* Fe_xTaS_2). A possible overall reaction for this process is:

$$(6x+10)TaS_2 + 5xFe_2O_3 \longrightarrow 3xTa_2O_5 + 10\,Fe_xTaS_2 + 12xS \tag{3.1}$$

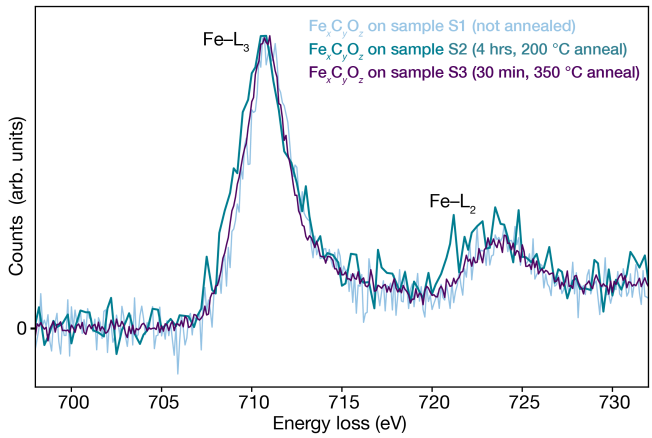


Figure 3.6: EEL spectra of $Fe_xC_yO_z$ films formed on flakes S1–S3. Cumulative EEL spectra of the $Fe_xC_yO_z$ composite films that formed during the $Fe(CO)_5$/acetone treatment on top of S1–S3. Spectra are normalized by the L_3 peak maxima.

To test this further, we examine the reactions of carbonyl-derived metal oxide films on nano-thick $2H-TaS_2$ flakes using high-resolution STEM and EELS measurements (Figure 3.1f, Figure 3.8). We find that $2H-TaS_2$ layers in direct contact with the films undergo oxidation, while crystalline Fe_xTaS_2 layers form underneath (Figure 3.8), congruent with

the proposed disproportionation. These data also show that Fe intercalation can take place through the basal plane of $2H-TaS_2$, with Fe diffusing both vertically and laterally through $2H-TaS_2$ crystals. Moreover, we find that the diffusivity of Fe enables intercalants to move from regions contacting the film to areas partially encapsulated with a chemically inert hexagonal boron nitride (hBN) (Figure Figure 3.1f). Notably, hBN-encapsulated regions do not contain Ta_2O_5 layers, demonstrating that pristine Fe_xTaS_2 crystals can be synthesized by combining vdW heterostructuring (capping with hBN) and nanoscale solid-state chemistry.

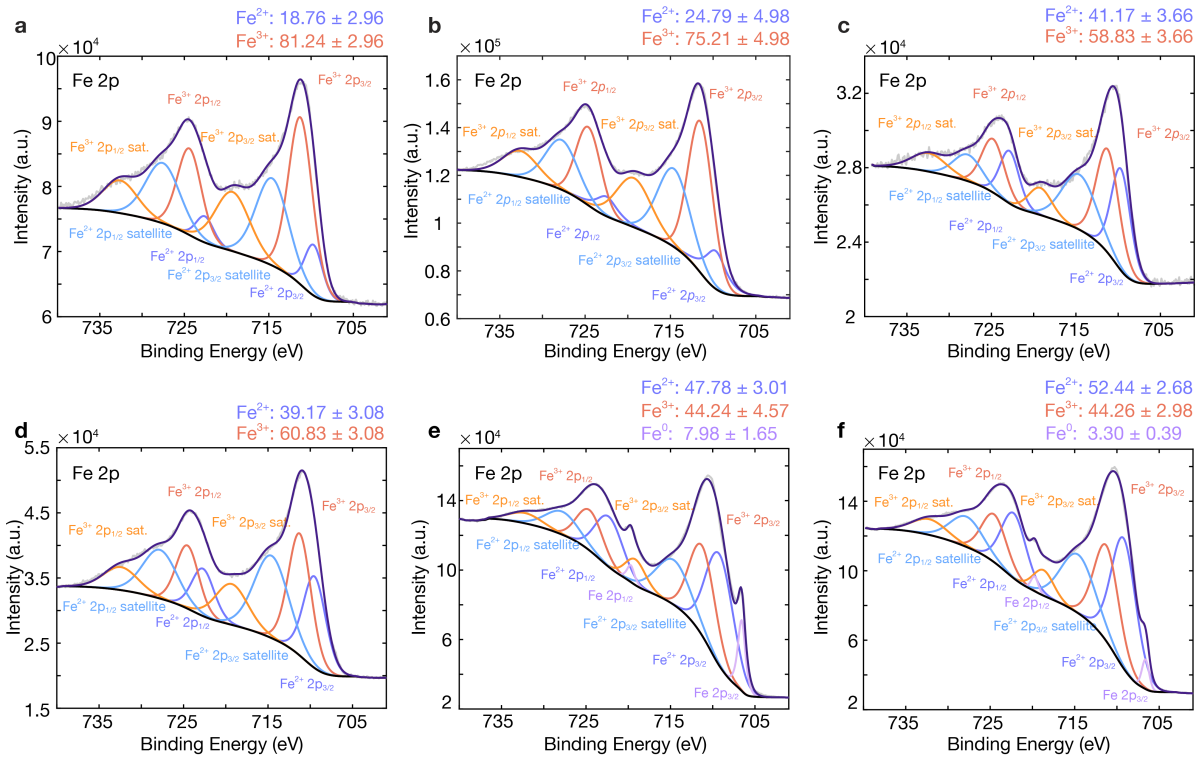


Figure 3.7: X-ray photoelectron spectroscopy (XPS) of Fe precursors. **(a–f)** XPS spectra and corresponding curve fits are presented for $Fe_xC_yO_z$ prepared by drop-casting: 370 mM $Fe(CO)_5$/isopropanol **(a)**, 370 mM $Fe(CO)_5$/isopropanol with subsequent annealing at 350 °C **(b)**, 370 mM $Fe(CO)_5$/ toluene **(c)**, 370 mM $Fe(CO)_5$/toluene with subsequent annealing at 350 °C **(d)**, evaporated Fe **(e)**, and evaporated Fe with subsequent annealing at 350 °C **(f)**. $Fe_xC_yO_z$ precursors were prepared on Si substrates, whereas the evaporated Fe precursor was prepared on 90 nm SiO_2/Si. Ratios of measured Fe components are indicated above each spectrum.

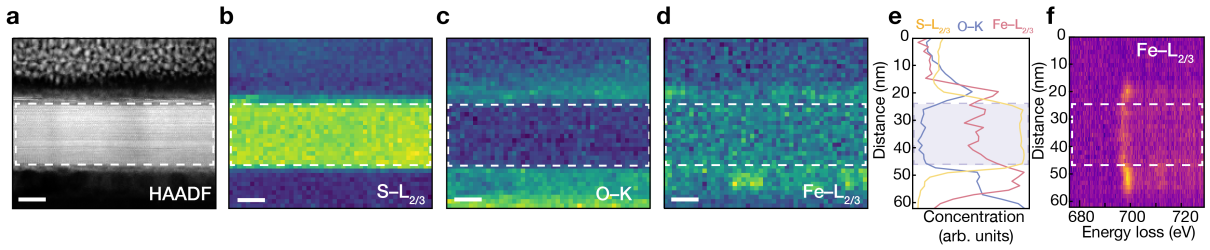


Figure 3.8: Spatially resolved electron energy loss spectroscopy (EELS) of sample S3. Simultaneously recorded HAADF-STEM image of S3 **(a)** and S **(b)**, O **(c)** and Fe **(d)** elemental concentration maps. **(e)** Vertical line profile of the S, O, and Fe concentration. Scale bars (a–d): 10 μm. **(f)** Vertical profile of the Fe energy loss spectrum. The dashed white line in (a–d,f) and solid blue rectangle in (e) mark the crystalline flake region.

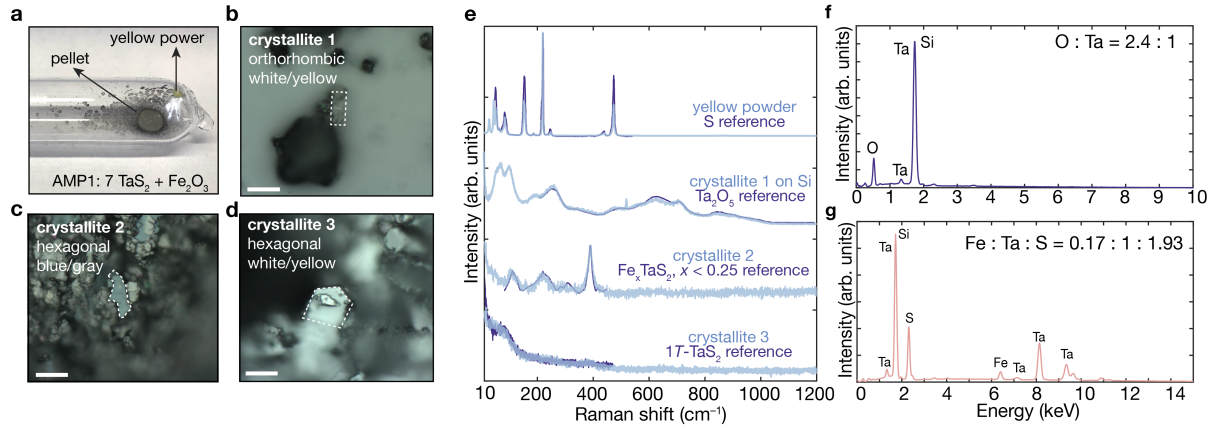


Figure 3.9: Solid-state reactions of polycrystalline TaS_2 and Fe_2O_3. **(a)** Image of sealed glass ampoule enclosing a pellet made by mixing polycrystalline TaS_2 and Fe_2O_3 after a 7-day heating period at 900 °C. **(b–d)** Optical micrographs of three types of micron-sized crystallites obtained after crushing the pellet from (a). These crystallites, outlined in white dashed lines, display different optical contrasts and crystallographic symmetries. Scale bars (b–d): 10 μm. **(e)** Raman spectra of crystallites 1–3 from (b–d). Experimental data is overlaid with reference spectra for bulk $1T-TaS_2$ synthesized herein, and literature spectra for Fe_xTaS_2[73], Ta_2O_5[165] and S [166]. **(f–g)** Representative cumulative SEM-EDS spectra of crystallites whose Raman matches Ta_2O_5 **(f)** and Fe_xTaS_2 **(g)**. Crystallites were placed on a Si chip during the SEM-EDS acquisition.

To confirm and explore the versatility of this chemistry, we also vacuum annealed mechanically exfoliated $2H-TaS_2$ crystals that were coated with a suspension of Fe_2O_3 nanopowder/nanoparticles or a thin layer of electron-beam evaporated Fe metal that subsequently

oxidizes upon air exposure according to XPS in Figure 3.7e,f (Figure 3.1a, middle and right). Both routes also produce Fe_xTaS_2 (Figure 3.2a,b). In addition, we find that the carbonyl-derived metal oxide films can simply be prepared by drop-casting or spin-coating solutions of $Fe(CO)_5$ in isopropanol and then exposing these surfaces to air (Figure 3.1a, left).

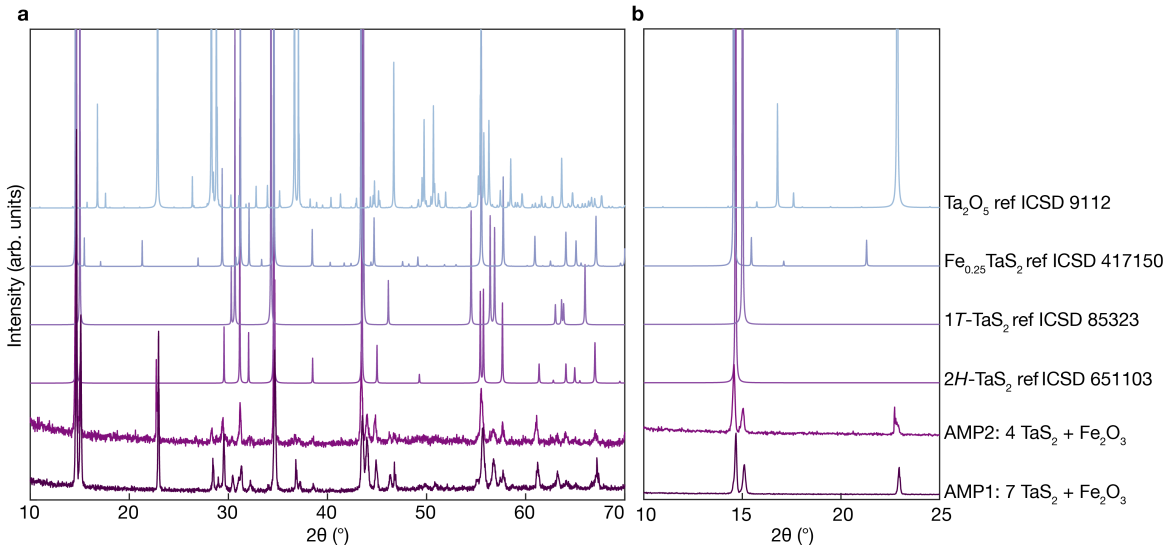


Figure 3.10: (a) PXRD patterns after heating polycrystalline TaS_2 and Fe_2O_3 mixed in a 4:1 or 7:1 stoichiometric ratio for 7 days at 900 °C. Experimental data is plotted with literature patterns for $2H-TaS_2$[162], $1T-TaS_2$[60], $Fe_{0.25}TaS_2$[37] and Ta_2O_5[167]. The experimentally observed PXRD peaks present a combination of peaks from the plotted reference patterns. The presence of $1T-TaS_2$ (representing unreacted TaS_2) implies an incomplete solid-state reaction between TaS_2 and Fe_2O_3 following 7-day heating at 900 °C. **(b)** Diffraction patterns from (b) expanded in the range 2θ= 10°–25°.

Intercalation and interlamellar transport from patterned oxide films

The observed solid-state nature of intercalation enables the precise patterning of carbonyl-derived oxide films onto 2D flakes (Figure 3.11). This precursor patterning now allows us to investigate in detail the effect of vacuum annealing conditions on the intercalation, lateral transport, and crystallographic ordering of Fe centers in few-layer $2H-TaS_2$ flakes. Nanoscale structural ordering of Fe centers was examined using temperature-dependent four-dimensional scanning transmission electron microscopy (4D-STEM). In this experiment, a ∼5.2 nm converged electron probe was scanned across a 1.3 μm × 0.3 μm window on an 11 nm thick $2H-TaS_2$ crystal (through a hole of diameter 2 μm in the underlying silicon nitride TEM membrane), immediately adjacent to the patterned oxide film. Electron diffraction

patterns were obtained at each probe position (Figure 3.12a). This experiment was repeated as the temperature of the TEM holder was increased from 14 °C to 350 °C. We find that nanoscale Fe ordering commences at 250 °C, as evidenced by the emergence of faint $\sqrt{3} \times \sqrt{3}$ Fe superlattice diffraction peaks (Figure 3.12b). This is consistent with our high-resolution scanning transmission electron microscopy (HRSTEM) and electron energy loss spectroscopy (EELS) experiments: Fe was absent in samples annealed up to 200 °C (Figure 3.1b–d and Figure 3.2).

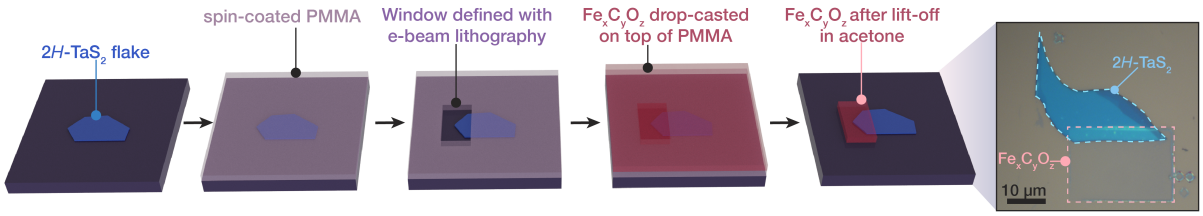


Figure 3.11: Precursor patterning process. Schematic of the lithographic patterning process for $Fe_xC_yO_z$ with a representative optical micrograph of the final product.

Further, 4D-STEM analysis revealed that, as expected for any solid-state reaction with a unidirectional reactant source, the amount of ordered Fe increased with higher temperatures and longer annealing times (Figure 3.13). As these diffraction-based experiments only provide insight into the structurally ordered Fe, 4D-STEM measurements were complemented with STEM-EDS examination of a 22 nm flake annealed ex-situ (Figure 3.12c). Compositional analysis of this crystal at three holes in the underlying membrane (centered approximately 1, 5, and 10 μm away from the oxide film) shows a steady decrease in Fe content (x of 0.30(3), 0.17(2), and 0.04(1), respectively) with increasing distance from the patterned film (Figure 3.12d). Additionally, selected area electron diffraction (SAED) patterns indicate a corresponding change in the Fe superlattice ordering from a well-defined $\sqrt{3} \times \sqrt{3}$ (Figure 3.12e) to a diffuse 2×2 superlattice (Figure 3.12f), ultimately disappearing entirely in hole 3 (Figure 3.12g). Thus, annealing $2H-TaS_2$ samples in contact with a lithographically defined Fe oxide film results in a gradient in Fe content over several microns in distance. Taken together, our findings reveal that the primary determinants for achieving the desired intercalation products are the annealing temperature, annealing time, positioning of the intercalant oxide film, and the dimensions of $2H-TaS_2$ flakes.

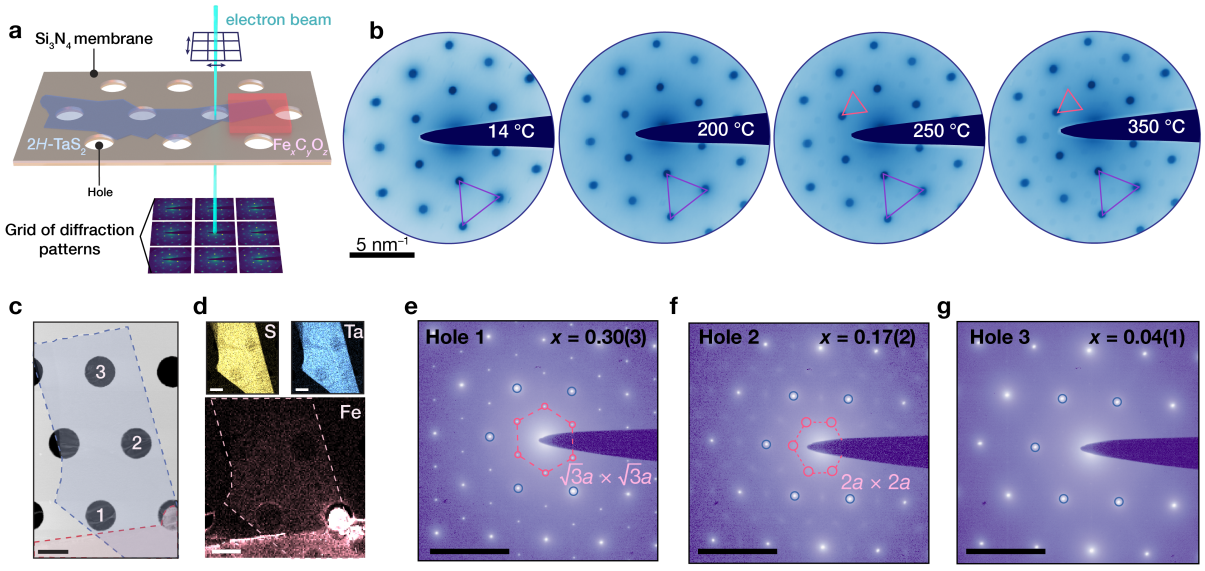


Figure 3.12: Probing uptake and diffusion of Fe in $2H-TaS_2$. **(a)** Schematic illustrating four-dimensional scanning transmission electron microscopy (4D-STEM) of a $2H-TaS_2$ flake with a patterned $Fe_xC_yO_z$ precursor. **(b)** Mean diffraction patterns, displayed on a logarithmic scale, of 4D-STEM datasets obtained during in-situ heating of a $2H-TaS_2$ flake with a patterned $Fe_xC_yO_z$ precursor. Diffraction reflections of the $2H-TaS_2$ lattice and the Fe superlattice are indicated in violet and red, respectively. The precursor was made by drop-casting a solution of $Fe(CO)_5$/isopropanol. Data was collected along the c-axis of the flake after a 30-minute temperature equilibration period. **(c)** Plan-view STEM micrograph ($\|$ c-axis) of a $2H-TaS_2$ crystal with a patterned $Fe_xC_yO_z$ precursor after ex-situ vacuum annealing for 1 hour at 350 °C. The $Fe_xC_yO_z$ precursor was made by drop-casting a solution of $Fe(CO)_5$/isopropanol. The $2H-TaS_2$ crystal and the $Fe_xC_yO_z$ patterned precursor are false-colored in blue and red, respectively. Number labels for the TEM grid holes are marked in white. Scale bar: 2 μm **(d)** STEM-EDS maps of sample (c). In the Fe EDS map, $2H-TaS_2$ is outlined in a dashed line. Scale bars: 2 μm. **(e–g)** Selected area electron diffraction (SAED) patterns of (c) obtained for grid hole 1 **(e)**, hole 2 **(f)**, hole 3 **(g)**. The Fe/Ta ratio (x) is marked on the SAED patterns. First-order diffraction peaks from the $2H-TaS_2$ lattice and the Fe superlattice are highlighted in blue and red, respectively. Scale bars (e–g): 5 nm^{-1}.

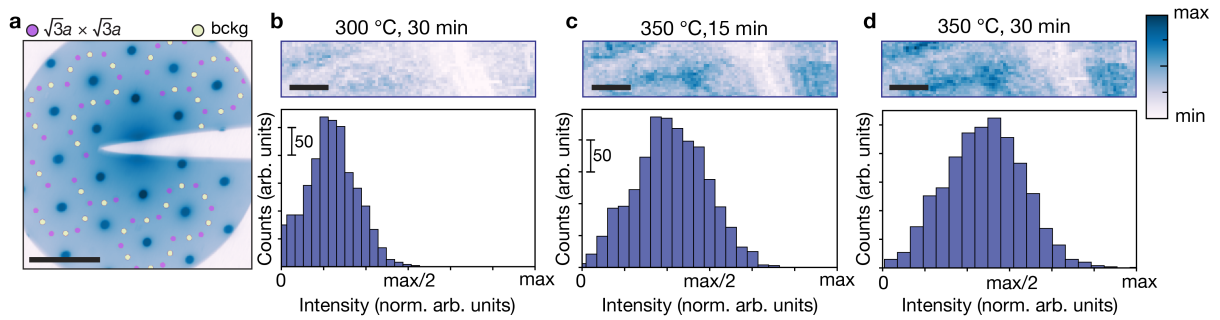


Figure 3.13: Analysis of temperature-dependent four-dimensional scanning transmission electron microscopy (4D-STEM) data. **(a)** Mean diffraction pattern, displayed on a logarithmic scale, overlaid with virtual detectors (masks) for: $\sqrt{3} \times \sqrt{3}$ (purple) and background (yellow). Diffraction peaks for the 2×2 superlattice were not detected, informing placement of the background detector. Scale bar: 5 nm^{-1}. **(b–d)** Virtual dark-field images and their histograms obtained after in-situ annealing at 300 °C for 30 minutes **(b)**, 350 °C for 15 minutes **(c)**, and 350 °C for 30 minutes **(d)**. Data in (b–d) were normalized to the maximal value across the three datasets, and increasing intensities of superlattice peaks are correlated with increasing concentrations of ordered Fe intercalants. Scale bars (b–d): 200 nm.

Evolution of electronic band structure of thin Fe_xTaS_2 with Fe content

The electronic ramifications of Fe^{2+} intercalation from these oxide films remain unanswered. If our proposed disproportionation chemistry (equation 1) is correct, we would expect electron transfer to the $2H-TaS_2$ host. We turn to angle-resolved photoemission spectroscopy (ARPES) measurements with submicron beam diameter to examine the effects of Fe intercalation from $Fe_xC_yO_z$ films on the electronic structure of low-dimensional $2H-TaS_2$. A $Fe_xC_yO_z$ film was patterned onto one end of an 11 nm $2H-TaS_2$ crystal, which was also partially encapsulated with a monolayer of hBN to prevent degradation of the measured region. This crystal was then annealed in high vacuum for 1 hour at 350 °C. As depicted in Figure 3.14a, photoemission spectra as a function of crystal momentum were acquired to measure the electronic band structure of the material over a range of distances away from the patterned $Fe_xC_yO_z$ film with spatial resolution on the order of 1 μm. We also acquired core-level spectra, confirming the presence of Fe in the measured area (Figure 3.15). Representative Fermi surface and energy versus momentum cuts along the Γ–K direction are presented in Figure 3.14b and Figure 3.14c, respectively. In measurements of bulk intercalated TMDs, cleaved surfaces can possess two terminations: intercalant termination or TMD termination [36, 168, 169]. The measured electronic features here are qualitatively consistent with a TMD-terminated surface, which provides evidence for minimal intercalation between the hBN and H-TaS_2 layers. Interestingly, we also observe that the Fermi surface cuts obtained at different points

away from the precursor exhibit distinct intensity distributions (Figure 3.16), indicating potential variations in electronic reconstruction across the crystal[168].

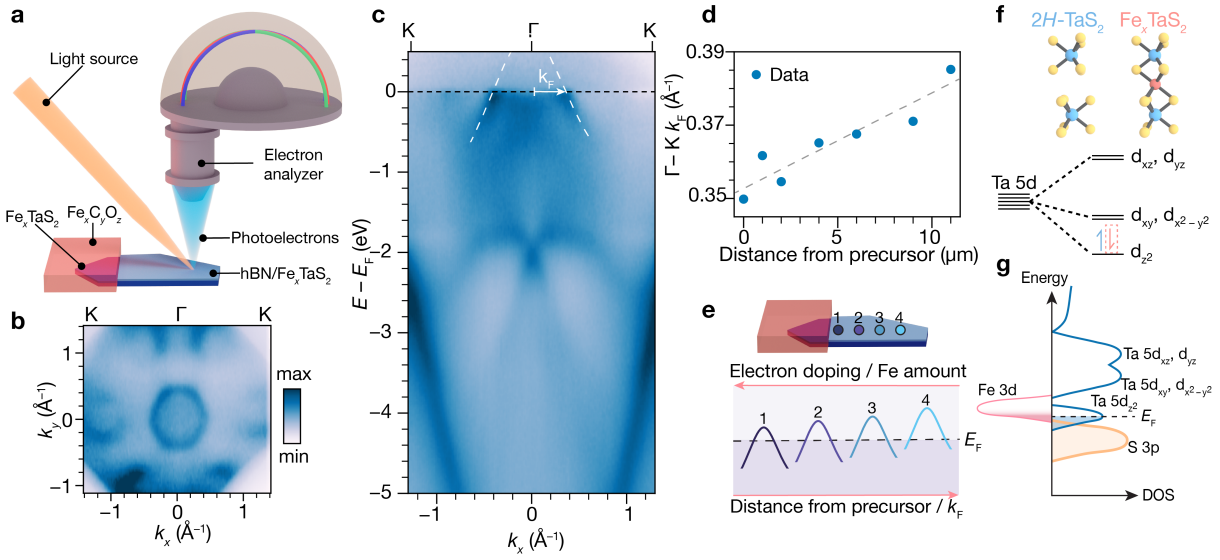


Figure 3.14: Spatially mapping the band structure of ultra-clean intercalated heterostructures with nanoARPES. **(a)** A schematic depicting the nanoARPES experiment conducted on a Fe_xTaS_2 encapsulated with monolayer hBN. The sample was prepared by selectively applying $Fe_xC_yO_z$ onto the area of $2H-TaS_2$ not covered by hBN, followed by vacuum annealing. **(b,c)** Normalized ARPES Fermi surface **(b)** and ARPES band dispersion along the Γ–K direction **(c)** of a hBN/Fe_xTaS_2 heterostructure at a 4 μm distance from the patterned $Fe_xC_yO_z$ precursor. In (c), the Fermi wavevector (k_F) is marked, denoting where the band forming the hole pocket around Γ intersects the Fermi level (E_F). This band is marked by a white dashed line. Data in (b-c) was obtained at 19 K with hν = 118 eV and linear horizontal (LH) polarization. **(d)** k_F along the Γ–K direction extracted from ARPES band-dispersions obtained at different distances from the $Fe_xC_yO_z$ precursor. The k_F values were obtained by fitting the momentum distribution curves (MDCs) at the Fermi level (E_F) to Lorentzians. The dashed gray line serves as a visual guide. **(e)** Schematic of the band forming the hole pocket at Γ as the distance from the precursor increases from spot 1 to 4. **(f)** Qualitative d-orbital splitting diagram for the trigonal prismatic Ta center in Fe_xTaS_2. A dashed electron in the d_{z^2} orbital denotes additional electron filling upon Fe intercalation, concomitant with charge transfer to $2H-TaS_2$. **(g)** Qualitative representation of the density of states of Fe-intercalated $2H-TaS_2$.

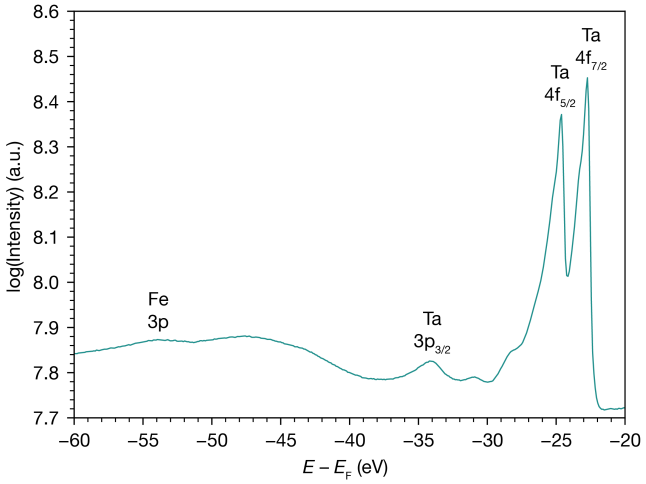


Figure 3.15: Core-level spectra of the Fe_xTaS_2/hBN heterostructure. A representative core-level spectrum of the Fe_xTaS_2/hBN heterostructure measured with nano angle-resolved photoemission spectroscopy (nanoARPES). Data was obtained with $h\nu = 160$ eV at a 4 μm distance from the patterned $Fe_xC_yO_z$ precursor. Core level energies are referenced to the Fermi edge.

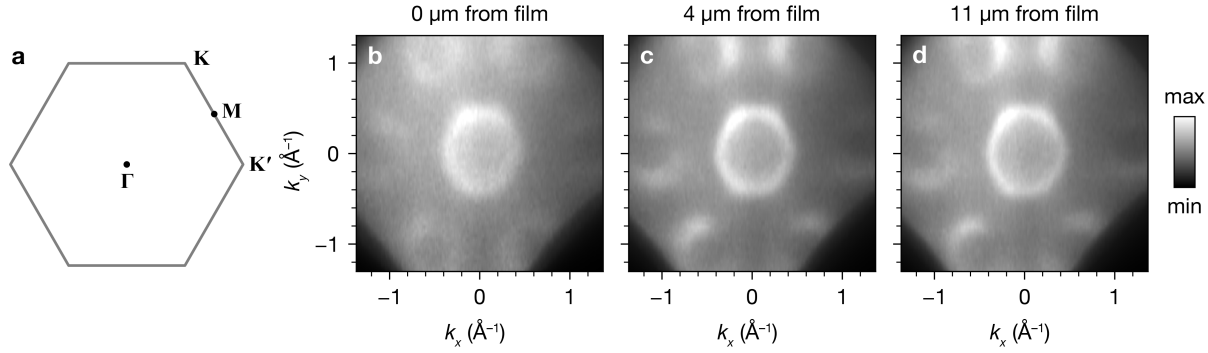


Figure 3.16: Intensity distribution of Fermi surface cuts. **(a)** Schematic of the Brillouin zone for the primitive TaS_2 lattice. High-symmetry points are labeled. **(b–d)** Isoenergy cuts at $E = E_F$ measured for the Fe_xTaS_2/hBN heterostructure at 0 μm **(b)**, 4 μm **(c)** and 11 μm **(d)** away from the $Fe_xC_yO_z$ film. The intensity distribution changes from 6-fold symmetric in (b) to 3-fold symmetric in (c,d). Data is not normalized.

A quantitative analysis of the nanoARPES datasets collected at various spots across the sample shows the evolution of the band structure with distance from the oxide film. By fitting the momentum distribution curves (MDCs) at the Fermi level (E_F) along Γ–K to Lorentzians (Figure 3.17), we extracted the Fermi wavevector (k_F) to quantify the size of the hole pocket

around Γ. This analysis reveals that the diameter of the central hole pocket increases as a function of distance away from the oxide film, with k_F increasing from 0.35 Å^{-1} to 0.39 Å^{-1} (Figure 3.14d). This increase in k_F, which is inversely proportional to electron filling, reveals a decrease in electron doping of the TaS_2 with distance away from the oxide film (Figure 3.14e). This doping trend mirrors the Fe concentration gradient uncovered by Raman mapping of this sample (Figure 3.18), as well as the STEM EDS and electron diffraction measurements of the sample presented in Figure 3.12c–g. As distance from oxide film correlates with the amount of intercalated Fe, these data provide a highly informative picture of the progress of the intercalation reaction itself. As Fe^{2+} is intercalated, the $2H-TaS_2$ host lattice is progressively electron-doped. In a simplified picture, this electron transfer to $2H-TaS_2$ results in an increased population of the band consisting largely of Ta d_{z^2} orbital character, which is at the Fermi level (Figure 3.14f,g)[30]. Although the experimental band structures of TMDs involve more complexity than this basic explanation[168, 170], increasing Fe^{2+} content leads to increased electron doping that in turn reduces the size of the central hole pocket of this Ta d_{z^2} band (Figure 3.14e). Therefore, the data of Figures 3.12 and 3.14 show how the Fe^{2+} content has structural and electronic implications, and the interplay between these factors is crucial for explaining the emergent magnetism in these materials[30].

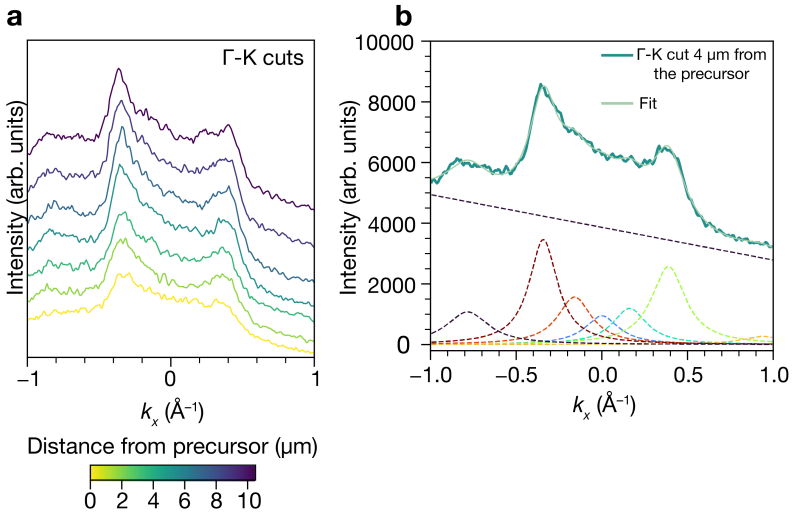


Figure 3.17: Quantitative analysis of nano angle-resolved photoemission spectroscopic (nanoARPES) data. **(a)** Momentum distribution curves (MDCs) at the Fermi level (E_F) along Γ–K extracted for datasets obtained at different distances from the $Fe_xC_yO_z$ precursor. **(b)** Fitting a representative MCD curve to Lorentzians.

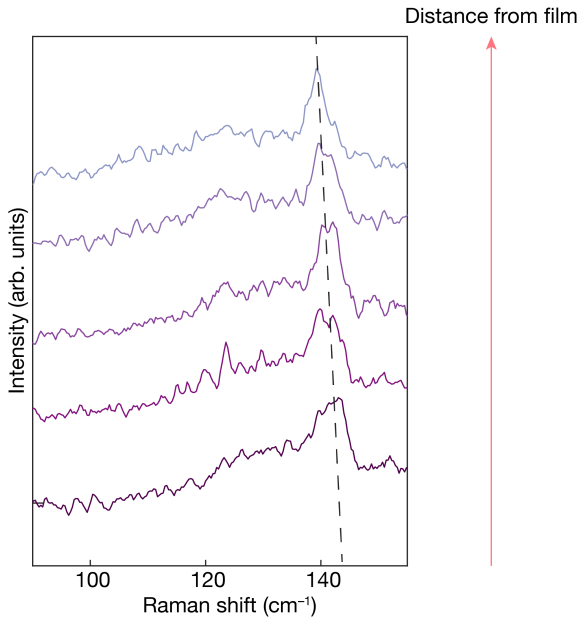


Figure 3.18: Raman spectra of the sample measured with nanoARPES. Raman spectra of the nanoARPES sample measured at different distances from the $Fe_xC_yO_z$ precursor. Fe-related Raman modes of the nanoAREPS sample display red-shifting with increasing distance from the $Fe_xC_yO_z$ precursor, indicating a corresponding decrease in the Fe concentration.

Intercalation compound heterostructures

Having unveiled this topotactic chemistry for intercalating TMDs with open-shell metal ions, we exploit this method to craft heterostructures of magnetic intercalation compounds. We demonstrate two paradigms for this combination of topotactic chemistry and vdW heterostructure assembly. In the first case, we intercalate a TMD heterostructure ($2H-TaS_2/2H$–NbS_2) with a single intercalant element (Fe), and in the second case, we create heterostructures using two different intercalants (Fe and Co) in a stack of the same TMD, $2H-TaS_2$.

Fe_xTaS_2 is ferromagnetic (FM) in the bulk[37–39] as well as in the few-layer limit[73]. In contrast, Fe_yNbS_2 is known to be antiferromagnetic (AFM) in the bulk[120, 156]. Consequently, the synthesis of Fe_xTaS_2/Fe_yNbS_2 heterostructures with clean interfaces would enable the construction of FM/AFM bilayers that may display technologically relevant magneto-electronic properties as a result of interfacial coupling between the dissimilar magnetic states[171–173]. To synthesize clean Fe_xTaS_2/Fe_yNbS_2, interfaces, we prepare $2H-TaS_2/2H$–NbS_2 heterostructures using vdW assembly, deposit a $Fe_xC_yO_z$ film from $Fe(CO)_5$/toluene solution, and anneal the heterostructure at 350 °C for 1.5 hours (Figure 3.19a). STEM-EDS mapping confirms the presence of Fe across the resulting heterostructure (Figure 3.19b) and estimates the Fe content to be 0.42 and 0.32 per $2H$–NbS_2 and $2H-TaS_2$, respectively. The presence of low frequency

Raman modes at 139 cm^{-1} and 181 cm^{-1} (Figure (Figure 3.19c) are consistent with $\sqrt{3} \times \sqrt{3}$ Fe superlattices in Fe_xTaS_2 and Fe_yNbS_2, respectively [73, 96, 174]. HRSTEM imaging of this $Fe_{0.32}NbS_2/Fe_{0.30}TaS_2$ assembly reveals an atomically flat and sharp heterointerface between the dissimilar 2D crystals (Figure (Figure 3.19d,e) with no amorphous oxide tunneling barrier (typically observed in heterostructures made from cleaved bulk crystals)[160, 161]. Moreover, atomic-resolution HRSTEM confirms that Fe ions decorate the interstitial between all vdW layers, including the 3.5-degree twisted heterointerface of Fe-intercalated $2H-TaS_2$ and $2H$–NbS_2 crystals (Figure 3.19e).

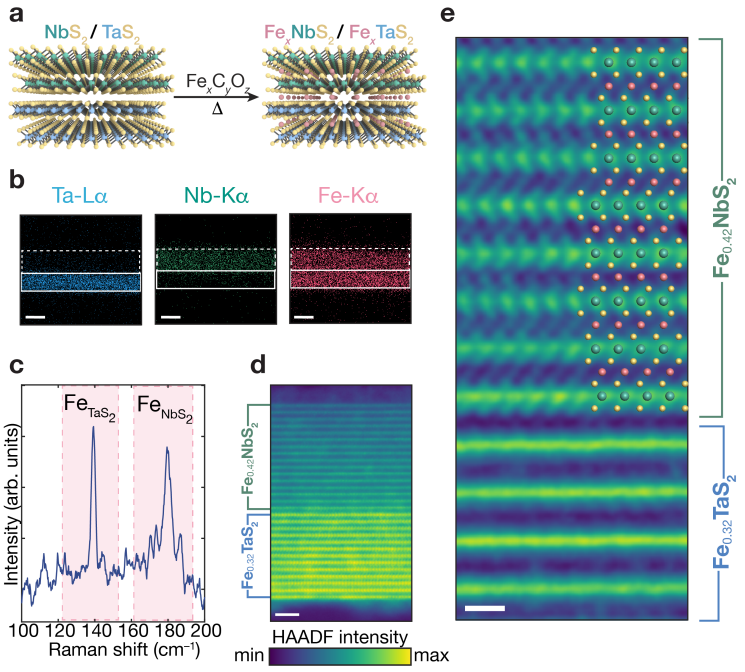


Figure 3.19: Synthesis and characterization of Fe-intercalated $2H$–$NbS_2/2H-TaS_2$ heterostructures. **(a)** Schematic illustrating the synthesis of Fe-intercalated heterostructure of $2H$–$NbS_2/2H-TaS_2$. **(b)** STEM energy-dispersive X-ray spectroscopy (EDS) maps perpendicular to the c-axis of the heterostructure synthesized as depicted in (a). The dashed and solid white lines mark the edges of $2H$–NbS_2 and $2H-TaS_2$, respectively. Scale bars: 10 nm. **(c)** Ultra-low frequency (ULF) Raman spectra of the heterostructure from (b). **(d)** High-resolution STEM image of the $Fe_{0.42}NbS_2/Fe_{0.32}TaS_2$ heterostructure from (b) along the $[10\bar{1}0]$ zone axis of the TaS_2 flake. The azimuthal misalignment (twist) angle is 3.5 determined using Kikuchi bands. Scale bar: 2 nm. **(e)** Atomic-resolution HAADF-STEM image of the heterostructure from (b) obtained along the $[10\bar{1}0]$ zone axis of the NbS_2 flake. Scale bar: 5 Å. Crystal structure of $Fe_{1/3}NbS_2$ from ref [175] is overlaid with the $2H$–NbS_2 flake.

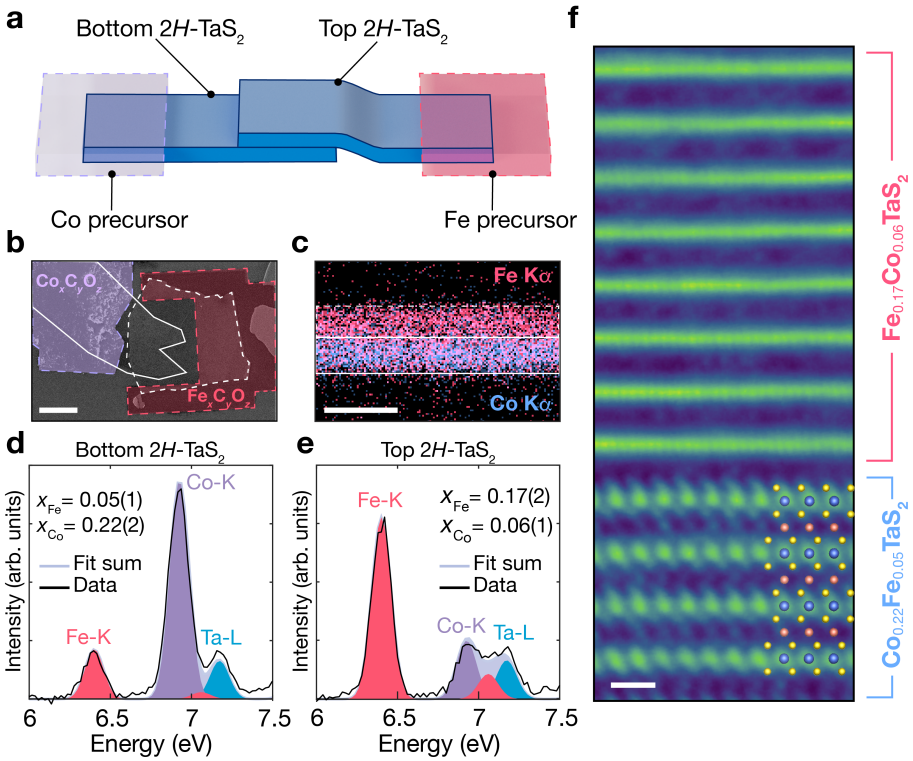


Figure 3.20: Synthesis and characterization of co-intercalated heterostructures. **(a)** Illustration of a heterostructure comprising two $2H-TaS_2$ flakes with the top and bottom one partially covered with the $Fe_xC_yO_z$ and $Co_xC_yO_z$ precursors, respectively. **(b)** Plan-view ($\|$ c-axis) scanning electron microscope (SEM) image of a heterostructure made according to the synthetic design in (a). The heterostructure with the patterned precursors was annealed for 1 hour at 350 °C. In the SEM image, $2H-TaS_2$ flakes are outlined in white, while the Co and Fe precursors are false-colored in violet and red, respectively. Scale bar: 5 μm. **(c)** STEM-EDS map of a cross-sectional TEM sample made from heterostructure (b). Scale bar: 20 nm. **(d,e)** Cumulative STEM-EDS spectra of the bottom **(d)** and top **(e)** $2H-TaS_2$ flakes from (b). In (d,e), marked x_M, where M = (Fe, Co), denotes the stoichiometric ratio between M and Ta. **(f)** Atomic-resolution HAADF-STEM image of the heterostructure from (b) obtained along the $[10\bar{1}0]$ zone axis of the bottom $2H-TaS_2$ flake. The azimuthal angle (twist) between the $2H-TaS_2$ flakes is 20 Crystal structure of $Fe_{1/3}TaS_2$ from ref [95] is overlaid with the bottom TaS_2 flake. Scale bar: 5 Å.

To create co-intercalated heterostructures, we pattern carbonyl-derived oxide films onto TMD stacks. This multi-precursor technique was applied to two stacked $2H-TaS_2$ flakes, with oxide precursors $Fe_xC_yO_z$ and $Co_xC_yO_z$ films patterned on the top and bottom $2H-TaS_2$ crystals, respectively (Figure 3.20a,b). After thermal annealing at 350 °C, we examine the overlapping region of the $2H-TaS_2$ flakes using STEM-EDS (Figure 3.20c–e). These measurements show that the top flake is principally Fe-rich and the bottom flake is Co-rich. Notably, although Fe and Co are present in both flakes, each flake contained a substantially higher concentration of the metal patterned directly onto it, implying that the lateral diffusion is considerably more facile than the vertical diffusion. This observed intercalant segregation distinguishes these heterostructures from bulk crystals grown with solid-state methods, where multiple metal intercalants disperse uniformly throughout the host lattice[176]. Atomic-resolution HAADF-STEM imaging of our heterostructures (Figure 3.20f) provides an explanation for this segregation, showing that the interface between the $2H-TaS_2$ crystals is atomically sharp and, importantly, azimuthally misaligned (twisted). Twisting creates an in-plane moiré superlattice[177, 178] and necessarily reduces the availability of optimal pseudo-octahedral intercalant sites. These results raise the possibility that controlling these azimuthal angles may be used to shape the gradient of co-intercalants and the resulting magnetism in tailored mixed heterostructures.

To demonstrate the magneto-electronic functionality facilitated by this approach, we conducted electronic transport assessments of the $Fe_{0.42}NbS_2/Fe_{0.32}TaS_2$ heterostructure that was presented in Figure 3.19b–e. 3.21a shows the fabricated mesoscopic device (labeled D1), comprising three distinct measurement regions, including Fe-intercalated $2H-TaS_2$ (region R1), Fe-intercalated $2H$–NbS_2 (region R3), and their composite heterostructure (region R2) (3.21a). In regions R1–R3, the temperature-dependent longitudinal resistance reveals an inflection near 30 K (Figure 3.22), suggesting a phase transition upon cooling. Additionally, upon cooling in a 12 T magnetic field, these inflections broaden and shift to higher temperatures for R1–R2 and lower temperatures for R3 (Figure 3.22), implying the magnetic origin of the phase transition consistent with ferromagnetism[37] in R1-R2 and antiferromagnetism in R3[179]. Further understanding of the long-range magnetic ordering in R1–R3 was gained through measurements of the magnetoresistance (MR) and field-dependent anomalous Hall resistance (R_{AHE}) (Figure 3.21b–c, Figure 3.23a–c), which reflect the interactions between the itinerant hole carriers and the magnetic moments. It is noteworthy that all regions exhibit a strong response to an out-of-plane magnetic field ($H \parallel c$) while showing negligible response to an in-plane field ($H \parallel ab$) (Figure 3.24). This confirms their strong magnetocrystalline anisotropy, a characteristic imperative for stabilizing magnetism in the ultrathin limit.

First, we turn to the detailed analysis of the magnetotransport of R1 and R3, which consist of a singular host lattice. Region R1 ($Fe_{0.32(1)}TaS_2$) manifests a hysteretic negative magnetoresistance with a bow-tie-shaped profile, characteristic of ferromagnets[37, 73] (Figure 3.21b,c and Figure 3.23a). Moreover, the presence of hysteresis in its R_{AHE} signal, which is proportional to magnetization, further supports the ferromagnetic characteristics of R1[37, 73] (Figure 3.21b,c and Figure 3.23a). Conversely, the magnetoresistance (MR) behavior

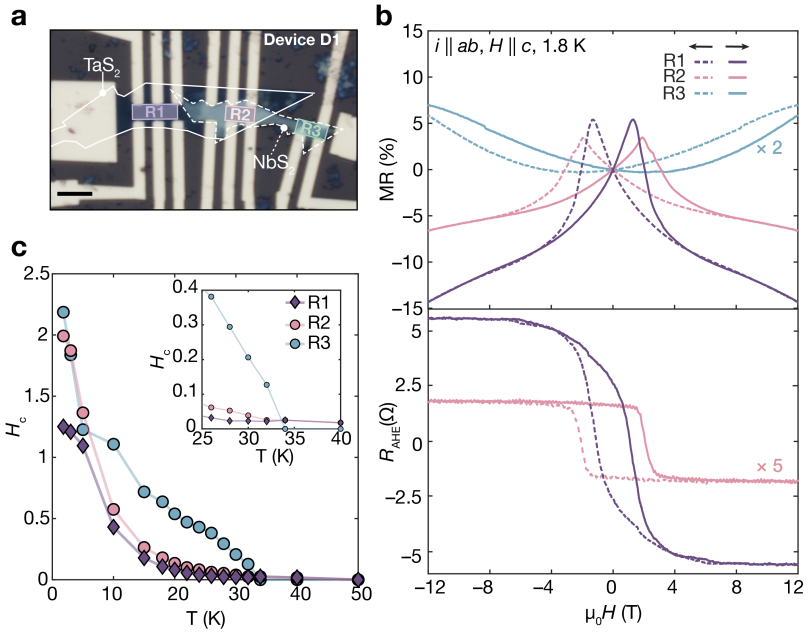


Figure 3.21: Magnetotransport of iron-intercalated $2H$–$NbS_2/2H-TaS_2$ heterostructures. **(a)** Optical micrograph of the measured mesoscopic device. Three distinct measured regions are false-colored and labeled: R1–$Fe_{0.32(1)}TaS_2$, R2–$Fe_{0.42(4)}NbS_2$ / $Fe_{0.31(2)}TaS_2$ and R3–$Fe_{0.32(3)}NbS_2$. **(b)** Field-dependent magnetoresistance (MR) and anomalous Hall resistance (R_{AHE}) recorded in regions R1–R3. **(c)** Temperature-dependent coercive field (H_c) for R1–R3. For R1–R2, the average of H_c is obtained from both MR and R_{AHE} measurements. Here, H_c refers to the field where MR reaches its maximum while R_{AHE} equals zero. Conversely, for R3, H_c is determined exclusively from MR data, defining it as the field where MR exhibits its minimum (upturn). The data presented in b,c was obtained after the initial thermal and field cycling of the device.

of R3 ($Fe_{0.32(3)}NbS_2$) mirrors that of metallic antiferromagnets, demonstrating positive MR below the Néel temperature and transitioning to negative MR above 40 K[179–181] (Figure 3.21b,c and Figure 3.23c). However, contrary to the expected behavior for antiferromagnets, R3 also exhibits hysteresis in its MR profile below the ordering temperature, suggesting the presence of uncompensated magnetic moments. Given that our samples deviate from stoichiometric $Fe_{0.33}NbS_2$, we propose that these uncompensated moments arise from intercalant disorder, which is known to introduce an uncompensated spin glass phase in bulk crystals of Fe_xNbS_2[121, 156]. The spin glass phase could become pinned by the surrounding antiferromagnetic moments, leading to the observed hysteretic behavior.

Having established R1 as ferromagnetic and R3 as antiferromagnetic with a minority uncompensated phase, the transport behavior of the heterostructure (R2) was examined (Figure 3.21b,c and Figure 3.23b). The magnetotransport characteristics of R2 are dominated

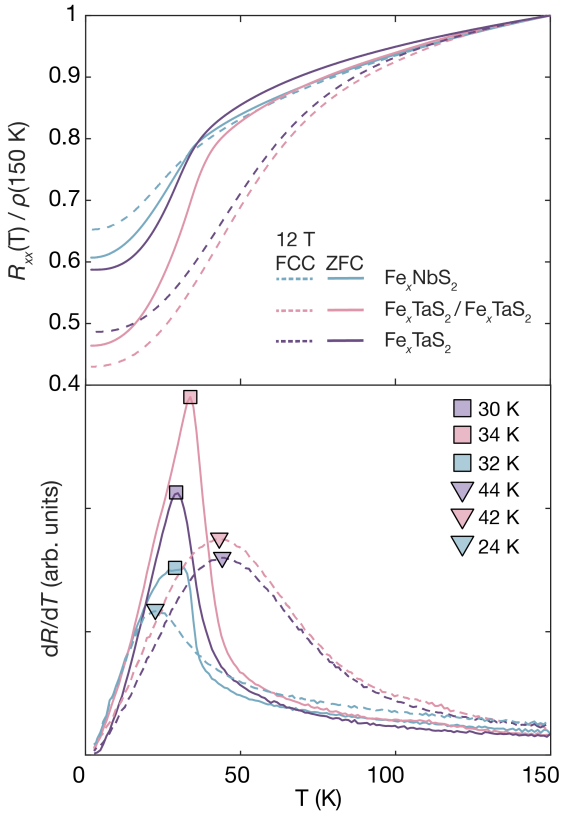


Figure 3.22: Temperature-dependent resistance of device D1. Temperature-dependent resistance and its first derivative (dR/dT) for R1–R3 upon zero-field cooling (ZFC) and cooling in a 12 T magnetic field ($H \parallel c$). Maxima of dR/dT curves are labeled.

by the $Fe_{0.31(2)}TaS_2$ segment of the heterostructure, aligning with the ferromagnetic behavior observed in R1 (Figure 3.21b,c and Figure 3.23a,b). However, following the initial thermal and field cycling, the coercive fields (H_c) of R2 consistently surpass those of R1 below the Néel transition of R3 (Figure 3.21c). This suggests that out-of-plane interactions across the ferromagnetic-antiferromagnetic heterostructure may be responsible for the high coercivity of R2. Consequently, the heterostructure behaves akin to an exchange spring magnet, a composite of dissimilar magnets whose interfacial interactions increase the coercivity[182]. These results underscore the potential of intercalated heterostructures, which are enabled by combining nanoscale topochemical reactions and vdW heterostructure assembly, as a versatile platform for designing and interrogating low-dimensional magnetic phenomena.

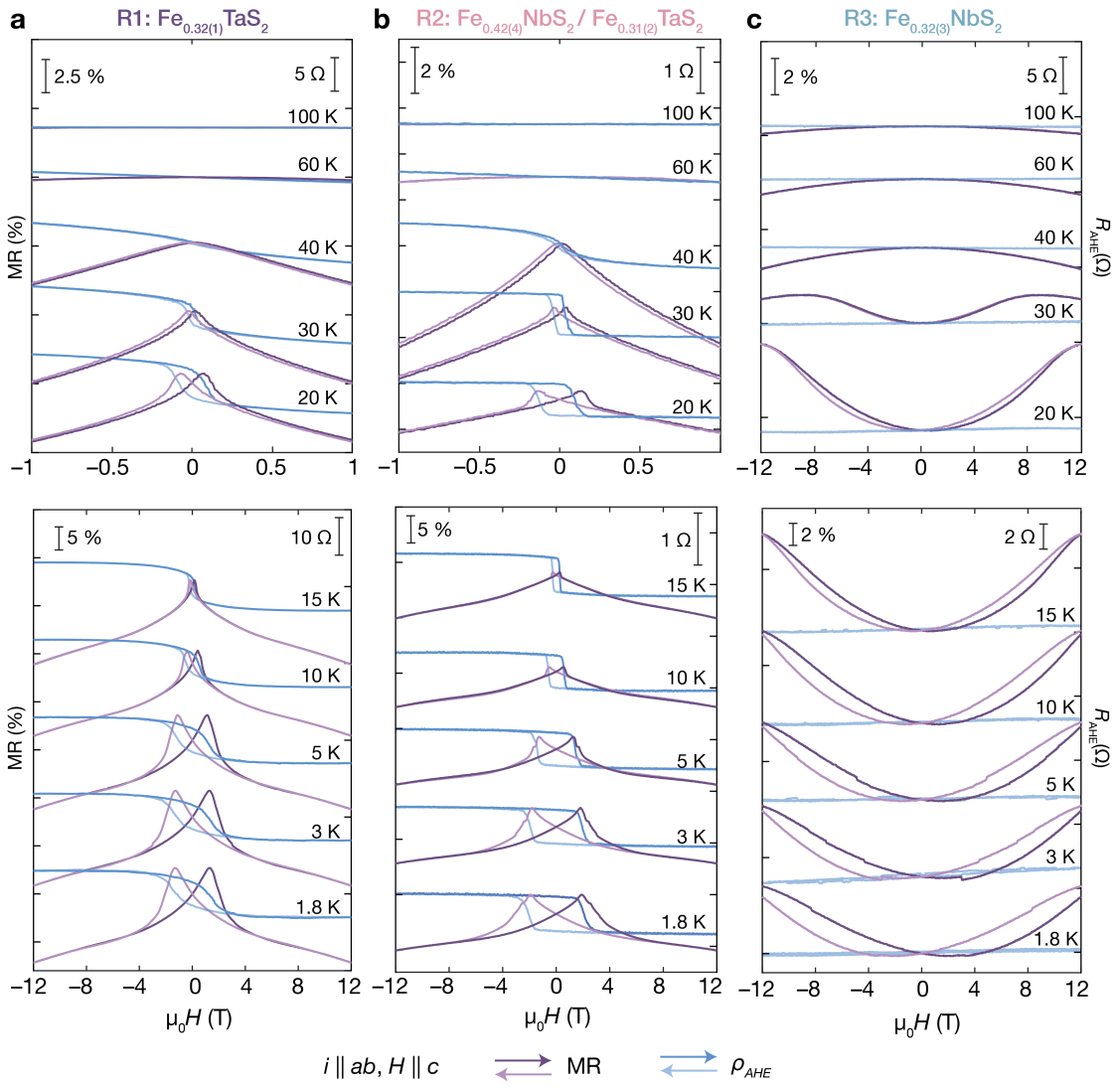


Figure 3.23: Temperature-dependent magnetotransport of device D1. **(a–c)** Temperature-dependent magnetoresistance (purple) and anomalous Hall resistance (blue) for R1 **(a)**, R2 **(b)** and R3 **(c)**. The stoichiometries of iron relative to the Ta/Nb stoichiometry were determined through STEM-EDS analysis of cross-sections prepared subsequent to magnetotransport experiments. Data was obtained after the initial thermal and field cycling of the device.

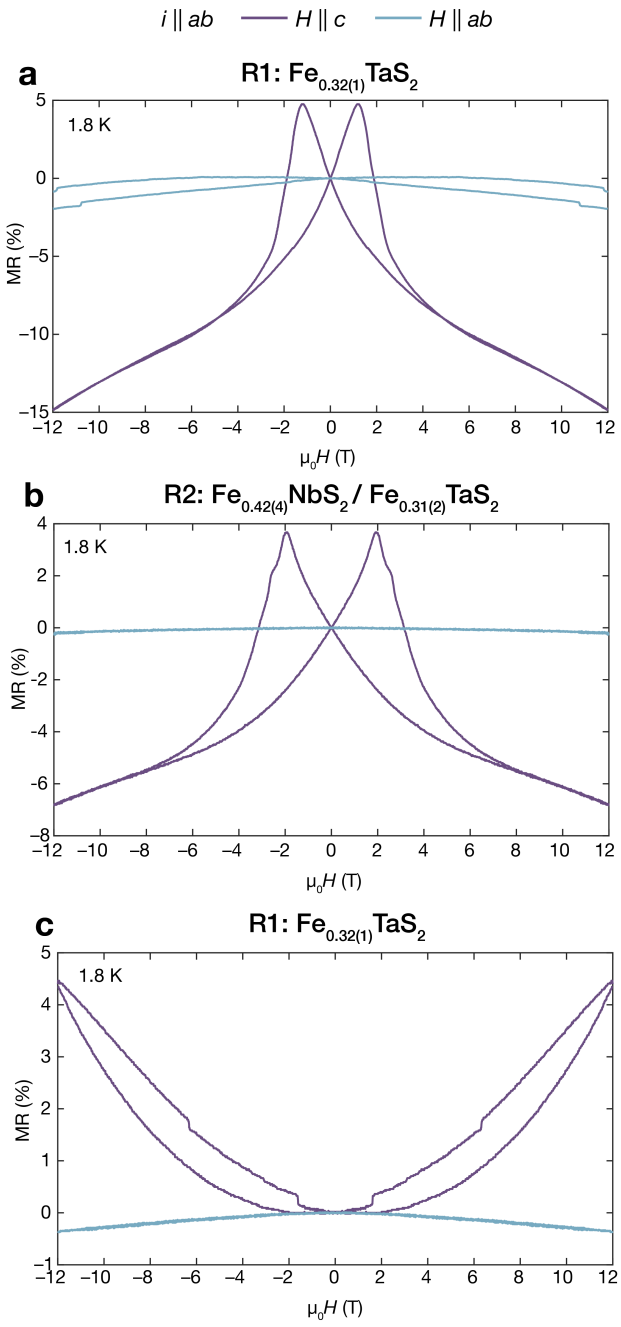


Figure 3.24: Angle-dependent MR of device D1. **(a–c)** MR of device D1 with the external magnetic field aligned parallel and perpendicular to the *c*-axis for regions R1 **(a)**, R2 **(b)**, and R3 **(c)**. During the measurements with $H \parallel ab$, the sample was rotated by approximately 4 degrees from the *ab*-axis, resulting in a non-zero field contribution in the $H \parallel c$ direction. The observed hysteresis in (a) with $H \parallel ab$ can be attributed to this misalignment.

3.4 Conclusion

This study demonstrates the successful synthesis of TMD heterostructures intercalated with open-shell transition metal ions by implementing vdW assembly and nanoscale solid-state topochemistry of the TMD with a transition metal oxide film. The intercalation process is comprehensively investigated for Fe_xTaS_2, using both bulk and atomic-scale structural and spectroscopic probes. We uncover that intercalation is thermally activated and accompanied by the disproportionation of oxide-exposed $2H-TaS_2$ layers. We observe that the intercalants diffuse from the region in contact with the oxide film, allowing for the fabrication of pristine few-layer magnetic intercalation compounds under hBN-encapsulated flakes. Leveraging these insights, we use patterning of metal carbonyl-derived oxide films to direct metal ions into well-defined vdW heterostructures, expanding the range of accessible low-dimensional magnetic intercalation compounds as well as producing magnetic multilayer systems with exceptionally clean surfaces and interfaces. Representative measurements of such heterostructures show transport behaviors signifying strong interfacial magnetic exchange effects that are only possible with atomically clean interfaces.

We envision the emergent physics of these heterostructures may be controlled by altering the thickness of constituent flakes and the intercalants' identity, stoichiometry, and homogeneity. Additionally, we expect that the synthesis of heterostructures with atomically sharp moiré heterointerfaces will offer exciting opportunities to both control the intercalation chemistry and also to fundamentally engineer complex magnetic behaviors. This customizability of vdW heteroepitaxy combined with nanoscale intercalation chemistry unlocks versatile opportunities to fine-tune the spin degree of freedom in materials, positioning intercalated heterostructures as compelling platforms for multi-component spintronic device architectures.

3.5 Methods Chapter 3

Synthesis of $2H-TaS_2$ bulk crystals. Single crystals of $2H-TaS_2$ were grown with chemical vapor transport (CVT) using powders of elemental Ta (-100 mesh, 99.98%, Nb 50 ppm, Alfa Aesar), S (99.999%, Acros Organics), and I_2 (99.999%, Spectrum Chemicals), which were used as received. Elemental Ta (176.3 mg, 1.00 equiv.) and S (62.7 mg, 2.00 equiv.) were sealed in a fused quartz ampule (14 mm inner diameter, 1 mm wall thickness, 15 cm long) under vacuum ($\sim 1 \times 10^{-5}$ Torr), along with 152.1 mg I_2 (5 mg/cm^3). The ampule was placed in an MTI OTF-1200X-II two-zone tube furnace with the hot zone maintained at 1000 °C and the cold (growth) zone maintained at 850 °C for 6 days, before cooling to room temperature at approximately 60 °C/hour.

Mechanical exfoliation of $2H-TaS_2$ and $2H$–NbS_2. Exfoliation of $2H-TaS_2$ (synthesized in this study or obtained from HQ Graphene) and $2H$–NbS_2 (HQ graphene) was performed in an Ar-filled glove box with Magic Scotch adhesive tape. Crystals were exfoliated onto 90 nm SiO_2/Si wafers (Nova Electronic Materials), which had been cleaned in an oxygen plasma cleaner for 2 minutes and then heated to 200 °C on the glove box hotplate.

Mechanical exfoliation of hexagonal boron nitride (hBN). Exfoliation of hBN (used as received from T. Taniguchi and K. Watanabe) was conducted using Magic Scotch tape in ambient conditions onto a 90 nm SiO_2/Si wafer (Nova Electronic Materials), which had been subjected to a 90-minute ozone cleaner treatment at 150 °C.

Determining thickness of flakes. The thickness of flakes used for cross-sectional imaging was obtained using HRSTEM after cross-sectioning. For other flakes, atomic force microscopy (Park Systems NX10) was used to determine the sample thickness.

Preparation of $M_xC_yO_z$ (M = Fe, Co) films. To prepare $M_xC_yO_z$ (M = Fe, Co), the following chemicals were used as received: iron(0) pentacarbonyl (>99.99 %, Sigma-Aldrich), dicobalt octacarbonyl (moistened with hexane (1-10%), ≥90 % (Co)) acetone (≥99.5 %, Fisher Scientific), and isopropanol (IPA) (≥99.5 %, Sigma-Aldrich). Acetonitrile (≥99.5 %, Fisher Scientific) and toluene (≥99.5 %, Fisher Scientific) were obtained from a Pure Process Technology solvent purification system, and acetone (Sigma-Aldrich) was degassed by the freeze-pump-thaw technique and then dried over $CaCl_2$ (Acros Organics). All glassware was oven-dried at 150 °C for a minimum of 2 hours before use. Two methodologies were used for preparing $M_xC_yO_z$ (M = Fe, Co): (1) prolonged soaking in a metal carbonyl solution and (2) drop-casting a metal carbonyl solution.

In the soaking method, a 10 mM solution of $Fe(CO)_5$ or $Co_2(CO)_8$ was prepared in toluene, acetonitrile, or acetone. Experiments in toluene were performed in an Ar-filled glove box, while experiments in acetonitrile and acetone were conducted on a Schenk line. Mechanically exfoliated $2H-TaS_2$ on a supporting substrate was immersed in the metal carbonyl solution for 14–48 hours, followed by three rinses with fresh solvent and then drying using an inert gas.

For the drop-casting approach, a solution of $Fe(CO)_5$ (380 mM) or $Co_2(CO)_8$ (2.5 mM) in IPA was prepared on a Schlenk line. To dissolve $Co_2(CO)_8$, the solution was stirred at 70 °C under N_2 for approximately 14 hours. Subsequently, the metal carbonyl solution was drop-cast onto mechanically exfoliated $2H-TaS_2$ while heating the sample to 80 °C in air.

Treatment of $2H-TaS_2$ with evaporated Fe. In a typical procedure, 10 nm of Fe was evaporated at 2 Å/second onto mechanically exfoliated $2H-TaS_2$ flakes in an e-beam evaporator under high-vacuum conditions ($\sim 10^{-6}$ Torr). Following the evaporation, the chips were moved in air to our home laboratory and stored in an Ar-filled glove box.

Treatment of $2H-TaS_2$ with Fe_2O_3 nanoparticles/nanopowder. A dispersion of Fe_2O_3 nanopowder (Sigma Aldrich, <50 nm particle size (BET)) in IPA or a dispersion of Fe_2O_3 nanoparticles in ethanol (Sigma Aldrich, ≤ 110 nm particle size, 15 wt. % in ethanol, ligands: [2-(2-Methoxyethoxy)ethoxy]acetic acid) was drop cast onto mechanically exfoliated $2H-TaS_2$ flakes.

Annealing samples after precursor treatment. Samples in contact with solid precursors were annealed in high-vacuum ($\sim 10^{-7}$ Torr) by rapidly warming to 120 °C at 60 °C/min with a 5-minute hold, followed by heating at 11.5 °C/min to 350 °C, and hold for 30 minutes to 1.5 hours at 350 °C, before cooling to room temperature at 13.5 °C/min.

Patterning of $M_xC_yO_z$ precursors. E-beam lithography (PMMA 950 A6 resist) was used to pattern $M_xC_yO_z$ films onto TMD heterostructures. Subsequently, a solution of

$Fe(CO)_5$ (380 mM) or $Co_2(CO)_8$ (2.5 mM) in IPA was drop-cast onto the lithographically-patterned chip. The PMMA was then lifted off by soaking the sample in acetone, followed by cleaning the sample in IPA and drying it with an N_2 jet. Samples patterned with both $Fe_xC_yO_z$ and $Co_xC_yO_z$ films were prepared by following this procedure twice to separately pattern the dissimilar metal oxide films.

Synthesis of $Fe_xC_yO_z$ bulk powders. Under an Ar atmosphere, iron(0) pentacarbonyl (5 mL, 38 mmol) was added to a glass vial, and mixed with 15 mL of toluene or 2-propanol on a Schlenk line. Under an N_2 atmosphere, the solution was allowed to dry at room temperature for approximately 2-3 days.

Solid-state reactions of polycrystalline $2H-TaS_2$ and Fe_2O_3. First, polycrystalline TaS_2 was prepared by grinding a stoichiometric mixture of Ta (-100 mesh, 99.98%, Nb 50 ppm, Alfa Aesar) and S (99.999%, Acros Organics) powders in a mortar and pestle for 10 minutes. This mixture was subsequently pressed into a pellet and sealed in a glass ampoule (14 mm inner diameter, 1 mm wall thickness, 10 cm long) under vacuum ($\sim 1 \times 10^{-5}$ Torr). The sealed ampoule was heated in a muffle furnace at 900 °C for 7 days with 1 °C/minute cooling and warming rates. The resulting polycrystalline powder was analyzed with powder x-ray diffraction, PXRD, and then mixed with Fe_2O_3 nanopowder (Sigma Aldrich, <50 nm particle size (BET)) in 4:1 and 7:1 molar ratios. These powder mixtures were then sealed in quartz ampoules and heated as described above for polycrystalline TaS_2. The products were analyzed using Raman spectroscopy and PXRD.

Sample preparation for transmission electron microscopy (TEM). Samples for imaging along the *c*-axis were prepared in an Ar-filled glovebox using the dry transfer method[73, 183]. Flakes were transferred onto a 200 nm silicon nitride holey TEM grid (Norcada), treated with an O_2 plasma for 5 minutes immediately before stacking.

Cross-sections of each flake for imaging along the crystallographic *ab*-plane were prepared by standard focused ion beam (FIB) lift-out procedure using Thermo Fisher Scientific Helios G4 and Scios 2 FIB-SEM systems[73, 183]. Prior to imaging at the National Center for Electron Microscopy (NCEM), samples underwent additional cleaning using the Fischiotone Ar nanomill set at milling angles of +15 deg and –10 degrees. Plasma cleaning of the milling holder was carried out beforehand to mitigate potential carbon contamination. Before atomic-resolution STEM imaging, TEM lamellae were annealed in high-vacuum (10^{-7} Torr) at 100–120 °C for 12 hours to decrease carbon contamination.

Transmission electron microscopy (TEM). Atomic-resolution high-angle annular dark-field STEM imaging of cross-sections presented in Figure 3.1b,c and Figure 3.2 was performed on a Thermo Fisher Spectra 300 X-CFEG operating at 120 kV with 24 mrad probe-forming convergence angle, using inner and outer collection angles of 68 and 200 mrad, respectively. The remaining HAADF-STEM imaging was conducted on TEAM I, a modified FEI Titan 80-300 microscope, operating at 80 kV with a beam current of 70 pA. The convergence angle was set to 30 mrad for data shown in Figure 3.1f, Figure 3.20f. A convergence angle of 17 mrad was used to collect data in Figure 3.20d,e. For atomic resolution imaging, stacks of images with a high frame rate (> 1 fps) were rigidly registered and summed[184] to increase the signal-to-noise ratio without introducing artifacts from

sample drift or scan noise.

Core-loss EELS measurements were performed on $2H-TaS_2$ flakes after treatment with $Fe(CO)_5$/acetone and subsequent annealing. Data were collected at cryogenic temperatures to reduce possible effects of radiation damage in the sample during long acquisitions using a Gatan 636 side-entry liquid nitrogen holder in an FEI Titan Themis CryoS/TEM operating at 120 kV equipped with a 965 GIF Quantum ER and a Gatan K2 Summit direct electron detector operating in electron counting mode. EEL spectrum images extending from the substrate into the protective surface layers and lateral distances spanning tens of nanometers were acquired throughout several regions of each sample. Spectra were summed over selected areas from each map to extract different regions for analysis—e.g., within the TMD flake or the precursor film—using Nion Swift image processing software[185]. These spectra were then combined across data sets from a given sample to produce high signal-to-noise ratio summed spectra. The energy alignment of EEL spectra was corrected using the well-defined Ca^{2+} edge as a reference. The Ca^{2+} signal was evident in the $Fe_xC_yO_z$ film because the acetone used was dried over $CaCl_2$.

Selected area electron diffraction (SAED) and STEM-EDS data were collected in FEI TitanX operating at 80 kV. SAED patterns were obtained with a 40 μm diameter aperture, which defined a selected diameter of ∼720 nm. STEM-EDS data was collected with a probe convergence angle of 10 mrad and a beam current of 150 pA–1 nA. The total acquisition time was 3–30 minutes, depending on the signal-to-noise ratio. Data was analyzed in the Bruker Esprit 1.9 software, and series fit deconvolution was implemented to resolve overlapping peaks. We note that the sulfur content of cross-sectional TMD samples varied significantly, ranging from 1 to 1.9 stoichiometric units, with thicker lamella regions having a higher sulfur content. In contrast, the sulfur content of plan-view samples is more consistent, ranging from 1.75 to 1.95 stoichiometric units. Thus, we hypothesize that the sulfur content may be significantly impacted by the FIB preparation process and/or the bakeout steps before the imaging.

Four-dimensional scanning transmission electron microscopy (4D-STEM) was performed in an FEI TitanX (80 keV, 0.55 mrad indicated convergence semi-angle) using a Gatan 652 Heating holder for in-situ heating experiments. The collected data was analyzed using the py4DSTEM Python package[186]. First, we used peak detection to locate the $2H-TaS_2$ Bragg peaks, used to subsequently construct the reciprocal vectors of the $2H-TaS_2$ host lattice. Next, $\sqrt{3}\times\sqrt{3}$ Fe superlattice reciprocal vectors were calculated from the symmetry relations to the $2H-TaS_2$ reciprocal vectors. Note, the $\sqrt{3}\times\sqrt{3}$ Fe superlattice was the only detectable Fe superlattice within our 4D-STEM datasets. Subsequently, we mathematically constructed virtual apertures that masked the entire diffraction space except for the Fe superlattice peak regions. The constructed virtual apertures were applied to the 4D-STEM diffraction data to integrate the Fe superlattice intensities at each probe position. A background (bg) virtual aperture was also defined to estimate the diffuse scattering background, subtracted from the integrated Fe superlattice intensities at each probe position.

X-ray photoelectron spectroscopy (XPS). All samples, transported in Ar-filled bags, were mounted onto stainless-steel stubs using double-sided tape under ambient conditions, which they were exposed to less than 5 minutes before loading into the XPS chamber.

Measurements were performed using a Thermo Scientific K-Alpha+ (Al Kα radiation, hν = 1486.6 eV) (Thermo Fisher Scientific Inc) equipped with an electron flood gun for charge neutralization. The AvantageTM package was used for data acquisition. Spectra were collected with a fixed-analyzer transmission mode with the X-ray beam size of 400 μm. Survey scans were collected with a pass energy of 200 eV, while high-resolution scans of individual elements were collected with a pass energy of 20–50 eV and a step size of 0.1 eV. Auto-Z (i.e., automated height adjustment to the highest intensity) was performed before each measurement to find the focal point of the analyzer. We collected 30 sweeps for measuring Fe and 40 sweeps for measuring Co to obtain the optimal signal-to-noise ratio. Data were analyzed using Thermo Scientific Avantage Data System software (version 5.9914), where a smart background was applied before peak deconvolution and integration. All spectra were charge corrected to the C 1s peak at 284.8 eV. The Fe 2p and Co 2p peak positions were assigned using established literature[187–195].

Powder X-ray diffraction (PXRD). PXRD data was collected in ambient conditions on a Bruker D8 Advance diffractometer using Cu Kα (λ = 1.5406 Å) radiation.

Fourier transform infrared spectroscopy (FTIR). Fourier transform infrared spectroscopy measurements were carried out on a Thermo Scientific Nicolet iS20 spectrometer utilizing KBr pellets. The preparation of samples for infrared spectroscopy was carried out in an Ar-filled glovebox.

Scanning electron microscopy (SEM) and energy dispersive X-ray spectroscopy (EDS). Compositional analysis of bulk crystals with SEM-EDS was performed using a Thermo Scientific Scios 2 FIB-SEM system with an accelerating voltage of 20–30 kV and an average beam current of 1.6 nA.

Confocal Raman spectroscopy. Ultra-low frequency (ULF) Raman spectroscopy (Horiba Multiline LabRam Evolution) was conducted using a 633 nm laser excitation at a power of 50–100 μW with 10–60 second acquisition times and 3–6 accumulations.

Nanofabrication of devices. To create electrical leads, samples were spin-coated with PMMA 950 A6 (Kayaku Advanced Materials) at 4000 rpm and cured on a hot plate in ambient conditions at 180 °C for 3 minutes. Next, electron beam lithography (Crestec CABL-UH Series Electron Beam Lithography System) was used to define the electrical contacts, which were treated with reactive ion etching (RIE) with a mixture of 70 sccm CHF_3 and 10 sccm O_2 (SEMI) for 1 minute to expose a fresh surface of the sample. Immediately after etching, Cr/Au (2 nm/100 nm) was thermally evaporated onto the sample and lifted off in acetone overnight.

Electron transport measurements. Four-probe transport measurements were conducted with conventional lock-in methods. In summary, a 5 μA alternating current (17.777 Hz) was introduced between the source and drain terminals while systematically varying the temperature using the PPMS DynaCool system. Simultaneously, the longitudinal (V_{xx}) and transverse voltage (V_{xy}) were recorded with the SR830 lock-in amplifier. Phase differences remained below 5, and resistances were computed following Ohm's law. Unless otherwise indicated, the field-dependent R_{xx} and R_{xy} data were symmetrized (anti-symmetrized) in accordance with established methods:[73, 134]

Preparation of samples for nanoARPES. A nanothick (∼10 nm) $2H-TaS_2$ flake was partially capped with monolayer hBN using the dry transfer method[73, 183]. Next, $Fe_xC_yO_z$ was patterned onto the uncapped portion of the heterostructure, followed by annealing to 350 °C. The sample was then electrically connected with metal leads using standard nanofabrication methods at the Marvell Nanofabrication Laboratory. The fabricated Cr/Au leads were electrically connected to the ARPES Cu puck using silver epoxy, which was cured at 120 °C for 15 minutes. Lastly, the sample was heated in the ARPES chamber at 100 °C overnight immediately before the ARPES experiments.

Nano angle-resolved photoemission spectroscopy (nanoARPES). nanoARPES data were collected at Beamline 7.0.2 of the Advanced Light Source (ALS) on the nanoARPES endstation using Scienta Omicron R4000 hemispherical electron analyzers. The beam diameter was approximately 1 μm. All measurements were conducted at the base temperature of 19 K with linear horizontal (LH) polarization at pressures lower than 5×10^{-11} Torr. Core-level measurements were conducted with a photon energy of 160 eV, while all other measurements were conducted with $h\nu = 118$ eV. Data analysis was conducted using the PyARPES software package[196]. High-symmetry cuts were normalized such that the integrated intensity for each momentum and energy distribution curve are equal in the plotted range. Fermi surface cuts in the main text were normalized to ensure that the integrated intensity of the k_x and k_y momentum distribution curves were equivalent.

Chapter 4

Encoding multistate charge order and chirality in endotaxial heterostructures

Parts of this section were adapted or reproduced from: Husremović, S.; Goodge, B. H.; Erodici, M. P.; Inzani, K.; Mier, A.; Ribet, S. M.; Bustillo, K. C.; Taniguchi, T.; Watanabe, K.; Ophus, C.; Griffin, S.; Bediako, D. K. *Nature Communications* **2023**, *14*, 6031.
[183]
Author contributions: S.H. and D.K.B. conceived the study. S.H. and A.M. fabricated the samples. S.H., B.H.G., M.E. and K.C.B. performed the experiments. K.I. and S.M.G. carried out the DFT computations. S.H., S.M.R., and C.O. developed the code for the virtual apertures. T.T. and K.W. provided the hBN crystals. S.H. and D.K.B. wrote the manuscript with input from all co-authors.

4.1 Abstract

High-density phase change memory (PCM) storage is proposed for materials with multiple intermediate resistance states, which have been observed in $1T-TaS_2$ due to charge density wave (CDW) phase transitions. However, the metastability responsible for this behavior makes the presence of multistate switching unpredictable in TaS_2 devices. Here, we demonstrate the fabrication of nanothick verti-lateral H–TaS_2/$1T$–TaS_2 heterostructures in which the number of endotaxial metallic H–TaS_2 monolayers dictates the number of resistance transitions in $1T-TaS_2$ lamellae near room temperature. Further, we also observe optically active heterochirality in the CDW superlattice structure, which is modulated in concert with the resistivity steps, and we show how strain engineering can be used to nucleate these polytype conversions. This work positions the principle of endotaxial heterostructures as a promising conceptual framework for reliable, non-volatile, and multi-level switching of structure, chirality,

and resistance.

4.2 Introduction

Charge density wave (CDW) materials host correlated electronic states typified by periodic lattice distortions and static modulations of conduction electrons[45]. Non-volatile memory and computing devices based on the principle of phase change memory (PCM)[197, 198] may leverage the intrinsic resistivity changes associated with CDW phase transitions[41, 199–203]. $1T-TaS_2$, a van der Waals (vdW) layered solid, is a prototypical CDW material in which the atomic lattice distorts in-plane to form 13-atom star-shaped clusters[71, 204]. The tiling of these clusters and the extent of commensuration with the underlying atomic lattice defines the CDW phases and the electronic properties of $1T-TaS_2$[71, 204–208]. Notwithstanding the in-plane nature of this CDW lattice distortion, interlayer coupling plays a key role in stabilizing intralayer charge order in $1T-TaS_2$. Accordingly, together with flake thickness[209–211] and doping levels[209, 212], vertical heterostructuring is a powerful route for engineering CDW transitions[62, 213–217]. For example, whereas in pristine, bulk $1T-TaS_2$ the commensurate (C) CDW phase only forms below about 180 K[71, 205] (and is only observed at much lower temperatures in exfoliated thin flakes[208]), electronically isolating monolayer $1T-TaS_2$ with thicker metallic slabs of H–TaS_2 has been shown to stabilize the C-CDW state in monolayer $1T-TaS_2$ at room temperature[62, 216]. To this end, the recent synthesis of endotaxial TaS_2 offers new mechanisms for accessing modular CDW systems[216].

In this work, we demonstrate an approach converse to preceding literature—employing moderate thermal annealing to interdisperse monolayer H–TaS_2 between few-layer $1T-TaS_2$ lamellae. In the resulting verti-lateral $1T-TaS_2/H$–TaS_2 heterostructures, decoupled $1T-TaS_2$ fragments undergo independent transitions from the disordered incommensurate (IC) to ordered commensurate CDW phase above room temperature. These transitions are hallmarked by synchronous stepwise switching of chirality and resistance with high predictability; the number of steps is encoded by the quantity and arrangement of H–TaS_2 layers. Thus, the developed materials represent a distinctive framework for deterministic engineering of multistate resistance and chirality changes in $1T-TaS_2$. Additionally, we find that the nucleation of H–TaS_2 polytype initiates at macrosocopic flake defects, a mechanistic insight we harness to showcase the potential of strain engineering for the rational design of verti-lateral TaS_2 heterostructures. Moreover, modulating the H–TaS_2 content tunes the proportion of heterochiral CDW superlattices, resulting in a range of optically detectable net chiralities. Therefore, our work provides an adaptable roadmap for the design of versatile optoelectronic phase change materials with reliable, multilevel, and multifunctional switching.

4.3 Results and Discussion

Commensuration in verti-lateral TaS_2 heterostructures.

Exfoliated $1T-TaS_2$ crystals were annealed in high vacuum at 350 °C for 30 minutes and then rapidly cooled to room temperature, engendering changes in optical contrast, indicative of structural transformations (Figure 4.1a). This thermally induced phase evolution was characterized by selected area electron diffraction (SAED) of TaS_2 flakes before and after annealing. Before annealing, SAED patterns of $1T-TaS_2$ flakes are consistent with the expected nearly commensurate (NC)-CDW structure (Figure 4.1b)[71]. In contrast, SAED data from annealed samples (Figure 4.1c) reveal the presence of two $\sqrt{13} \times \sqrt{13}$ heterochiral superlattices. The CDW enantiomorphs, α (L) and β (R), possess supercells that are rotated $\pm$13.9 degrees relative to the unit cell of $1T-TaS_2$ (Figure 4.1d)[71, 218, 219]. Additionally, the SAED data of annealed $1T-TaS_2$ flakes are consistent with a C-CDW phase at room temperature [62, 216]. These ensemble changes in extent of CDW commensuration in heat-treated flakes were also evinced by linearly polarized Raman spectroscopy (Figure 4.1e, Figure 4.2c). Raman spectra obtained in visually distinct regions of annealed flake S1 (Figure 4.1e) show a strong correlation between the red-channel optical contrast change upon annealing (ΔOCR) and the sharpness of low-frequency (40–100 cm^{-1}) Raman modes related to CDWs[220–222]. The CDW spectral peaks become increasingly well-defined from regions 3 to 1 (R3–R1), a behavior that is tightly correlated with progressive ΔOCR. Furthermore, as ΔOCR becomes more negative, new Raman spectral features emerge at 64 cm^{-1}, 89 cm^{-1}, 123 cm^{-1} and 230 cm^{-1}. The manifestation of new peaks and general sharpening of Raman features is consistent with Brillouin zone folding of $1T-TaS_2$ as it undergoes the transition from the nearly commensurate CDW (NC-CDW) to C-CDW[220–222].

To unveil the relationship between ΔOCR, CDW commensuration and atomic lattice structure of these annealed $1T-TaS_2$ crystals, atomic resolution differential-phase-contrast scanning transmission electron microscopy (DPC-STEM) imaging and analysis (Figure 4.1f–j) was performed on cross-sectional samples made from optically distinct regions of flakes S1 (Figure 4.1a) and S2 (Figure 4.2). Representative DPC-STEM micrographs, depicted in Figure 4.1g–j, reveal that thermal annealing induces a partial transition from the $1T$ (octahedrally coordinated Ta) to the H (trigonal prismatic Ta) structure. The H polytype forms within the $1T-TaS_2$ matrix (*i.e.*, endotaxially), overwhelmingly as monolayers, separating generally thicker fragments of $1T-TaS_2$. At boundaries between regions with dissimilar ΔOCR, the number of H–TaS_2 layers varies across a single $1T-TaS_2$ flake, constructing lateral heterostructures with atomically sharp interfaces (Figure 4.1i). Furthermore, these DPC-STEM data show how $1T-TaS_2$ slabs separated by a H–TaS_2 layer slip relative to each other, resulting in the misalignment of the Ta centers (vertical lines in Figure 4.1g–j) in mixed polymorph heterostructures.

We find that optical contrast measurements are a powerful and convenient tool for identifying polymorph composition, owing to the linear relationship between ΔOCR upon annealing and the number of H–TaS_2 layers, determined from DPC-STEM (Figure 4.1f).

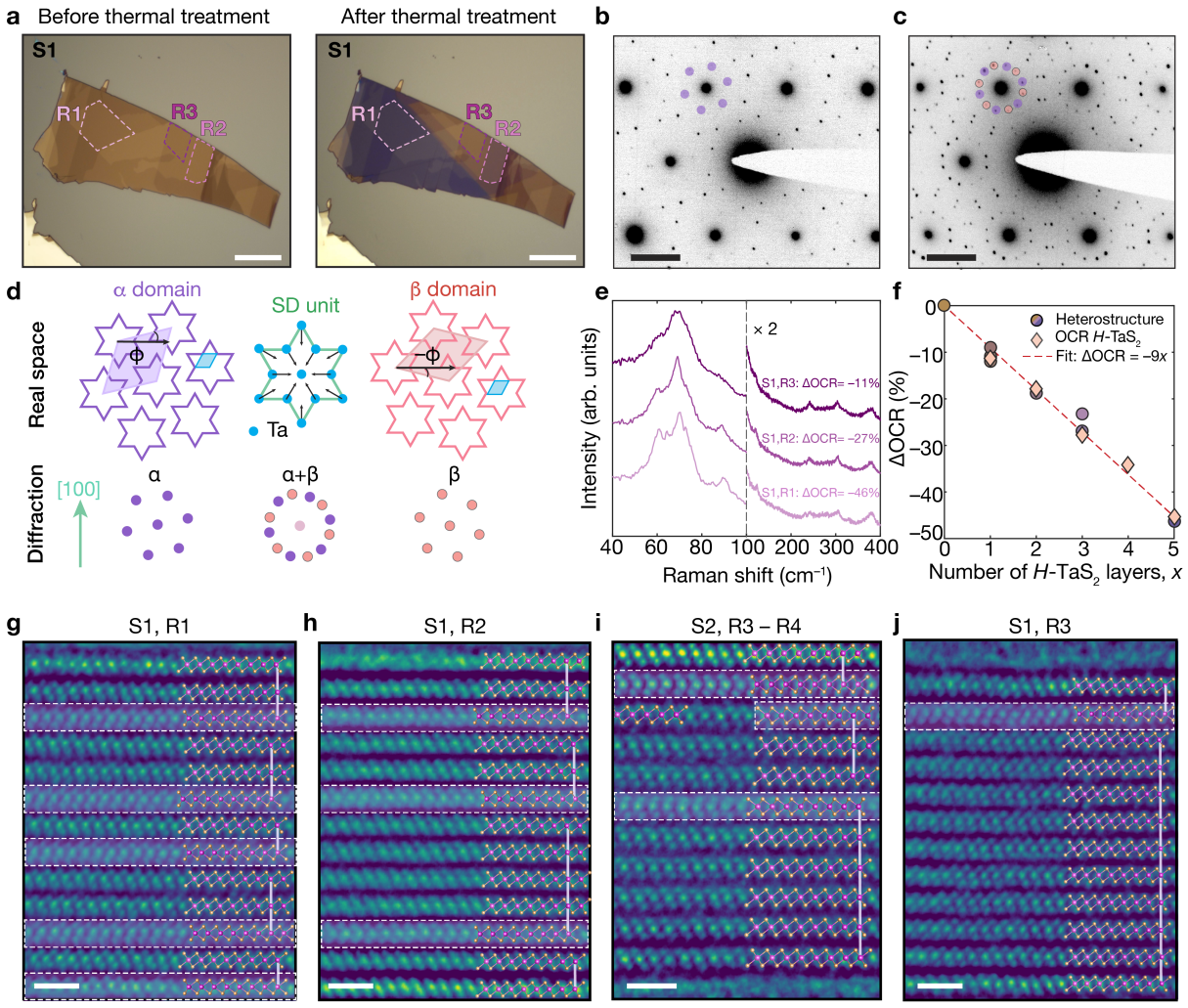


Figure 4.1: Polytype and charge CDW transformations in TaS_2 flakes. **(a)** Optical micrographs of a $1T-TaS_2$ flake, labeled S1, before and after thermal annealing on 90 nm SiO_2/Si. Scale bars: 15 μm. **(b,c)** Room temperature selected area electron diffraction (SAED) patterns of a representative $1T-TaS_2$ flake before **(b)** and after **(c)** thermal annealing. Scale bars: 2 nm^{-1}. **(d)** Schematic of real space α and β CDW domains (top) and diffraction patterns for α, β, and $\alpha + \beta$ (bottom). **(e)** Linearly polarized Raman spectra in selected regions of S1 after thermal annealing. **(f)** Relationship between ΔOCR and the number of H–TaS_2 layers in distinct regions of S1 and S2 (a $1T-TaS_2$ sample) after annealing. This data is overlaid with the thickness dependence of OCR for $2H$–TaS_2 on 90 nm SiO_2/Si substrate (ref [73]). **(g–j)** DPC-STEM images along the $[10\bar{1}0]$ zone axis of: region R1 of S1 **(g)**, area R2 of S1 **(h)**, regions R3–R4 of S2 **(i)**, and region R3 of S1 **(j)** overlaid with structures of $1T-TaS_2$ (ref [60]) and H–TaS_2 (ref[162]). H–TaS_2 layers are highlighted and Ta ions aligned along the c-axis are connected with pink lines. Scale bars in (g)–(j) are 1 nm.

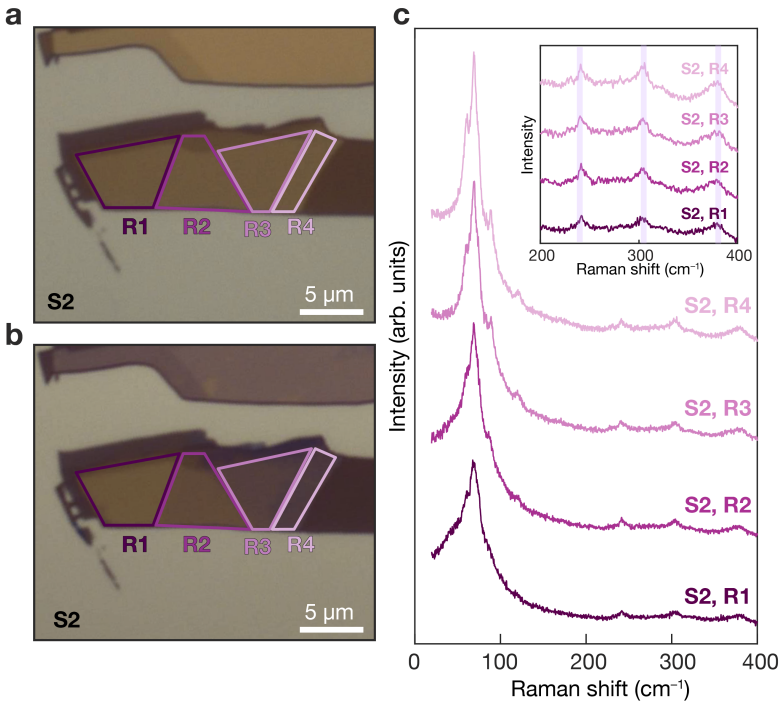


Figure 4.2: Thermally induced polytype and CDW transformations of sample S2. Optical micrographs of flake S2 before **(a)** and after **(b)** thermal annealing. **(c)** Raman spectra in different regions of S2 after annealing.

This relationship mirrors, and stems from, the linear scaling between layer count and OCR for freestanding few-layer H–TaS_2[73]. Therefore, crystal sections with a more negative ΔOCR (*i.e.*, appearing increasingly blue) contain a greater number of layers of the H polymorph. Taken together with the increased sharpness and number of CDW Raman modes (Figure 4.1e), these data establish that the formation of monolayer H structures leads to increased order of $1T$−TaS_2 C-CDW domains, consistent with prior work with thicker H–TaS_2 slabs[62, 216] and bulk mixed polytype TaS_2 phases[68, 205, 218, 223].

The ensemble room-temperature ordering of CDW domains in TaS_2 heterostructures with different polytype compositions was further probed using SAED. Our findings support that samples comprising $\geq 20\%$ of H–TaS_2 manifest an ordered C-CDW phase, characterized by sharp CDW reflections (Figure 4.3b–d). In contrast, the CDW reflections observed in samples with $< 20\%$ H–TaS_2 appear less well-defined and exhibit peak splitting and angular blurring (Figure 4.3a). Accordingly, we infer that crystals containing less than 20% H–TaS_2 content host a disordered C-CDW phase with likely coexistence of some NC-CDW domains. Notably, the chirality of CDW domains (Figure 4.1d) could be exploited for next-generation switching devices, making the nano-scale structural understanding of C-CDWs in TaS_2 heterostructures integral for their potential applications.

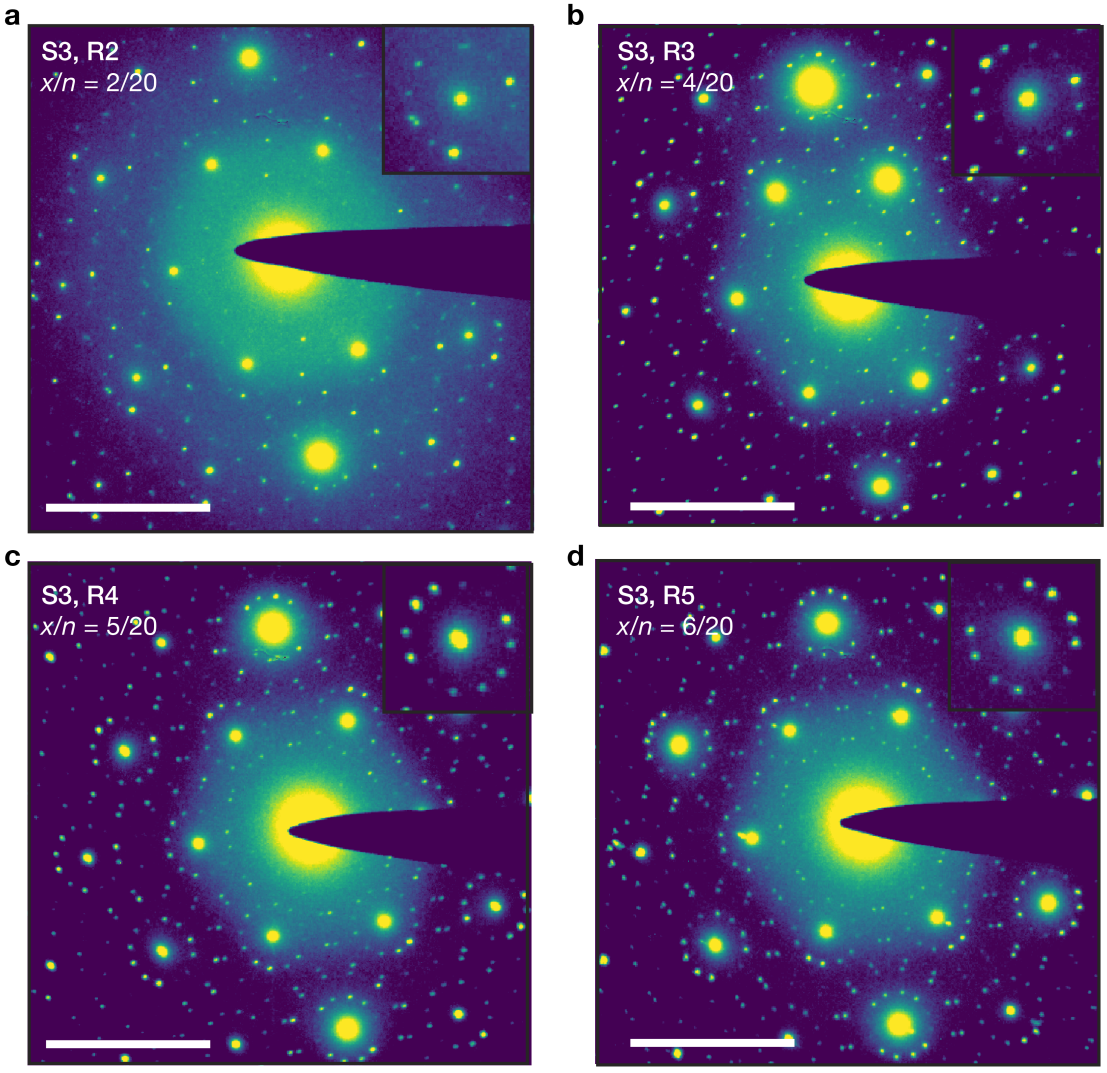


Figure 4.3: Selected area electron diffraction (SAED) of heterostructures with different polytype compositions. **(a–d)** SAED patterns of flake S3 in regions R2 **(a)**, R3 **(b)**, R4 **(c)** and R5 **(d)**. Scale bars are 5 nm^{-1}.

Diverse chirality in polytype heterostructures

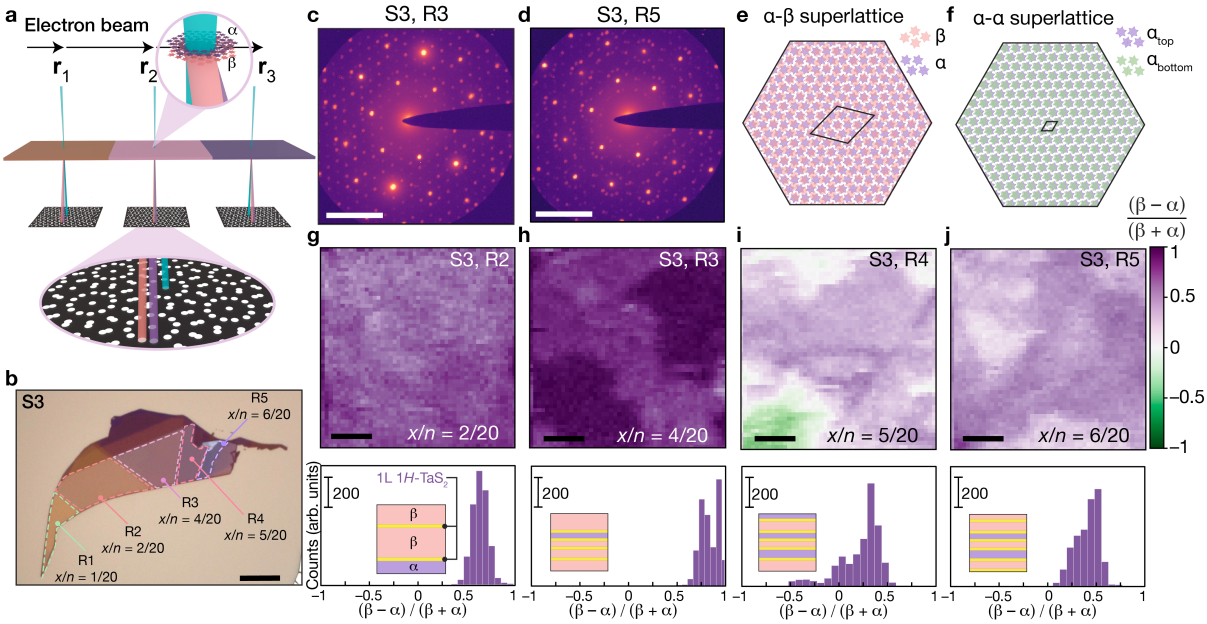


Figure 4.4: Mapping heterochiral CDW domains with four-dimensional scanning transmission electron microscopy (4D-STEM). **(a)** Schematic illustrating 4D-STEM of annealed $1\,T$−TaS_2 samples. Three compositionally distinct flake regions are labeled as $\mathbf{r_1}$, $\mathbf{r_2}$ and $\mathbf{r_3}$. The two heterochiral superlattices are marked as α and β. **(b)** Optical micrograph of a 20-layer annealed $1\,T$−TaS_2 sample S3. Regions of interest and their H–TaS_2 proportion (x/n, where x = number of H–TaS_2 layers and n = total number of layers), calculated from optical contrast measurements, are labeled. Scale bar: 10 μm. **(c,d)** The maximal diffraction patterns, displayed on a logarithmic scale, for S3–R3 **(c)** and S3–R5 **(d)**. Scale bars: 5 nm^{-1}. **(e,f)** Illustration of CDW superstructures for α,β **(e)** and α,α **(f)**. Unit cells of the CDW superstructures are outlined in black. **(g–j)** $(\beta - \alpha)$ / $(\beta + \alpha)$ virtual dark-field images and their histograms for R2–R5 regions of S3. Insets show the proposed sample composition and plausible chirality stacking based on the H–TaS_2 content and 4D-STEM analysis of each region. We note that only the net chirality can be determined, and the exact stacking sequence of the chirality shown here is one of several possibilities as the precise sequence cannot be obtained from plan-view 4D-STEM. All 4D-STEM data was acquired at room temperature. Scale bars in (g)–(j): 50 nm.

The heterochirality of CDW superlattices in H–TaS_2/1T–TaS_2 at room temperature was mapped with nano-scale resolution using four-dimensional scanning transmission electron microscopy (4D-STEM), establishing that the α and β enantiomorphs are stacked along the c-axis to form vertical CDW superstructures (Figure 4.4). In 4D-STEM, a converged electron probe is scanned across a sample in a 2D array, while recording 2D diffraction data at each probe position (Figure 4.4a)[224]. We obtained 4D-STEM datasets of a 20-layer flake, S3 (Figure 4.4b), parallel to the c-axis with $\sim$ 5.5 nm spatial resolution in regions R2–R5. These regions exhibit progressively sharper Raman spectral features (Figure 4.5) and larger H/T ratios from measurements of ΔOCR. For R2–R5, Bragg reflections associated with both commensurate α and β enantiomorphs are present in nanodiffraction patterns (Figure 4.4c,d). Thus, the CDW enantiomorphs are coexistent in a $\sim$ 5.5 nm area, revealing their formation in the out-of-plane ($\|$ c-axis) direction. We note that CDW superstructures can be vertically stacked in two configurations across the H–TaS_2 interface: heterochiral (α–β) (Figure 4.4e) and homochiral (α–α) (Figure 4.4f), each hosting inequivalent CDW cluster interlayer stackings and charge distributions (Figure 4.6)[219]. The interlayer arrangement of CDW clusters in polytype heterostructures exhibits notable distinctions compared to both 1T−TaS_2 flakes and homointerfaces. In pristine 1T−TaS_2, CDW clusters can be perfectly eclipsed because their building blocks—Ta ions—are directly aligned in the out-of-plane direction[70, 225]. In contrast, in polytype heterostructures, Ta ions in 1T−TaS_2 slabs across H–TaS_2 interfaces must be laterally offset (Figure 4.1g–j). Thus, CDW clusters in neighboring 1T−TaS_2 slabs must assume a staggered arrangement, resulting in distinct CDW superlattice patterns (Figure 4.4e–f, Figure 4.6).

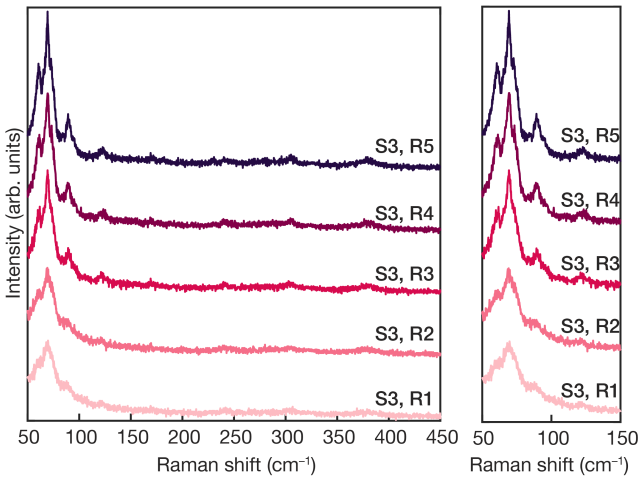


Figure 4.5: Raman response of sample S3. Linearly polarized Raman spectra of flake S3 taken in regions R1–R5 after thermal annealing.

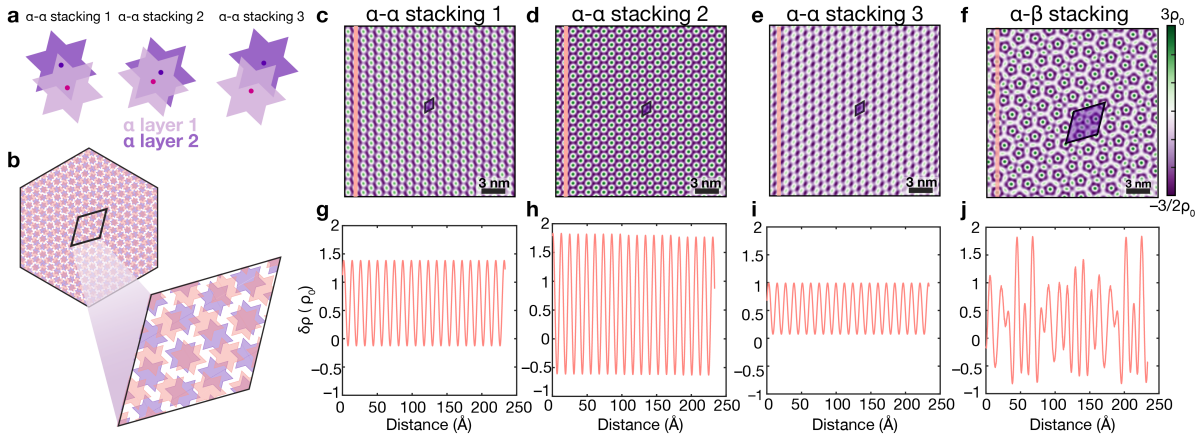


Figure 4.6: Modeling of the CDW order parameter in TaS_2 heterostructures. **(a)** Non-degenerate SOD stacking arrangements for the α–α out-of-plane superstructures. **(b)** Stacking arrangements for α–β out-of-plane superlattices. Unit cell of the CDW moiré superstructure is indicated in black. Real-space CDW order parameter ($\delta\rho(\mathbf{r})$) simulated for the following out-of-plane arrangements: **(c)** α–α stacking 1, **(d)** α–α stacking 2, **(e)** α–α stacking 3 and **(f)** α–β stacking. Violet-shaded regions represent the unit cell of the CDW moiré superstructure. **(g–j)** Line profiles of (c)–(f) in regions marked with orange lines.

Next, integrated intensities of α and β diffraction spots were evaluated at each probe position (see "Methods" section for details)[186] to reconstruct dark-field images associated with the difference in superlattice ratios, defined as: $(\beta - \alpha)/(\beta + \alpha)$ (Figure 4.4g–j). The resultant enantiomorphic ratio maps reveal a minor extent of in-plane variation within each heterostructure (see histograms in Figures 2 g–j), potentially arising from domain pinning defects. Nevertheless, 4D-STEM data and high-resolution TEM analysis (Figure 4.7) consistently point to coexisting, out-of-plane α and β superstructures regardless of the H/T composition. However, the polymorph composition appears to influence the α/β proportion. For example, a less than 45% mean difference in ratio of diffraction pattern intensity from enantiomorphic phases was measured for R4 and R5 at room temperature (Figure 4.4i,j). Conversely, a larger mean enantiomorphic disproportion exceeding 65% was obtained for R2 and R3 (Figure 4.4g,h). This can be understood by considering that changing the polymorph composition alters the size and number of $1T$−TaS_2 fragments hosting the two heterochiral CDWs, thereby engendering changes in the overall chirality. A high enantiomorphic disproportion is therefore the most likely for less transformed samples with larger $1T$−TaS_2 fragments, which would then dominate the overall chirality.

The chirality of TaS_2 heterostructures can also be assessed optically, as enantiomorphic disproportion engenders Raman optical activity (ROA): a distinct Raman response to right- and left-circularly polarized light[225, 226]. For $1T$−TaS_2 displaying ROA, the integrated area ratio of E_g(I) and E_g(II) modes differs in the $\sigma^+\sigma^-$ and $\sigma^-\sigma^+$ Raman polarization

configurations (Figure 4.8a), where $\sigma^i\sigma^s$ $(i, s = +/-)$ are phonon helicities of the incident and scattered light[226]. Note, a stronger ROA signals a higher enantiomorphic disproportion and a larger overall chirality. Representative chirality-dependent optical measurements of sample S4 (Figure 4.9) are shown in Figure 4.8. We find that ROA decreases from region R1 (x/n =3/20) to R3 (x/n =5/20), signaling decreasing overall chirality for an increasing H–TaS_2 layer count (Figure 4.8b–d). These results are consistent with our 4D-STEM findings; highly transformed regions, on average, exhibit a weaker overall chirality compared to medium transformed regions (Figure 4.4g–j). Notably, our verti-lateral heterostructures exhibit a broad spectrum of possible overall chiralities, distinguishing them from $1T-TaS_2$ flakes/homointerfaces and heavily transformed H–TaS_2/$1T$–TaS_2 heterostructures, which can only manifest a single enantiomorphic state[216, 225]. Specifically, the former are homochiral, comprising fully of α or β[225], while the latter have been shown to be achiral, hosting an equal proportion of α and β[216]. Accordingly, our verti-lateral heterostructures may enable chiral opto-electronic memory schemes through their wide array of chiral states that can generate strong optical responses at room temperature.

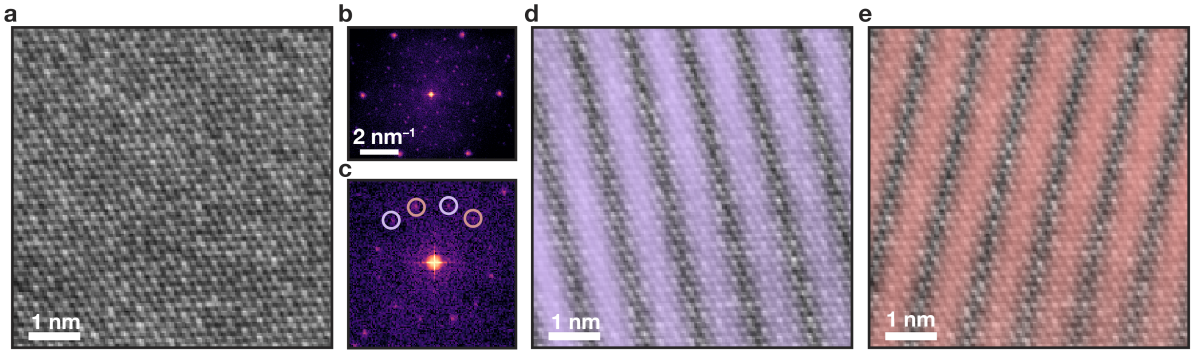


Figure 4.7: High-resolution TEM of TaS_2 heterostructures. **(a)** HRTEM micrograph of a representative H–TaS_2/$1T$–TaS_2 heterostructure. (**b**) Fast Fourier transform (FFT) of (a). **(c)** Enlarged view of (b) in the vicinity of the zero frequency peak. **(d)** Overlay of (a) and the inverse FFT (iFFT) image generated from the components indicated by violet circles in (c). The iFFT (violet lines) represents the α fringes. **(e)** Overlay of (a) and the inverse FFT (iFFT) image from the components indicated by orange circles in (c). The iFFT (orange lines) represents the β fringes.

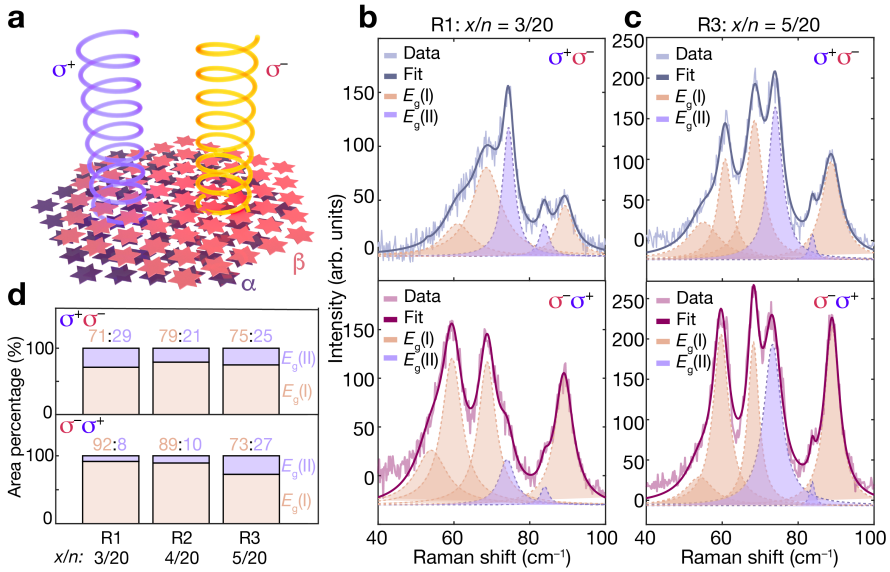


Figure 4.8: Optical detection of chirality in TaS_2 heterostructures. **(a)** Schematic of a polarization-dependent Raman measurement. **(b,c)** Raman spectra in the circular contrarotating polarization configurations ($\sigma^+\sigma^-$ and $\sigma^-\sigma^+$) obtained for region R1 **(b)** and region R3 **(c)** of a 20-layer sample S4. Lorentzian peak fits and the cumulative fits are displayed. **(d)** Stacked bar charts displaying the normalized area percentage of E_g(I) and E_g(II) modes measured in the two contrarotating Raman polarization configurations (top: $\sigma^+\sigma^-$, bottom: $\sigma^-\sigma^+$) for R1–R3 of S4. For (b)–(d), x/n denotes the H–TaS_2 proportion. Data was obtained at room temperature.

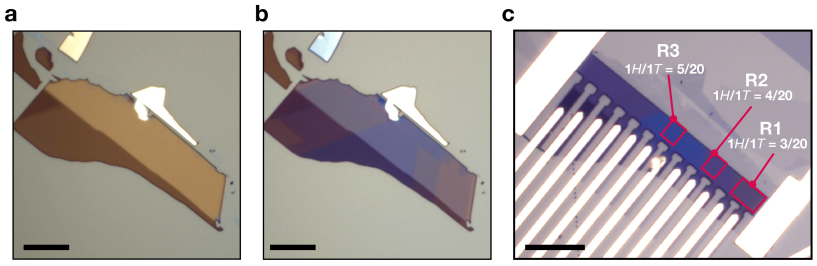


Figure 4.9: Polytype transformations of sample S4. **(a–c)** Optical micrograph of S4 before annealing **(a)**, after annealing **(b)**, and after nanofabrication **(c)**. Regions of interest are marked.

Multistate resistance and chirality switching.

Electronic properties of these heterochiral endotaxial polytype heterostructures were probed using variable-temperature transport measurements. In these studies, we monitored the temperature-dependent longitudinal resistance (R_{xx}) of mesoscopic devices fabricated from S1 (Figure 4.10a) and S4 (Figure 4.9). Measurements from compositionally distinct regions (Figure 4.10b) were used to establish the relationship between polytype composition and the IC-to-C CDW phase transition behavior. For all measured regions, transport below 300 K is dominated by the metallic H–TaS_2 layers (decreasing resistance with decreasing temperature), while transport above room temperature traces CDW transitions of $1T$−TaS_2 lamellae (Figure 4.10c,d). These transport data were complemented with temperature-dependent 4D-STEM of representative heterostructures to provide structural insight (Figure 4.11a–c). Above room temperature, $1T$−TaS_2 transforms from the IC (more conductive) to the C (more insulating) CDW phase with a hysteresis between cooling and warming profiles (Figure 4.10c–d, Figure 4.11a)[71]. As a general observation, increasing H–TaS_2 content leads to narrowing of the thermal hysteresis (Figure 4.10c), which indicates stabilization of the ordered C-CDW state. These observations lie in agreement with our confocal Raman measurements; consistently sharper CDW Raman features are observed for samples with a higher H–TaS_2 content (Figure 4.1, Figure 4.2, Figure 4.5).

Interestingly, the formation of H–TaS_2 layers dictates the stepwise evolution of resistance and chirality with temperature in these endotaxial polytype heterostructures. Upon cooling, we observe a series of stepped resistance increases (Figure 4.10d), with the step count matching the number of $1T$−TaS_2 slabs determined from DPC-STEM images of device cross-sections. Thus, the H–TaS_2-separated $1T$−TaS_2 lamellae behave as isolated crystals with distinct IC–C CDW transitions, likely due to the electronic decoupling imposed by the metallic (H–TaS_2) spacers[216]. For this reason, the number of H spacer layers deterministically encodes the number of resistance steps, and the profile (magnitude of resistivity change) of each step is governed by the various thicknesses of the $1T$−TaS_2 segments; thicker $1T$−TaS_2 slabs exhibit sharper CDW transitions, as observed in freestanding $1T$−TaS_2 crystals[210, 211]. We note that resistance traces upon warming are noticeably broadened relative to the respective cooling sweeps. This may be understood by considering that strength of defect pinning is contingent on the CDW phase[208, 210, 220, 227]. Defects may exert stronger pinning effects on the CDW domains in the localized C-CDW state compared to the "melted" IC-CDW phase, leading to less well-defined transitions upon warming. Nevertheless, the stepwise resistance transitions are highly reproducible in subsequent cooling cycles (Figure 4.10d, Figure 4.12, Figure 4.13). Moreover, in addition to the resistance steps upon cooling, temperature-dependent 4D-STEM reveals stepwise appearance of the α (L) and β (R) C-CDW enantiomorphs in concert with vanishing of the achiral IC phase (Figure 4.11a–c). Thus, the IC-C CDW transition in our endotaxial heterostructures is marked both by simultaneous evolution of resistance and overall chirality (Figure 4.11c), defined by the proportion of chiral superlattices: (α-β)/(α+β+IC). This synchronous switching sets the stage for optoelectronic devices combining charge and chirality degrees of freedom.

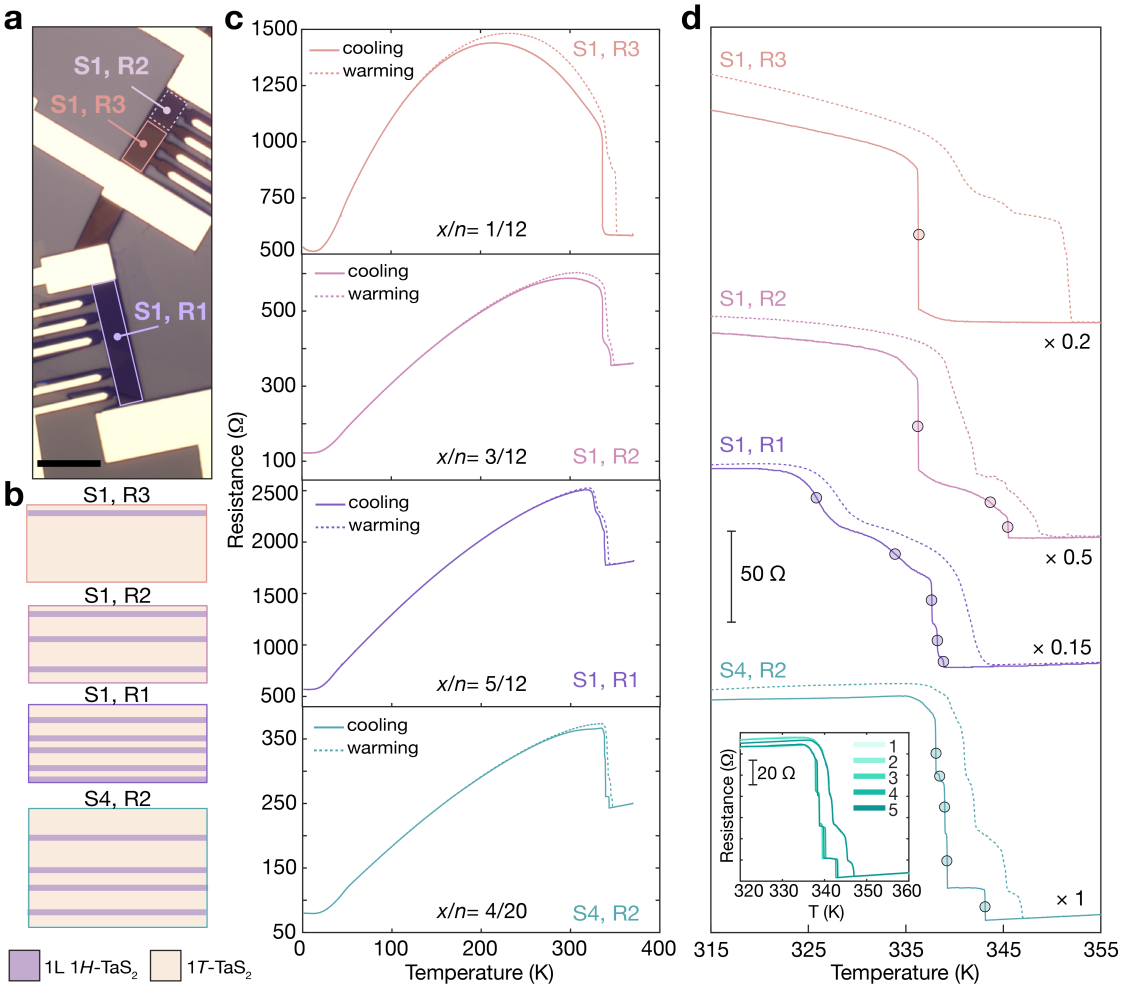


Figure 4.10: Multistate resistance switching in TaS_2 heterostructures. **(a)** Optical micrograph of a mesoscopic device fabricated from annealed flake S1. Scale bar: 10 μm. **(b)** Diagrams of sample composition for S1 and S4. For S1, diagrams are derived from atomic resolution DPC-STEM data, while for S4 the structure is proposed based on the ΔOCR-derived H–TaS_2 content. Note, for S4, the H–TaS_2 layers are randomly placed in the model. **(c)** Temperature-dependent resistance of S1 in regions R1–R3 and S4 in region R2. The marked x/n denotes the H–TaS_2 proportion. **(d)** High-temperature section of (c). Curves were vertically shifted for clarity. Inflection points in the cooling curve are marked by a circle. Scaling factors of the resistance curves are indicated on the right. Inset shows the resistance modulation of S4–R2 in five thermal cycles. Temperature ramp rate in (c)–(d) was 1 K/min.

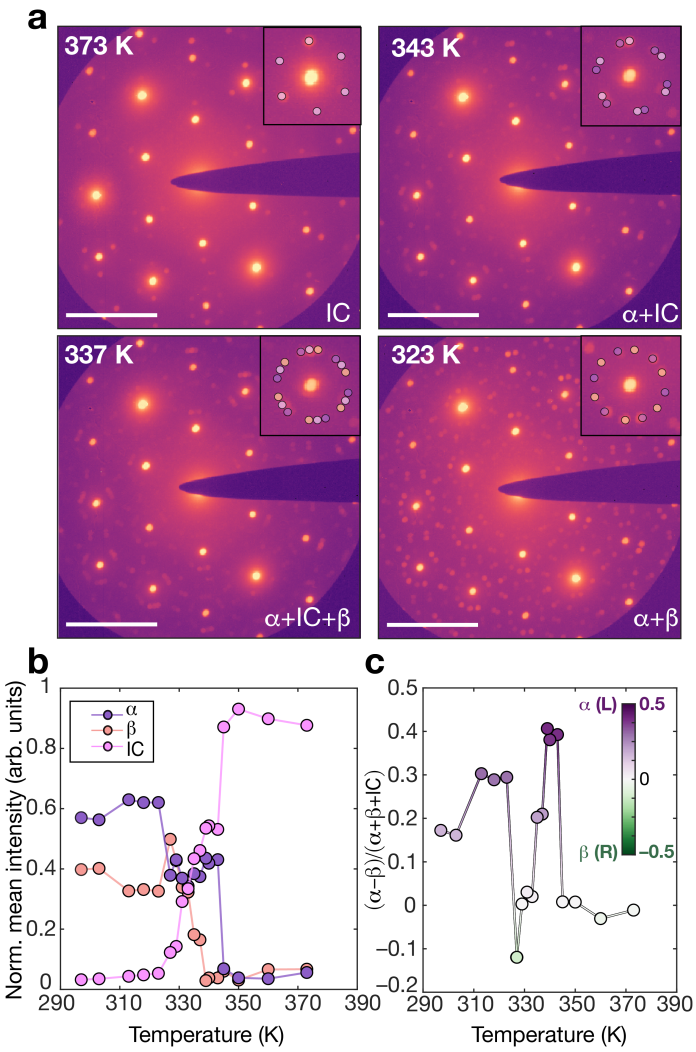


Figure 4.11: Multistate chirality switching in TaS_2 heterostructures. **(a)** Representative temperature-dependent 4D-STEM diffraction patterns, displayed on a logarithmic scale, for a 20-layer heterostructure with five H–TaS_2 lamella. Insets display a zoomed-in view of a primary Bragg spot with labeled CDW superstructure peaks. Scale bars: 5 nm^{-1}. **(b)** Normalized mean intensity of α, β and incommensurate (IC) diffraction peaks in 4D-STEM datasets obtained at different temperatures for the heterostructure in (a). **(c)** Temperature-dependent $(\alpha - \beta)/(\alpha + \beta + \text{IC})$ calculated from (b). Heating was performed in situ and the data were acquired upon cooling from 373 K at 1 K/min.

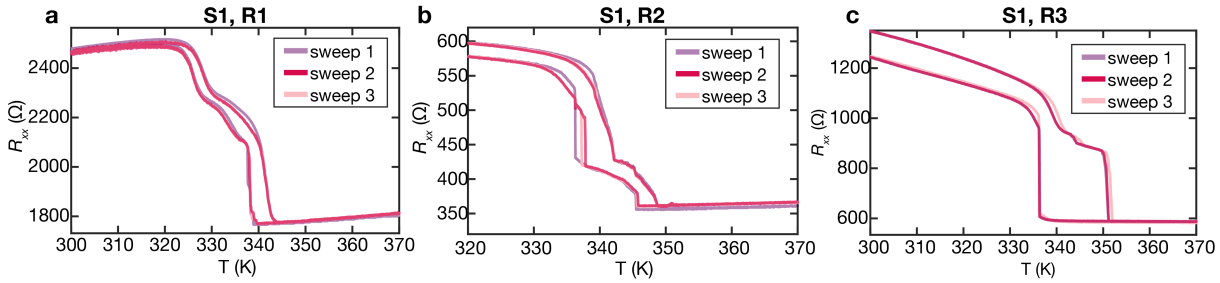


Figure 4.12: Reproducibility of resistance profiles for sample S1. **(a–c)** Resistance of sample S1 in regions R1 **(a)**, R2 **(b)** and R3 **(c)** across three temperature sweeps. The sweep rate was kept constant at 1 K/min for all thermal cycles.

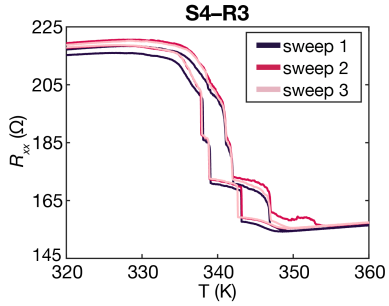


Figure 4.13: Transport measurements of sample S4. Temperature-dependent resistance of S4 in region R3 across three thermal sweeps. The temperature sweep rate was 1 K/min.

Polytype nucleation and designer heterostructures.

Lastly, having established the structure and multistate electronic/chiral switching in TaS_2 endotaxial heterostructures, we turn to considering the mechanism of nucleation of these polytype transformations, finding them to be facilitated by wrinkles and folds. We observed that polymorph transitions in $1T-TaS_2$ flakes, evidenced by changes in ΔOCR and sharpness of Raman spectral features associated with CDW modes, generally emanate from wrinkles, tears and folds in flakes (Figure 4.14a–c, Figure 4.15). These microscale structural defects inevitably introduce differential stress, which can be accommodated by strain (Figure 4.14d)[228–230], and this strain in turn can alter the energetic barrier between polytypes[231–234]. Accordingly, one explanation for the emanation of H–TaS_2 at these features, is a strain-induced decreased energetic barrier for the H–T transformation, facilitating in nucleation of polytypic domains near stress points. In addition, differential stress in layered materials can also be accommodated by shear and slip between layers (Figure 4.14e)[228].

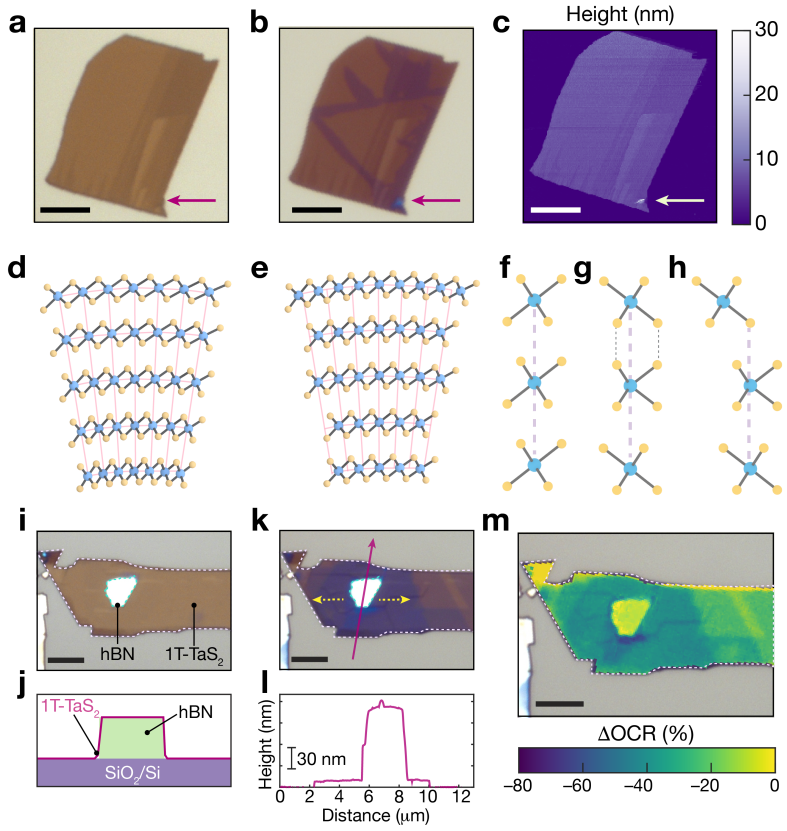


Figure 4.14: Nucleation of endotaxial polytype transformation. **(a,b)** Optical image of a $1T-TaS_2$ flake before **(a)** and after **(b)** thermal annealing. A flake fold is marked with a magenta arrow. **(c)** Atomic Force Microscopy (AFM) map of (b). **(d,e)** Models of $1T-TaS_2$ bending at a fold or wrinkle that are accommodated by in-plane strain **(d)** or interlayer shear and slip **(e)**. Models in (d) and (e) are adapted from ref [228]. **(f–h)** Stacking configurations of three TaS_2 structures: interface of three $1T-TaS_2$ layers **(f)**, $1T$–TaS_2/$1H$–TaS_2/$1T$–TaS_2 interface without layer sliding **(g)** and $1T$–TaS_2/$1H$–TaS_2/$1T$–TaS_2 interface with shifting of the topmost $1T-TaS_2$ layer **(h)**. Violet dashed vertical lines in (f)–(h) indicate the alignment of Ta ions between the three TaS_2 layers. Black dashed lines in (g) represent direct vertical overlap of sulfur ions between the topmost and middle layers. **(i,j)** Optical micrograph **(i)** and illustration **(j)** of an hBN/$1T-TaS_2$ heterostructure before annealing. **(k)** Optical micrograph of flake in (i) after annealing. Yellow arrows indicate the direction of propagation of the blue H–TaS_2 domains. **(l)** AFM height profile of flake in (i,k) in the region marked with a magenta arrow. **(m)** Map of ΔOCR after annealing overlaid on the optical micrograph (k). Flake outlines are added in (i), (k) and (m). All scale bars are 5 μm.

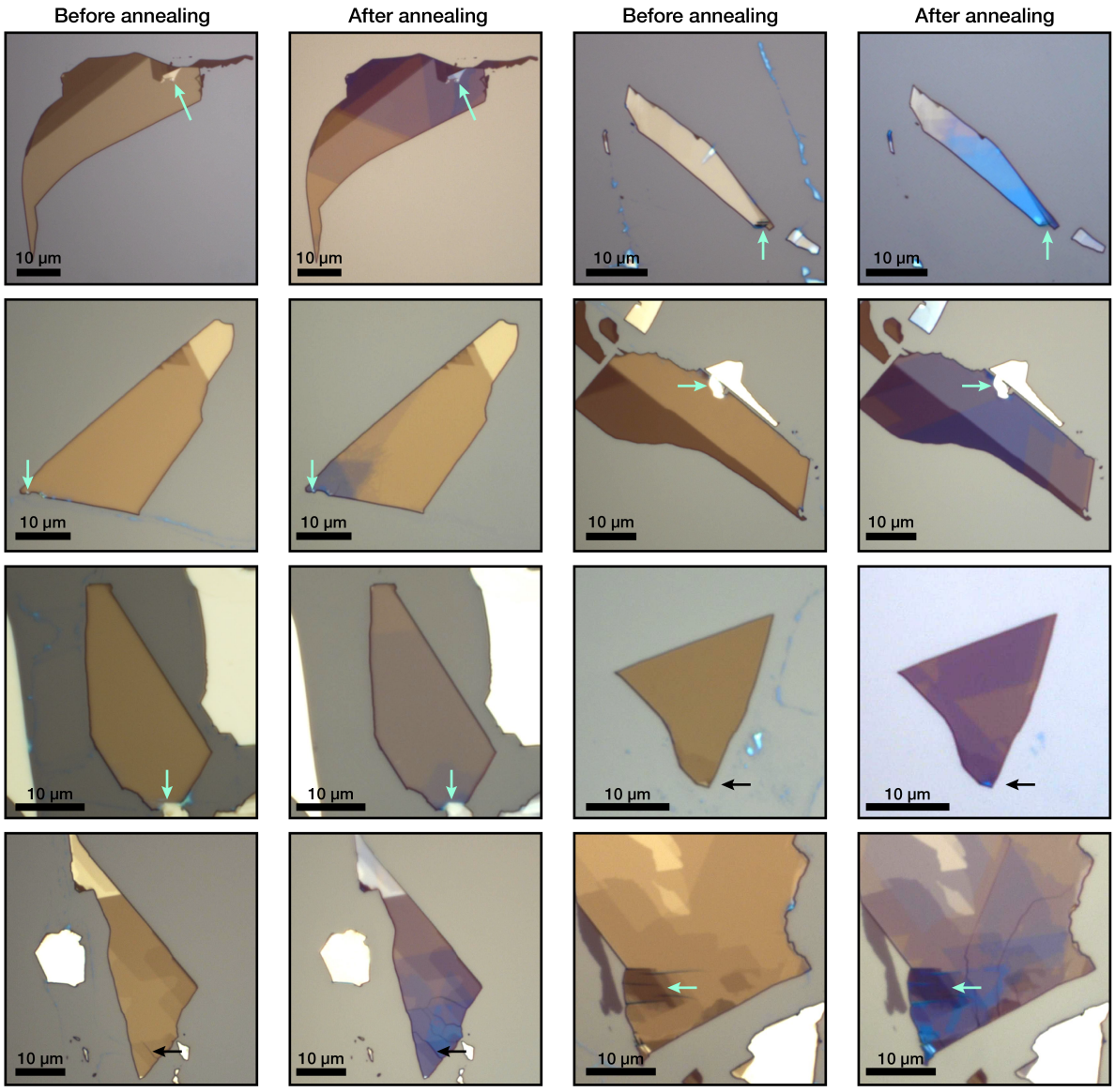


Figure 4.15: Nucleation of polytype transformations at macroscopic flake defects. Optical micrographs of flakes before and after thermal annealing at 350 °C for 30 minutes. Arrows point to macroscopic flake defects (folds, wrinkles).

This leads to the formation of extended shear dislocations[228], which as we observed in Figures 4.1g–j, appear to be a prerequisite for the formation of $1T$–TaS_2/$1H$–TaS_2/$1T$–TaS_2 interfaces from $1T-TaS_2$[223]. Specifically, in native $1T-TaS_2$, the Ta ions are directly aligned in the out-of-plane direction (Figure 4.14f). However, upon transformation of one layer to H–TaS_2, crystallographic stacking with direct S–S overlap would be encountered (Figure 4.14g). We find this configuration to be, on average, 8 meV per Å^2 higher in energy according to density functional theory calculations. To eliminate this unfavorable interlayer interaction, one of the $1T-TaS_2$ layers can slip across the trigonal prismatic interface (Figure 4.14h), precisely as observed in Figure 4.1g–j. Note that interlayer slips are readily present at flake folds, wrinkles and tears in 2D materials. Thus, polytype domains may form more readily in those defect regions of $1T-TaS_2$. We surmise that polytype transitions nucleate at macroscopic defect points due to the formation of extended dislocations and/or decreasing of the $1T$-H energy barrier due to strain.

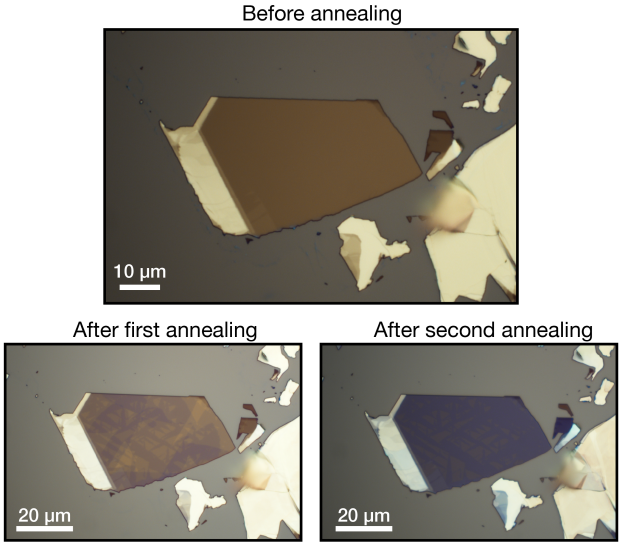


Figure 4.16: Polytype transformations with successive heating cycles. **(a–c)** Optical micrographs of a $1T-TaS_2$ flake before annealing **(a)**, after the first **(b)** and after the second **(c)** 30 minute annealing cycle at 350 °C.

We build upon these nanoscale insights to demonstrate that mechanical/strain engineering of $1T-TaS_2$ may be used for rational design of vertical/lateral TaS_2 heterostructures. To this end, we stacked a 14-layer $1T-TaS_2$ crystal onto a $\sim$ 112 nm-thick hexagonal boron nitride (hBN) flake to deliberately impart local stress onto the region of the $1T-TaS_2$ flake in the vicinity of hBN (Figure 4.14i,j). Indeed, after annealing, the H–TaS_2 polytype formation, evidenced by ΔOCR, radiates away from the hBN/TaS_2 interface (Figure 4.14k–m). It is important to note that coincident vertical/lateral heterostrucures are only formed upon annealing at moderate temperatures for short time periods, as extended or repeated heating leads to formation of predominantly homogeneous structures (Figure 4.16)[216]. Accordingly, intricate, multi-component device architectures could be realized by combining substrate patterning with moderate thermal annealing conditions.

4.4 Conclusion

In conclusion, we have demonstrated that highly tunable, verti-lateral polytype heterostrucures of $1T-TaS_2$ and H–TaS_2 can be synthesized by moderate thermal annealing of nano-thick $1T-TaS_2$ flakes. Stress points in $1T-TaS_2$ are nucleation sites for the H–TaS_2 domains, resulting in multi-component flakes with coexisting vertical and lateral heterostructures. The polytype composition of these heterostructures can now be conveniently determined using the optical contrast methodology developed in this work, enhancing the accessibility for characterizing and studying complex TaS_2 crystals. Further, we use electron microscopy, Raman spectroscopy and electronic transport studies to show that altering the $H/1T$ ratio opens manifold possibilities for tailoring structural and electronic behavior of mixed polymorph crystals. Interlayer coupling between $1T-TaS_2$ fragments is interrupted by H–TaS_2 layers, and the increasing content of H–TaS_2 correlates with greater CDW commensuration, the appearance of optically detectable heterochiral CDW superlattices, and tunable chirality by modulating the α/β ratios. Furthermore, decoupled $1T-TaS_2$ fragments transition from the IC-CDW to the C-CDW state independently at high temperatures and the resulting temperature-driven, multistate phase transition is highly predictable: the number and size of resistance and steps is defined by the count and placement of H–TaS_2 layers within the polytype heterostructure. Moreover, the changes in resistance are accompanied by corresponding changes in chirality, resulting in simultaneous modifications of both optical and electrical properties. Given the precedent for fast switching in $1T-TaS_2$ using electrical[41, 61, 200, 208, 219, 235–237] and optical fields[70, 238], endotaxial H–TaS_2/$1T$–TaS_2 heterostructures offer a rich framework as designer CDW materials that should exhibit multi-level switching between chiral CDW phases. The ability to predictably fabricate and control such well-defined phase change materials using low-energy external stimuli is a highly promising roadmap towards next-generation computing and data storage.

4.5 Methods Chapter 4

Mechanical exfoliation of $1T$–TaS_2

The mechanical exfoliation of $1T-TaS_2$ (HQ Graphene) is done in an Ar glovebox using an adhesive tape (Magic Scotch). The crystals are exfoliated onto 90 nm SiO_2/Si wafers, whose oxide layer is formed by dry chlorination followed by annealing in forming gas (Nova Electronic Materials). First, wafers are cut into $\sim 1 \times 1$ cm pieces and cleaned for 2 minutes in an oxygen plasma cleaner. The chips are then heated to 200 °C on the glovebox hotplate while tessellating a sizeable ($\sim 3 \times 3$ mm) $1T-TaS_2$ crystal with the adhesive tape. Following this, chips are taken off the hotplate, and placed shiny-side-up onto the tape while still warm. The chips are then pressed for 10 minutes with finger pressure. Lastly, the tape is swiftly taken off the chips.

Mechanical exfoliation of hexagonal boron nitride (hBN)

The mechanical exfoliation of hBN (used as received from T. Taniguchi and K. Watanabe) is performed in atomospheric conditions. First, a 90 nm SiO_2/Si wafer (Nova Electronic Materials) is cut into $\sim 1 \times 1$ cm pieces and cleaned for 90 minutes in an ozone cleaner. Immediately before the chip cleaning is complete, 3 hBN crystals ($\sim$1.5 mm $\times$ 1.5 mm) are tessellated with an adhesive tape (Magic Scotch). Promptly after cleaning the chips, they are placed shiny-side-up onto the tape and pressed for 10 minutes with finger pressure. After this, the tape is swiftly taken off the chips.

Thermal annealing of $1T$–TaS_2 crystals

The $1T-TaS_2$ flakes were annealed in high-vacuum (approximately 10^{-7} Torr) by rapidly warming to 120 °C at 60 °C/min with a 5 minute hold. This is followed by heating at 11.5 °C/min to 350 °C and a 30 minute hold at 350 °C, before rapidly cooling to room temperature at 13.5 °C/min.

Determination of layer count for TaS_2 flakes

For flakes S1 and S2 that were studied by differential-phase-contrast scanning transmission electron microscopy (DPC-STEM)[239], we counted the number of layers in the atomic resolution data. For all other flakes, the number of layers was identified using optical contrast (OC) measurements, following the relationship between OC and thickness established in ref [240]. The OC data was commonly obtained in conjunction with atomic force microscopy (AFM) to corroborate the OC-derived thickness.

Preparation of samples for transmission electron microscopy (TEM)

For *c*-axis imaging, we prepared our samples within an Ar glovebox using a custom-built transfer stage. This involved using a polymeric stamp composed of a poly(bisphenol A carbonate) (PC) film covering a polydimethylsiloxane (PDMS) square on a glass slide. The PC/PDMS stamp was created by initially preparing a solution of PC in chloroform with a concentration of 5 % w/w. The solution was then dispensed onto a glass slide using a pipette and evenly distributed by placing it between two glass slides, which were promptly separated. Subsequently, the slides were positioned with the PC side facing up on a hotplate set at 120 °C for 5 minutes, resulting in the formation of a relatively uniform PC film. This PC film was then precision-cut into small squares, approximately 2 mm × 2 mm in size, using a razor blade. Additionally, squares of PDMS, measuring approximately 4 mm × 4 mm, were prepared and affixed to glass slides. To complete the stamp, a PC square was centered within the PDMS square. Finally, the stamp was placed with the polymer side facing up on a hotplate set at 120 °C for 2 minutes. Next, the PC/PDMS stamp is used to pick up $1T-TaS_2$ flakes. To this end, $1T-TaS_2$ flakes of interest were covered in PC for 3 minutes at 160 °C, followed by rapid cooling to room temperature. Then, flakes adhered to the PC/PDMS stamp were placed onto a 200 nm silicon nitride holey TEM grid (Norcada) by melting the PC polymer at 160 °C. The TEM grid underwent a 5-minute cleaning process with O_2 plasma immediately before stacking to enhance flake adhesion. After stacking, the PC film was dissolved in chloroform for 20 minutes under ambient atmosphere, washed in isopropanol and dried with flowing N_2.

For imaging along the crystallographic *ab*-plane, cross-sectional TEM samples were prepared by standard the standard focused ion beam (FIB) lift-out procedure using Thermo Fisher Scientific Helios G4 and Scios 2 FIB-SEM systems. A 200 nm coating of Pt was deposited over the region of interest using an electron beam at 5 kV and 1.6 nA. This was followed by a deposition of 2.5 μm Pt using a gallium-ion beam at 8 kV and 0.12 nA. The initial lift-out was performed with a 30 kV Ga beam and 3 nA probe current, followed by a 1 nA current for the lift-out cleaning. Next, the sample was milled with 30 kV and 0.5 nA until reaching ~ 1 μm thickness, followed by 16 kV and 0.23 nA thinning to 0.5 μm. Next, a 5 kV beam, operated between 77-48 pA, was used to thin the sample to electron transparency. Lastly, final polishing was done at 2 kV and 43 pA.

Nanofabrication of mesoscopic devices from TaS_2 heterostructures

All nanofabrication steps were performed in the Marvell Nanofabrication Laboratory. In a typical procedure, electron beam lithography (100 kV Crestec CABL-UH Series Electron Beam Lithography System) was used to define electrical contacts. PMMA (polymethyl methacrylate) e-Beam resist was used for this purpose (950 PMMA A6, MicroChem). After lithography, reactive ion etching (RIE) with a mixture of 70 sccm CHF_3 and 10 sccm O_2 (Semigroup RIE Etcher) was used to remove top TaS_2 layers and expose a fresh surface

immediately before evaporating Cr/Pt (1 nm/100 nm) (NRC thermal evaporator). After overnight metal lift-off in acetone, electron-beam lithography was used to define a Hall bar-shaped etch mask. Etching of the Hall bar was accomplished by reactive ion etching with 70 sccm SHF_6 and 8.75 sccm O_2 (Semigroup RIE Etcher). After the SHF_6/O_2 treatment, samples were cleaned for 20 seconds in a 40 sccm O_2 plasma and consecutively the PMMA resist was dissolved in acetone for 20–30 minutes.

Transmission electron microscopy Selected area electron diffraction (SAED) patterns were obtained with a 40 μm diameter aperture aperture (defining a selected diameter of $\sim$720 nm on the sample) using FEI TitanX TEM operated at 60–80 kV.

Four-dimensional scanning transmission electron microscopy (4D-STEM) was performed on FEI TitanX (80 keV, 0.3 mrad indicated convergence semi-angle) with the Gatan 652 Heating holder for in-situ heating experiments. The 4D-STEM data was analyzed with the py4DSTEM Python package[186]. First, peak detection in py4DSTEM was used to identify the primary Bragg peaks and construct the reciprocal vectors of the host lattice. Next, CDW reciprocal vectors were calculated from symmetry relations to the primary Bragg vectors. Subsequently, we constructed virtual apertures that mask the entirety of the diffraction space except for the CDW (α, β or IC) satellite peak regions (Supplementary Figure 6a,b). These CDW virtual apertures were then applied to the 4D-STEM diffraction data to integrate the CDW intensities at each probe position. Note, we only integrated over the CDW satellite peaks around the second and third order primary Bragg peaks to minimize the diffuse scattering contribution. Further, we also defined a background (bg) virtual aperture to measure the diffuse scattering background for each diffraction pattern (Supplementary Figure 6a,b). This background was subtracted from the integrated CDW intensities at each probe position for a more accurate calculation of enantiomorphic disproportion. Lastly, for the in-situ heating data, we constructed small virtual apertures that exclude overlap regions between the IC and the α/β peaks (Supplementary Figure 6b).

Differential phase contrast (DPC) STEM images[239] were collected on a Thermo Fisher Scientific Spectra 300 X-CFEG operating at 300 kV with a probe convergence angle of 21.4 mrad. The inner and outer collection angles of the quadrant detector were 15 and 54 mrad respectively. DPC-STEM images were reconstructed from the component images output by each quadrant using the py4DSTEM package[186].

Raman spectroscopy

Ultra-low frequency (ULF) Raman spectra (Horiba Multiline LabRam Evolution) of TaS_2 heterostructures were obtained using a 633 nm laser excitation with the corresponding ULF notch filters at a power of 50–80 μW with 10 second acquisition times and 3 accumulations.

Circularly polarized Raman spectroscopy was performed in backscattering configuration along the ZZ direction. A 100 x objective (N.A. = 0.80) was used for focusing the incident beam onto the sample and for collecting the scattered light. The Raman laser spot size was $\sim$ 1 μm. Circularly polarized light was achieved by using two linear polarizers (LP1 and LP2) and a $\lambda/4$ waveplate (Supplementary Figure 12).

Electron transport measurements.

Transport measurements were performed using standard lock-in techniques. Briefly, a 1 μA alternating current (17.777 Hz) was applied between the source and drain contacts while sweeping the temperature in the PPMS DynaCool system. Concurrently, the longitudinal (Vxx) voltage was measured with the SR830 lock-in amplifier. All phases were ≤ 5, and the resistances were determined from Ohm's law. All data displayed in this work displays the four-probe resistance except for the measurement for S1-R1, which was taken in the 3-probe configuration.

Density functional theory calculations

Density Functional Theory (DFT) calculations were carried out using the Vienna *Ab initio* Simulation Package (VASP)[135–138] with projector augmented wave (PAW) pseudopotentials[139, 140] including Ta $5pd$, $6s$ and S $3sp$ electrons as valence. The plane-wave energy cutoff was set to 400 eV and the k-point grids were Gamma-centred with a k-point spacing of $0.3\,\text{Å}^{-1}$ for the $1T$ phase and $0.2\,\text{Å}^{-1}$ for the $1H$ phase, which gave an energy convergence of 1 meV per atom. The convergence criteria for the electronic self-consistent loop was set to 10^{-7} eV. Structural optimizations were done using the PBEsol[241] exchange-correlation functional until the residual forces on the ions were less than $0.001\,\text{eV}\,\text{Å}^{-1}$.

The energy gain for the interlayer slip observed by DPC-STEM was determined by DFT calculations on mixed phase structures. A shift between $1H$ and $1T$ layers of $(2a/3,\ b/3)$, where a and b are the $1H$ lattice parameters, was introduced to eliminate direct S-S overlap. This shift is comparable to the offset between layers in the 6R-TaS_2 phase. In a 6-layer $1H/1T$-$\alpha/1T$-α stack, the energy gain with interlayer slip was $8\,\text{meV}\,\text{Å}^{-2}$.

Chapter 5

Intercalation simultaneously tunes spin and charge order in polytype heterostructures

Contributing authors: Husremović, S.; Goodge B.; Zhang, W.; Dandu M.; Craig I.; Kennedy R. E.; Erodici M.; Koh K.; Griffin, S. M.; Analytis, J.; Raja A.; Bediako, D. K.

Author contributions: S.H. and D.K.B. conceived the study. S.H. and W.Z. prepared the samples. S.H. and B.G. carried out TEM experiments. B.G. conducted the EELS measurements. S.H. and E. R. K. carried out the FFT analysis. S.H., M.D., and M.E. performed the Raman experiments. S.H., M.E. and K.K. performed the pulsing experiments. C.I. conducted the DFT. calculations.

5.1 Introduction

Investigating correlated systems with multiple electronic orders has been a central focus of academic research. The ultimate goal is to elucidate the interplay and stability of these orders in order to leverage them for technological advancements and new computing paradigms[242]. In particular, systems with coexisting quantum phases have garnered great interest due to their potential for multifunctional electronic devices. These systems offer a unique opportunity to encode, store, and retrieve information by exploiting the distinct phases and the interplay between them. To this end, transition metal dichalcogenides (TMDs) have been extensively explored due to their ability to host charge density waves (CDWs), superconductivity, and long-range magnetic order[11, 30, 243–245]. However, these phases often compete, with the simultaneous presence of multiple phases being rare. For instance, in intercalated TMDs, small amounts of intercalation can destabilize the CDW ground state, leading to enhanced superconductivity[11, 243–246]. However, above a certain intercalation threshold, superconductivity is suppressed, and long-range magnetism emerges[11, 73, 246].

The recently developed tuning mechanisms for layered materials may enable the realization of coexisting competing phases that are not achievable in bulk TMD systems grown using traditional solid-state methods. Namely, owing to the layered nature of TMDs, they can be exfoliated[14, 22], integrated into two-dimensional (2D) heterostructures[4, 22, 247] and prepared as 2D intercalation compounds[73]. These chemical alterations create opportunities to investigate the interplay between dimensionality, competing quantum phases, and electron correlations, paving the way for the realization of complex coexistence of competing quantum orders that can be harnessed for computing applications.

In this work, we synthesize Fe-intercalated polytype heterostructures of TaS_2 by treating 2D $1T-TaS_2$ crystals with a solid Fe precursor, followed by thermal annealing. The annealing process simultaneously initiates a partial polytype transition of $1T-TaS_2$ to H–TaS_2 and a solid-state intercalation reaction between the precursor and flake, resulting in the formation of complex Fe-intercalated polytype heterostructures (TH-Fe_xTaS_2) in a single synthetic step. The synthesized heterostructures comprise homotypic and heterotypic polytype interfaces—all found to host intercalants. In TH-Fe_xTaS_2, the commensurate CDW (C-CDW) phase originating from $1T-TaS_2$ layers exhibits remarkable robustness and persistence above room temperature, notwithstanding the presence of ordered intercalant superstructures. At lower temperatures, the intercalants engender long-range ferromagnetism, which coexists with the C-CDW phase. Notably, the CDW ordering temperature decreases with increasing Fe content, confirming the competing nature of these structural phases. However, Fe ordering can also pin CDW domains in crystals with nominally higher CDW disorder. This yields a metastable "trapped" CDW state, wherein the crystals remain in their low-temperature phase even above 350 K, where CDW domains of ordered crystals have already melted. Our study highlights that intercalation can be leveraged as a means to fabricate complex heterostructures with robust charge and spin ordering, thereby providing a new platform for the development of multifunctional materials suitable for electronic applications.

5.2 Results and Discussion

Synthesis of Fe-intercalated polytype heterostructures

Two-dimensional (2D) iron-intercalated polytype heterostructures of tantalum TaS_2 were fabricated using the synthetic method described in Chapter 3. In a typical procedure, exfoliated crystals of $1T-TaS_2$ were treated with a carbonyl-derived iron precursor followed by vacuum annealing at or above 250°C (Figure 5.1a). The thermal annealing step results in two concurrent chemical transformations: a partial polytype transition of $1T-TaS_2$ to H–TaS_2 and a nanoscale solid-state intercalation reaction between the solid Fe precursor and TaS_2. These transformations result in intricate intercalated polytype heterostructures, referred to as TH-Fe_xTaS_2. To examine the complex structure of these systems, we cross-sectioned TH-Fe_xTaS_2 crystals and imaged them with atomic-resolution high-angle annular dark-field scanning transmission electron microscopy (HAADF-STEM), as seen in Figure 5.1b.

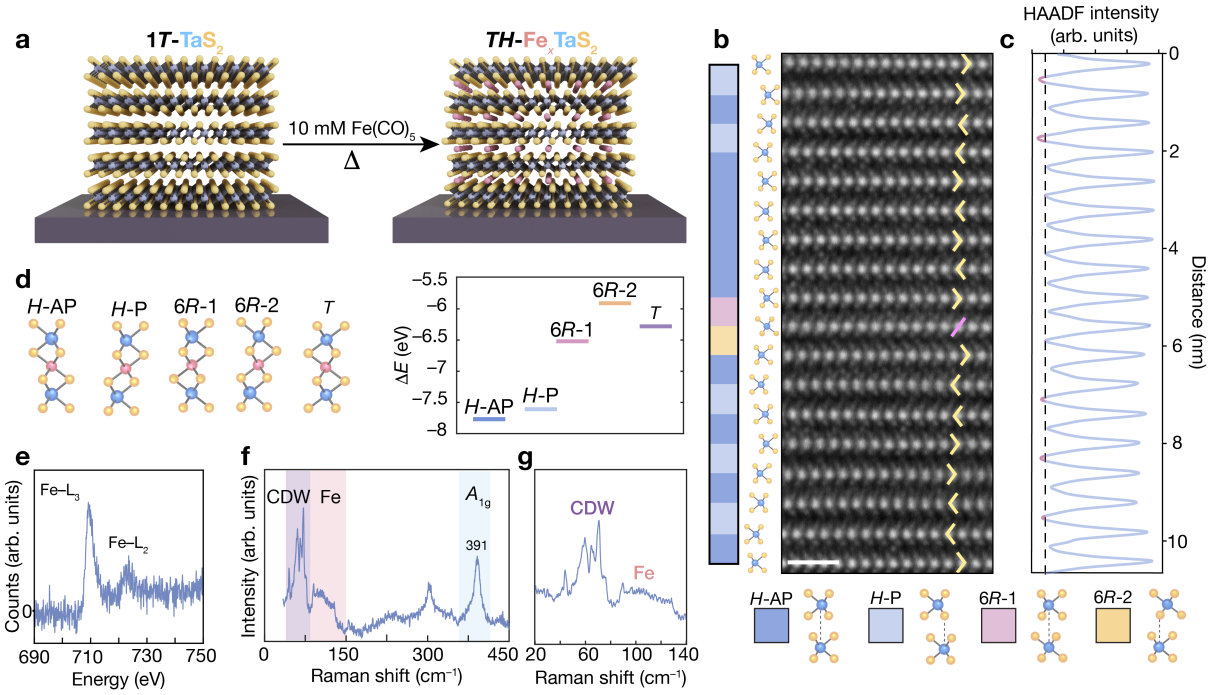


Figure 5.1: Synthesis of Fe-intercalated polytype heterostructures. **(a)** Schematic depiction of the synthetic process for creating Fe-intercalated polytype heterostructures (TH-Fe_xTaS_2) from two-dimensional (2D) $1T-TaS_2$ crystals. **(b)** Room-temperature atomic-resolution HAADF-STEM micrograph of a cross-sectioned TH-Fe_xTaS_2 crystal along the $[10\bar{1}0]$ zone axis of polytype heterostructure. Yellow and pink markings on the HAADF image signify H–TaS_2 and $1T-TaS_2$ layers, respectively. The atomic model of the imaged layers is depicted on the left, with adjacent colors signifying the type of crystallographic stacking according to the legend below the HAADF image. The Fe/Ta ratio of the crystal is 0.17(2) from STEM-EDS analysis. Scale bar: 1 nm. **(c)** Averaged vertical line profile of the image in (b) obtained along the direction of the layers. A dashed line is placed at the HAADF intensity measured for a fragment of H–AP layers from the top of the heterostructure. **(d)** Structures of distinct interlayer stacking registries intercalated with Fe and their corresponding change in energy upon intercalation (ΔE) calculated using DFT. **(e)** Cumulative EEL spectrum of the sample from (b). **(f)** Raman spectrum of TH-Fe_xTaS_2 crystal from (b) prior to cross-sectioning. Data is collected on a solid Si_3N_4/Si support at room temperature. The spectral regions where dominant modes originate from the Fe superlattice, CDW supercell, and the host-lattice A_{1g} mode [73, 96, 183] are highlighted. **(g)** Raman spectrum (f) in the low-frequency range. The sharp CDW-related modes and the broader Fe-related modes are marked.

HAADF-STEM micrographs revealed different interlayer stacking registries with homotypic and heterotypic polytype interfaces (Figure 5.1b). The observed heterogeneity in interlayer stacking can be attributed to interlayer slips during the polytype transformation process, which serve to prevent the direct overlap of sulfur ions in adjacent layers[183]. Notably, all detected interlayer registries contain pseudo-octahedral interstitial sites amenable to intercalation (Figure 5.1b). Moreover, HAADF-STEM imaging confirmed that, indeed, intercalants are found in these interstitial sites, with the HAADF-STEM intensity in the interlayer spacings being non-zero (Figure 5.1b,c).

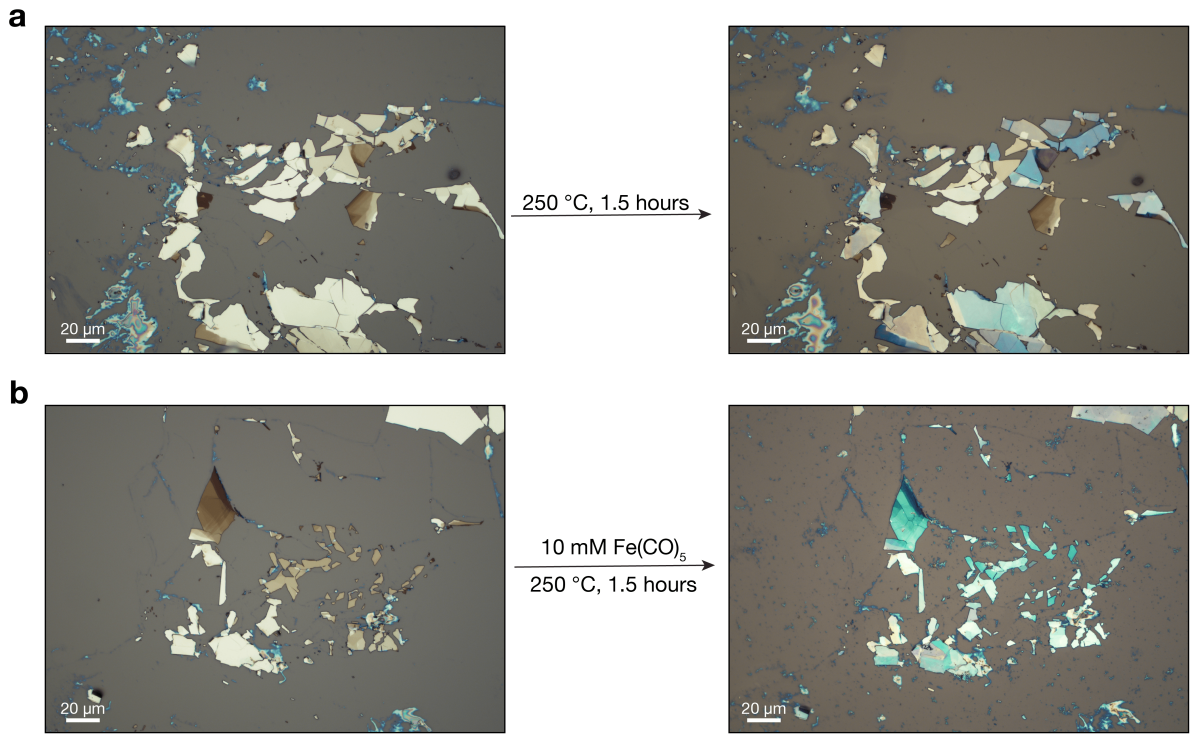


Figure 5.2: Optical contrast changes of $1T-TaS_2$ resulting from annealing only versus thermally-driven intercalation. **(a,b)** Optical images of $1T-TaS_2$ before and after: vacuum annealing at 250 °C **(a)** and treatment with a Fe precursor followed by vacuum annealing at 250 °C **(b)**.

Interestingly, we observed that the HAADF intensity is generally lower between the parallel-stacked H–TaS_2 layers (H–P) compared to the antiparallel-stacked H–TaS_2 layers (H–AP), implying a preferential interaction in the latter interfaces (Figure 5.1b,c). Antiparallel H–TaS_2 stacking (H–P) is found in bulk intercalated H-Fe_xTaS_2 crystals, indicating that it is the thermodynamically favorable configuration[37, 38, 40, 73]. In the H–AP configuration, the adjacent layers of H–TaS_2 are rotated by 180°, leading to a direct alignment of the tantalum (Ta) ions across the trigonal prismatic interfaces. On the other hand, in the parallel H–TaS_2

stacking (H–P) configuration, adjacent layers are identical but translationally offset[177]. This yields a configuration where the metals are aligned with sulfur ions across the trigonal prismatic interfaces[177]. We calculated the intercalation energy of all experimentally observed stacking configurations and the homotypic $1T-TaS_2$ interfaces using density functional theory (DFT). These calculations confirmed that intercalated H–AP interfaces are the most thermodynamically favorable, with the highest energy stabilization upon intercalation (Figure 5.1d). Moreover, DFT evinces that intercalation is generally less favorable for interfaces comprising $1T-TaS_2$ layers (Figure 5.1d). This suggests that intercalation destabilizes the $1T-TaS_2$ phase, explaining why bulk Fe-intercalated $1T-TaS_2$ is largely elusive[245]. This is congruent with our experimental observations; thermal annealing of $1T-TaS_2$ following chemical treatment yields a considerably larger optical contrast change compared to annealing in the absence of the Fe precursor (Figure 5.2). The observed optical contrast changes, which signify polytype transitions[183], indicate that Fe intercalation destabilizes $1T-TaS_2$ polytype, thus enhancing its conversion into the thermodynamically stable H–TaS_2 phase. Nevertheless, metastable configurations comprising both H–TaS_2 and $1T-TaS_2$ can be stabilized by annealing chemically treated crystals for short time durations and at lower temperatures of 250°C.

We supplement our atomic-resolution imaging with elemental composition analysis using electron energy loss spectroscopy (EELS) and STEM paired with energy dispersive X-ray spectroscopy (STEM-EDS). This elemental analysis is crucial as the intercalants could be tantalum (Ta) that has 'self-intercalated' upon heating[248] and not the desired Fe intercalants. EEL spectra show distinct features of Fe (Figure 5.1e), while STEM-EDS reveals a Fe-to-Ta ratio of 0.17(2) in this crystal. The presence of Fe is also evident in the Raman spectra of TH-Fe_xTaS_2, displaying a strong A_{1g} mode near 390 cm^{-1}, characteristic Fe_xTaS_2 with disordered intercalants[73] (Figure 5.1f,g). Furthermore, the Raman frequency of the A_{1g} mode supports that the lattice is electron-doped, as anticipated in the intercalation process[73]. Intriguingly, we also observe sharp Raman modes in the ultralow frequency (ULF) region, characteristic of the commensurate CDW phase (C-CDW) in $1T-TaS_2$ layers (Figure 5.1g). Notably, in unintercalated polytype heterostructures, the C-CDW phase exhibits enhancement compared to $1T-TaS_2$, with its ordering temperature increasing from below 180 K to above room temperature[62, 216]. However, the persistence of C-CDW enhancement in intercalated samples is surprising; intercalation typically eliminates C-CDW ordering due to structural and charge perturbations engendered by intercalants[11, 243–245]. Since our atomic-resolution imaging confirms that Fe is presented in the interfaces with $1T-TaS_2$ (Figure 5.1b,c), this raises the question if Fe and CDW structural domains segregate in the ab plane, with CDW being absent where Fe is present.

Coexistence of Fe and CDW superstructures

To investigate if Fe and CDW ordering can coexist, we prepared samples suitable for plan-view imaging ($\parallel$ c-axis), enabling us to examine structural inhomogeneities in the ab plane. We carried out selected area electron diffraction (SAED) and Raman spectroscopy measurements

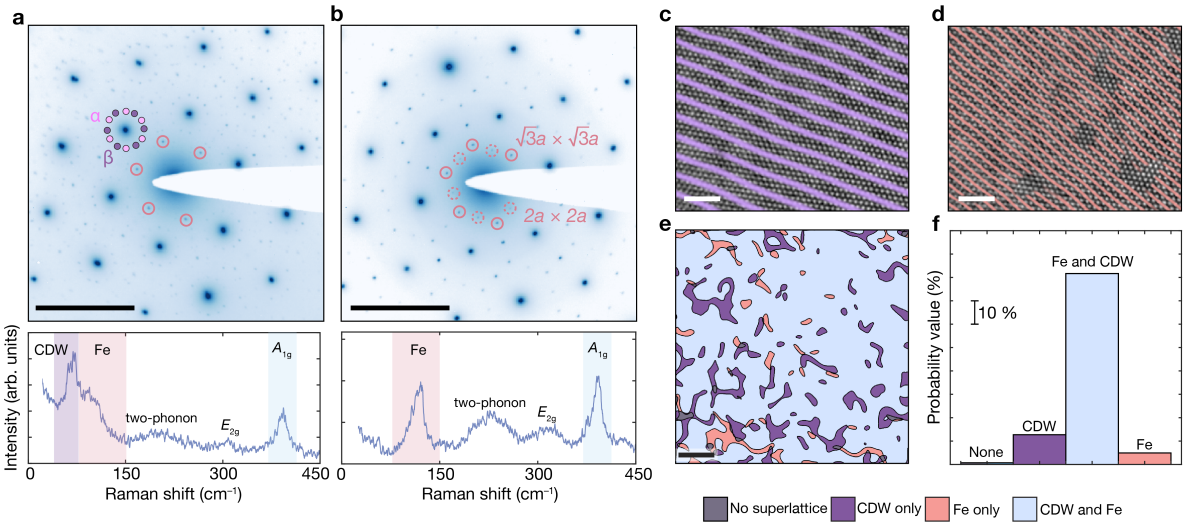


Figure 5.3: Coexistence of intercalant and CDW superlattice ordering in *TH*-Fe_xTaS_2 heterostructures. **(a,b)** Pairs of Raman spectra and SAED patterns of two *TH*-Fe_xTaS_2 heterostructures on electron-transparent Si_3N_4 TEM grids. For each sample, Raman spectra and SAED patterns were collected in nearly identical regions of the crystal. The first-order Fe superlattice and CDW superstructure reflections are marked in the SAED patterns. The strongly reflecting spots originate from the host lattice (*TH*-TaS_2). The spectral regions where phonon modes for different superlattices are expected[73, 96, 183] are highlighted. **(c,d)** Atomic-resolution plan-view ($\parallel$ *c*-axis) HAADF-STEM image of the heterostructure from (a) overlaid with the inverse FFT (iFFT) image generated from a CDW superlattice peak **(c)** and a Fe superlattice peak **(d)**. Scale bars (c,d): 2 nm. **(e)** Superlattice domain map of sample from (a) generated using FFT analysis. Scale bar: 5 nm. **(f)** Histogram of the domain map from (e).

in nearly identical regions (within 1 μm of each other) on an array of $1T-TaS_2$ crystals that underwent chemical treatment and were annealed at 250 °C for 1.5 hours. Our observations revealed two distinct types of crystals, and their representative structural analyses are depicted in Figure 5.3a,b. In the first group of crystals, SAED indicated the presence of C-CDW chiral mirror domains (α and β), consistent with the CDW structure of unintercalated polytype heterostructures (Figure 5.3a)[62, 183]. Additionally, faint $\sqrt{3} \times \sqrt{3}$ Fe superlattice patterns, indicative of clustering of disordered intercalants, were detected coeval with the CDW superstructures (Figure 5.3a). The Raman spectra of these samples mirrored the SAED results, displaying sharp C-CDW modes in the ultralow frequency (ULF) region and broad Fe-related modes (Figure 5.3a, bottom). Conversely, the second group of crystals exhibited only Fe-related superstructures in both SAED and Raman spectra (Figure 5.3b). In these crystals, the Fe-related Raman modes are more well-defined and blue-shifted, suggesting

higher Fe concentrations compared to crystals in the first group (Figure 5.3a,b). Overall, these findings suggest that higher Fe intercalation levels prompt a transformation of samples into H-Fe_xTaS_2, erasing the C-CDW phase hosted by the $1T-TaS_2$ layers. On the other hand, lower Fe concentrations allow for the coexistence of Fe and C-CDW ordering, albeit with generally inhomogeneous intercalants. We note that while SAED and Raman provide a micron-scale perspective of CDW and Fe ordering, pronounced segregation of phases may still occur on an atomic scale. To investigate this possibility further, we imaged crystals displaying CDW and Fe ordering in SAED with atomic-resolution HAADF-STEM imaging along the c-axis. Utilizing Fourier transform analysis, we observed that C-CDW and Fe superlattice fringes commonly coexist in these samples (Figure 5.3c,d). While breaks in periodicity, indicating disorder, were observed for both phases, these breaks were seemingly uncorrelated (Figure 5.3c–f). Moreover, the most prevalent domains host a coexistence of CDW and Fe ordering (Figure 5.3e,f). Although plan-view imaging does not capture out-of-plane disorder, combined with our cross-sectional imaging, these data support the idea that CDW and Fe domains can spatially coincide, offering opportunities for their magnetoelectronic interplay.

Effects of intercalation on long-range spin and charge ordering

To unveil how intercalation shapes spin and charge ordering in TH-Fe_xTaS_2 crystals, we conducted variable-temperature transport measurements on Fe-intercalated polytype heterostructures (Figure 5.4a). Three devices, D1–D3, were studied, with D1 serving as a reference polytype heterostructure without Fe. On the other hand, D2 and D3 are intercalated, as evidenced by their broad Fe-related Raman modes and blue-shifting of the A_{1g} mode compared to D1 (Figure 5.4b). However, these shifts are more pronounced in D3 (Figure 5.4b)[73] indicating it contains a higher Fe concentration compared to D2. Notably, all devices display CDW-related Raman modes (Figure 5.4b), and sharp resistance changes above 280 K that reflect CDW transitions from the low-resistance incommensurate (IC) phase to the high-resistance C-CDW phase[71, 183] (Figure 5.4c,d). However, the CDW transition temperatures decrease from D1–D3 (Figure 5.4c,d), correlating with increasing Fe amount. These data indicate that intercalation frustrates the CDW ordering, but does not eliminate this phase completely.

Having established the persistence of charge ordering in D1–D3, we now turn to examining if these devices exhibit long-range spin ordering (magnetism). To this end, we measure their magnetoresistance profiles (Figure 5.4e–g) at cryogenic temperatures. Magnetoresistance curves of D1 and D2 exhibit similar properties: nearly linear positive magnetoresistance and overlapping forward and backward field sweeps (Figure 5.4e,f), congruent with a lack of long-range magnetic order. Conversely, D3 exhibits hysteretic MR and anomalous Hall effect up to 30 K, confirming the presence of ferromagnetism (Figure 5.4g)[73]. Although the hysteretic profiles are broad for this device, pointing to intercalant disorder, the coercivities are still high, exceeding 1.5 T at 1.8 K (Figure 5.4g). We note that at cryogenic temperatures, the transport properties are dominated by the metallic $2H-TaS_2$ layers and CDW ordering cannot be electronically assessed concurrent with ferromagnetism.

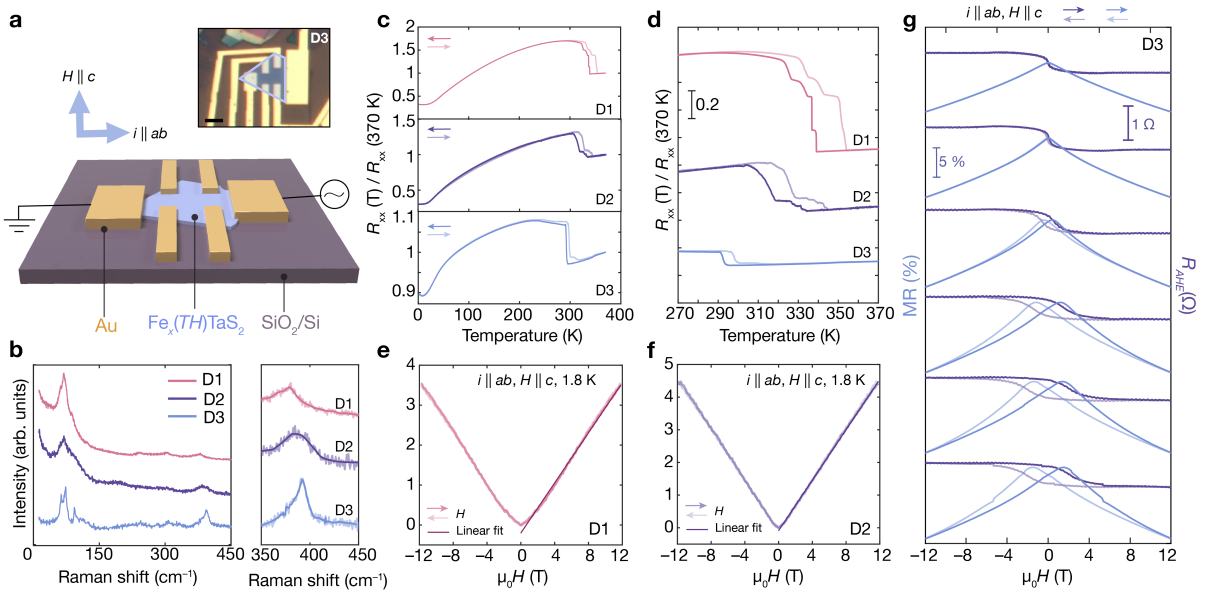


Figure 5.4: Electronic evidence of spin and charge ordering in *TH*-TaS_2 heterostructures. **(a)** Schematic of a *TH*-Fe_xTaS_2 device on SiO_2/Si. Inset: Optical micrograph of device D3. Scale bar: 2 μm. **(b)** Raman spectra of measured devices, labeled D1—D3. Device D1 is a polytype heterostructure (*TH*-TaS_2) without Fe, D2 is lightly intercalated with Fe/Ta ratio (x) of 0.02(1) from STEM-EDS, D3 evinces Raman features consistent with $0.04 < x < 0.2$. **(c)** Temperature-dependent normalized resistance ($R_{xx}(T)/R_{xx}(370K)$) for devices D1–D3. **(d)** High-temperature segment of (c). Curves are vertically shifted for clarity. **(e,f)** Magnetoresistance of D1 **(e)** and D2 **(f)** at 1.8 K. Linear fit to the data is shown. **(g)** Magnetoresistance (MR) and field-dependent anomalous Hall resistance (R_{AHE}) of device D3 as a function of temperature. Curves are vertically offset for clarity.

Coexistence of CDWs and magnetism

Subsequently, cryogenic Raman spectroscopy was used to probe CDW structure of D3 below its magnetic ordering transition. Two regions of D3 were investigated: the primary measurement channel (region R1) and an area near the sample edge (region R2). Representative data at 7.6 K are depicted in Figure 5.5a,b. Strong CDW-related modes are observed for both R1 and R2, confirming the coexistence of C-CDW ordering with ferromagnetism in these regions.

Notable differences are observed in the Fe-related and CDW-related modes of R1 and R2 (Figure 5.5b). The predominant Fe-related mode in R1 appears broader and redshifted compared to that in R2. This indicates stronger intercalant ordering in R2, which may be a result of a slightly higher Fe concentration in this region. Additionally, CDW-related modes of R1 are generally sharper compared to those of R2, indicative of stronger CDW disorder in R2[220]. Furthermore, the height difference between p_2 and p_3 is markedly different between

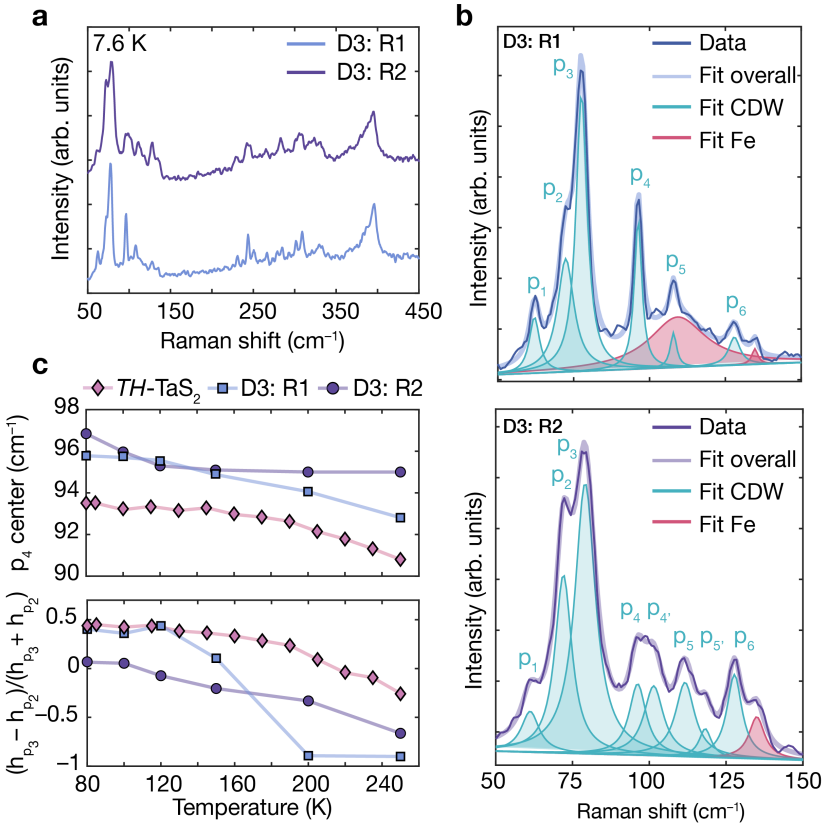


Figure 5.5: Optical measurements of the interplay between intercalant and CDW ordering. **(a)** Raman spectra at 7.6 K of device D3 in the main channel area (region R1) and near the edge of the device (region R2). **(b)** Low-frequency spectral region of (a) with Lorentzian peak fits and the cumulative fits displayed. Lorentzian fits for CDW-related modes and Fe-related mores are green and red, respectively. The CDW modes are marked with labels for easier comparison between R1 and R2. **(c)** Top: Temperature-dependent Raman frequency of the CDW-related mode p_4 in device regions D3: R1 and D3: R2, along with a unintercalated *TH*-TaS_2 heterostructure. Bottom: The corresponding temperature-dependent normalized height difference of CDW-related modes, p_2 and p_3. Peak positions and heights were determined from Lorentzian fits. Optical contrast measurements[183] reveal that the polytype heterostructure comprises five *H*-TaS_2 layers out of a total of 20 TaS_2 layers.

these regions, giving rise to distinct spectral profiles. Lastly, R2 evinces peak splitting of p_4 and p_5, giving rise to new blueshifted modes labeled p_4' and p_5'. The peak splitting in R2 suggests the presence of two distinct crystallographic environments, possibly due to intercalant clustering in this area, which is a phenomenon observed in other TMDs[155]. Taken together, these observations indicate that Fe and CDW ordering have an inverse relationship—ordering of one leads to disordering of the other.

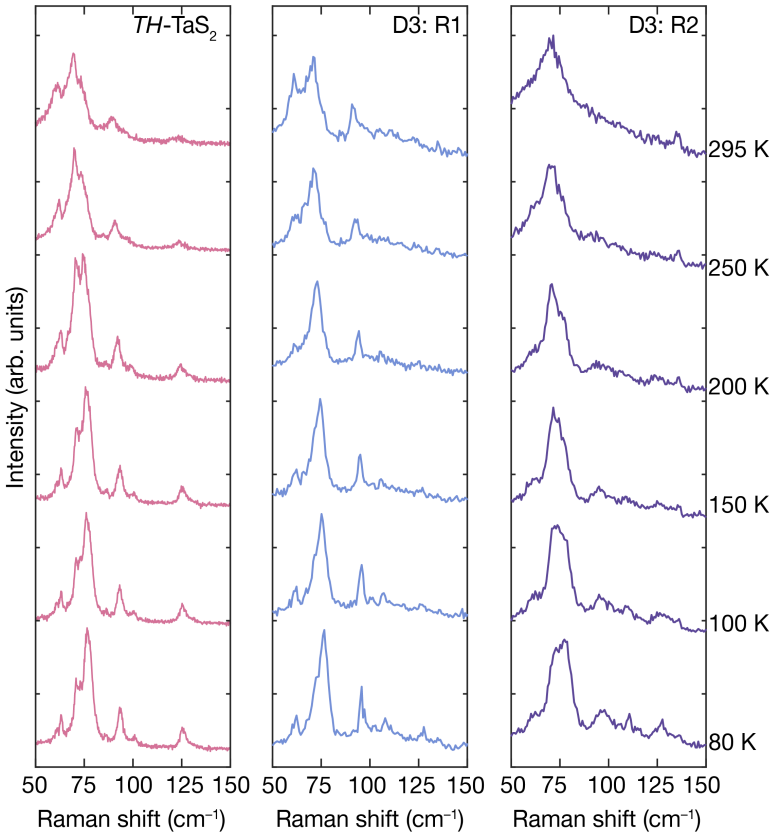


Figure 5.6: Temperature-dependent Raman spectra of D3:R1, D3: R2 and a unintercalated *TH*-TaS_2 heterostructure. Optical contrast measurements[183] indicate that the polytype heterostructure comprises 5 *H*-TaS_2 layers out of a total of 20 TaS_2 layers.

Next, we compare the Raman spectra of R1 and R2 to a reference heterostructure sample without Fe. Generally, spectral features of R1 align more closely with the reference compared to R2 (Figure 5.6, Figure 5.5c). For instance, the normalized height difference between modes p_3 and p_2 generally matches between R1 and the reference sample. Conversely, this measure in R2 corresponds more closely to the 200 K data for the reference, once again indicating a higher CDW disorder in R2. This notwithstanding, both R1 and R2 exhibit a general blueshift of CDW modes compared to the unintercalated heterostructure—a phenomenon typically attributed to bond stiffening due to the presence of intercalants[96, 249]. These data overall

corroborate that CDW and Fe domains can coexist and influence each other, with increased Fe ordering leading to an increase in CDW disorder. We note that intercalation-induced defects may be complex, and introduce CDW phase slips (introduction of discommensurations) or CDW amplitude changes[250]. These changes may engender asymmetry of CDW clusters[251, 252], irregularities in the C-CDW superlattice[251–253], metallic defects and narrow metallic domain walls[252].

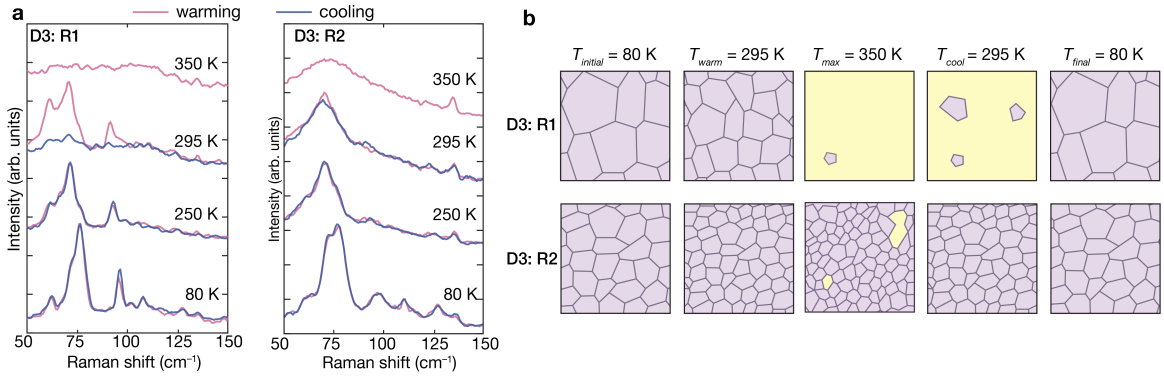


Figure 5.7: Effects of intercalant ordering on the thermal hysteresis of the CDW phase. **(a)** Raman spectra measured upon cooling from 350 K (blue) and warming from 7.6 K (red) for device D3 in regions R1 (main measurement channel) and R2 (edge of the device). **(b)** Cartoon illustration of the potential temperature-dependent domain evolution for D3: R1 and D3: R2. Black lines represent disordered CDW domains and domain walls. Violet and yellow regions represent C-CDW and IC-CDW domains, respectively.

Next, we examine the effects of Fe intercalants on the thermal hysteresis of CDWs by measuring Raman spectra upon cooling and warming for regions R1 and R2 of sample D3 (Figure 5.7a). While R1 shows a strong temperature hysteresis at 295 K, matching the transport data for D3, CDW modes of R2 do not exhibit thermal hysteresis and remain prominent even at 350 K. This suggests that temperatures above 350 K would be needed to melt the CDW domains. Such resistance to thermal perturbations could be manifested due to strong pinning by the ordered Fe intercalants[63, 250], which effectively act as defects preventing the evolution of CDW domains (Figure 5.7b). A proposed illustration CDW domain evolution for R1 and R2 is illustrated in Figure 5.7b. We hypothesize intercalants may pin CDW domains, leading to a metastable CDW configuration in R2, where the sample is trapped in its low-temperature phase up to 350 K. Again, these data indicate that Fe ordering is a strong tuning knob for CDW ordering and that crystal with complex charge and spin ordering can be realized using Fe intercalation of endotaxial heterostructures.

In light of the coexistence of C-CDW phases and magnetism, we seek to investigate whether their interplay may be harnessed for electronic manipulation of spin ordering. Given that CDWs are responsive to electric fields[208], we examine if electrical pulsing could induce changes in magnetism. To this end, we perform electrical pulsing measurements on sample D3,

applying 10 ms pulses with increasing amplitudes at distinct points in the magnetic hysteresis cycle (Figure 5.8). We observe that the magnetic history exerts a significant influence on the resistance changes, with these changes generally following the direction of the hysteresis loop. These findings suggest that electrical pulses induce changes in spin ordering. However, further investigation is necessary to delineate the origin of this effect and the role of CDWs in this phenomenon.

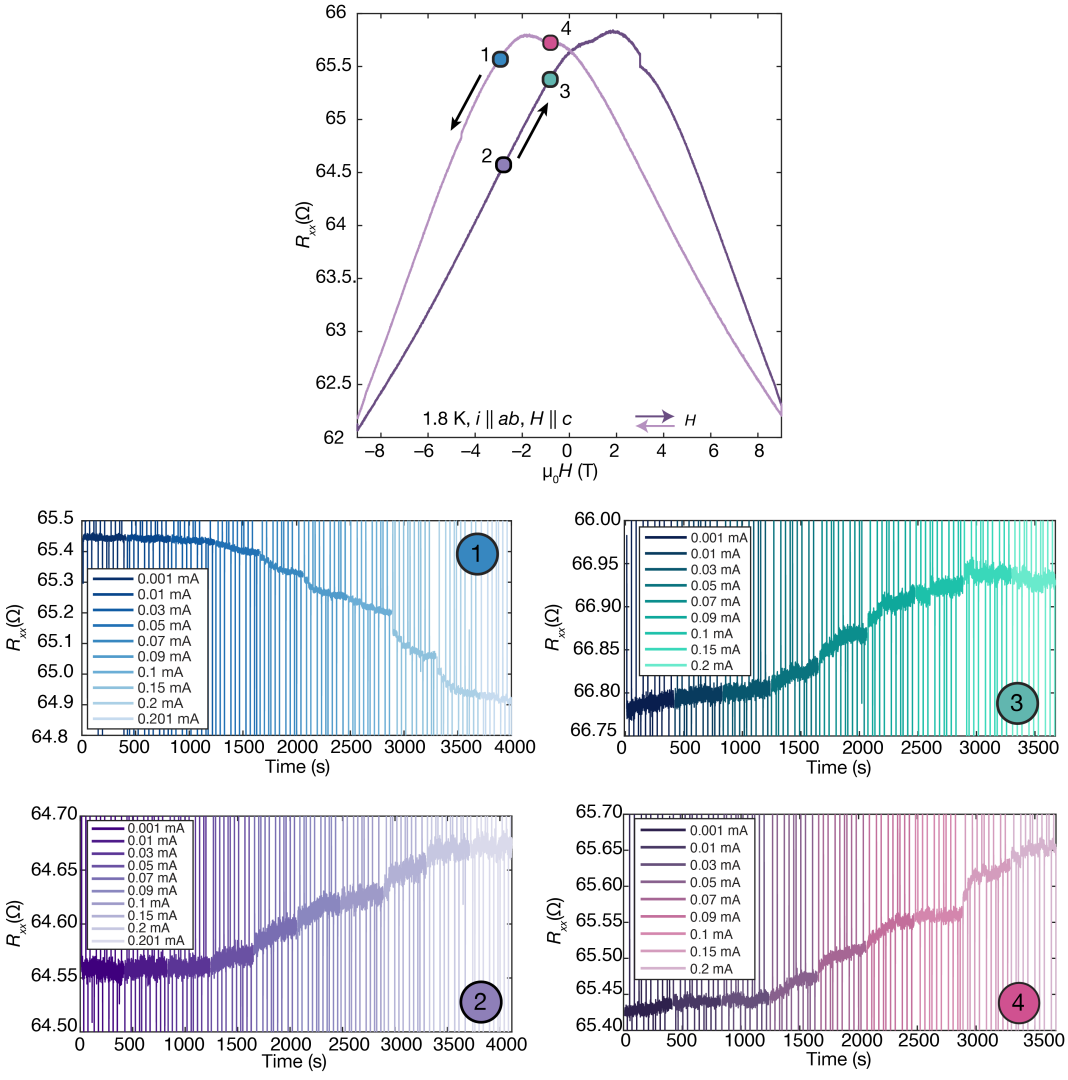


Figure 5.8: Switching of magnetic states in device D3 with 10 ms electrical pulses. Change in the resistance R_{xx} of D3 upon applying 10 ms pulses with increasingly larger amplitudes at four distinct sports in the magnetic hysteresis cycle. For each pulse amplitude, 10 triggers were applied with 20 seconds between consecutive triggers. Data was collected at 1.8 K with $H \parallel c$.

5.3 Conclusion

In this work, we demonstrate the synthesis of Fe-intercalated polytype heterostructures of TaS_2 where structural CDW and Fe domains coexist. Consequently, the intercalation process simultaneously adjusts the spin ordering (magnetism) and charge ordering (CDWs) in this system. Generally, as the amount of Fe intercalant increases, there is a decrease in CDW ordering, leading to a reduction in the CDW transition temperature. Surprisingly, however, the C-CDW phase remains robust up to room temperature, even in the presence of a high amount of Fe that induces magnetism.

Additionally, we discover that Fe ordering can pin CDW domains in crystals with nominally higher CDW disorder, creating a metastable "trapped" CDW state. This state allows the crystals to maintain their low-temperature phase even at temperatures exceeding 350 K, where CDW domains in ordered crystals typically melt. Lastly, we find that ferromagnetism and C-CDW phases may coexist at low temperatures, opening doors to study and exploit the interplay between these quantum phases.

5.4 Methods Chapter 5

This section generally combines the methodology detailed in Chapters 2, 3, and 4. Thus, herein, we will detail only the methods that are unique to this chapter.

Cryogenic Raman spectroscopy

Cryogenic Raman spectroscopy of unintercalated samples

Temeprature-dependent Raman spectroscopy (Horiba Multiline LabRam Evolution) was conducted in an optical cryostat (Cryo Industries of America) using 633 nm continuous wave laser with an ultra-low frequency filter. Spectra were typically collected with 50–80 μW power and an 1800 gr/mm grating, with 20-second acquisition times and 2-4 accumulations. The laser beam was focused on the sample into a spot size of approximately 1 μm.

Cryogenice Raman measurements of sample D3

Raman measurements were carried out with a 532 nm diode-pumped solid-state laser (Coherent^{TM} Sapphire SF NX) as the excitation source. A Volume Bragg grating (VBG) based BragGrate^{TM} Bandpass filter is used in reflecting geometry to clean up the laser line. The laser is focused (<1 μm dia) onto the sample loaded on the Agile Temperature Sample mount (ATSM) in Montana Cryostation s200 with a 100x objective (NA=0.9). The Raman signal is collected in backscattering geometry and dispersed with Andor^{TM} Kymera 328i spectrometer using 1800l/mm grating that enables a resolution of $\sim$0.72 cm^{-1} at 532 nm on the detector (TE-cooled Andor^{TM} Newton DU970P EMCCD). To attenuate the Rayleigh

scattered laser line, three VBG-based BragGrate^{TM} notch filters each with an OD > 3 and a spectral bandwidth < 5 cm^{-1} are aligned in series in the output beam path before the spectrometer. The excitation power on the sample was kept below 100μW to avoid any heating effects.

We note that while reference samples and D3 were measured using different lasers, there are no expected Raman shifts in the discussed modes as a consequence of the laser difference[254].

Pulsing experiments

Electrical pulses were applied using a Keithley 6221 current source.

Density Functional Theory (DFT) calculations

We performed Density Functional Theory (DFT) calculations within the Vienna Ab Initio Simulation Package (VASP). We used projector augmented wave (PAW) pseudopotentials containing valences of $3d^6 4s^2$, $5p^6 5d^3 6s^2$ and $3s^2 3p^4$ for Fe, Ta, and S respectively. All DFT calculations were performed at the GGA+U level using the PBEsol functional and a Liechtenstein-type on-site Hubbard correction on the iron d-orbitals with U=4.0 and J=0.7. All calculations were performed using 14x14x2 and 7x7x2 Γ-centered k-point grid for a Ta_2S_4 and Ta_8S_{16} slabs respectively, an energy cutoff of 600 meV, and vacuum height of 21 Å. Lattice constants were either optimized to force tolerance of 0.1 meV/Å for the slab unit cell at constant volume or taken to exactly match the experiment. Experimental geometries for T and HT layers correspond to extracting bilayer interfaces from the referenced bulk 1T and 6R structures without modification to form slab structures with a 21 Å vacuum. All calculations used first-order Methfessel-Paxton with $\sigma = 0.2$ eV with a negligible entropy contribution. SOC was excluded.

Chapter 6

Local interface effects direct global charge ordering in a van der Waals heterostructure

Contributing authors: Husremović, S.; McGraw, V.; Dandu M.; Xie L.; Ryu, S. H.; Jozwiak, C.; Bostwick, A.; Rotenberg, E.; Taniguchi, T.; Watanabe, K.; Raja A.; Inzani K.; Bediako, D. K.

Author contributions: S.H and V.M contributed equally to this work. S.H., V.M. and D.K.B conceived the study. S.H. and V.M. fabricated the samples. S.H., L.X., J.C., B.A., and R.E. performed the ARPES measurements. S.H. conducted the TEM studies. V.M. and M.D carried out the optical measurements. K.I. carried out the DFT computations. T.T. and K.W. provided the hBN crystals.

6.1 Introduction

Charge density waves (CDWs) are correlated electronic systems that exhibit periodic lattice distortions, which template modulations in charge density.[45] This intrinsic charge ordering strongly influences the measured resistance, rendering CDW phase transitions promising for information storage and processing applications. $1T-TaS_2$, a layered van der Waals (vdW) crystal, has garnered significant attention for next-generation electronics due to its high-temperature CDW phase transitions accompanied by sharp resistance changes. Below $\sim$ 500 K[61–63], intralayer CDW distortion clusters form in $1T-TaS_2$, leading to metal-to-insulator phase transitions as the in-plane tiling of clusters evolves with temperature [71, 183, 205, 255]. The metallic incommensurate CDW (IC-CDW) phase, observed between 500 K and 350 K, exhibits sparse and irregular cluster arrangements. In contrast, the NC-CDW phase, typically seen between 350 K and 180 K, is marked by the formation of cluster domains separated by metallic discommensuration networks[60, 71, 204, 255–257]. Below $\sim$ 180 K,

the discommensuration networks disappear, resulting in the insulating commensurate phase (C-CDW) with a $\sqrt{13}a \times \sqrt{13}a$ periodicity, where a is the in-plane parameter constant of $1\,T-TaS_2$ [183, 255].

While $1\,T-TaS_2$ is typified by in-plane lattice distortions, the out-of-plane stacking of CDW clusters changes across the CDW phases and strongly influences the electronic properties[64, 68–72, 258]. As follows, modulating interlayer interactions of $1\,T-TaS_2$ by incorporating it into heterostructures is a compelling means of fine-tuning its properties[259]. Recent studies have demonstrated the potential of this approach by stabilizing a robust, room-temperature C-CDW phase in polytype heterostructures of $1\,T-TaS_2$ and H-TaS_2 grown using moderate thermal annealing of $1\,T-TaS_2$ [62, 183, 216]. However, the use of vdW assembly to integrate $1\,T-TaS_2$ and other layered CDW crystals into heterostructures remains largely unexplored[213, 260, 261] despite its theoretical promise[262, 263] and the structural tunability that this approach offers.

In vdW assembly, dissimilar crystals can be stacked without commensuration restrictions, enabling unprecedented control over interfacial hybridization and charge transfer characteristics—both playing a defining role in CDW phases[264, 265]. Moreover, compared to traditional methods for controlling these properties, such as atomic/ionic doping[212, 266–268], vdW assembly introduces fewer atomic defects and inhomogeneities into the system[269, 270]. Additionally, the characteristics of vdW heterostructures are modulated by the presence of interfacial moiré patterns, formed when vertically stacked vdW crystals display azimuthal misorientation (twist) and/or differences in lattice constants [177, 271]. At small twist angles and lattice mismatch values, the lattice reconstructs to minimize the area of high-energy stacking domains, which reduces the interlayer staking energy but introduces strain. This intrinsic moiré strain was remarkably shown to template the CDW domains in $1\,T$-$TiTe_2$/$1\,T$-$TiSe_2$[272]. Engineering intrinsic moiré strain could be a powerful tuning knob for $1\,T-TaS_2$, due to its responsiveness to extrinsic strain[261, 273, 274]. Nevertheless, research on $1\,T-TaS_2$ heterostructures remains limited[213, 260], with the absence of twist-dependent measurements hindering the understanding of how charge transfer, strain, and hybridization contribute to ensemble CDW properties.

In this work, we investigate the optical and electronic properties of heterostructures comprising vertically stacked nano-thick crystals of $1\,T-TaS_2$ and monolayer $1H-WSe_2$. By systematically varying the thickness of $1\,T-TaS_2$ and its azimuthal misalignment with $1H-WSe_2$, we elucidate that intrinsic moiré strain and interfacial charge transfer encode the global CDW ordering in few-layer $1\,T-TaS_2$. Specifically, local charge transfer, which is independent of the twist angle, induces increased CDW disorder and lowers the IC-CDW—NC-CDW transition temperature. This trend notwithstanding, we consistently measure a more pronounced CDW suppression for heterostructures with small interlayer twist angles. We attribute this effect to moiré strain, evident in our transmission electron microscopy (TEM) studies and Raman measurements of $1H-WSe_2$. Our study additionally extends to the optoelectronic characteristics of $1H-WSe_2$, where we find that the exciton binding energy and exciton dissociation dynamics are affected by the interlayer twist angle. This indicates that heterostructuring offers a means to concurrently engineer electronic phases in

both $1T-TaS_2$ and $1H-WSe_2$ through targeted adjustments of local interfacial interactions. As follows, this work paves a path toward deterministic engineering of electronic and optical phases in heterostructures integrating CDW materials and semiconductors.

6.2 Results and Discussion

Electronic properties of $1T-TaS_2/1H-WSe_2$ heterostructures

We fabricate mesoscopic devices from vertical heterostructures comprised of nanometer-thick $1T-TaS_2$ and monolayer $1H-WSe_2$, which are encapsulated with hexagonal boron nitride (hBN) to prevent sample degradation and ensure pristine interfaces (Figure 6.1a). Each $1T-TaS_2$ crystal is partially covered with $1H-WSe_2$, enabling the creation of two distinct regions within each device: hBN/TaS_2/hBN (region R1) and hBN/WSe_2/TaS_2/hBN (region R2), as illustrated in Figure 6.1a. This device geometry allows us to directly probe the electronic influence of $1H-WSe_2$ on $1T-TaS_2$ by comparing the transport properties of R1 and R2. We fabricated devices for electron transport consisting of 6-, 8-, 15-, and 26-layer $1T-TaS_2$, designated as D1–D4, and subsequently measured their temperature-dependent longitudinal resistance (R_{xx}). Each device displays transport features indicative of the transition from the metallic IC-CDW phase to the more insulating NC-CDW phase, including sharp resistance changes and a pronounced hysteresis in the cooling and warming profiles (Figure 6.1b,c).

Our measurements reveal that the CDW phase transitions above room temperature are substantially influenced by the presence of $1H-WSe_2$ (Figure 6.1c). For the thinner devices, D1 and D2, the CDW ordering temperature is consistently higher for R1 ($1T-TaS_2$ region) compared to R2 ($1T-TaS_2/1H-WSe_2$ region), as seen in Figure 6.1c–d. This trend, observed across cooling and warming sweeps, indicates that interactions with $1H-WSe_2$ enhance CDW disorder in $1T-TaS_2$ and destabilize the more ordered NC-CDW phase[209, 266]. On the other hand, for thicker devices (D3 and D4), a measurable difference between R1 and R2 is only observed upon warming, with R2 exhibiting a lower NC-CDW—IC-CDW ordering temperature (Figure 6.1c,d). This corroborates that interactions with $1H-WSe_2$ introduce CDW disorder, whose pinning effect is seemingly dependent of the CDW phase [183, 208, 210, 220, 227]. Namely, CDW defects may introduce stronger pinning on the NC-CDW state with localized domains compared to the "melted" IC-CDW phase, engendering a stronger CDW suppression upon warming[183]. As a general observation, the CDW ordering temperature is increasingly affected with decreasing sample thickness, supporting that local interface effects are driving the observed ensemble changes. Additionally, the presence of CDW modulation for D2, which exhibits a large twist angle between $1T-TaS_2$ and $1H-WSe_2$, suggests that at least one factor contributing to the CDW disorder is independent of the twist angle. Origin of the CDW disorder in the $1T-TaS_2/1H-WSe_2$ will be discussed in detail later.

While electron transport measurements demonstrate a clear CDW modulation in the high-temperature range, questions remain regarding the low-temperature electronic characteristics

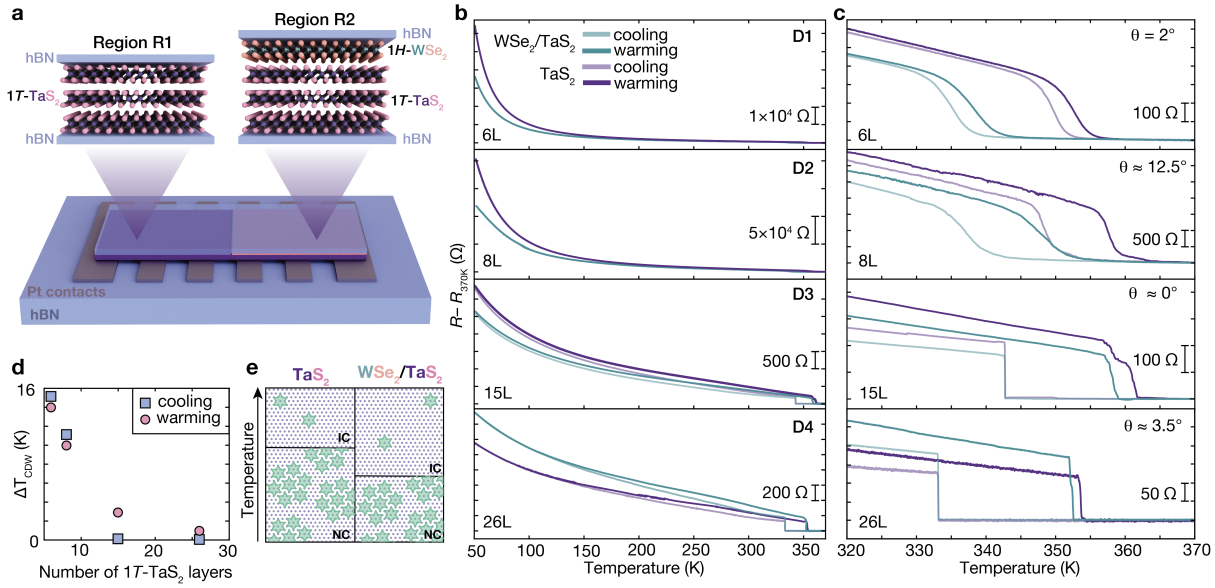


Figure 6.1: Electronic measurements of CDW phase transitions in $1H-WSe_2/1T-TaS_2$ heterostructures. **(a)** Schematic of $1H-WSe_2/1T-TaS_2$ heterostructure device for electron transport measurements. Each $1T-TaS_2$ crystal is fully encapsulated in hBN and partially covered with monolayer $1H-WSe_2$, yielding a $1T-TaS_2$–only region (region R1) and a $1T-TaS_2/1H-WSe_2$ region (region R2). Electrical contact with the $1T-TaS_2$ crystal is made using prepatterned Pt contacts fabricated on hBN. **(b)** Temperature-dependent longitudinal resistance (R_{xx}) of devices fabricated according to (a) containing 6-, 8-, 15-, and 26-layer $1T-TaS_2$. These devices are labeled D1–D4, respectively. The twist angle (θ) between $1T-TaS_2$ and $1H-WSe_2$ is marked for each device. For D1, θ is derived from TEM, while for D2–D4, θ is inferred from the edge alignment of $1T-TaS_2$ and $1H-WSe_2$ in optical micrographs. **(c)** High-temperature (320–370 K) section of (b). **(d)** Relationship between ΔT_{CDW} and the number of $1T-TaS_2$ layers, where ΔT_{CDW} is defined as the difference in the CDW ordering temperatures for R1 and R2 in the 330 K – 360 K range. The CDW ordering temperatures were calculated from the resistance inflections upon cooling and warming for devices D1–D4. **(d)** Schematic illustrating that few-layer $1T-TaS_2/1H-WSe_2$ heterostructures display a lower NCCDW–ICCDW transition temperature compared to $1T-TaS_2$.

of $1T-TaS_2$ and its heterostructures with $1H-WSe_2$. Across all devices, we observed a significant rise in resistance below 150 K, indicating the onset of C-CDW ordering (Figure 6.1b)[208, 209, 211]. However, our measurements were limited to temperatures above 50 K due to the high resistance exhibited by the samples below this threshold. Additionally, the absence of hysteresis features in the low-temperature range has impeded our ability to compare the electronic properties of R1 and R2 (Figure 6.1b). To address these open questions, we prepared samples for nano angle-resolved photoemission spectroscopy (nanoARPES) measurements. The submicron beam diameter in nanoARPES facilitated an independent assessment of the electronic band structure for sample regions R1 (hBN/$1T-TaS_2$/hBN section) and R2 (hBN/$1H-WSe_2$/$1T-TaS_2$/hBN section).

Figure 2 displays the ARPES band dispersion along the Γ–M direction for R1 (Figure 6.2a) and R2 (Figure 6.2b). For R1, the electronic bands evince clear features of the strong electronic reconstruction in the presence of the $\sqrt{13}a \times \sqrt{13}a$ CDW superlattice: flat band centered at Γ and opening of pseudogaps for the occupied band near E_{valence}[52, 69, 275, 276]. This is consistent with our band structure calculations (Figure 6.2a), and previous studies of bulk $1T-TaS_2$ crystals[52, 69, 275, 276]. The band structure of R2 is qualitatively similar to that of R1 but with increased blurriness (Figure 6.2b). Since nanoARPES is highly surface sensitive, we posit this is due to the attenuation of the signal from $1T-TaS_2$ due to the overlaying $1H-WSe_2$. For a more quantitative comparison of R1 and R2, we examine their respective momentum distribution curves (MDCs) centered at $E = E_{\text{valence}} - 0.2$ eV, summing over a 0.2 eV energy range. The MDCs of R1 and R2 exhibit similar features, with some differences in the dispersion of bands centered at Γ. While some of these differences may arise from the aforementioned signal attenuation, they are also consistent with modulations in the chemical potential or CDW commensuration between R1 and R2. Consequently, these data suggest that interfacing $1T-TaS_2$ with $1H-WSe_2$ may introduce electronic ramifications to the band structure of $1T-TaS_2$.

Effects of charge transfer and moiré strain on the CDW suppression

To shed light on the mechanism driving CDW suppression in $1T-TaS_2/1H-WSe_2$ heterostructures, we utilize Raman spectroscopy. Raman spectra reflect the CDW domain structure through distinct Raman-active modes linked to vibrations of the CDW lattice[220, 221, 226, 254, 277]. Thus, changes in CDW ordering are typically evinced by modifications in the energy, broadness, and intensity of CDW-related Raman modes[220]. First, we investigate the Raman modes of three nearly aligned $1T-TaS_2/1H-WSe_2$ samples fabricated from 3-, 6-, and 40-layer $1T-TaS_2$ partially covered with monolayer $1H-WSe_2$ (Figure 6.3a). These samples, labeled S1–S3, display noticeable differences in their temperature-dependent Raman spectra. Whereas the CDW modes of S3 appeared unaffected by the presence of $1H-WSe_2$, the Raman spectra of S1 and S2 are significantly altered in contact with $1H-WSe_2$ (Figure 6.3a). Specifically, for S1–S2, CDW-related Raman modes in the heterostructure regions consistently exhibit broadening and attenuation compared to the $1T-TaS_2$ regions (Figure 6.3a). Additionally, a significant redshift of up to 2 cm^{-1} is observed for heterostructures

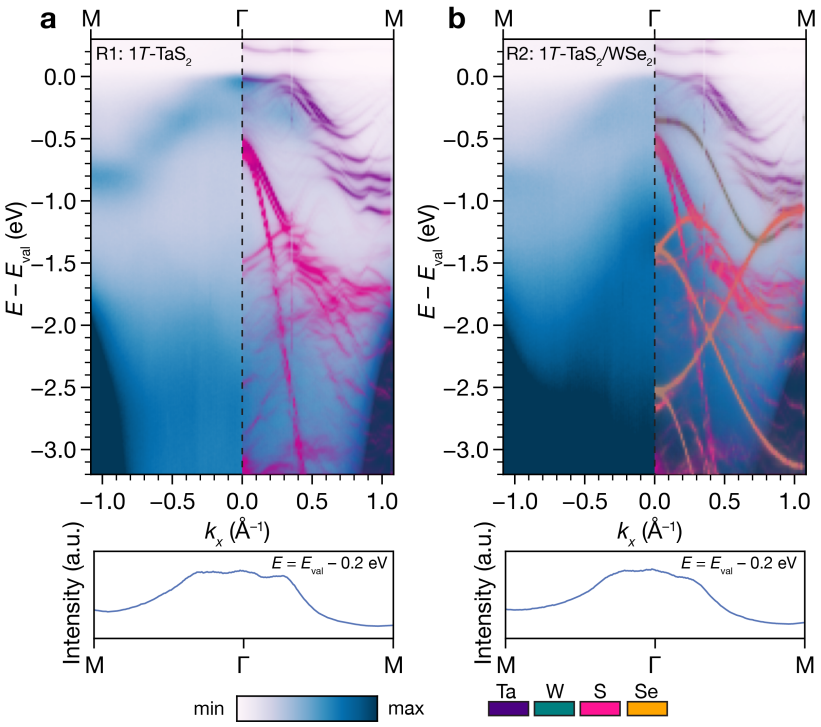


Figure 6.2: Electronic band structure of $1T-TaS_2$ and its heterinterface with $1H-WSe_2$. **(a,b)** ARPES band dispersions along the Γ–M direction (top) and their corresponding momentum distribution curves (MDCs) for regions R1 **(a)** and R2 **(b)**. These regions consist of (from top to bottom): R1 (monolayer hBN/monolayer WSe_2/9-layer $1T-TaS_2$/$\sim$ 10 nm hBN) and R2 (monolayer hBN/monolayer WSe_2/9-layer $1T-TaS_2$/$\sim$ 10 nm hBN). The calculated bands for $1T-TaS_2$ and $1T-TaS_2/1H-WSe_2$, respectively, are overlaid with the experimental data in panels (a) and (b). Sample was prepared on Si, and the twist angle between $1T-TaS_2$ and $1H-WSe_2$ was estimated to be $\approx 2°$ from the edge alignment of flakes in optical images. Data in (a–b) was obtained at 20 K with $h\nu = 97.8$ eV and linear horizontal (LH) polarization. The MDCs shown at the bottom of (a,b) are centered at $E = E_{\text{valence}} - 0.2$ eV and integrated over a 0.2 eV range.

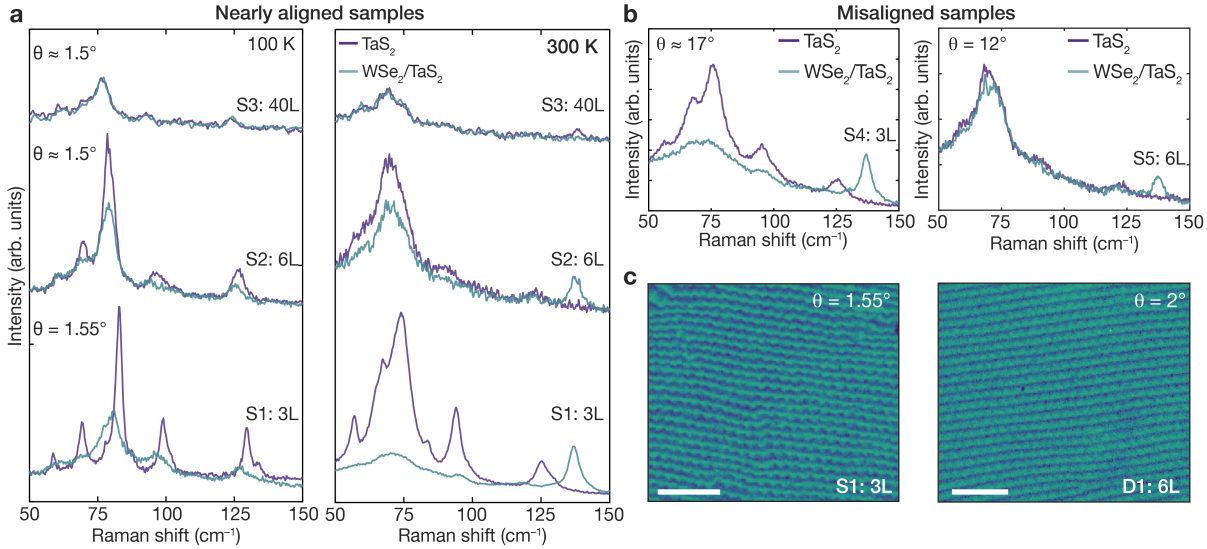


Figure 6.3: Thickness and twist dependence of CDW ordering in $1T-TaS_2/1H-WSe_2$ heterostructures. **(a)** Raman spectra measured at 100 K (left) and 300 K (right) for azimuthally nearly aligned $1T-TaS_2/1H-WSe_2$ heterostructures consisting of 3, 6, and 40 layers (S1–S3). **(b)** Raman spectra obtained at 300 K for azimuthally misaligned $1T-TaS_2/1H-WSe_2$ heterostructures (S4 and S5) with three and six layers of $1T-TaS_2$, respectively. For S1–S5, $1T-TaS_2$ flakes are partially interfaced with monolayer $1H-WSe_2$ and encapsulated with hBN. Presented spectra are not normalized, and interlayer twist (θ) is indicated for each sample. For S1 and S5, θ is determined from TEM diffraction, while for S2–S4, θ is determined from the alignment of flake edges in optical images. **(c)** Dark-field transmission electron microscopy (TEM) images of nearly aligned samples S1 and D1. Micrographs in (c) were constructed from the closest first-order peaks of $1T-TaS_2$ and $1H-WSe_2$. Scale bars: 50 nm.

at 100 K, with the greatest redshifting measured for the thinnest (S1) sample (Figure 6.3a, left). These observations align with our transport measurements: consistently stronger CDW suppression was manifested by thinner samples. Having established that CDW suppression persists from 100 K to 300 K in nearly aligned heterostructures S1 and S2, we investigated azimuthally misaligned heterostructures S4 and S5, comprising 3- and 6-layer $1T-TaS_2$, respectively. In general, while the intensity attenuation and broadening of modes persisted in misaligned heterostructures, this effect was consistently more pronounced in nearly aligned heterostructures with the same number of layers (Figure 6.3a,b, Figure 6.4, Figure 6.5). This indicates a twist-dependent aspect of CDW suppression, possibly stemming from the evolution of charge transfer, hybridization, or moiré strain due to varying interlayer alignment.

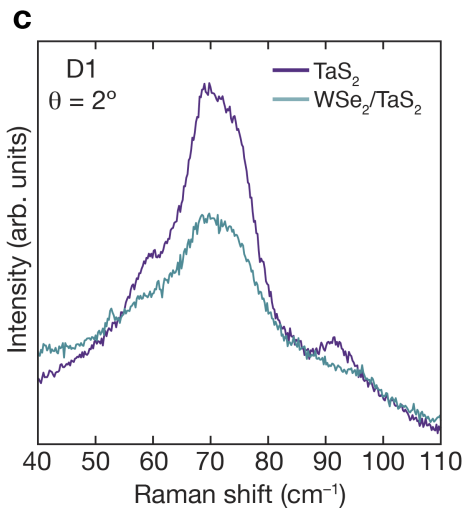


Figure 6.4: Raman spectra of device D1. Raman spectra were measured for two distinct regions of device D1 fabricated from an nearly aligned heterostructure of 6-layer $1T-TaS_2$ and monolayer $1H-WSe_2$. Azimuthal alignment, derived from TEM diffraction, is denoted.

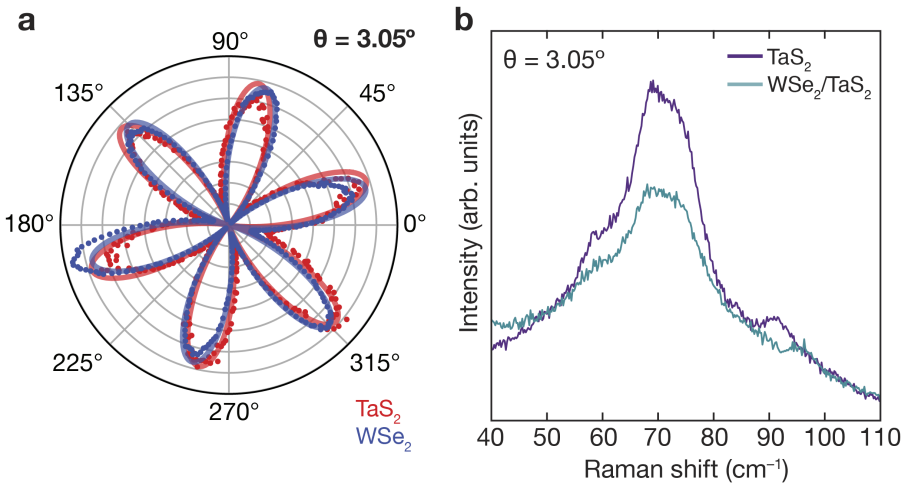


Figure 6.5: CDW suppression in an nearly aligned heterostructure of 5-layer $1T-TaS_2$ interfaced with $1H-WSe_2$. **(a)** Second-harmonic generation (SHG) measurement of the azimuthal alignment between $1T-TaS_2$ and $1H-WSe_2$. **(b)** Raman spectra measured for the heterostructure and the $1T-TaS_2$-only regions.

First, we investigate whether moiré strain could account for the increased CDW disorder in nearly aligned samples by examining the lattice reconstruction of D1 and S1 using dark-field TEM (Figure 6.3c). The dark-field micrographs reveal intensity variations that are indicative of reconstructed lattice domains (Figure 6.3c)[177, 271, 278, 279]. In contrast, moiré reconstruction is not expected in misaligned samples with large twist angles. Therefore, our TEM findings support the notion that moiré reconstruction and the accompanying strain are plausible explanations for the twist-dependent properties. We note that the small lattice mismatch of 2% between $1T-TaS_2$ and $1H-WSe_2$ enables the observation of lattice reconstruction, primarily driven by lattice dilations in heterobilayers[177]. Lattice dilations, defined as volumetric strain, are local changes in volume compared to a rigid moiré. They are manifested as periodic stretching and expansion of layers, creating high-energy and low-energy regions, corresponding to higher and lower effective lattice mismatches, respectively [177]. Consequently, as lattice reconstructions can amplify strain within the system, they potentially influence the ordering of CDWs [272].

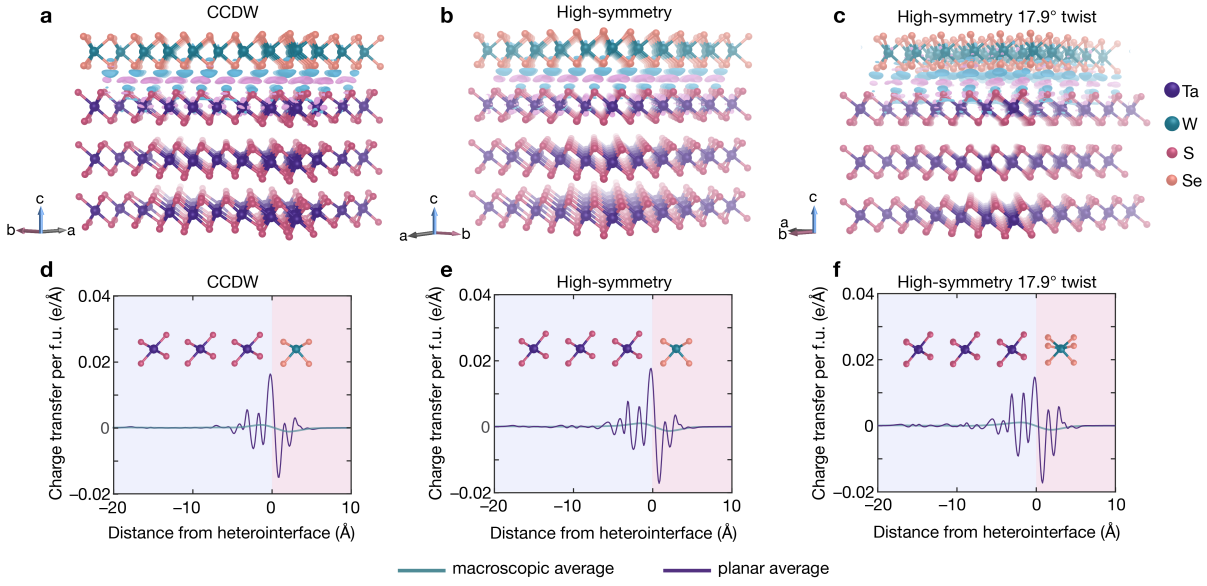


Figure 6.6: Local charge transfer characteristics across CDW phases and twist angles. Charge transfer (top) and the corresponding planar and macroscopic averages (bottom) for 3-layer $1T-TaS_2$ interfaced with monolayer $1H-WSe_2$ for: an azimuthally nearly aligned heterostructure in the C-CDW phase **(a)**, azimuthally nearly aligned heterostructure in the high-symmetry metallic phase **(b)** and a twisted interface with 17.9° misalignment between the high-symmetry $1T-TaS_2$ and $1H-WSe_2$ layers **(c)**. The pink and blue regions in the charge transfer plots (top) represent charge accumulation and depletion, respectively. Isosurface cutoff was set to 0.0003 eV for (a,b) and 0.0004 eV for (c).

Next, we explore whether the observed CDW suppression trends could be alternatively

explained by variations in charge transfer as a function of interlayer alignment. To this end, we carried out density functional theory to calculate the charge transfer characteristics of heterostructures composed of three layers of $1T-TaS_2$ and monolayer $1H-WSe_2$. Three cases were investigated: (1) C-CDW in $1T-TaS_2$ layers (Figure 6.6a), (2) high-symmetry $1T-TaS_2$ with no charge density wave (Figure 6.6b), and (3) a twisted interface with 17.9° between high-symmetry $1T-TaS_2$ and $1H-WSe_2$ layers (Figure 6.6c). Across all examined configurations, the calculated charge transfer characteristics are very similar (Figure 6.6a–c). Specifically, only the singular $1T-TaS_2$ layer directly interfaced with $1H-WSe_2$ is electron-doped, while $1H-WSe_2$ is hole-doped. The calculated charge transfer is congruent with the band alignment expected for $1T-TaS_2$ and $1H-WSe_2$. Moreover, the ionicity of the layers participating in charge transfer increases; electron density decreases for bonds and increases at the ionic sites (Figure 6.6a–c). These ionicity changes may engender modulations of the electron–phonon coupling[280], thereby frustrating the CDW ordering.

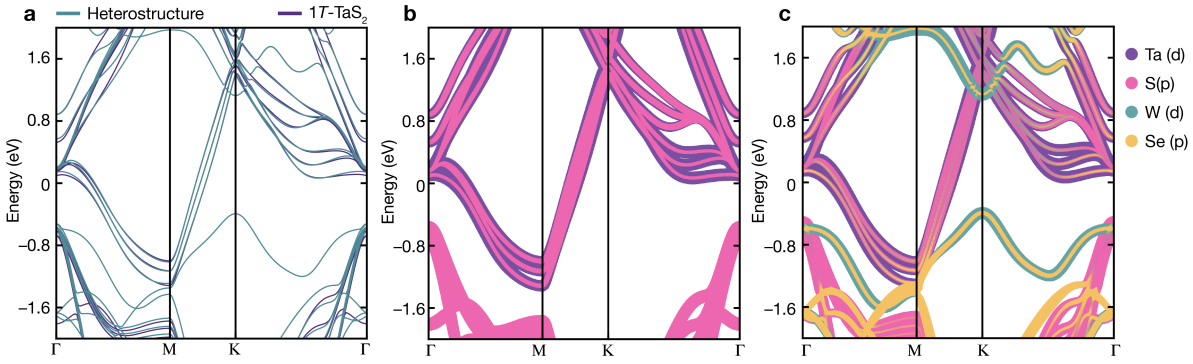


Figure 6.7: Band structure calculations of the high-symmetry nearly aligned heterostructure and standalone $1T-TaS_2$. **(a)** Overlaid band structures of the high-symmetry 3-layer $1T-TaS_2$ and its heterostructure with monolayer $1H-WSe_2$. **(b,c)** Orbital-projected band structures of standalone high-symmetry 3-layer $1T-TaS_2$ **(b)** and its heterostructure with monolayer $1H-WSe_2$ **(c)**.

Given that charge transfer does not significantly change with twist angle and CDW phase, we propose that charge modulation at the interface with $1H-WSe_2$ is responsible for the general trend of suppression observed across nearly aligned and misaligned heterostructures. Notably, this charge transfer is confined to a singular $1T-TaS_2$ layer yet impacts the ensemble ordering of the entire sample. This discovery underscores the significant role of interlayer interactions in $1T-TaS_2$. Our calculations also reveal minimal effects of hybridization even in nearly aligned heterostructures, where hybridization effects should be the most evident (Figure 6.7). Thus, combining theory and experimental data, we propose that charge transfer contributes to an overarching trend of increased CDW disorder in $1T-TaS_2/1H-WSe_2$ heterostructures, while moiré strain amplifies this suppression in nearly aligned samples .

Effects of heterostructuring on the optical properties of $1H-WSe_2$

To further examine the role of moiré-induced strain, we inspect the phonon modes of $1H-WSe_2$ in the azimuthally nearly aligned (S2) and misaligned (S5) samples, whose CDW-related Raman modes were displayed in Figure 6.3a,b. For S5, the Raman modes of $1H-WSe_2$ exhibit minimal changes in the standalone region versus the heterostructure. In contrast, strong modifications of $1H-WSe_2$ Raman modes are observed for the azimuthally nearly aligned sample, S2, in contact with $1T-TaS_2$. Specifically, in the heterostructure region, the Raman mode at 250 cm^{-1}, comprising of degenerate E'/A_1'[281, 282], is strongly suppressed, while phonon modes above 250 cm^{-1}, encompassing the out-of-plane $2LA(M)$, A_2'', and $A_1'(M)$[281, 282] are red-shifted and broadened. These trends in twist-dependent Raman modes of $1H-WSe_2$ are consistent across few-layer heterostructures (Figure 6.9). We note that in-plane E modes are typically strongly affected by external and intrinsic moiré strain in transition metal dichalcogenides (TMDs)[283–286]. In contrast, out-of-plane A modes are less sensitive to strain[285, 287], but have been reported to have a twist-dependent shift in heterobilayers[284], shift under biaxial strain[288], and broaden under tensile strain[289–292]. While charge doping renormalizes A modes[293, 294] and generally quenches Raman modes [295], our calculations do not show a strong correlation between twist angle and doping in our system, consistent with this being a minor effect in other heterobilayers[289]. Thus, our experimental and theoretical results suggest that moiré strain modifies the Raman modes of $1H-WSe_2$.

We now examine how the optoelectronic characteristics of $1H-WSe_2$ are affected by the presence of $1T-TaS_2$. To this end, reflection contrast (RC) was measured for S2 and S5. For both samples, significant broadening of the RC signal was detected in the heterostructure region compared $1H-WSe_2$ (Figure 6.9b). This spectral broadening is consistent with a decreased exciton lifetime resulting from ultrafast charge transfer to $1T-TaS_2$ [296, 297]. While broadening is observed in nearly aligned (S2) and misaligned (S5) samples, the A_{1s} exciton of $1H-WSe_2$ is significantly broader in the nearly aligned heterostructure, indicating a faster charge transfer rate compared to the misaligned case. Interestingly, RC of the nearly aligned sample (S2) evinces an additional peak below A_{1s} exciton at all temperatures (Figure 6.8b and Figure 6.10), indicating strong light absorption around these energies. From the band structure calculations (see Figure 6.7), this peak could arise from excitation across the electronic states (filled states in $1H-WSe_2$ to empty states in $1T-TaS_2$) in between K and Γ. Note that this transition is absent in the photoluminescence spectra (Figure 6.8c) and persists across the measured temperatures (Figure 6.10). Further experimental and theoretical investigations are needed to probe this new spectroscopic feature in the nearly aligned heterostructures and elucidate the twist-dependent exciton dissociation dynamics.

To further delineate the effect of $1T-TaS_2$ on $1H-WSe_2$, we examine the photoluminescence spectra (PL) of S2 and S5. The PL intensity of A_{1s} exciton of $1H-WSe_2$ is significantly quenched in both nearly aligned and misaligned heterostructures(6.8c). This can be explained by charge transfer from $1H-WSe_2$ to $1T-TaS_2$ where the photoexcited electrons and holes in $1H-WSe_2$ relax into lower energy states provided by $1T-TaS_2$ (See band

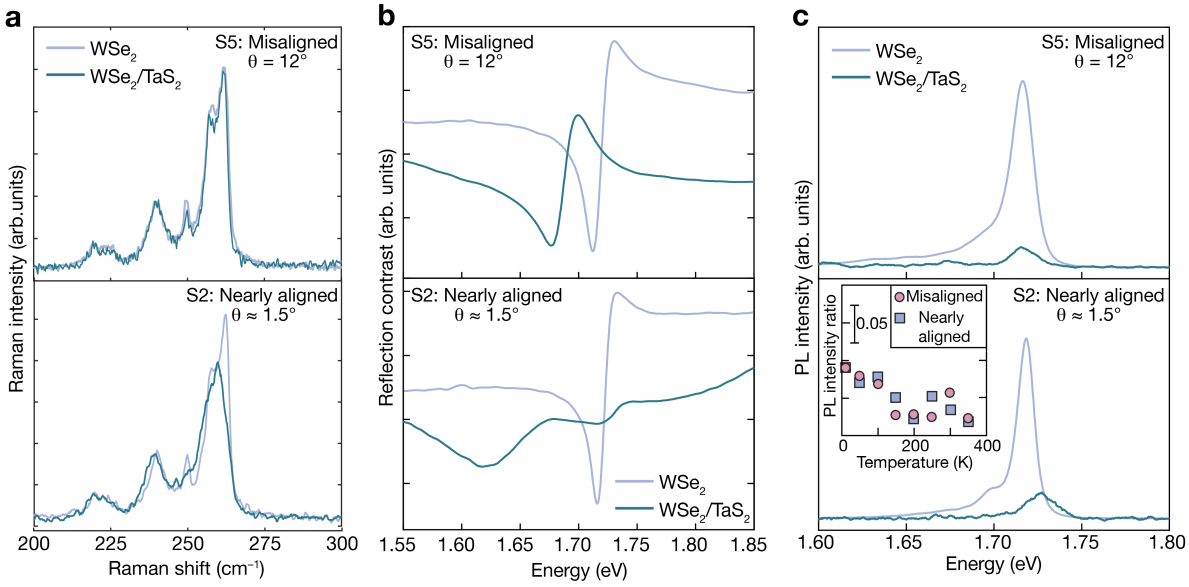


Figure 6.8: Effects of heterostructuring on the optical properties of $1H-WSe_2$. **(a–c)** Raman spectra **(a)**, reflection contrast **(b)** and photoluminescence **(c)** for the azimuthally misaligned heterostructure S5 (top) and the azimuthally nearly aligned heterostructure S2 (bottom). The inset in (c) displays the temperature-dependent PL intensity ratio of the nearly aligned (S2) and misaligned (S5) samples. This ratio is obtained by dividing the integrated intensity of the A_{1s} exciton in the heterostructure region by that in the $1H-WSe_2$ region.

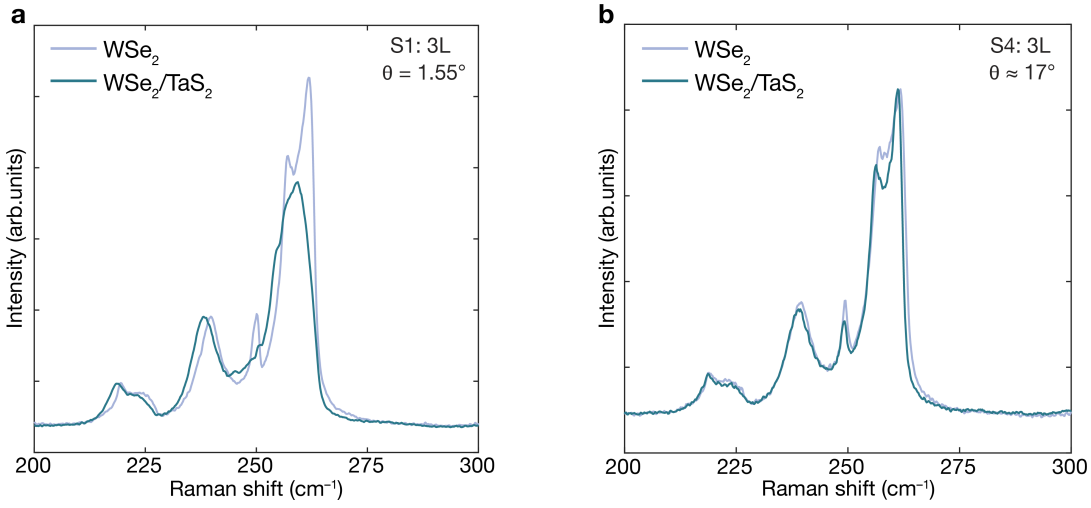


Figure 6.9: Raman spectra of $1H-WSe_2$ for the nearly aligned (S1) and misaligned (S3) heterostructures of 3-layer $1T-TaS_2$ and monolayer $1H-WSe_2$.

structure calculations in Figure 6.7). Such charge transfer in vdW heterostructures has been shown to occur on an ultrafast timescale (sub-ps)[298] relative to the radiative lifetime of excitons, facilitating efficient quenching of the PL. In the case of $1T-TaS_2/1H-WSe_2$, band structure calculations indicate that energy minima in $1T-TaS_2$ (Γ) and $1H-WSe_2$ (K) are mismatched in momentum (Figure 6.7). Hence, such an indirect nature of charge transfer across $1T-TaS_2/1H-WSe_2$ correlates with the insensitivity of PL quenching to the twist angle (Figure 6.8c, inset).

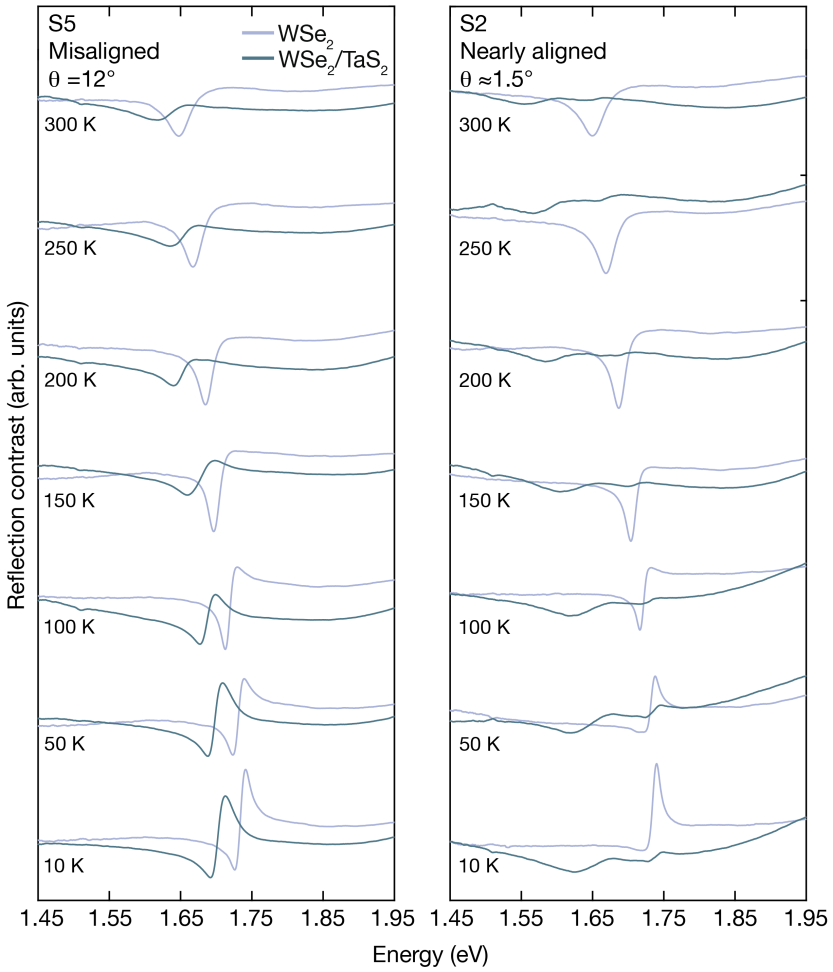


Figure 6.10: Temperature-dependence reflection contrast (RC) for samples S5 and S2.

The nearly aligned and misaligned heterostructures also exhibit differences in A_{1s} exciton energy relative to the isolated $1H-WSe_2$ as seen from both PL and RC spectra (Figure 6.8b,c and Figure 6.10). Such a variation in the exciton peak position in vdW heterostructures may arise from the net change of electronic band gap and exciton binding energy due to dielectric screening [299], charge doping [300], interlayer coupling [287] and strain [283]. The A_{1s} exciton

energy shows a dominant red shift in the RC spectra on the misaligned sample. Strong screening of Coulomb interactions in $1H-WSe_2$ from the charge density within $1T-TaS_2$ causes a reduction in the quasiparticle bandgap and exciton binding energy, resulting in a net red-shift in the A_{1s} exciton energy. Despite an identical dielectric screening effect expected in the nearly aligned heterostructure, an evident blue-shift of exciton energy in both RC and PL indicates an interplay of other mechanisms. We do not expect a strong modulation in the electronic coupling (i.e. band hybridization) with twist angle since our band structures reveal that there is no hybridization of $1T-TaS_2$ with $1H-WSe_2$ at the K point (Figure 6.7), where the CB maximum and VB minimum of $1H-WSe_2$ are located. Inferences of similar charge transfer and doping for different twist angles from the calculations and PL quenching hint at the role of moiré strain[283, 284] and the corresponding band gap renormalization[287] from the moiré superlattice in the nearly aligned sample.

6.3 Conclusion

Here, we investigate the optoelectronic implications of heterostructuring $1T-TaS_2$ with monolayer $1H-WSe_2$. We examine heterostructures with varying numbers of $1T-TaS_2$ layers and interlayer alignments, revealing that the CDW is suppressed upon contact with $1H-WSe_2$, with this effect being enhanced by decreasing sample thickness and minimizing the interlayer twist angle. The IC-CDW to NC-CDW transition is strongly influenced by the presence of $1H-WSe_2$ in thin samples, as evidenced by electron transport measurements. Moreover, nanoARPES confirms strong band renormalization in ultrathin $1T-TaS_2$ samples and reveals electronic ramifications of heterostruring with $1H-WSe_2$. Moreover, Raman spectroscopy reveals systematic evidence of CDW disorder in $1T-TaS_2/1H-WSe_2$ heterostructures, which is enhanced in nearly aligned samples. These nearly aligned samples were analyzed with dark-field TEM, revealing evidence of twist-dependent moiré reconstruction. Correlating these experimental observations with theoretical insights, we deduce that strain resulting from lattice reconstructions is the most plausible explanation for the increased CDW suppression observed in nearly aligned heterostructures. We also find that charge transfer, irrespective of twist, consistently leads to CDW suppression in thin samples contacting $1H-WSe_2$. Density functional theory (DFT) elucidates that this charge transfer is localized to the $1T-TaS_2$ layer directly interacting with $1H-WSe_2$, underscoring the significance of out-of-plane interactions in CDW ordering of $1T-TaS_2$.

Additionally, we observe modifications in the optoelectronic properties of $1H-WSe_2$ upon contact with $1T-TaS_2$. Specifically, the broadening RC and quenching of PL point to rapid exciton dissociation dynamics in contact with $1T-TaS_2$. Moreover, we measure twist-dependent shifts in PL and RC, coupled with increased broadening and emergence of a new RC mode in nearly aligned samples. These data suggest that moiré effects may alter exciton energies and dissociation dynamics. As follows, our study demonstrates that interfacing CDW crystals and semiconductors is a powerful framework to simultaneously tune their respective electronic properties, opening doors to the development of novel device

schemes.

6.4 Methods Chapter 6

Parts of the following methods section are adapted or reproduced from the graduate thesis of Valerie McGraw[301], who is a coauthor of this work.

hBN exfoliation

Chips of SiO_2/Si were cut into $\sim 1 \times 1$ cm squares and subjected to ozone cleaning for ~ 60 minutes at 150 °C. Immediately before concluding the cleaning, 2-4 hexagonal boron nitride (hBN) crystals (received from T. Taniguchi and K. Watanabe), were tessellated using Magic Scotch tape. The SiO_2/Si chips were then removed from the ozone cleaner and pressed onto the tape for 10 minutes with finger pressure before removing the tape from the chips.

1T−TaS_2 exfoliation

First, 90 nm SiO_2/Si chips were plasma cleaned for 2-3 minutes. Next, the chips were heated on a hotplate in an Ar glovebox for ~ 1 hour. Before completing the cleaning, a $\sim 2 \times 2$ mm piece of a 1T−TaS_2 crystal (HQ graphne) was tessellated using Magic Scotch tape. The chips were then pressed onto the tape for 10 minutes with finger pressure and then quickly peeled off the tape to yield thin flakes on the substrate.

2H-WSe_2 exfoliation

First, 285 nm SiO_2/Si chips were cleaned using ozone for $\sim$ 30-60 minutes. Next, the chips were heated on a hotplate in an Ar glovebox at 200 °C for at least 1 hour. Before concluding the cleaning, a $\sim 2 \times 2$ mm piece of 2H-WSe_2 (HQ graphene) was tessellated using Magic Scotch tape and pressed onto a piece of Gel-Pak 4 polydimethysiloxane (PDMS) film secured on a glass slide. Following the heating, the chips were pressed onto the PDMS for ~ 30 seconds and then lifted off from the PDMS.

Fabrication of bottom contacts

Bottom contacts were patterned using electron-beam lithography (Crestec CABL-UH Series Electron Beam Lithography System) onto atomically flat 10–30 nm hBN flakes. Initially, the contacts did not extend past the edge of the hBN crystals. Next, 7–10 nm of metal (Pt or Au) was evaporated onto the lithographically defined contacts, which were subsequently lifted off in acetone overnight. Following stacking, electron-beam lithography and thermal evaporation were used to pattern 0.5 nm Cr/100 nm Au extended contacts.

Fabrication of vdW heterostructures

Stacking was done in an Ar-filled glovebox using the dry transfer method with a PC/PDMS stamp[73]. The $1T-TaS_2$ flakes were always exfoliated 1–2 days before stacking to prevent sample degradation. All samples for Raman studies were prepared on 90 nm SiO_2/Si substrate, which enhances the weak signal from $1T-TaS_2$.

Electron transport measurements

A constant alternating current of 0.1-0.5 μA (17.777 Hz) was applied between source and drain contacts and 4-probe V_{xx} was measured using a lock-in amplifier (Stanford Research SR830). Measurements were collected between pairs of contacts ensuring individual assessment of R1 and R2. All measurements were performed in a Quantum Design Physical Property Measurement System (PPMS). Due to the relatively large bandgap of $1H-WSe_2$ compared to $1T-TaS_2$, $1H-WSe_2$ does not contribute significantly to the measured transport behavior.

Raman spectroscopy

Raman spectroscopy (Horiba Multiline LabRam Evolution) was conducted using 633 nm continuous wave laser with an ultra-low frequency filter. Spectra were typically collected with 50–80 μW power and an 1800 gr/mm grating, with 20-second acquisition times and 2-4 accumulations. For temperature-dependent measurements, samples were measured in an optical cryostat (Cryo Industries of America), which was evacuated to $\sim 10^{-6}$ Torr and cooled with liquid nitrogen. The samples were placed with thermally conductive vacuum grease onto a copper puck, which is temperature-controlled using resistive heating (LakeShore Cryotronics Model 325). Due to fluctuations in the system, temperatures reported throughout are accurate to $\pm$ 5 K. The laser beam was focused on the sample into a spot size of approximately 1 μm.

Photoluminescence and Reflection contrast

Temperature-dependent Photoluminescence (PL) and Reflection contrast (RC) spectroscopy were performed on the samples mounted in a Montana Cryostation S200. For the PL measurements, a 532 nm diode-pumped solid-state laser (Coherent^{TM} Sapphire SF NX) is used as the excitation source. For the RC measurements, a Quartz Tungsten Halogen Research Light Source (Oriel instruments) is used as the broadband excitation source. The excitation beam is focused ($< 1\mu$m dia) onto the sample loaded on the Agile Temperature Sample mount (ATSM) with a 100x objective (NA=0.9). The emission or reflection signal from the sample is collected in back-scattering geometry and dispersed with AndorTM Kymera 328i spectrometer using 300 l/mm grating onto the detector (TE-cooled Andor^{TM} Newton DU970P EMCCD). The laser excitation power on the sample was kept below 1μW.

Transmission electron microscopy

Selected area electron diffraction (SAED) patterns, used for determining interlayer twist, were obtained with a 40 μm diameter aperture (defining a selected diameter of $\sim$720 nm on the sample) using FEI TitanX TEM operated at 60–80 kV. Dark-field TEM was also obtained using FEI TitanX TEM with a 10 μm–20 μm objective aperture.

Density functional theory

Density functional theory (DFT) calculations were carried out on heterostructures composed of three layers of 1T-TaS_2 and one layer of 1H-WSe_2. Three cases were investigated: a commensurate charge density wave in the TaS_2 layers (CCDW); high-symmetry 1T-TaS_2 with no charge density wave (HS); and a twisted interface with 17.9° between high-symmetry TaS_2 and WSe_2 layers. The twisted heterostructure was generated using the TWISTER code [302, 303]. Structures had AA stacking with all metal centers nearly aligned except across the twisted interface. In all cases, the vacuum region between slabs was greater than 35 Å.

Nano angle-resolved photoemission spectroscopy (nanoARPES)

nanoARPES data were collected at Beamline 7.0.2 of the Advanced Light Source (ALS) on the nanoARPES endstation using Scienta Omicron R4000 hemispherical electron analyzers. The beam diameter was approximately 1 μm. All measurements were conducted at the base temperature of 20 K with linear horizontal (LH) polarization at pressures lower than 5×10^{-11} Torr. Data analysis was conducted using the PyARPES software package[196].

Density functional theory calculations

Spin-polarized DFT calculations were carried out using the Vienna *Ab initio* Simulation Package (VASP) [135–138] with projector augmented wave (PAW) pseudopotentials [139, 140] including Ta 5pd6s, W 5spd6s, S 3sp and Se 4sp electrons as valence. The plane-wave energy cutoff was set to 400 eV and the k-point grids were Gamma-centred with a k-point spacing less than 0.2 Å^{-1}, which gave an energy convergence of 1 meV per atom. The convergence criteria for the electronic self-consistent loop was set to 10^{-6} eV.

A Hubbard-U correction was applied to capture the charge distribution in the CCDW. A U of 2.86 eV was applied within the Dudarev approach [304] to the d orbitals of the Ta located at the center of the Star of David distortion, following the self-consistent calculation of U in [305]. This captures a band gap opening in TaS_2 between the spin-polarized bands at the Fermi level, in contrast to the metallic HS structure.

Structural optimizations were done using the PBEsol [241] exchange-correlation functional until the residual forces on the ions were less than 0.001 eV Å^{-1} for the CCDW and HS structures, whereas the twisted structure was fixed with van der Waals gaps set to those of the optimized HS structure. The percentage strain in the constituent layers of the heterostructures

is given by comparison to the lattice parameters of individually optimized TaS_2 trilayers and WSe_2 monolayer in Table 6.1.

Table 6.1: DFT parameters for $1T-TaS_2/1H-WSe_2$ heterostructures. In-plane lattice parameter (a) and percentage strain for the heterostructures compared to the individual constituents. All structures are optimized for a monolayer of WSe_2 and a trilayer of TaS_2.

Structure	a (Å)	$\Delta a/a$ (%)	
		TaS_2	WSe_2
WSe_2	3.273		
HS-TaS_2	3.326		
HS-TaS_2 — WSe_2	3.312	-0.41	1.21
CCDW-TaS_2	12.012		
CCDW-TaS_2 — WSe_2	11.955	-0.48	1.30
Twisted HS-TaS_2 — WSe_2	18.441	-0.42	1.20

Orbital-projected band structures were plotted using the SUMO package [306], and unfolded band structures using EASYUNFOLD [307].

Charge transfer plots were generated by subtracting the charge densities of individual TaS_2 and WSe_2 fragments from the charge density of the heterostructure. No structure relaxation was performed for the individual fragments; atom positions were identical to those in the optimized heterostructure. This charge density difference was summed within planes perpendicular to the c-axis parallel and normalized per formula unit within a layer. The macroscopic average of this 1D charge difference was calculated as a running average performed three times over periods of 3.03 Å, to smooth over the periodic features of the structure. 1D plots were calculated using the VASPKIT code [308]. Charge density difference was visualized using VESTA [309].

Chapter 7

Conclusions and outlook

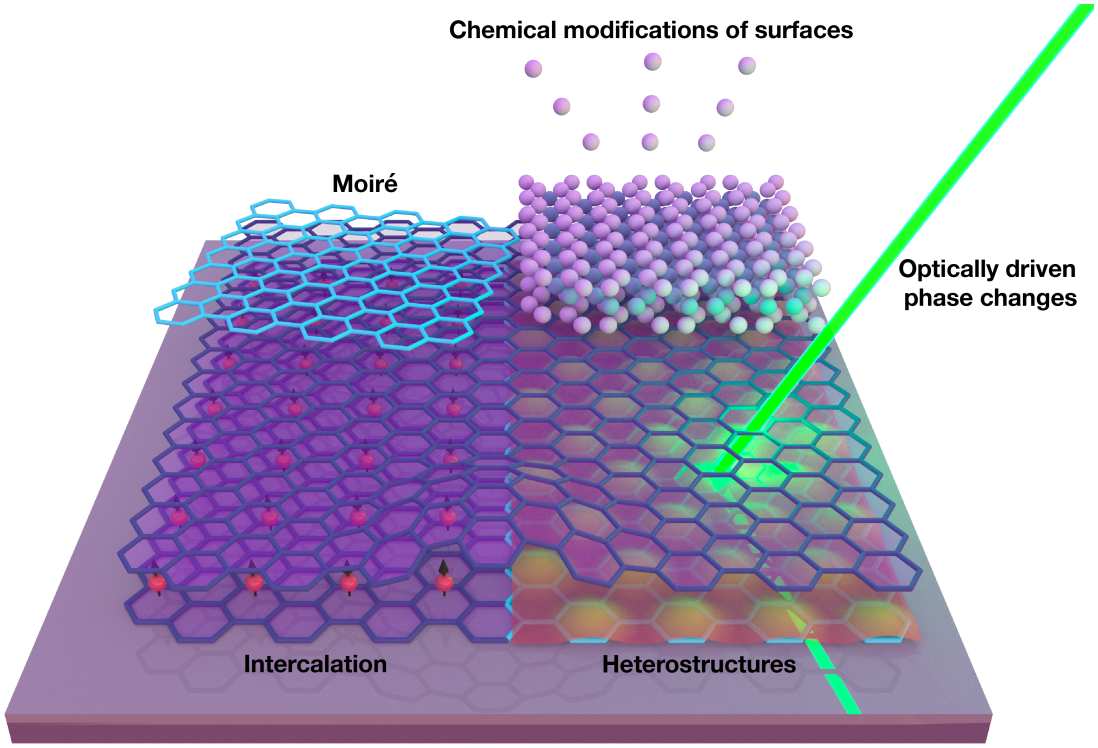


Figure 7.1: Opportunities for tuning the properties of 2D crystals.

In this thesis, intercalation and heterostructure design served as the primary methods for tuning the properties of 2D magnets and CDWs. However, the work presented here only scratches the surface of what is possible.

The majority of this thesis focused on Fe intercalation, which induces robust magnetism

in intercalated TMDs but primarily exhibits strong ferromagnetism with a significant out-of-plane anisotropy. Exploring ways to tune this anisotropy could be fruitful for developing new materials and switching paradigms for Fe_xTaS_2. DFT calculations in Chapter 2 indicated that increasing interlayer spacing enhances the anisotropy and potentially raises the ordering temperatures. It would be worthwhile to investigate if dual intercalation with larger ions could increase the interlayer spacing. Furthermore, studying the effects of strain on these materials could yield valuable insights. However, developing materials with largely different magnetic properties will require extending the intercalation approach to include other magnetic ions.

We note that Fe-intercalated polytype heterostructures may also benefit from strain-dependent measurements, given the sensitivity of both CDWs and magnetism to strain. Moreover, exploring how CDW ordering evolves with the application of external magnetic and electrical fields will shed light on the interplay between CDWs and magnetism.

Finally, our investigation into magnetic heterostructures marks the initial steps toward uncovering interface-driven magnetism. Altering the constituent layers and intercalants and incorporating engineered twist angles could unveil novel facets of the phase diagram for magnetic 2D crystals, paving the way for functional devices.

Bibliography

(1) Novoselov, K. S.; Geim, A. K.; Morozov, S. V.; Jiang, D.-e.; Zhang, Y.; Dubonos, S. V.; Grigorieva, I. V.; Firsov, A. A. Electric field effect in atomically thin carbon films. *Science* **2004**, *306*, 666–669.

(2) Geim, A. K.; Novoselov, K. S. The rise of graphene. *Nature Materials* **2007**, *6*, 183–191.

(3) Zhou, H.; Xie, T.; Taniguchi, T.; Watanabe, K.; Young, A. F. Superconductivity in rhombohedral trilayer graphene. *Nature* **2021**, *598*, 434–438.

(4) Cao, Y.; Fatemi, V.; Fang, S.; Watanabe, K.; Taniguchi, T.; Kaxiras, E.; Jarillo-Herrero, P. Unconventional superconductivity in magic-angle graphene superlattices. *Nature* **2018**, *556*, 43–50.

(5) Yankowitz, M.; Chen, S.; Polshyn, H.; Zhang, Y.; Watanabe, K.; Taniguchi, T.; Graf, D.; Young, A. F.; Dean, C. R. Tuning superconductivity in twisted bilayer graphene. *Science* **2019**, *363*, 1059–1064.

(6) Pixley, J. H.; Andrei, E. Y. Ferromagnetism in magic-angle graphene. *Science* **2019**, *365*, 543–543.

(7) Choi, Y.; Kim, H.; Peng, Y.; Thomson, A.; Lewandowski, C.; Polski, R.; Zhang, Y.; Arora, H. S.; Watanabe, K.; Taniguchi, T.; Alicea, J.; Nadj-Perge, S. Correlation-driven topological phases in magic-angle twisted bilayer graphene. *Nature* **2021**, *589*, 536–541.

(8) Ajayan, P.; Kim, P.; Banerjee, K. Two-dimensional van der Waals materials. *Physics Today* **2016**, *69*, 38–44.

(9) Dresselhaus, M.; Division, N. A. T. O. S. A., *Intercalation in Layered Materials*; Basic Life Sciences; Springer US: 1986.

(10) Lévy, F., *Intercalated Layered Materials*; Springer Netherlands: 1979.

(11) Wang, Z.; Li, R.; Su, C.; Loh, K. P. Intercalated phases of transition metal dichalcogenides. *SmartMat* **2020**, *1*, e1013.

(12) Jeong, J. H.; Kang, S.; Kim, N.; Joshi, R.; Lee, G.-H. Recent trends in covalent functionalization of 2D materials. *Physical Chemistry Chemical Physics* **2022**, *24*, 10684–10711.

(13) Gong, C.; Li, L.; Li, Z.; Ji, H.; Stern, A.; Xia, Y.; Cao, T.; Bao, W.; Wang, C.; Wang, Y.; Qiu, Z. Q.; Cava, R. J.; Louie, S. G.; Xia, J.; Zhang, X. Discovery of intrinsic ferromagnetism in two-dimensional van der Waals crystals. *Nature* **2017**, *546*, 265–269.

(14) Fei, Z.; Huang, B.; Malinowski, P.; Wang, W.; Song, T.; Sanchez, J.; Yao, W.; Xiao, D.; Zhu, X.; May, A. F.; Wu, W.; Cobden, D. H.; Chu, J.-H.; Xu, X. Two-dimensional itinerant ferromagnetism in atomically thin Fe_3GeTe_2. *Nature Materials* **2018**, *17*, 778–782.

(15) Jiang, X.; Liu, Q.; Xing, J.; Liu, N.; Guo, Y.; Liu, Z.; Zhao, J. Recent progress on 2D magnets: fundamental mechanism, structural design and modification. *Applied Physics Reviews* **2021**, *8*, 031305.

(16) Cao, Y.; Huang, Z.; Yin, Y.; Xie, H.; Liu, B.; Wang, W.; Zhu, C.; Mandrus, D.; Wang, L.; Huang, W. Overview and advances in a layered chiral helimagnet $Cr_{1/3}NbS_2$. *Materials Today Advances* **2020**, *7*, 100080.

(17) Du Trémolet de Lacheisserie, É.; Gignoux, D.; Schlenker, M., *Magnetism*; Kluwer Academic Publishers: Norwell: 2002.

(18) Kittel, C. In 8th ed.; John Wiley & Sons: New York, NY, 2005; Chapter 12, pp 323–360.

(19) Van der Pals, P. v. E.; Gaspard, P. Two-dimensional quantum spin Hamiltonians: Spectral properties. *Physical Review E* **1994**, *49*, 79.

(20) Pires, A. S. T. In *Theoretical Tools for Spin Models in Magnetic Systems*; 2053-2563; IOP Publishing: 2021, pp 1–16.

(21) Spaldin, N. A., *Magnetic materials: fundamentals and applications*; Cambridge university press: 2010.

(22) Gibertini, M.; Koperski, M.; Morpurgo, A. F.; Novoselov, K. S. Magnetic 2D materials and heterostructures. *Nature Nanotechnology* **2019**, *14*, 408–419.

(23) Gong, C.; Zhang, X. Two-dimensional magnetic crystals and emergent heterostructure devices. *Science* **2019**, *363*, eaav4450.

(24) Mermin, N. D.; Wagner, H. Absence of ferromagnetism or antiferromagnetism in one- or two-dimensional isotropic Heisenberg models. *Physical Review Letters* **1966**, *17*, 1133–1136.

(25) Hohenberg, P. C. Existence of long-range order in one and two dimensions. *Physical Review* **1967**, *158*, 383.

(26) Ising, E. Beitrag zur Theorie des Ferromagnetismus. *Zeitschrift für Physik* **1925**, *31*, 253–258.

(27) LENZ, W. Beitrag zum verstandnis der magnetischen erscheinunge in festen korpern. *Physikalische Zeitschrift* **1920**, *21*, 613–615.

(28) Onsager, L. Crystal statistics. I. A two-dimensional model with an order-disorder transition. *Physical Review* **1944**, *65*, 117.

(29) Orchard, A. F., *Magnetochemistry*; Oxford University Press: 2003.

(30) Xie, L. S.; Husremovic, S.; Gonzalez, O.; Craig, I. M.; Bediako, D. K. Structure and magnetism of iron-and chromium-intercalated niobium and tantalum disulfides. *Journal of the American Chemical Society* **2022**, *144*, 9525–9542.

(31) Wilson, J. A.; Yoffe, A. D. The transition metal dichalcogenides discussion and interpretation of the observed optical, electrical and structural properties. *Advances in Physics* **1969**, *18*, 193–335.

(32) Hulliger, F.; Pobitschka, E. On the magnetic behavior of new $2H$-NbS_2-type derivatives. *Journal of Solid State Chemistry* **1970**, *1*, 117–119.

(33) Van Laar, B.; Rietveld, H.; Ijdo, D. Magnetic and crystallographic structures of Me_xNbS_2 and Me_xTaS_2. *Journal of Solid State Chemistry* **1971**, *3*, 154–160.

(34) Friend, R. H.; Beal, A. R.; Yoffe, A. D. Electrical and magnetic properties of some first row transition metal intercalates of niobium disulphide. *Philosophical Magazine* **1977**, *35*, 1269–1287.

(35) Rao, G. V. S.; Shafer, M. W. In *Intercalated Layered Materials*, Lévy, F., Ed.; Springer Netherlands: Dordrecht, the Netherlands, 1979, pp 99–199.

(36) Ko, K. T.; Kim, K.; Kim, S. B.; Kim, H. D.; Kim, J. Y.; Min, B. I.; Park, J. H.; Chang, F. H.; Lin, H. J.; Tanaka, A.; Cheong, S. W. RKKY ferromagnetism with Ising-like spin states in intercalated $Fe_{1/4}TaS_2$. *Physical Review Letters* **2011**, *107*, 247201.

(37) Morosan, E.; Zandbergen, H. W.; Li, L.; Lee, M.; Checkelsky, J. G.; Heinrich, M.; Siegrist, T.; Ong, N. P.; Cava, R. J. Sharp switching of the magnetization in $Fe_{1/4}TaS_2$. *Physical Review B* **2007**, *75*, 104401.

(38) Checkelsky, J. G.; Lee, M.; Morosan, E.; Cava, R. J.; Ong, N. P. Anomalous Hall effect and magnetoresistance in the layered ferromagnet $Fe_{1/4}TaS_2$: The inelastic regime. *Physical Review B* **2008**, *77*, 014433.

(39) Chen, C.-W.; Chikara, S.; Zapf, V. S.; Morosan, E. Correlations of crystallographic defects and anisotropy with magnetotransport properties in Fe_xTaS_2 single crystals ($0.23 \leq x \leq 0.35$). *Physical Review B* **2016**, *94*, 054406.

(40) Hardy, W. J.; Chen, C. W.; Marcinkova, A.; Ji, H.; Sinova, J.; Natelson, D.; Morosan, E. Very large magnetoresistance in $Fe_{0.28}TaS_2$ single crystals. *Physical Review B* **2015**, *91*, 054426.

(41) Yoshida, M.; Suzuki, R.; Zhang, Y.; Nakano, M.; Iwasa, Y. Memristive phase switching in two-dimensional $1T$-TaS_2 crystals. *Science Advances* **2015**, *1*, e1500606.

(42) Zhu, H.; Han, H. In *Journal of Physics: Conference Series*, 2022; Vol. 2338, p 012028.

(43) Chen, C.-W.; Choe, J.; Morosan, E. Charge density waves in strongly correlated electron systems. *Reports on Progress in Physics* **2016**, *79*, 084505.

(44) Zhu, X.; Guo, J.; Zhang, J.; Plummer, E. Misconceptions associated with the origin of charge density waves. *Advances in Physics: X* **2017**, *2*, 622–640.

(45) Grüner, G., *Density Waves in Solids*; Perseus Publishing: Cambridge, Massachusetts, 1994.

(46) Peierls, R. E., *Quantum theory of solids*; Clarendon Press: 1996.

(47) Whangbo, M.-H. In *Crystal Chemistry and Properties of Materials with Quasi-One-Dimensional Structures: A Chemical and Physical Synthetic Approach*; Springer: 1986, pp 27–85.

(48) Hoffmann, R., *Solids and surfaces: a chemist's view of bonding in extended structures*; John Wiley & Sons: 2021.

(49) Canadell, E.; Doublet, M.-L.; Iung, C., *Orbital approach to the electronic structure of solids*; Oxford University Press: 2012.

(50) Albright, T. A.; Burdett, J. K.; Whangbo, M.-H., *Orbital interactions in chemistry*; John Wiley & Sons: 2013.

(51) Law, K. T.; Lee, P. A. 1T-TaS_2 as a quantum spin liquid. *Proceedings of the National Academy of Sciences* **2017**, *114*, 6996–7000.

(52) Rossnagel, K. On the origin of charge-density waves in select layered transition-metal dichalcogenides. *Journal of Physics: Condensed Matter* **2011**, *23*, 213001.

(53) Zhu, X.; Cao, Y.; Zhang, J.; Plummer, E.; Guo, J. Classification of charge density waves based on their nature. *Proceedings of the National Academy of Sciences* **2015**, *112*, 2367–2371.

(54) Ryu, H.; Chen, Y.; Kim, H.; Tsai, H.-Z.; Tang, S.; Jiang, J.; Liou, F.; Kahn, S.; Jia, C.; Omrani, A. A.; Shim, J. H.; Hussain, Z.; Shen, Z.-X.; Kim, K.; Min, B. I.; Hwang, C.; Crommie, M. F.; Mo, S.-K. Persistent Charge-Density-Wave Order in Single-Layer $TaSe_2$. *Nano Letters* **2018**, *18*, 689–694.

(55) Naito, M.; Tanaka, S. Electrical Transport Properties in 2H-NbS_2, -$NbSe_2$, -TaS_2 and -$TaSe_2$. *Journal of the Physical Society of Japan* **1982**, *51*, 219–227.

(56) Liu, R.; Tonjes, W.; Greanya, V.; Olson, C.; Frindt, R. Fermi surface of 2H-$TaSe_2$ and its relation to the charge-density wave. *Physical Review B* **2000**, *61*, 5212.

(57) Johannes, M.; Mazin, I.; Howells, C. Fermi-surface nesting and the origin of the charge-density wave in $NbSe_2$. *Physical Review B* **2006**, *73*, 205102.

(58) Johannes, M.; Mazin, I. Fermi surface nesting and the origin of charge density waves in metals. *Physical Review B* **2008**, *77*, 165135.

(59) Calandra, M.; Mazin, I.; Mauri, F. Effect of dimensionality on the charge-density wave in few-layer 2H-$NbSe_2$. *Physical Review B* **2009**, *80*, 241108.

(60) Spijkerman, A.; de Boer, J. L.; Meetsma, A.; Wiegers, G. A.; van Smaalen, S. X-ray crystal-structure refinement of the nearly commensurate phase of $1T$-TaS_2 in (3+2)-dimensional superspace. *Physical Review B* **1997**, *56*, 13757.

(61) Geremew, A. K.; Rumyantsev, S.; Kargar, F.; Debnath, B.; Nosek, A.; Bloodgood, M. A.; Bockrath, M.; Salguero, T. T.; Lake, R. K.; Balandin, A. A. Bias-voltage driven switching of the charge-density-wave and normal metallic phases in $1T$-TaS_2 thin-film devices. *ACS Nano* **2019**, *13*, 7231–7240.

(62) Sung, S. H.; Agarwal, N.; El Baggari, I.; Kezer, P.; Goh, Y. M.; Schnitzer, N.; Shen, J. M.; Chiang, T.; Liu, Y.; Lu, W.; Sun, Y.; Kourkoutis, L. F.; Heron, J. T.; Sun, K.; Hovden, R. Endotaxial stabilization of 2D charge density waves with long-range order. *Nature Communications* **2024**, *15*, 1403.

(63) Fazekas, P.; Tosatti, E. Electrical, structural and magnetic properties of pure and doped $1T$-TaS_2. *Philosophical Magazine B* **1979**, *39*, 229–244.

(64) Butler, C.; Yoshida, M.; Hanaguri, T.; Iwasa, Y. Mottness versus unit-cell doubling as the driver of the insulating state in $1T$-TaS_2. *Nature Communications* **2020**, *11*, 2477.

(65) Hellmann, S.; Rohwer, T.; Kalläne, M.; Hanff, K.; Sohrt, C.; Stange, A.; Carr, A.; Murnane, M. M.; Kapteyn, H. C.; Kipp, L.; Bauer, M.; Rossnagel, K. Time-domain classification of charge-density-wave insulators. *Nature Communications* **2012**, *3*, 1069.

(66) Dardel, B.; Grioni, M.; Malterre, D.; Weibel, P.; Baer, Y.; Lévy, F. Temperature-dependent pseudogap and electron localization in $1T$-TaS_2. *Physical Review B* **1992**, *45*, 1462.

(67) Rossnagel, K.; Smith, N. Spin-orbit coupling in the band structure of reconstructed $1T$-TaS_2. *Physical Review B* **2006**, *73*, 073106.

(68) Robbins, M. O.; Marseglia, E. X-ray studies of the charge-density wave transitions in TaS_2. *Philosophical Magazine B* **1980**, *42*, 705–715.

(69) Ritschel, T.; Trinckauf, J.; Koepernik, K.; Büchner, B.; Zimmermann, M. v.; Berger, H.; Joe, Y. I.; Abbamonte, P.; Geck, J. Orbital textures and charge density waves in transition metal dichalcogenides. *Nature Physics* **2015**, *11*, 328–331.

(70) Stahl, Q.; Kusch, M.; Heinsch, F.; Garbarino, G.; Kretzschmar, N.; Hanff, K.; Rossnagel, K.; Geck, J.; Ritschel, T. Collapse of layer dimerization in the photo-induced hidden state of $1T$-TaS_2. *Nature Communications* **2020**, *11*, 1–7.

(71) Scruby, C.; Williams, P.; Parry, G. The role of charge density waves in structural transformations of $1T$-TaS_2. *Philosophical Magazine* **1975**, *31*, 255–274.

(72) Tanda, S.; Sambongi, T.; Tani, T.; Tanaka, S. X-ray study of charge density wave structure in $1T$-TaS_2. *Journal of the Physical Society of Japan* **1984**, *53*, 476–479.

(73) Husremović, S.; Groschner, C. K.; Inzani, K.; Craig, I. M.; Bustillo, K. C.; Ercius, P.; Kazmierczak, N. P.; Syndikus, J.; Van Winkle, M.; Aloni, S.; Taniguchi, T.; Watanabe, K.; Griffin, S. M.; Bediako, D. K. Hard ferromagnetism down to the thinnest limit of iron-intercalated tantalum disulfide. *Journal of the American Chemical Society* **2022**, *144*, 12167–12176.

(74) Huang, B.; Clark, G.; Navarro-Moratalla, E.; Klein, D. R.; Cheng, R.; Seyler, K. L.; Zhong, D.; Schjhmidgall, E.; McGuire, M. A.; Cobden, D. H.; Yao, W.; Xiao, D.; Jarillo-Herrero, J.; Xu, X. Layer-dependent ferromagnetism in a van der Waals crystal down to the monolayer limit. *Nature* **2017**, 270–273.

(75) Deng, Y.; Yu, Y.; Song, Y.; Zhang, J.; Wang, N. Z.; Sun, Z.; Yi, Y.; Wu, Y. Z.; Wu, S.; Zhu, J.; Wang, J.; Chen, X. H.; Zhang, Y. Gate-tunable room-temperature ferromagnetism in two-dimensional Fe_3GeTe_2. *Nature* **2018**, *563*, 94–99.

(76) Jiang, S.; Shan, J.; Mak, K. F. Electric-field switching of two-Dimensional van Der Waals magnets. *Nature Materials* **2018**, *17*, 406–410.

(77) Huang, B.; Clark, G.; Klein, D. R.; MacNeill, D.; Navarro-Moratalla, E.; Seyler, K. L.; Wilson, N.; McGuire, M. A.; Cobden, D. H.; Xiao, D.; Yao, W.; Jarillo-Herrero, P.; Xu, X. Electrical control of 2D magnetism in bilayer CrI_3. *Nature Nanotechnology* **2018**, *13*, 544–548.

(78) Jiang, S.; Li, L.; Wang, Z.; Mak, K. F.; Shan, J. Controlling magnetism in 2D CrI_3 by electrostatic doping. *Nature Nanotechnology* **2018**, *13*, 549–553.

(79) Burch, K. S. Electric switching of magnetism in 2D. *Nature Nanotechnology* **2018**, *13*, 532.

(80) Halperin, B. I. On the Hohenberg-Mermin-Wagner theorem and its limitations. *Journal of Statistical Physics* **2019**, *175*, 521–529.

(81) Zhang, S.; Xu, R.; Luo, N.; Zou, X. Two-dimensional magnetic materials: structures, properties and external controls. *Nanoscale* **2021**, *13*, 1398–1424.

(82) Dijkstra, J.; Zijlema, P. J.; van Bruggen, C. F.; Haas, C.; de Groot, R. A. Band-structure calculations of $Fe_{1/3}TaS_2$ and $Mn_{1/3}TaS_2$, and transport and magnetic properties of $Fe_{0.28}TaS_2$. *Journal of Physics: Condensed Matter* **1989**, *1*, 6363–6379.

(83) Choe, J.; Lee, K.; Huang, C.-L.; Trivedi, N.; Morosan, E. Magnetotransport in Fe-intercalated TS_2: comparison between Ti and Ta. *Physical Review B* **2019**, *99*, 64420.

(84) Sirica, N.; Vilmercati, P.; Bondino, F.; Pis, I.; Nappini, S.; Mo, S.-K.; Fedorov, A. V.; Das, P. K.; Vobornik, I.; Fujii, J.; Li, L.; Sapkota, D.; Parker, D. S.; Mandrus, D. G.; Mannella, N. The nature of ferromagnetism in the chiral helimagnet $Cr_{1/3}NbS_2$. *Communications Physics* **2020**, *3*, 65.

(85) Obeysekera, D.; Gamage, K.; Gao, Y.; Cheong, S. W.; Yang, J. The magneto-transport properties of $Cr_{1/3}TaS_2$ with chiral magnetic solitons. *Advanced Electronic Materials* **2021**, *7*, 1–8.

(86) Cai, R.; Xing, W.; Zhou, H.; Li, B.; Chen, Y.; Yao, Y.; Ma, Y.; Xie, X. C.; Jia, S.; Han, W. Anomalous Hall effect mechanisms in the quasi-two-dimensional van Der Waals ferromagnet $Fe_{0.29}TaS_2$. *Physical Review B* **2019**, *100*, 54430.

(87) Zheng, G.; Wang, M.; Zhu, X.; Tan, C.; Wang, J.; Albarakati, S.; Aloufi, N.; Algarni, M.; Farrar, L.; Wu, M.; Yao, Y.; Tian, M.; Zhou, J.; Wang, L. Tailoring Dzyaloshinskii-Moriya interaction in a transition metal dichalcogenide by dual-intercalation. *Nature Communications* **2021**, *12*, 3639.

(88) Su, J.; Wang, M.; Liu, G.; Li, H.; Han, J.; Zhai, T. Air-stable 2D intrinsic ferromagnetic Ta_3FeS_6 with four months durability. *Advanced Science* **2020**, *7*, 2001722.

(89) Chen, K. P.; Chung, F. R.; Wang, M.; Koski, K. J. Dual element intercalation into 2D layered Bi_2Se_3 nanoribbons. *Journal of the American Chemical Society* **2015**, *137*, 5431–5437.

(90) Koski, K. J.; Cha, J. J.; Reed, B. W.; Wessells, C. D.; Kong, D.; Cui, Y. High-Density chemical intercalation of zero-valent copper into Bi_2Se_3 nanoribbons. *J. Am. Chem. Soc.* **2012**, *134*, 7584–7587.

(91) Wang, M.; Williams, D.; Lahti, G.; Teshima, S.; Dominguez Aguilar, D.; Perry, R.; Koski, K. J. Chemical Intercalation of Heavy Metal, Semimetal, and Semiconductor Atoms into 2D Layered Chalcogenides. *2D Materials* **2018**, *5*, 45005.

(92) Motter, J. P.; Koski, K. J.; Cui, Y. General Strategy for zero-valent intercalation into two-dimensional layered nanomaterials. *Chemistry of Materials* **2014**, *26*, 2313–2317.

(93) Koski, K. J.; Wessells, C. D.; Reed, B. W.; Cha, J. J.; Kong, D.; Cui, Y. Chemical intercalation of zerovalent metals into 2D layered Bi_2Se_3 nanoribbons. *Journal of the American Chemical Society* **2012**, *134*, 13773–13779.

(94) Navarro-Moratalla, E.; Island, J. O.; Mañas-Valero, S.; Pinilla-Cienfuegos, E.; Castellanos-Gomez, A.; Quereda, J.; Rubio-Bollinger, G.; Chirolli, L.; Silva-Guillén, J. A.; Agraït, N.; Steele, G. A.; Guinea, F.; van der Zant, H. S. J.; Coronado, E. Enhanced superconductivity in atomically thin TaS_2. *Nature Communications* **2016**, *7*, 11043.

(95) Wijngaard, J. H.; Hass, C.; Devillers, M. A. C. Optical and magneto-optical properties of $Fe_{0.28}TaS_2$. *Journal of Physics: Condensed Matter* **1991**, *3*, 6913–6923.

(96) Fan, S.; Neal, S.; Won, C.; Kim, J.; Sapkota, D.; Huang, F.; Yang, J.; Mandrus, D. G.; Cheong, S.-W.; Haraldsen, J. T.; Musfeldt, J. L. Excitations of intercalated metal monolayers in transition metal dichalcogenides. *Nano Letters* **2021**, *21*, 99–106.

(97) Horibe, Y.; Yang, J.; Cho, Y.-H.; Luo, X.; Kim, S. B.; Oh, Y. S.; Huang, F.-T.; Asada, T.; Tanimura, M.; Jeong, D.; Cheong, S.-W. Color theorems, chiral domain topology, and magnetic properties of Fe_xTaS_2. *Journal of the American Chemical Society* **2014**, *136*, 8368–8373.

(98) Su, T.; Huang, J.; Wang, Q.; Zhang, X.; Zhou, L.; Tang, M.; Zhang, C.; Yuan, H.; Zhao, W.; Wang, Z.; Yuan, H.; Wang, X. Investigation of phonon modes in $2H$-TaX_2 (X = S/Se) flakes with electrostatic doping. *Journal of Applied Physics* **2021**, *130*, 105302.

(99) Valencia-Ibáñez, S.; Jiménez-Guerrero, D.; Salcedo-Pimienta, J. D.; Vega-Bustos, K.; Cárdenas-Chirivi, G.; López-Manrique, L.; Herrera-Vasco, E.; Galvis, J. A.; Hernández, Y.; Giraldo-Gallo, P. Raman spectroscopy of few-layers TaS_2 and Mo-doped TaS_2 with enhanced superconductivity. *Advanced Electronic Materials* **2022**, *8*, 2200457.

(100) Narita, H.; Ikuta, H.; Hinode, H.; Uchida, T.; Ohtani, T.; Wakihara, M. Preparation and physical properties of Fe_xTaS_2 ($0.15 \leq x \leq 0.50$) Compounds. *Journal of Solid State Chemistry* **1994**, 148–151.

(101) Waszczak, J. V.; DiSalvo, F. J.; Eibschütz, M.; Mahajan, S.; Hull, G. W. Ferromagnetism in metallic intercalated compounds Fe_xTaS_2 ($0.20 \leq x \leq 0.34$). *Journal of Applied Physics* **2003**, *52*, 2098–2100.

(102) Eibschütz, M.; DiSalvo, F.; Hull Jr, G.; Mahajan, S. Ferromagnetism in metallic Fe_xTaS_2 ($x \sim 0.28$). *Applied Physics Letters* **1975**, *27*, 464–466.

(103) Mangelsen, S.; Hansen, J.; Adler, P.; Schnelle, W.; Bensch, W.; Mankovsky, S.; Polesya, S.; Ebert, H. Large anomalous Hall effect and slow relaxation of the magnetization in $Fe_{1/3}TaS_2$. *The Journal of Physical Chemistry C* **2020**, *124*, 24984–24994.

(104) Pugh, E. M. Hall effect and the magnetic properties of some ferromagnetic materials. *Physical Review Journals* **1930**, *36*, 1503–1511.

(105) Pugh, E. M.; Lippert, T. W. Hall e.m.f. and intensity of magnetization. *Physical Review Journals* **1932**, *42*, 709–713.

(106) May, A. F.; Ovchinnikov, D.; Zheng, Q.; Hermann, R.; Calder, S.; Huang, B.; Fei, Z.; Liu, Y.; Xu, X.; McGuire, M. A. Ferromagnetism near room temperature in the cleavable van Der Waals crystal Fe_5GeTe_2. *ACS Nano* **2019**, *13*, 4436–4442.

(107) Zhang, Y.; Chu, J.; Yin, L.; Shifa, T. A.; Cheng, Z.; Cheng, R.; Wang, F.; Wen, Y.; Zhan, X.; Wang, Z.; He, J. Ultrathin magnetic 2D single-crystal CrSe. *Advanced Materials* **2019**, *31*, 1900056.

(108) Bonilla, M.; Kolekar, S.; Ma, Y.; Diaz, H. C.; Kalappattil, V.; Das, R.; Eggers, T.; Gutierrez, H. R.; Phan, M.-H.; Batzill, M. Strong room-temperature ferromagnetism in VSe_2 monolayers on van der Waals substrates. *Nature Nanotechnology* **2018**, *13*, 289–293.

(109) O'Hara, D. J.; Zhu, T.; Trout, A. H.; Ahmed, A. S.; Luo, Y. K.; Lee, C. H.; Brenner, M. R.; Rajan, S.; Gupta, J. A.; McComb, D. W.; Kawakami, R. K. Room Temperature Intrinsic Ferromagnetism in Epitaxial Manganese Selenide Films in the Monolayer Limit. *Nano Letters* **2018**, *18*, 3125–3131.

(110) Kim, M.; Kumaravadivel, P.; Birkbeck, J.; Kuang, W.; Xu, S. G.; Hopkinson, D. G.; Knolle, J.; McClarty, P. A.; Berdyugin, A. I.; Ben Shalom, M.; Gorbachev, R. V.; Haigh, S. J.; Liu, S.; Edgar, J. H.; Novoselov, K. S.; Grigorieva, I. V.; Geim, A. K. Micromagnetometry of two-dimensional ferromagnets. *Nature Electronics* **2019**, *2*, 457–463.

(111) Blundell, S., *Magnetism in Condensed Matter*; Oxford University Press: Oxford; New York, 2001, pp 119–120.

(112) Pathria, R. K.; Beale, P. D. In *Statistical Mechanics (Third Edition)*, Pathria, R. K., Beale, P. D., Eds.; Academic Press: Boston, 2011, pp 401–469.

(113) Fisher, M. E.; Ma, S.; Nickel, B. G. Critical exponents for long-range interactions. *Physical Review Letters* **1972**, *29*, 917–920.

(114) Chiew, Y. L.; Miyata, M.; Koyano, M.; Oshima, Y. Clarification of the ordering of intercalated Fe Atoms in Fe_xTiS_2 and its effect on the magnetic properties. *Acta Crystallographica Section B* **2021**, *77*, 441–448.

(115) Negishi, S.; Negishi, H.; Sasaki, M.; Inoue, M. Monte Carlo simulation of intercalated atomic distributions in layered dichalcogenide. *Molecular Crystals and Liquid Crystals* **2000**, *341*, 69–74.

(116) Negishi, S.; Negishi, H.; Sasaki, M.; Inoue, M. Simulation of atomic distribution of guest atoms in layered $1T$-TiS_2 crystal using Monte Carlo method and its effect on the magnetic properties and local structures. *Journal of the Physical Society of Japan* **2000**, *69*, 2514–2530.

(117) Illing, B.; Fritschi, S.; Kaiser, H.; Klix, C. L.; Maret, G.; Keim, P. Mermin-Wagner fluctuations in 2D amorphous solids. *The Proceedings of the National Academy of Sciences* **2017**, *114*, 1856–1861.

(118) Haley, S. C.; Maniv, E.; Wu, S.; Cookmeyer, T.; Torres-Londono, S.; Aravinth, M.; Maksimovic, N.; Moore, J.; Birgeneau, R. J.; Analytis, J. G. Long-range, non-local switching of spin textures in a frustrated antiferromagnet. *Nature Communications* **2023**, *14*, 4691.

(119) Wu, S.; Xu, Z.; Haley, S. C.; Weber, S. F.; Acharya, A.; Maniv, E.; Qiu, Y.; Aczel, A. A.; Settineri, N. S.; Neaton, J. B.; Analytis, J. G.; Birgeneau, R. J. Highly tunable magnetic phases in transition-metal dichalcogenide $Fe_{1/3+\delta}NbS_2$. *Physical Review X* **2022**, *12*, 21003.

(120) Nair, N. L.; Maniv, E.; John, C.; Doyle, S.; Orenstein, J.; Analytis, J. G. Electrical switching in a magnetically intercalated transition metal dichalcogenide. *Nature Materials* **2020**, *19*, 153–157.

(121) Maniv, E.; Nair, N. L.; Haley, S. C.; Doyle, S.; John, C.; Cabrini, S.; Maniv, A.; Ramakrishna, S. K.; Tang, Y.-L.; Ercius, P.; Ramesh, R.; Tserkovnyak, Y.; Reyes, A. P.; Analytis, J. G. Antiferromagnetic switching driven by the collective dynamics of a coexisting spin glass. *Science Advances* **2021**, *7*, eabd8452.

(122) Little, A.; Lee, C.; John, C.; Doyle, S.; Maniv, E.; Nair, N. L.; Chen, W.; Rees, D.; Venderbos, J. W. F.; Fernandes, R. M.; Analytis, J. G.; Orenstein, J. Three-state nematicity in the triangular lattice antiferromagnet $Fe_{1/3}NbS_2$. *Nature Materials* **2020**, *19*, 1062–1067.

(123) Amaladass, E. P.; Satya, A. T.; Sharma, S.; Vinod, K.; Srinivas, V.; Sundar, C. S.; Bharathi, A. Magnetization and magneto-transport studies on $Fe_2VAl_{1-x}Si_x$. *Journal of Alloys and Compounds* **2015**, *648*, 34–38.

(124) Jobst, J.; Kisslinger, F.; Weber, H. B. Detection of the Kondo effect in the resistivity of graphene: artifacts and strategies. *Physical Review B* **2013**, *88*, 1–6.

(125) Liu, H.; Xue, Y.; Shi, J. A.; Guzman, R. A.; Zhang, P.; Zhou, Z.; He, Y.; Bian, C.; Wu, L.; Ma, R.; Chen, J.; Yan, J.; Yang, H.; Shen, C. M.; Zhou, W.; Bao, L.; Gao, H. J. Observation of the Kondo effect in multilayer single-crystalline VTe_2 Nanoplates. *Nano Letters* **2019**, *19*, 8572–8580.

(126) Zhao, M.; Chen, B.-B.; Xi, Y.; Zhao, Y.; Xu, H.; Zhang, H.; Cheng, N.; Feng, H.; Zhuang, J.; Pan, F.; Xu, X.; Hao, W.; Li, W.; Zhou, S.; Dou, S. X.; Du, Y. Kondo holes in the two-dimensional itinerant Ising ferromagnet Fe_3GeTe_2. *Nano Letters* **2021**, *21*, 6117–6123.

(127) Wen, Y.; Liu, Z.; Zhang, Y.; Xia, C.; Zhai, B.; Zhang, X.; Zhai, G.; Shen, C.; He, P.; Cheng, R.; Yin, L.; Yao, Y.; Getaye Sendeku, M.; Wang, Z.; Ye, X.; Liu, C.; Jiang, C.; Shan, C.; Long, Y.; He, J. Tunable room-temperature ferromagnetism in two-dimensional Cr_2Te_3. *Nano Letters* **2020**, *20*, 3130–3139.

(128) Zhu, R.; Zhang, W.; Shen, W.; Wong, P. K. J.; Wang, Q.; Liang, Q.; Tian, Z.; Zhai, Y.; Qiu, C.; Wee, A. T. S. Exchange bias in van der Waals $CrCl_3/Fe_3GeTe_2$ heterostructures. *Nano Letters* **2020**, *20*, 5030–5035.

(129) Dolui, K.; Petrović, M. D.; Zollner, K.; Plecháč, P.; Fabian, J.; Nikolić, B. K. Proximity spin–orbit torque on a two-dimensional magnet within van der Waals heterostructure: current-driven antiferromagnet-to-ferromagnet reversible nonequilibrium phase transition in bilayer CrI_3. *Nano Letters* **2020**, *20*, 2288–2295.

(130) Wang, Y.; Wang, C.; Liang, S.-J.; Ma, Z.; Xu, K.; Liu, X.; Zhang, L.; Admasu, A. S.; Cheong, S.-W.; Wang, L.; Chen, M.; Liu, Z.; Cheng, B.; Ji, W.; Miao, F. Strain-sensitive magnetization reversal of a van der Waals magnet. *Advanced Materials* **2020**, *32*, e2004533.

(131) Zhong, J.; Wang, M.; Liu, T.; Zhao, Y.; Xu, X.; Zhou, S.; Han, J.; Gan, L.; Zhai, T. Strain-sensitive ferromagnetic two-dimensional Cr_2Te_3. *Nano Research* **2022**, *15*, 1254–1259.

(132) Xu, Y.; Ray, A.; Shao, Y.-T.; Jiang, S.; Lee, K.; Weber, D.; Goldberger, J. E.; Watanabe, K.; Taniguchi, T.; Muller, D. A.; Mak, K. F.; Shan, J. Coexisting ferromagnetic–antiferromagnetic state in twisted bilayer CrI_3. *Nature Nanotechnology* **2022**, *17*, 143–147.

(133) Song, T.; Sun, Q.-C.; Anderson, E.; Wang, C.; Qian, J.; Taniguchi, T.; Watanabe, K.; McGuire, M. A.; Stöhr, R.; Xiao, D.; Cao, T.; Wrachtrup, J.; Xu, X. Direct visualization of magnetic domains and moiré magnetism in twisted 2D magnets. *Science* **2021**, *374*, 1140–1144.

(134) Gao, A.; Liu, Y.-F.; Hu, C.; Qiu, J.-X.; Tzschaschel, C.; Ghosh, B.; Ho, S.-C.; Bérubé, D.; Chen, R.; Sun, H.; Zhang, Z.; Zhang, X.-Y.; Wang, Y.-X.; Wang, N.; Huang, Z.; Felser, C.; Agarwal, A.; Ding, T.; Tien, H.-J.; Akey, A.; Gardener, J.; Singh, B.; Watanabe, K.; Taniguchi, T.; Burch, K. S.; Bell, D. C.; Zhou, B. B.; Gao, W.; Lu, H.-Z.; Bansil, A.; Lin, H.; Chang, T.-R.; Fu, L.; Ma, Q.; Ni, N.; Xu, S.-Y. Layer Hall effect in a 2D topological axion antiferromagnet. *Nature* **2021**, *595*, 521–525.

(135) Kresse, G.; Hafner, J. Ab initio molecular dynamics for liquid metals. *Physical Review B* **1993**, *47*, 558–561.

(136) Kresse, G.; Hafner, J. Ab initio molecular-dynamics simulation of the liquid-metal–amorphous-semiconductor transition in germanium. *Physical Review B* **1994**, *49*, 14251–14269.

(137) Kresse, G.; Furthmüller, J. Efficient iterative schemes for ab initio total-energy calculations using a plane-wave basis set. *Physical Review B* **1996**, *54*, 11169–11186.

(138) Kresse, G.; Furthmüller, J. Efficiency of ab-initio total energy calculations for metals and semiconductors using a plane-wave basis set. *Computational Materials Science* **1996**, *6*, 15–50.

(139) Kresse, G.; Joubert, D. From ultrasoft pseudopotentials to the projector augmented-wave method. *Physical Review B* **1999**, *59*, 1758–1775.

(140) Blöchl, P. E. Projector augmented-wave method. *Physical Review B* **1994**, *50*, 17953–17979.

(141) Csonka, G. I.; Perdew, J. P.; Ruzsinszky, A.; Philipsen, P. H. T.; Lebègue, S.; Paier, J.; Vydrov, O. A.; Ángyán, J. G. Assessing the performance of recent density functionals for bulk solids. *Physical Review B* **2009**, *79*, 155107.

(142) Liechtenstein, A. I.; Anisimov, V. I.; Zaanen, J. Density-functional theory and strong interactions: Orbital ordering in Mott-Hubbard insulators. *Physical Review B* **1995**, *52*, R5467.

(143) Gibert, M.; Zubko, P.; Scherwitzl, R.; Íñiguez, J.; Triscone, J.-M. Exchange bias in $LaNiO_3$–$LaMnO_3$ superlattices. *Nature Materials* **2012**, *11*, 195–198.

(144) Jiang, J.; Xiao, D.; Wang, F.; Shin, J.-H.; Andreoli, D.; Zhang, J.; Xiao, R.; Zhao, Y.-F.; Kayyalha, M.; Zhang, L.; Wang, K.; Zang, J.; Liu, C.; Samarth, N.; Chan, M. H. W.; Chang, C.-Z. Concurrence of quantum anomalous Hall and topological Hall effects in magnetic topological insulator sandwich heterostructures. *Nature Materials* **2020**, *19*, 732–737.

(145) Fu, H.; Liu, C.-X.; Yan, B. Exchange bias and quantum anomalous Hall effect in the $MnBi_2Te_4/CrI_3$ heterostructure. *Science Advances* **2020**, *6*, eaaz0948.

(146) Baibich, M. N.; Broto, J. M.; Fert, A.; Van Dau, F. N.; Petroff, F.; Etienne, P.; Creuzet, G.; Friederich, A.; Chazelas, J. Giant magnetoresistance of (001) Fe/(001) Cr magnetic superlattices. *Physical Review Letters* **1988**, *61*, 2472.

(147) Heinze, S.; Von Bergmann, K.; Menzel, M.; Brede, J.; Kubetzka, A.; Wiesendanger, R.; Bihlmayer, G.; Blügel, S. Spontaneous atomic-scale magnetic skyrmion lattice in two dimensions. *Nature Physics* **2011**, *7*, 713–718.

(148) Moreau-Luchaire, C.; Moutafis, C.; Reyren, N.; Sampaio, J.; Vaz, C. A. F.; Van Horne, N.; Bouzehouane, K.; Garcia, K.; Deranlot, C.; Warnicke, P.; Wohlhüter, P.; George, J.-M.; Weigand, M.; Raabe, J.; Cros, V.; Fert, A. Additive interfacial chiral interaction in multilayers for stabilization of small individual skyrmions at room temperature. *Nature Nanotechnology* **2016**, *11*, 444–448.

(149) Boulle, O.; Vogel, J.; Yang, H.; Pizzini, S.; de Souza Chaves, D.; Locatelli, A.; Menteş, T. O.; Sala, A.; Buda-Prejbeanu, L. D.; Klein, O.; Belmeguenai, M.; Roussigné, Y.; Stashkevich, A.; Chérif, S. M.; Aballe, L.; Foerster, M.; Chshiev, M.; Auffret, S.; Miron, I. M.; Gaudin, G. Room-temperature chiral magnetic skyrmions in ultrathin magnetic nanostructures. *Nature Nanotechnology* **2016**, *11*, 449–454.

(150) Nakagawa, N.; Hwang, H. Y.; Muller, D. A. Why some interfaces cannot be sharp. *Nature Materials* **2006**, *5*, 204–209.

(151) Harrison, W.; Kraut, E.; Waldrop, J.; Grant, R. Polar heterojunction interfaces. *Physical Review B* **1978**, *18*, 4402.

(152) Miyadai, T.; Kikuchi, K.; Kondo, H.; Sakka, S.; Arai, M.; Ishikawa, Y. Magnetic Properties of $Cr_{1/3}NbS_2$. *Journal of the Physical Society of Japan* **1983**, *52*, 1394–1401.

(153) Togawa, Y.; Koyama, T.; Takayanagi, K.; Mori, S.; Kousaka, Y.; Akimitsu, J.; Nishihara, S.; Inoue, K.; Ovchinnikov, A. S.; Kishine, J. Chiral magnetic soliton lattice on a chiral helimagnet. *Physical Review Letters* **2012**, *108*, 107202.

(154) Zhang, C.; Zhang, J.; Liu, C.; Zhang, S.; Yuan, Y.; Li, P.; Wen, Y.; Jiang, Z.; Zhou, B.; Lei, Y.; Zheng, D.; Song, C.; Hou, Z.; Mi, W.; Schwingenschlögl, U.; Manchon, A.; Qiu, Z. Q.; Alshareef, H. N.; Peng, Y.; Zhang, X.-X. Chiral Helimagnetism and one-dimensional magnetic solitons in a Cr-intercalated transition metal dichalcogenide. *Advanced Materials* **2021**, *33*, 2101131.

(155) Goodge, B. H.; Gonzalez, O.; Xie, L. S.; Bediako, D. K. Consequences and control of multiscale order/disorder in chiral magnetic textures. *ACS nano* **2023**, *17*, 19865–19876.

(156) Maniv, E.; Murphy, R. A.; Haley, S. C.; Doyle, S.; John, C.; Maniv, A.; Ramakrishna, S. K.; Tang, Y.-L.; Ercius, P.; Ramesh, R.; Reyes, A. P.; Long, J. R.; Analytis, J. G. Exchange bias due to coupling between coexisting antiferromagnetic and spin-glass orders. *Nature Physics* **2021**, *17*, 525–530.

(157) Park, P.; Cho, W.; Kim, C.; An, Y.; Kang, Y.-G.; Avdeev, M.; Sibille, R.; Iida, K.; Kajimoto, R.; Lee, K. H.; Ju, W.; Cho, E.-J.; Noh, H.-J.; Han, M. J.; Zhang, S.-S.; Batista, C. D.; Park, J.-G. Tetrahedral triple-Q magnetic ordering and large spontaneous Hall conductivity in the metallic triangular antiferromagnet $Co_{1/3}TaS_2$. *Nature Communications* **2023**, *14*, 8346.

(158) Takagi, H.; Takagi, R.; Minami, S.; Nomoto, T.; Ohishi, K.; Suzuki, M.-T.; Yanagi, Y.; Hirayama, M.; Khanh, N. D.; Karube, K.; Saito, H.; Hashizume, D.; Kiyanagi, R.; Tokura, Y.; Arita, R.; Nakajima, T.; Seki, S. Spontaneous topological Hall effect induced by non-coplanar antiferromagnetic order in intercalated van der Waals materials. *Nature Physics* **2023**, 1–8.

(159) Šmejkal, L.; Sinova, J.; Jungwirth, T. Emerging research landscape of altermagnetism. *Physical Review X* **2022**, *12*, 040501.

(160) Yamasaki, Y.; Moriya, R.; Arai, M.; Masubuchi, S.; Pyon, S.; Tamegai, T.; Ueno, K.; Machida, T. Exfoliation and van der Waals heterostructure assembly of intercalated ferromagnet $Cr_{1/3}TaS_2$. *2D Materials* **2017**, *4*, 041007.

(161) Arai, M.; Moriya, R.; Yabuki, N.; Masubuchi, S.; Ueno, K.; Machida, T. Construction of van der Waals magnetic tunnel junction using ferromagnetic layered dichalcogenide. *Applied Physics Letters* **2015**, *107*, 103107.

(162) Johnston, D.; Keelan, B. Superconductivity and magnetism of $M_x(H_2O)_yTaS_2$ layered cointercalation compounds. *Solid State Communications* **1984**, *52*, 631–634.

(163) Tan, H.; Verbeeck, J.; Abakumov, A.; Van Tendeloo, G. Oxidation state and chemical shift investigation in transition metal oxides by EELS. *Ultramicroscopy* **2012**, *116*, 24–33.

(164) Leapman, R. D.; Grunes, L. A.; Fejes, P. L. Study of the L_{23} edges in the $3d$ transition metals and their oxides by electron-energy-loss spectroscopy with comparisons to theory. *Physical Review B* **1982**, *26*, 614–635.

(165) Manukumar, K.; Viswanatha, R.; Nagaraju, G. Ionic liquid–assisted hydrothermal synthesis of Ta_2O_5 nanoparticles for lithium-ion battery applications. *Ionics* **2020**, *26*, 1197–1202.

(166) Valerjevich, K. E.; Alexeevich, S. V.; Viktorovich, E. A. Nanostructure of matrices for sulfur constructional composites: methodology, methods and research tools.

(167) Stephenson, N.; Roth, R. Structural systematics in the binary system Ta_2O_5–WO_3. V. The structure of the low-temperature form of tantalum oxide L-Ta_2O_5. *Acta Crystallographica Section B: Structural Crystallography and Crystal Chemistry* **1971**, *27*, 1037–1044.

(168) Xie, L. S.; Gonzalez, O.; Li, K.; Michiardi, M.; Gorovikov, S.; Ryu, S. H.; Fender, S. S.; Zonno, M.; Jo, N. H.; Zhdanovich, S.; Jozwiak, C.; Bostwick, A.; Husremovic, S.; Erodici, M. P.; Mollazadeh, C.; Damascelli, A.; Rotenberg, E.; Ping, Y.; Bediako, D. K. Comparative electronic structures of the chiral helimagnets $Cr_{1/3}NbS_2$ and $Cr_{1/3}TaS_2$. *Chemistry of Materials* **2023**, *35*, 7239–7251.

(169) Edwards, B.; Dowinton, O.; Hall, A. E.; Murgatroyd, P. A. E.; Buchberger, S.; Antonelli, T.; Siemann, G.-R.; Rajan, A.; Morales, E. A.; Zivanovic, A.; Bigi, C.; Belosludov, R. V.; Polley, C. M.; Carbone, D.; Mayoh, D. A.; Balakrishnan, G.; Bahramy, M. S.; King, P. D. C. Giant valley-Zeeman coupling in the surface layer of an intercalated transition metal dichalcogenide. *Nature Materials* **2023**, *22*, 459–465.

(170) Mattheiss, L. F. Band structures of transition-metal-dichalcogenide layer compounds. *Physical Review B* **1973**, *8*, 3719.

(171) Albarakati, S.; Xie, W.-Q.; Tan, C.; Zheng, G.; Algarni, M.; Li, J.; Partridge, J.; Spencer, M. J. S.; Farrar, L.; Xiong, Y.; Tian, M.; Wang, X.; Zhao, Y.-J.; Wang, L. Electric control of exchange bias effect in $FePS_3$–Fe_5GeTe_2 van der Waals heterostructures. *Nano Letters* **2022**, *22*, 6166–6172.

(172) Lachman, E.; Murphy, R. A.; Maksimovic, N.; Kealhofer, R.; Haley, S.; McDonald, R. D.; Long, J. R.; Analytis, J. G. Exchange biased anomalous Hall effect driven by frustration in a magnetic kagome lattice. *Nature Communications* **2020**, *11*, 560.

(173) Kong, Z.; Kaminsky, C. J.; Groschner, C. K.; Yun, Y.; Husremović, S.; Xie, L. S.; Kim, R. S.; Yano, J.; Bediako, D. K. Near room-temperature intrinsic exchange bias in an Fe intercalated $ZrSe_2$ spin glass. *Journal of the American Chemical Society* **2023**, *145*, 20041–20052.

(174) Nagao, K.; Koyano, M.; Katayama, S.; Yamamura, Y.; Tsuji, T. Raman scattering from intercalation compounds Fe_xNbS_2 under high pressure. *Physica Status Solidi (B)* **2001**, *223*, 281–285.

(175) Anzenhofer, K.; Van Den Berg, J.; Cossee, P.; Helle, J. The crystal structure and magnetic susceptibilities of $MnNb_3S_6$, $FeNb_3S_6$, $CoNb_3S_6$ and $NiNb_3S_6$. *Journal of Physics and Chemistry of Solids* **1970**, *31*, 1057–1067.

(176) Pan, S.; Tang, L.; Bai, Y.; Tang, J.; Zhang, Z.; Chen, B.; Guo, Y.; Zhu, J.; Xu, G.; Xu, F. Fe and Cr co-intercalation in 2*H*–NbS_2 single crystals for realization of perpendicular magnetic anisotropy and large anomalous Hall effect. *Physical Review Materials* **2023**, *7*, 034407.

(177) Van Winkle, M.; Craig, I. M.; Carr, S.; Dandu, M.; Bustillo, K. C.; Ciston, J.; Ophus, C.; Taniguchi, T.; Watanabe, K.; Raja, A.; Griffin, S. M.; Bediako, D. K. Rotational and dilational reconstruction in transition metal dichalcogenide moiré bilayers. *Nature Communications* **2023**, *14*, 2989.

(178) Weston, A.; Castanon, E. G.; Enaldiev, V.; Ferreira, F.; Bhattacharjee, S.; Xu, S.; Corte-León, H.; Wu, Z.; Clark, N.; Summerfield, A.; Hashimoto, T.; Gao, Y.; Wang, W.; Hamer, M.; Read, H.; Fumagalli, L.; Kretinin, A. V.; Haigh, S. J.; Kazakova, O.; Geim, A. K.; Fal'ko, V. I.; Gorbachev, R. Interfacial ferroelectricity in marginally twisted 2D semiconductors. *Nature Nanotechnology* **2022**, *17*, 390–395.

(179) Haley, S. C.; Weber, S. F.; Cookmeyer, T.; Parker, D. E.; Maniv, E.; Maksimovic, N.; John, C.; Doyle, S.; Maniv, A.; Ramakrishna, S. K.; Reyes, A. P.; Singleton, J.; Moore, J. E.; Neaton, J. B.; Analytis, J. G. Half-magnetization plateau and the origin of threefold symmetry breaking in an electrically switchable triangular antiferromagnet. *Phys. Rev. Res.* **2020**, *2*, 043020.

(180) Liu, P.; Zhu, H.; Wu, Q.; Lu, Y.; Pu, Y. Unconventional magneto-transport properties of the layered antiferromagnet $Fe_{1/3}NbS_2$. *Applied Physics Letters* **2022**, *121*.

(181) Yamada, H.; Takada, S. Magnetoresistance of antiferromagnetic metals due to s-d interaction. *Journal of the Physical Society of Japan* **1973**, *34*, 51–57.

(182) Kneller, E. F.; Hawig, R. The exchange-spring magnet: a new material principle for permanent magnets. *IEEE Transactions on Magnetics* **1991**, *27*, 3588–3560.

(183) Husremović, S.; Goodge, B. H.; Inzani, K.; Mier, A.; Ribet, S. M.; Bustillo, K. C.; Taniguchi, T.; Watanabe, K.; Ophus, C.; Griffin, S. M.; Bediako, D. K. Encoding multistate charge order and chirality in endotaxial heterostructures. *Nature Communications* **2023**, *14*, 6031.

(184) Savitzky, B. H.; El Baggari, I.; Clement, C. B.; Waite, E.; Goodge, B. H.; Baek, D. J.; Sheckelton, J. P.; Pasco, C.; Nair, H.; Schreiber, N. J.; Hoffman, J.; Admasu, A. S.; Kim, J.; Cheong, S.-W.; Bhattacharya, A.; Schlom, D. G.; McQueen, T. M.; Hovden, R.; Kourkoutis, L. F. Image registration of low signal-to-noise cryo-STEM data. *Ultramicroscopy* **2018**, *191*, 56–65.

(185) Meyer, C.; Dellby, N.; Hachtel, J. A.; Lovejoy, T.; Mittelberger, A.; Krivanek, O. Nion Swift: open source image processing software for instrument control, data acquisition, organization, visualization, and analysis using Python. *Microscopy and Microanalysis* **2019**, *25*, 122–123.

(186) Savitzky, B. H.; Zeltmann, S. E.; Hughes, L. A.; Brown, H. G.; Zhao, S.; Pelz, P. M.; Pekin, T. C.; Barnard, E. S.; Donohue, J.; Rangel DaCosta, L.; Kennedy, E.; Xie, Y.; Janish, M. T.; Schneider, M. M.; Herring, P.; Gopal, C.; Anapolsky, A.; Dhall, R.; Bustillo, K. C.; Ercius, P.; Scott, M. C.; Ciston, J.; Minor, A. M.; Ophus, C. py4DSTEM: a software package for four-dimensional scanning transmission electron microscopy data analysis. *Microscopy and Microanalysis* **2021**, *27*, 712–743.

(187) Yamashita, T.; Hayes, P. Analysis of XPS spectra of Fe^{2+} and Fe^{3+} ions in oxide materials. *Applied Surface Science* **2008**, *254*, 2441–2449.

(188) Roosendaal, S.; Van Asselen, B.; Elsenaar, J.; Vredenberg, A.; Habraken, F. The oxidation state of Fe(100) after initial oxidation in O_2. *Surface Science* **1999**, *442*, 329–337.

(189) Graat, P. C.; Somers, M. A. Simultaneous determination of composition and thickness of thin iron-oxide films from XPS Fe 2p spectra. *Applied Surface Science* **1996**, *100*, 36–40.

(190) Biesinger, M. C.; Payne, B. P.; Grosvenor, A. P.; Lau, L. W.; Gerson, A. R.; Smart, R. S. C. Resolving surface chemical states in XPS analysis of first row transition metals, oxides and hydroxides: Cr, Mn, Fe, Co and Ni. *Applied Surface Science* **2011**, *257*, 2717–2730.

(191) Mills, P.; Sullivan, J. A study of the core level electrons in iron and its three oxides by means of X-ray photoelectron spectroscopy. *Journal of Physics D: Applied Physics* **1983**, *16*, 723.

(192) Hawn, D. D.; DeKoven, B. M. Deconvolution as a correction for photoelectron inelastic energy losses in the core level XPS spectra of iron oxides. *Surface and interface analysis* **1987**, *10*, 63–74.

(193) Muhler, M.; Schlögl, R.; Ertl, G. The nature of the iron oxide-based catalyst for dehydrogenation of ethylbenzene to styrene 2. Surface chemistry of the active phase. *Journal of Catalysis* **1992**, *138*, 413–444.

(194) Kalasina, S.; Kongsawatvoragul, K.; Phattharasupakun, N.; Phattharaphuti, P.; Sawangphruk, M. Cobalt oxysulphide/hydroxide nanosheets with dual properties based on electrochromism and a charge storage mechanism. *RSC Advances* **2020**, *10*, 14154–14160.

(195) Fantin, R.; Van Roekeghem, A.; Benayad, A. Revisiting Co 2p core-level photoemission in $LiCoO_2$ by in-lab soft and hard X-ray photoelectron spectroscopy: A depth-dependent study of cobalt electronic structure. *Surface and Interface Analysis* **2023**, *55*, 489–495.

(196) Stansbury, C.; Lanzara, A. PyARPES: an analysis framework for multimodal angle-resolved photoemission spectroscopies. *SoftwareX* **2020**, *11*, 100472.

(197) Lankhorst, M. H.; Ketelaars, B. W.; Wolters, R. A. Low-cost and nanoscale non-volatile memory concept for future silicon chips. *Nature Materials* **2005**, *4*, 347–352.

(198) Wuttig, M.; Yamada, N. Phase-change materials for rewriteable data storage. *Nature Materials* **2007**, *6*, 824–832.

(199) Stojchevska, L.; Vaskivskyi, I.; Mertelj, T.; Kusar, P.; Svetin, D.; Brazovskii, S.; Mihailovic, D. Ultrafast switching to a stable hidden quantum state in an electronic crystal. *Science* **2014**, *344*, 177–180.

(200) Vaskivskyi, I.; Mihailovic, I.; Brazovskii, S.; Gospodaric, J.; Mertelj, T.; Svetin, D.; Sutar, P.; Mihailovic, D. Fast electronic resistance switching involving hidden charge density wave states. *Nature Communications* **2016**, *7*, 11442.

(201) Tuma, T.; Pantazi, A.; Le Gallo, M.; Sebastian, A.; Eleftheriou, E. Stochastic phase-change neurons. *Nature Nanotechnology* **2016**, *11*, 693–699.

(202) Wen, W.; Zhu, Y.; Dang, C.; Chen, W.; Xie, L. Raman spectroscopic and dynamic electrical investigation of multi-state charge-wave-density phase transitions in $1T$-TaS_2. *Nano Letters* **2019**, *19*, 1805–1813.

(203) Patel, T.; Okamoto, J.; Dekker, T.; Yang, B.; Gao, J.; Luo, X.; Lu, W.; Sun, Y.; Tsen, A. W. Photocurrent imaging of multi-memristive charge density wave switching in two-dimensional $1T$-TaS_2. *Nano Letters* **2020**, *20*, 7200–7206.

(204) Wilson, J. Solution of the $1T_2$ discommensurate state of $1T$-TaS_2. An example of rotated hexagonal discommensuration. *Journal of Physics: Condensed Matter* **1990**, *2*, 1683.

(205) Wilson, J. A.; Di Salvo, F.; Mahajan, S. Charge-density waves and superlattices in the metallic layered transition metal dichalcogenides. *Advances in Physics* **1975**, *24*, 117–201.

(206) Burk, B.; Thomson, R. E.; Zettl, A.; Clarke, J. Charge-density-wave domains in 1T-TaS_2 observed by satellite structure in scanning-tunneling-microscopy images. *Phys. Rev. Lett.* **1991**, *66*, 3040–3043.

(207) Wu, X. L.; Lieber, C. M. Direct observation of growth and melting of the hexagonal-domain charge-density-wave phase in 1T-TaS_2 by scanning tunneling microscopy. *Physical Review Letters* **1990**, *64*, 1150–1153.

(208) Tsen, A. W.; Hovden, R.; Wang, D.; Kim, Y. D.; Okamoto, J.; Spoth, K. A.; Liu, Y.; Lu, W.; Sun, Y.; Hone, J. C.; Kourkoutis, L. F.; Kim, P.; Pasupathy, A. N. Structure and control of charge density waves in two-dimensional $1T$-TaS_2. *Proceedings of the National Academy of Sciences* **2015**, *112*, 15054–15059.

(209) Yu, Y.; Yang, F.; Lu, X. F.; Yan, Y. J.; Cho, Y. H.; Ma, L.; Niu, X.; Kim, S.; Son, Y. W.; Feng, D.; Li, S.; Cheong, S. W.; Chen, X. H.; Zhang, Y. Gate-tunable phase transitions in thin flakes of $1T$-TaS_2. *Nature Nanotechnology* **2015**, *10*, 270–276.

(210) Ishiguro, Y.; Bogdanov, K.; Kodama, N.; Ogiba, M.; Ohno, T.; Baranov, A.; Takai, K. Layer number dependence of charge density wave phase transition between nearly-commensurate and incommensurate phases in $1T$-TaS_2. *The Journal of Physical Chemistry C* **2020**, *124*, 27176–27184.

(211) Yoshida, M.; Zhang, Y.; Ye, J.; Suzuki, R.; Imai, Y.; Kimura, S.; Fujiwara, A.; Iwasa, Y. Controlling charge-density-wave states in nano-thick crystals of 1T-TaS_2. *Scientific Reports* **2014**, *4*, 1–5.

(212) Li, L.; Lu, W.; Zhu, X.; Ling, L.; Qu, Z.; Sun, Y. Fe-doping–induced superconductivity in the charge-density-wave system 1T-TaS_2. *Europhysics Letters* **2012**, *97*, 67005.

(213) Wang, Z.; Chu, L.; Li, L.; Yang, M.; Wang, J.; Eda, G.; Loh, K. P. Modulating charge density wave order in a 1T-TaS_2/Black phosphorus heterostructure. *Nano Letters* **2019**, *19*, 2840–2849.

(214) Vaňo, V.; Amini, M.; Ganguli, S. C.; Chen, G.; Lado, J. L.; Kezilebieke, S.; Liljeroth, P. Artificial heavy fermions in a van der Waals heterostructure. *Nature* **2021**, *599*, 582–586.

(215) Ravnik, J.; Vaskivskyi, I.; Gerasimenko, Y.; Diego, M.; Vodeb, J.; Kabanov, V.; Mihailovic, D. D. Strain-Induced metastable topological networks in laser-fabricated TaS_2 polytype heterostructures for nanoscale devices. *ACS Applied Nano Materials* **2019**, *2*, 3743–3751.

(216) Sung, S. H.; Schnitzer, N.; Novakov, S.; El Baggari, I.; Luo, X.; Gim, J.; Vu, N. M.; Li, Z.; Brintlinger, T. H.; Liu, Y.; Lu, W.; Sun, Y.; Deotare, P. B.; Sun, K.; Zhao, L.; Kourkoutis, L. F.; Heron, J. T.; Hovden, R. Two-dimensional charge order stabilized in clean polytype heterostructures. *Nature Communications* **2022**, *13*, 413.

(217) Ribak, A.; Skiff, R. M.; Mograbi, M.; Rout, P. K.; Fischer, M. H.; Ruhman, J.; Chashka, K.; Dagan, Y.; Kanigel, A. Chiral superconductivity in the alternate stacking compound 4Hb-TaS_2. *Science Advances* **2020**, *6*, eaax9480.

(218) Kuwabara, M.; Hashimoto, H.; Endoh, H. Study of the commensurate superstructure in 4Hb-TaS_2 by high resolution electron microscopy. *Japanese Journal of Applied Physics* **1986**, *25*, L1.

(219) Liu, L.; Song, X.; Dai, J.; Yang, H.; Chen, Y.; Huang, X.; Huang, Z.; Ji, H.; Zhang, Y.; Wu, X.; Sun, J.-T.; Zhang, Q.; Zhou, J.; Huang, Y.; Qiao, J.; Ji, W.; Gao, H.-J.; Wang, Y. Unveiling Electronic Behaviors in Heterochiral Charge-Density-Wave Twisted Stacking Materials with 1.25 nm Unit Dependence. *ACS Nano* **2023**.

(220) He, R.; Okamoto, J.; Ye, Z.; Ye, G.; Anderson, H.; Dai, X.; Wu, X.; Hu, J.; Liu, Y.; Lu, W.; Sun, Y.; Pasupathy, A. N.; Tsen, A. W. Distinct surface and bulk charge density waves in ultrathin 1T-TaS_2. *Physical Review B* **2016**, *94*, 201108.

(221) Duffey, J.; Kirby, R.; Coleman, R. Raman scattering from 1T-TaS_2. *Solid State Communications* **1976**, *20*, 617–621.

(222) Sugai, S.; Murase, K.; Uchida, S.; Tanaka, S. Comparison of the soft modes in tantalum dichalcogenides. *Physica B+C* **1981**, *105*, 405–409.

(223) Van Landuyt, J.; Van Tendeloo, G.; Amelinckx, S. Electron diffraction study of inter- and intrapolytypic phase transitions in transition metal dichalcogenides. I. Electron diffraction patterns. *Physica Status Solidi (A)* **1974**, *26*, 359–376.

(224) Ophus, C. Four-dimensional scanning transmission electron microscopy (4D-STEM): From scanning nanodiffraction to ptychography and beyond. *Microscopy and Microanalysis* **2019**, *25*, 563–582.

(225) Zhao, Y.; Nie, Z.; Hong, H.; Qiu, X.; Han, S.; Yu, Y.; Liu, M.; Qiu, X.; Liu, K.; Meng, S.; Tong, L.; Zhang, J. Spectroscopic visualization and phase manipulation of chiral charge density waves in 1T-TaS_2. *Nature Communications* **2023**, *14*, 2223.

(226) Yang, H. F.; He, K. Y.; Koo, J.; Shen, S. W.; Zhang, S. H.; Liu, G.; Liu, Y. Z.; Chen, C.; Liang, A. J.; Huang, K.; Wang, M. X.; Gao, J. J.; Luo, X.; Yang, L. X.; Liu, J. P.; Sun, Y. P.; Yan, S. C.; Yan, B. H.; Chen, Y. L.; Xi, X.; Liu, Z. K. Visualization of chiral electronic structure and anomalous optical response in a material with chiral charge density waves. *Physical Review Letters* **2022**, *129*, 156401.

(227) Su, J.-D.; Sandy, A. R.; Mohanty, J.; Shpyrko, O. G.; Sutton, M. Collective pinning dynamics of charge-density waves in 1T-TaS_2. *Phys. Rev. B* **2012**, *86*, 205105.

(228) Han, E.; Yu, J.; Annevelink, E.; Son, J.; Kang, D. A.; Watanabe, K.; Taniguchi, T.; Ertekin, E.; Huang, P. Y.; van der Zande, A. M. Ultrasoft slip-mediated bending in few-layer graphene. *Nature Materials* **2020**, *19*, 305–309.

(229) Sun, Y.; Liu, K. Strain engineering in functional 2-dimensional materials. *Journal of Applied Physics* **2019**, *125*, 082402.

(230) Kim, J. M.; Haque, M. F.; Hsieh, E. Y.; Nahid, S. M.; Zarin, I.; Jeong, K.-Y.; So, J.-P.; Park, H.-G.; Nam, S. Strain engineering of low-dimensional materials for emerging quantum phenomena and functionalities. *Advanced Materials* **2022**, 2107362.

(231) Song, S.; Keum, D. H.; Cho, S.; Perello, D.; Kim, Y.; Lee, Y. H. Room temperature semiconductor–metal transition of $MoTe_2$ thin films engineered by strain. *Nano Letters* **2016**, *16*, 188–193.

(232) Fair, K.; Ford, M. Phase transitions and optical properties of the semiconducting and metallic phases of single-layer MoS_2. *Nanotechnology* **2015**, *26*, 435705.

(233) Li, X.; Wu, M.; Xu, B.; Liu, R.; Ouyang, C. Compressive strain induced dynamical stability of monolayer 1T-MX_2 (M= Mo, W; X= S, Se). *Materials Research Express* **2017**, *4*, 115018.

(234) Thomas, A.; Vikram, K.; Muthu, D.; Sood, A. Structural phase transition from 1H to 1T' at low pressure in supported monolayer WS_2: Raman study. *Solid State Communications* **2021**, *336*, 114412.

(235) Hollander, M. J.; Liu, Y.; Lu, W.-J.; Li, L.-J.; Sun, Y.-P.; Robinson, J. A.; Datta, S. Electrically driven reversible insulator–metal phase transition in 1T-TaS_2. *Nano Letters* **2015**, *15*, 1861–1866.

(236) Song, X.; Liu, L.; Chen, Y.; Yang, H.; Huang, Z.; Hou, B.; Hou, Y.; Han, X.; Yang, H.; Zhang, Q.; Zhang, T.; Zhou, J.; Huang, Y.; Zhang, Y.; Gao, H.-J.; Wang, Y. Atomic-scale visualization of chiral charge density wave superlattices and their reversible switching. *Nature Communications* **2022**, *13*, 1843.

(237) Taheri, M.; Brown, J.; Rehman, A.; Sesing, N.; Kargar, F.; Salguero, T. T.; Rumyantsev, S.; Balandin, A. A. Electrical gating of the charge-density-wave phases in two-dimensional hBN/1T-TaS_2 devices. *ACS Nano* **2022**, *16*, 18968–18977.

(238) Zong, A.; Shen, X.; Kogar, A.; Ye, L.; Marks, C.; Chowdhury, D.; Rohwer, T.; Freelon, B.; Weathersby, S.; Li, R.; Yang, J.; Checkelsky, J.; Wang, X.; Gedik, N. Ultrafast manipulation of mirror domain walls in a charge density wave. *Science Advances* **2018**, *4*, eaau5501.

(239) Lazić, I.; Bosch, E. G.; Lazar, S. Phase contrast STEM for thin samples: integrated differential phase contrast. *Ultramicroscopy* **2016**, *160*, 265–280.

(240) Li, H.; Wu, J.; Huang, X.; Lu, G.; Yang, J.; Lu, X.; Xiong, Q.; Zhang, H. Rapid and reliable thickness identification of two-dimensional nanosheets using optical microscopy. *ACS Nano* **2013**, *7*, 10344–10353.

(241) Perdew, J. P.; Ruzsinszky, A.; Csonka, G. I.; Vydrov, O. A.; Scuseria, G. E.; Constantin, L. A.; Zhou, X.; Burke, K. Restoring the density-gradient expansion for exchange in solids and surfaces. *Physical Review Letters* **2008**, *100*, 136406.

(242) Nakata, Y.; Sugawara, K.; Chainani, A.; Oka, H.; Bao, C.; Zhou, S.; Chuang, P.-Y.; Cheng, C.-M.; Kawakami, T.; Saruta, Y.; Fukumura, T.; Zhou, S.; Takahashi, T.; Sato, T. Robust charge-density wave strengthened by electron correlations in monolayer 1T-$TaSe_2$ and 1T-$NbSe_2$. *Nature Communications* **2021**, *12*, 1–9.

(243) Hall, J.; Ehlen, N.; Berges, J.; van Loon, E.; van Efferen, C.; Murray, C.; Rösner, M.; Li, J.; Senkovskiy, B. V.; Hell, M.; Rolf, M.; Heider, T.; Asensio, M. C.; Avila, J.; Plucinski, L.; Wehling, T.; Grüneis, A.; Michely, T. Environmental control of charge density wave order in monolayer 2H-TaS_2. *ACS Nano* **2019**, *13*, 10210–10220.

(244) Morosan, E.; Zandbergen, H. W.; Dennis, B.; Bos, J.; Onose, Y.; Klimczuk, T.; Ramirez, A.; Ong, N.; Cava, R. J. Superconductivity in Cu_xTiSe_2. *Nature Physics* **2006**, *2*, 544–550.

(245) Niu, Q.; Zhang, W.; Chan, Y. T.; O'Farrell, E. C. T.; Doganov, R.; Yip, K. Y.; Lai, K. T.; Yu, W. C.; Özyilmaz, B.; Stewart, G. R.; Kim, J. S.; Goh, S. K. Stabilization of antiferromagnetism in 1T-$Fe_{0.05}TaS_2$. *Physical Review Research* **2020**, *2*, 023297.

(246) Maksimovic, N.; Day, R.; Liebman-Peláez, A.; Wan, F.; Jo, N.-H.; Jozwiak, C.; Bostwick, A.; Rotenberg, E.; Griffin, S.; Singleton, J.; Analytis, J. G. Strongly correlated itinerant magnetism near superconductivity in $NiTa_4Se_8$. *Physical Review B* **2022**, *106*, 224429.

(247) Chen, S.; Huang, C.; Sun, H.; Ding, J.; Jena, P.; Kan, E. Boosting the Curie temperature of two-dimensional semiconducting CrI_3 monolayer through van der Waals heterostructures. *The Journal of Physical Chemistry C* **2019**, *123*, 17987–17993.

(248) Bonilla, M.; Kolekar, S.; Li, J.; Xin, Y.; Coelho, P. M.; Lasek, K.; Zberecki, K.; Lizzit, D.; Tosi, E.; Lacovig, P.; Lizzit, S.; Batzill, M. Compositional phase change of early transition metal diselenide (VSe_2 and $TiSe_2$) ultrathin films by postgrowth annealing. *Advanced Materials Interfaces* **2020**, *7*, 2000497.

(249) Tsang, J.; Shafer, M. Raman spectroscopy of intercalated layered structure compounds. *Solid State Communications* **1978**, *25*, 999–1002.

(250) Mutka, H.; Housseau, N. The pinning of the charge density wave to irradiation-induced defects satellite reflection dark-field micrographs of 1*T*-TaS_2. *Philosophical Magazine A* **1983**, *47*, 797–816.

(251) Fujisawa, Y.; Shimabukuro, T.; Kojima, H.; Kobayashi, K.; Demura, S.; Sakata, H. In *Journal of Physics: Conference Series*, 2017; Vol. 871, p 012003.

(252) Zhang, W.; Gao, J.; Cheng, L.; Bu, K.; Wu, Z.; Fei, Y.; Zheng, Y.; Wang, L.; Li, F.; Luo, X.; Liu, Z.; Sun, Y.; Yin, Y. Visualizing the evolution from Mott insulator to Anderson insulator in Ti-doped 1*T*-TaS_2. *NPJ Quantum Materials* **2022**, *7*, 8.

(253) Lutsyk, I.; Szalowski, K.; Krukowski, P.; Dabrowski, P.; Rogala, M.; Kozlowski, W.; Le Ster, M.; Piskorski, M.; Kowalczyk, D. A.; Rys, W.; Dunal, R.; Nadolska, A.; Toczek, K.; Przybysz, P.; Lacinska, E.; Binder, J.; Wysmolek, A.; Olszowska, N.; Kolodziej, J. J.; Gmitra, M.; Hattori, T.; Kuwahara, Y.; Bian, G.; Chiang, T.-C.; Kowalczyk, P. J. Influence of structural defects on charge density waves in 1*T*-TaS_2. *Nano Research* **2023**, *16*, 11528–11539.

(254) Lacinska, E. M.; Furman, M.; Binder, J.; Lutsyk, I.; Kowalczyk, P. J.; Stepniewski, R.; Wysmolek, A. Raman Optical Activity of 1*T*-TaS_2. *Nano Letters* **2022**, *22*, 2835–2842.

(255) Hovden, R.; Tsen, A. W.; Liu, P.; Savitzky, B. H.; Baggari, I. E.; Liu, Y.; Lu, W.; Sun, Y.; Kim, P.; Pasupathy, A. N.; Kourkoutis, L. F. Atomic lattice disorder in charge-density-wave phases of exfoliated dichalcogenides (1T-TaS¡sub¿2¡/sub¿). *Proceedings of the National Academy of Sciences* **2016**, *113*, 11420–11424.

(256) Yamamoto, A. Hexagonal domainlike structure in 1*T*-TaS_2. *Physical Review B* **1983**, *27*, 7823.

(257) Yamada, Y.; Takatera, H. Origin of the stabilization of the nearly commensurate phase in 1*T*-TaS_2. *Solid State Communications* **1977**, *21*, 41–44.

(258) Ritschel, T.; Berger, H.; Geck, J. Stacking-driven gap formation in layered 1*T*-TaS_2. *Physical Review B* **2018**, *98*, 195134.

(259) Martino, E.; Pisoni, A.; Ćirić, L.; Arakcheeva, A.; Berger, H.; Akrap, A.; Putzke, C.; Moll, P. J. W.; Batistić, I.; Tutiš, E.; Forró, L.; Semeniuk, K. Preferential out-of-plane conduction and quasi-one-dimensional electronic states in layered $1T$-TaS_2. *npj 2D Materials and Applications* **2020**, *4*, 7.

(260) Chen, M.; Zhou, B.; Wang, F.; Xu, L.; Jiang, K.; Shang, L.; Hu, Z.; Chu, J. Interlayer coupling and the phase transition mechanism of stacked MoS_2/TaS_2 heterostructures discovered using temperature dependent Raman and photoluminescence spectroscopy. *RSC Advances* **2018**, *8*, 21968–21974.

(261) Zhao, R.; Wang, Y.; Deng, D.; Luo, X.; Lu, W. J.; Sun, Y.-P.; Liu, Z.-K.; Chen, L.-Q.; Robinson, J. Tuning phase transitions in $1T$-TaS_2 via the substrate. *Nano Letters* **2017**, *17*, 3471–3477.

(262) Li, Y.; Xiao, H.; Zhou, P.; Cao, J. Electronic structures of twist-stacked $1T$-TaS_2 bilayers. *Physics Letters A* **2019**, *383*, 2302–2308.

(263) Goodwin, Z. A. H.; Fal'ko, V. I. Moiré modulation of charge density waves. *Journal of Physics: Condensed Matter* **2022**, *34*, 494001.

(264) Wei, M. J.; Lu, W. J.; Xiao, R. C.; Lv, H. Y.; Tong, P.; Song, W. H.; Sun, Y. P. Manipulating charge density wave order in monolayer $1T - TiSe_2$ by strain and charge doping: A first-principles investigation. *Physical Review B* **2017**, *96*, 165404.

(265) Dreher, P.; Wan, W.; Chikina, A.; Bianchi, M.; Guo, H.; Harsh, R.; Mañas-Valero, S.; Coronado, E.; Martínez-Galera, A. J.; Hofmann, P.; Miwa, J. A.; Ugeda, M. M. Proximity effects on the charge density wave order and superconductivity in single-layer $NbSe_2$. *ACS Nano* **2021**, *15*, 19430–19438.

(266) Liu, Y.; Ang, R.; Lu, W. J. Superconductivity induced by Se-doping in layered charge-density-wave system $1T$-$TaS_{2-x}Se_x$. *Appl. Phys. Lett.* **2013**, *102*, 192602.

(267) Jung, J.; Jin, K.-H.; Kim, J.; Yeom, H. W. Control over a wide phase diagram of 2D correlated electrons by surface doping; $K/1T$-TaS_2. *Nano Letters* **2023**, *23*, 8029–8034.

(268) Chen, X. M.; Miller, A. J.; Nugroho, C.; De La Peña, G. A.; Joe, Y. I.; Kogar, A.; Brock, J. D.; Geck, J.; MacDougall, G. J.; Cooper, S. L.; Fradkin, E.; Van Harlingen, D. J.; Abbamonte, P. Influence of Ti doping on the incommensurate charge density wave in $1T$-TaS_2. *Physical Review B* **2015**, *91*, 245113.

(269) Nessralla, J.; Larson, D. T.; Taniguchi, T.; Watanabe, K.; Kaxiras, E.; Bediako, D. K. Modulating the electrochemical intercalation of graphene interfaces with α-$RuCl_3$ as a solid-state electron acceptor. *Nano Letters* **2023**.

(270) Bediako, D. K.; Rezaee, M.; Yoo, H.; Larson, D. T.; Zhao, S. F.; Taniguchi, T.; Watanabe, K.; Brower-Thomas, T. L.; Kaxiras, E.; Kim, P. Heterointerface effects in the electrointercalation of van der Waals heterostructures. *Nature* **2018**, *558*, 425–429.

(271) Kazmierczak, N. P.; Van Winkle, M.; Ophus, C.; Bustillo, K. C.; Carr, S.; Brown, H. G.; Ciston, J.; Taniguchi, T.; Watanabe, K.; Bediako, D. K. Strain fields in twisted bilayer graphene. *Nature Materials* **2021**, *20*, 956–963.

(272) Zhao, W. M.; Zhu, L.; Nie, Z.; Li, Q. Y.; Wang, Q. W.; Dou, L. G.; Hu, J. G.; Xian, L.; Meng, S.; Li, S. C. Moiré enhanced charge density wave state in Twisted ${}_1T-\mathrm{TiTe_2}/{}_1T-\mathrm{TiSe_2}$ Heterostructures. *Nature Materials 2021 21:3* **2021**, *21*, 284–289.

(273) Nicholson, C. W.; Petocchi, F.; Salzmann, B.; Witteveen, C.; Rumo, M.; Kremer, G.; Ivashko, O.; Von Rohr, F. O.; Werner, P.; Monney, C. Gap collapse and flat band induced by uniaxial strain in $1T$-$\mathrm{TaS_2}$. *Physical Review B* **2024**, *109*, 035167.

(274) Gan, L.-Y.; Zhang, L.-H.; Zhang, Q.; Guo, C.-S.; Schwingenschlögl, U.; Zhao, Y. Strain tuning of the charge density wave in monolayer and bilayer $1T$-$\mathrm{TaS_2}$. *Physical Chemistry Chemical Physics* **2016**, *18*, 3080–3085.

(275) Wang, Y. D.; Yao, W. L.; Xin, Z. M.; Han, T. T.; Wang, Z. G.; Chen, L.; Cai, C.; Li, Y.; Zhang, Y. Band insulator to Mott insulator transition in $1T$-$\mathrm{TaS_2}$. *Nature Communications* **2020**, *11*, 4215.

(276) Sohrt, C.; Stange, A.; Bauer, M.; Rossnagel, K. How fast can a Peierls–Mott insulator be melted? *Faraday discussions* **2014**, *171*, 243–257.

(277) Albertini, O. R.; Zhao, R.; McCann, R. L.; Feng, S.; Terrones, M.; Freericks, J. K.; Robinson, J. A.; Liu, A. Y. Zone-center phonons of bulk, few-layer, and monolayer $1T$-$\mathrm{TaS_2}$: Detection of commensurate charge density wave phase through Raman scattering. *Physical Review B* **2016**, *93*, 214109.

(278) Yoo, H.; Engelke, R.; Carr, S.; Fang, S.; Zhang, K.; Cazeaux, P.; Sung, S. H.; Hovden, R.; Tsen, A. W.; Taniguchi, T.; Watanabe, K.; Yi, G.-C.; Kim, M.; Luskin, M.; Tadmor, E. B.; Kaxiras, E.; Kim, P. Atomic and electronic reconstruction at the van der Waals interface in twisted bilayer graphene. *Nature Materials* **2019**, *18*, 448–453.

(279) Weston, A.; Zou, Y.; Enaldiev, V.; Summerfield, A.; Clark, N.; Zólyomi, V.; Graham, A.; Yelgel, C.; Magorrian, S.; Zhou, M.; Zultak, J.; Hopkinson, D.; Barinov, A.; Bointon, T. H.; Kretinin, A.; Wilson, N. R.; Beton, P. H.; Fal'ko, V. I.; Haigh, S. J.; Gorbachev, R. Atomic reconstruction in twisted bilayers of transition metal dichalcogenides. *Nature Nanotechnology* **2020**, *15*, 592–597.

(280) Meijerink, A.; Blasse, G.; Sytsma, J.; de Mello Donega, C.; Ellens, A. Electron-phonon coupling in rare earth compounds. *Acta Physica Polonica A* **1996**, *90*, 109–119.

(281) Terrones, H.; Del Corro, E.; Feng, S.; Poumirol, J. M.; Rhodes, D.; Smirnov, D.; Pradhan, N. R.; Lin, Z.; Nguyen, M. A. T.; Elías, A. L.; Mallouk, T. E.; Balicas, L.; Pimenta, M. A.; Terrones, M. New first order Raman-active modes in few layered transition metal dichalcogenides. *Scientific Reports* **2014**, *4*, 4215.

(282) Shi, W.; Lin, M.-L.; Tan, Q.-H.; Qiao, X.-F.; Zhang, J.; Tan, P.-H. Raman and photoluminescence spectra of two-dimensional nanocrystallites of monolayer WS2 and WSe2. *2D Materials* **2016**, *3*, 025016.

(283) Lv, Y.; Abid, M.; Cheng, H.; Coileáin, C. Ó.; Sofin, R. S.; Chang, C.-R.; Wu, H.-C. Strain-dependent optical properties of monolayer WSe_2. *The Journal of Physical Chemistry C* **2023**, *127*, 22682–22691.

(284) Rahman, S.; Sun, X.; Zhu, Y.; Lu, Y. Extraordinary phonon displacement and giant resonance Raman enhancement in WSe_2/WS_2 moiré heterostructures. *ACS Nano* **2022**, *16*, 21505–21517.

(285) Quan, J.; Linhart, L.; Lin, M.-L.; Lee, D.; Zhu, J.; Wang, C.-Y.; Hsu, W.-T.; Choi, J.; Embley, J.; Young, C.; Taniguchi, T.; Watanabe, K.; Shih, C.-K.; Lai, K.; MacDonald, A. H.; Tan, P.-H.; Libisch, F.; Li, X. Phonon renormalization in reconstructed MoS_2 moiré superlattices. *Nature Materials* **2021**, *20*, 1100–1105.

(286) Roy, S.; Yang, X.; Gao, J. Uniaxial strain tuning of upconversion photoluminescence in monolayer WSe_2. *Advanced Photonics Research* **2023**, 2300220.

(287) Liu, K.; Zhang, L.; Cao, T.; Jin, C.; Qiu, D.; Zhou, Q.; Zettl, A.; Yang, P.; Louie, S. G.; Wang, F. Evolution of interlayer coupling in twisted molybdenum disulfide bilayers. *Nature Communications* **2014**, *5*, 4966.

(288) Yagmurcukardes, M.; Bacaksiz, C.; Unsal, E.; Akbali, B.; Senger, R. T.; Sahin, H. Strain mapping in single-layer two-dimensional crystals via Raman activity. *Physical Review B* **2018**, *97*, 115427.

(289) Wu, L.; Cong, C.; Shang, J.; Yang, W.; Chen, Y.; Zhou, J.; Ai, W.; Wang, Y.; Feng, S.; Zhang, H.; Liu, Z.; Yu, T. Raman scattering investigation of twisted WS_2/MoS_2 heterostructures: interlayer mechanical coupling versus charge transfer. *Nano Research* **2021**, *14*, 2215–2223.

(290) Wang, Y.; Cong, C.; Qiu, C.; Yu, T. Raman spectroscopy study of lattice vibration and crystallographic orientation of monolayer MoS_2 under uniaxial strain. *Small* **2013**, *9*, 2857–2861.

(291) Rice, C.; Young, R.; Zan, R.; Bangert, U.; Wolverson, D.; Georgiou, T.; Jalil, R.; Novoselov, K. Raman-scattering measurements and first-principles calculations of strain-induced phonon shifts in monolayer MoS_2. *Physical Review B* **2013**, *87*, 081307.

(292) Zhang, X.; Qiao, X.-F.; Shi, W.; Wu, J.-B.; Jiang, D.-S.; Tan, P.-H. Phonon and Raman scattering of two-dimensional transition metal dichalcogenides from monolayer, multilayer to bulk material. *Chemical Society Reviews* **2015**, *44*, 2757–2785.

(293) Debnath, R.; Maity, I.; Biswas, R.; Raghunathan, V.; Jain, M.; Ghosh, A. Evolution of high-frequency Raman modes and their doping dependence in twisted bilayer MoS_2. *Nanoscale* **2020**, *12*, 17272–17280.

(294) Fan, S.; Yun, S. J.; Yu, W. J.; Lee, Y. H. Tailoring quantum tunneling in a vanadium-doped $WSe_2/SnSe_2$ heterostructure. *Advanced Science* **2020**, *7*, 1902751.

(295) Dandu, M.; Watanabe, K.; Taniguchi, T.; Sood, A. K.; Majumdar, K. Spectrally tunable, large Raman enhancement from nonradiative energy transfer in the van der Waals heterostructure. *ACS Photonics* **2020**, *7*, 519–527.

(296) Hill, H. M.; Rigosi, A. F.; Raja, A.; Chernikov, A.; Roquelet, C.; Heinz, T. F. Exciton broadening in WS_2/graphene heterostructures. *Physical Review B* **2017**, *96*, 205401.

(297) Rigosi, A. F.; Hill, H. M.; Li, Y.; Chernikov, A.; Heinz, T. F. Probing interlayer interactions in transition metal dichalcogenide heterostructures by optical spectroscopy: MoS_2/WS_2 and $MoSe_2/WSe_2$. *Nano Letters* **2015**, *15*, 5033–5038.

(298) Shrestha, S.; Cotlet, M. Interfacial charge transfer in atomically thin 2D transition-metal dichalcogenide heterostructures. *ACS Applied Optical Materials* **2023**, *1*, 1192–1207.

(299) Raja, A.; Chaves, A.; Yu, J.; Arefe, G.; Hill, H. M.; Rigosi, A. F.; Berkelbach, T. C.; Nagler, P.; Schüller, C.; Korn, T.; Nuckolls, C.; Hone, J.; Brus, L. E.; Heinz, T. F.; Reichman, D. R.; Chernikov, A. Coulomb engineering of the bandgap and excitons in two-dimensional materials. *Nature Communications* **2017**, *8*, 15251.

(300) Chernikov, A.; Van Der Zande, A. M.; Hill, H. M.; Rigosi, A. F.; Velauthapillai, A.; Hone, J.; Heinz, T. F. Electrical tuning of exciton binding energies in monolayer WS_2. *Physical Review Letters* **2015**, *115*, 126802.

(301) McGraw, V. Modification of Two-Dimensional Charge Density Wave Materials Through Electrochemical Intercalation and Interfacial Interactions, Ph.D. Thesis, University of California, Berkeley, 2024.

(302) Naik, S.; Naik, M. H.; Maity, I.; Jain, M. Twister: construction and structural relaxation of commensurate moiré superlattices. *Computer Physics Communications* **2022**, *271*, 108184.

(303) Naik, M. H.; Jain, M. Ultraflatbands and shear solitons in moiré patterns of twisted bilayer transition metal dichalcogenides. *Physical Review Letters* **2018**, *121*, Publisher: American Physical Society, 266401.

(304) Dudarev, S. L.; Botton, G. A.; Savrasov, S. Y.; Humphreys, C. J.; Sutton, A. P. Electron-energy-loss spectra and the structural stability of nickel oxide: An LSDA+U study. *Physical Review B* **1998**, *57*, 1505–1509.

(305) Boix-Constant, C.; Mañas-Valero, S.; Córdoba, R.; Baldoví, J. J.; Rubio, Á.; Coronado, E. Out-of-plane transport of 1*T*-TaS_2/graphene-based van der Waals heterostructures. *ACS Nano* **2021**, *15*, 11898–11907.

(306) Ganose, A. M.; Jackson, A. J.; Scanlon, D. O. sumo: command-line tools for plotting and analysis of periodic *ab initio* calculations. *Journal of Open Source Software* **2018**, *3*, 717.

(307) Zhu, B.; Kavanagh, S. R.; Scanlon, D. easyunfold: a Python package for unfolding electronic band structures. *Journal of Open Source Software* **2024**, *9*, 5974.

(308) Wang, V.; Xu, N.; Liu, J.-C.; Tang, G.; Geng, W.-T. VASPKIT: a user-friendly interface facilitating high-throughput computing and analysis using VASP code. *Computer Physics Communications* **2021**, *267*, 108033.

(309) Momma, K.; Izumi, F. VESTA: a three-dimensional visualization system for electronic and structural analysis. *Journal of Applied Crystallography* **2008**, *41*, 653–658.